Characterization of a Crustal Transition Zone in Northern Tibet using Magnetotelluric Modelling

by

Florian Le Pape

A thesis submitted to The Faculty of Science, National University of Ireland, Galway in fulfilment of the requirements for the degree of

Doctor of Philosophy

2013

Supervision by:

Prof. Dr. Alan G. Jones
Dublin Institute
for Advanced Studies
Dublin, Ireland

Dr. Colin Brown
National University
of Ireland
Galway, Ireland

School of Cosmic Physics
Geophysics Section
Dublin Institute
for Advanced Studies
Dublin, Ireland

Faculty of Science
Department of
Earth and Ocean Sciences
National University of Ireland
Galway, Ireland

ABSTRACT

The overall objective of the final phase of the INDEPTH (International Deep Profiling of Tibet and Himalaya) project has been to develop a better understanding of the structure and evolution of the northern margins of the Tibetan plateau, namely the Kunlun and Altyn Tagh faults. For the Kunlun Fault, both INDEPTH Phase III and new Phase IV magnetotelluric (MT) data were investigated using 2D isotropic and anisotropic modelling, as well as 3D modelling. The resulting resistivity models characterize a northwards penetrative extension of the partially molten Tibetan middle crust, crossing the subvertical Kunlun Fault. Furthermore, the anisotropic observations highlighted by the INDEPTH MT modelling define progressive finger-like melt intrusion beneath the Kunlun Shan. However, this intrusion may not be homogeneous along the whole of the northern Tibetan border along the Kunlun Fault, as its depth and horizontal extension are likely to vary. The partial melt associated with the anisotropic anomaly observed on the INDEPTH resistivity models may have been triggered by strain heating associated with heat production during ductile deformation in a mid-crustal shear zone located beneath the Kunlun fault in the southern Kunlun ranges. This shear zone might be characterized by different levels of strain along the whole of the northern Tibetan border and may have developed into separated channels where the Songpan-Ganzi partially molten crust flows to the north, mechanically weakening the Kunlun crust. Melt penetration across the Kunlun Fault through intrusive channels likely accommodates crustal shortening in northern Tibet, but may also characterize a transition zone between the weak partially molten crust of the plateau and the more rigid Qaidam lithosphere, associated with the growth of the plateau to the north.

Peer Reviewed Papers:

Le Pape, F., Jones, A. G.,Vozar, J. & Wenbo,W. (2012). Penetration of crustal melt beyond the Kunlun Fault into northern Tibet. Nature Geoscience 5, 330-335.

ACKNOWLEDGMENTS

First I would like to thank my supervisor Alan Jones for his scientific advice and inspiration, and for encouraging me to think more independently during my PhD. He has also given me the opportunity to meet with scientists all around the world and to present my work on many occasions.

My gratitude also goes out to my second adviser Colin Brown for his guidance and for entrusting me with this research.

Thank you to Mark Muller, Jan Vozar and Javier Fuella for their significant support, advice and inspiration.

I also would like to thank Wenbo Wei, Martyn Unsworth, Larry Brown, Alan Jones, Jan Vozar, Sheng Jin, Gaofeng Ye, Jianen Jing, Hao Dong, Letian Zhang, Chengliang Xie and particularly the China University of Geosciences, Beijing (CUGB) MT fieldwork crew for their strong support during the INDEPTH IV MT field campaign.

Thank you to Martyn Unsworth and the INDEPTH team for providing the INDEPTH III MT data. I am also very grateful to the CUGB for sharing additional magnetotelluric data to the INDEPTH IV profile, which enabled me to complete this work. Thank you also to Hao Dong and Gaofeng Ye for providing matlab ws3dinv graphics 3D interface.

I am also grateful to Marianne Karplus and Matthew Agius for sharing their work and data, and for the constructive discussions we had about Tibet.

I would like to thank the Science Foundation of Ireland (SFI) for the financial support and also the Irish Centre for High Performance Computing (ICHEC) for availing the STOKES cluster to carry out the numerical computations.

I also would like to thank all colleagues and friends from DIAS for all the science shared but most of all for the joyful atmosphere and enthusiasm they all bring in the building as it kept me going and motivated.

Finally, I would like to thank my parents and family for their love and significant support.

CONTENTS

Below is a list of symbols and nomenclature used within this thesis and their meanings as well as their SI units. Vectors are defined by an arrow above the symbols whereas matrices/tensors are highlighted by bold-face symbols. Descriptions separated by a coma characterize different definition for one symbol.

Symbol	Description (SI units)
A	Ampere
Ag	silver
$\vec{B}$ / $\vec{b}$	magnetic induction (Tesla)
β	phase tensor skew angle (°); partitioning between tube and cube distributions
C	Schmucker-Weidelt transfer function (m); Archie's law empirical; coefficient; conductance (S); Coulomb
$\mathbf{C}$	telluric distortion tensor
Cl	chlor
Cu	copper
$\vec{D}$ / $\vec{d}$	electric displacement in frequency/time domain ($C.m^{-2}$)
δ	penetration depth (m); loss angle (°)
ΔV	activation volume ($cm^3.mol^{-1}$)
$\vec{E}$ / $\vec{e}$	electric field in frequency/time domain ($V.m^{-1}$)
D_i	ion coefficient of diffusion ($m^2.s^{-1}$)
E_a	activation energy (J)
ϵ	dielectric permittivity ($F.m^{-1}$)
ϵ_0	free space dielectric permittivity ($F.m^{-1}$)
ϵ_{eff}	effective dielectric permittivity ($F.m^{-1}$)
η	porosity
f	frequency (Hz)
F	Faraday (unit); forward modelling operator
Fe	iron
$\vec{H}$ / $\vec{h}$	magnetic field ($S.m^{-1}$)
H_r	Haven ratio
i	complex number
Im	imaginary part of a complex number
J	Joule

continued on next page

continued from previous page

Symbol	Description (SI units)
$\vec{J}$ / $\vec{j}$	electric current density ($A.m^{-2}$)
k	wave number (m^{-1})
K	dielectric constant; geomagnetic activity index; Kelvin
k_B	Boltzmann constant ($1.38 \times 10^{-23} J.K^{-1}$)
K_{eff}	effective dielectric constant
$\mathbf{L_c}$	closeness regularization operator
$\mathbf{L_s}$	smoothness regularization operator
$\mathbf{m}$	inversion model
$\mathbf{m_0}$	a priori model
m	cementation factor
$\mathbf{M}$	magnetotelluric tensor
Mg	magnesium
μ	magnetic permeability ($V.s.A^{-1}.m^{-1}$)
μ_0	magnetic constant: $4\pi x10^{-7}$ $V.s.A^{-1}.m^{-1}$
n	Archie's law empirical coefficient
N_i	ion concentration ($mol.L^{-1}$)
nt	nano Tesla
P	pressure (Pa)
Pa	Pascal
ϕ	impedance tensor phase; volume fraction; objective function
$\mathbf{\Phi}$	phase tensor
q	electric charge density ($C.m^{-3}$); factor equal to ik
q_i	ion electric charge (C)
$\mathbf{R}$	rotation matrix
R	resistance (Ω)
Re	real part of a complex number
ρ	electric resistivity (Ω.m)
ρ_a	apparent resistivity (Ω.m)
ρ_s	accumulation of charges on interface surface ($C.m^{-2}$)
S	Siemens
SO_4	sulfate
S_w	brine saturation
σ	electric conductivity ($S.m^{-1}$)
σ_{eff}	effective conductivity; bulk conductivity ($S.m^{-1}$)
σ_s	electrolyte conductivity ($S.m^{-1}$)

continued on next page

continued from previous page

Symbol	Description (SI units)
σ_m	rock matrix conductivity ($S.m^{-1}$)
σ_f	conductivity of the conductive phase ($S.m^{-1}$)
t	time (s)
T	period (s); temperature (°C or K); Tesla
τ_c	closeness parameter
τ_s	smoothness parameter
V	Volt
$\mathbf{V}$	covariance matrix
Vp	P wave velocity ($m.s^{-1}$)
Vs	shear wave velocity ($m.s^{-1}$)
ω	angular frequency (s^{-1})
Ω	Ohm
X_m	melt fraction
x,y,z	Cartesian coordinates
$\mathbf{Z}$	impedance tensor (Ω)
∞	infinity
$\|a\|$	absolute value of a
∇	Nabla operator
Δ	Laplacian operator
$\frac{\partial}{\partial t}$	time partial derivative
$\vec{X}$	vector
$\mathbf{X}$	matrix, tensor
$\mathbf{X}, \mathbf{X}^t$	matrix X and transpose matrix X
AC	Alternating Current
ATF	Altyn Tagh Fault
BBMT	Broadband Magnetotelluric
DC	Direct Current
EEJ	Equatorial Electrojet
ELF	Extra Low Frequency
EM	Electromagnetic
ERC	Equatorial Ring current
FTB	Fold-Thrust Belt
GDS	Geomagnetic Deep Sounding
GHS	Greater Himalayan Sequence
GPS	Global Positioning System

continued on next page

continued from previous page

Symbol	Description (SI units)
Hi-CLIMB	Himalayan-Tibetan Continental Lithosphere During Mountain Building
HPHT	High-Pressure High-Temperature
INDEPTH	InterNational Deep Profiling of Tibet and the Himalaya
ITS	Indus Tsangpo Suture (same as IZS)
IZS	Indus Zsangpo Suture (same as ITS)
JRS	Jinsha River Suture
KF	Kunlun Fault
LHS	Lesser Himalayan Sequence
LMT	Long Period Magnetotelluric
LVZ	Low velocity Zone
MBT	Main boundary thrust
MCT	Main Central Thrust
MHT	Main Himalayan Thrust
MT	Magnetotelluric
NASA	National Aeronautics and Space Administration
NKT	North Kunlun Thrust
NLCG	Non-Linear Conjugate Gradients
NOOA	National Oceanic and Atmospheric Administration
PASSCAL	Program for Array Seismic Studies of the Continental Lithosphere
PEJ	Polar Electrojet
RMS	Root Mean Square
SKF	South Kunlun Fault
SKS	S-wave traversing the outer core as a P-wave
SMS	S-wave Moho reflection
STD	South Tibetan Detachment
TE	Transverse Electric
TM	Transverse Magnetic
TTS	Tanggula Thrust System
ULF	Ultra Low Frequency
VLF	Very Low Frequency

Below is the Geologic Time Scale from [*Walker and Geissman*, 2009].

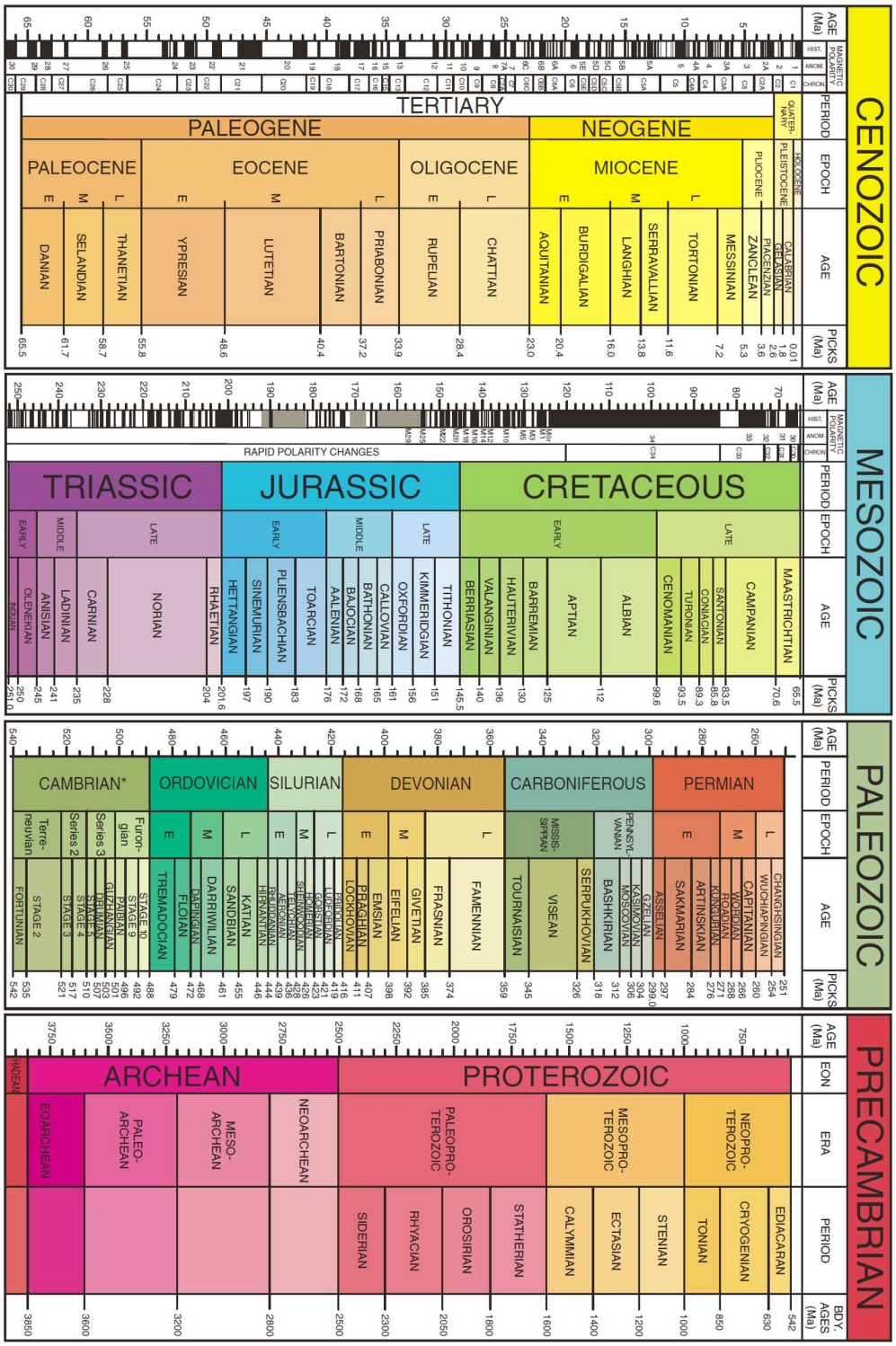

1 INTRODUCTION

Although the India-Eurasia collision likely occurred over the past 70-50 Ma, the Himalayan-Tibetan orogen is the result of a great succession of tectonic events that shaped and transformed its constituent terranes since at least the Neoproterozoic. The surface geology of the Himalayan-Tibetan orogen highlights a complex history and evolution characterized by million years of subduction, arc magmatism and terrane accretion associated with the closure of major oceans. With such heterogeneities, the Paleozoic-Mesozoic tectonic signature would have affected the rheology of the lithosphere and the distribution of the Cenozoic deformation in Tibet [*Yin and Harrison*, 2000; *Searle et al.*, 2011]. Compared to the rigid blocks defined by the Himalayan foreland to the south, the Tarim and Qaidam Basins to the north, and the Sichuan Basin to the east, the Tibetan Plateau is a weaker region presenting a thin mechanical lithosphere or equivalent elastic thickness of 0-20 km [*Jordan and Watts*, 2005].

Over the last decades, various models have been proposed to describe the overall crustal deformation in Tibet. Those models are still debated and uncertainties regarding the type of continental deformation involved in Tibet remain. In comparison with the Himalayas, the Tibetan plateau presents few exposed deep crustal rocks and therefore mainly relies on xenoliths and geophysical data for interpretation of its deep structure [*Searle et al.*, 2011]. Since the early eighties, the Tibetan crust and upper mantle has been constrained by major international geophysical investigations such, as Sino-French experiments [*Hirn et al.*, 1995; *Wittlinger et al.*, 1996], and the PASSCAL (Program for Array Seismic Studies of the Continental Lithosphere) [*Owens and Zandt*, 1997], INDEPTH (InterNational Deep Profiling of Tibet and the Himalaya) [*Zhao et al.*, 1993; *Nelson et al.*, 1996; *Tilmann et al.*, 2003; *Unsworth et al.*, 2005; *Karplus et al.*, 2011], and Hi-CLIMB (Himalayan-Tibetan Continental Lithosphere During Mountain Building) [*Hetényi et al.*, 2007; *Nábelek et al.*, 2009] projects. In the framework of those projects, seismic surveys and magnetotelluric measurements as well as magmatism and xenolith studies in Tibet have revealed major differences between southern and northern lithospheric structures.

Since 1992, the INDEPTH project has significantly contributed to the establishment of the main geodynamic models characterizing the lithospheric structure of the Tibetan plateau. The first phase of INDEPTH started with a Himalayan survey involving a deep seismic reflection transect. In addition to imaging a significant Moho depth, the survey also revealed the active "decollement" beneath India and Asia dipping to the north and revealing the top of the Indian lower crust [*Zhao et al.*, 1993]. Following the success of INDEPTH I, the project initiated by scientists from China and the US, has grown into a major international collaboration as institutes and universities from Germany, Canada and Ireland got involved.

During INDEPTH II, the investigations moved northwards onto the Lhasa block in southern Tibet and the geophysical techniques used in the project broadened out with the introduction of passive seismic and magnetotelluric imaging. Magnetotelluric (MT) data generated from the recording of the Earth's natural electromagnetic variations, can be used to image the electrical resistivity structure of the lithosphere. The method is particularly sensitive to the presence of interconnected fluids. Therefore, INDEPTH MT surveys have been particularly useful in revealing the presence of partial melt in the Tibetan crust since its introduction in the project in 1995. The main INDEPTH II observations, characterized by seismic bright spots [*Brown et al.*, 1996], high electrical conductivity [*Chen et al.*, 1996] and low seismic velocities in the crust [*Kind et al.*, 1996], highlighted the presence of fluids and partially molten material in the crust of southern Tibet [*Nelson et al.*, 1996]. Those results initiated the development of the Himalayan channel flow and Tibetan crustal flow models.

During INDEPTH III, the investigations moved into central and northern Tibet. In this phase of the project, the two main goals were to get a better constraint on the proposed crustal flow model for Tibet but also to define the extension of the Indian lithospheric mantle and characterize the processes involved in the uplift of the northern part of the plateau. In central Tibet, INDEPTH III highlighted a significant change in the lithospheric structure of the plateau probably associated with the downwelling of the subducting Indian plate [*Tilmann et al.*, 2003]. The phase III of the project also revealed high electrical conductivity in the middle-to-lower crust of central and northern Tibet interpreted as partial melts [*Solon et al.*, 2005; *Unsworth et al.*, 2004] associated with the presence of unusually high temperatures [*Mechie et al.*, 2004]. Those particular observations lead to the conclusion that partial melt is likely widespread in the Tibetan crust and reinforced the proposed crustal flow model.

Following the MT INDEPTH III results in northern Tibet [*Unsworth et al.*, 2004], the new INDEPTH phase IV was initiated to develop a better understanding of the structure and evolution of the northern margins of the Tibetan plateau defined by the Kunlun and Altyn Tagh faults. This phase of the project aims to study to the active growth of the plateau to the north. INDEPTH IV raises the issues on underthrusting of the Asian lithosphere beneath the Tibetan plateau along the Kunlun Mountains, possible flow of Tibetan crust up to the southern edge of the Qaidam basin [*Karplus et al.*, 2011] but also on the impact and scale of the major northern faults in depth.

The work presented in this thesis focusses on the magnetotelluric modelling of data for the INDEPTH phase III and new INDEPTH phase IV MT transects recorded across the Kunlun fault, in order to characterize the transition between the particularly weak Tibetan plateau lithosphere and its surrounding rigid blocks, associated with the growth of the plateau into the Asian continent. This thesis is divided into four parts. In part one, an overview of the Himalayan-Tibetan orogen is presented through three different chapters focussing on the geology of the main terranes, the history and evolution of the orogen and a description of the main geodynamic models and deeper structures constrained by geophysical studies. In the second part, the theory of magnetotellurics is introduced by defining the electrical properties of the Earth, the MT natural sources and the main concepts associated with the technique. The third part describes the main results associated with the revised modelling of the INDEPTH III data and the modelling of the new IN-

DEPTH IV data using 2D isotropic, 2D anisotropic and 3D synthetic modelling as well as 3D inversions. A final interpretation chapter includes the comparison of the main MT results with both recent seismic studies, and the new estimates of melt fractions from the evaluation of the conductance for the 2D anisotropic MT models, in order to construct a tectonic model responsible for the observed resistivity anomalies. The last part of the thesis focusses on the main conclusions and includes the appendices and bibliography.

Part I

THE HIMALAYAN-TIBETAN OROGEN: OVERVIEW

2 TERRANES AND SUTURES

Although the area of Tibet investigated in this thesis characterizes only a small portion of the Himalayan-Tibetan orogen (Fig. 2.1), the whole terranes and sutures associated with the India-Asia collision were covered in this chapter. The orogen may be divided into several individual blocks, nevertheless it remains important to introduce the whole system in order to get a broader understanding of the geodynamic processes involved in the collision.

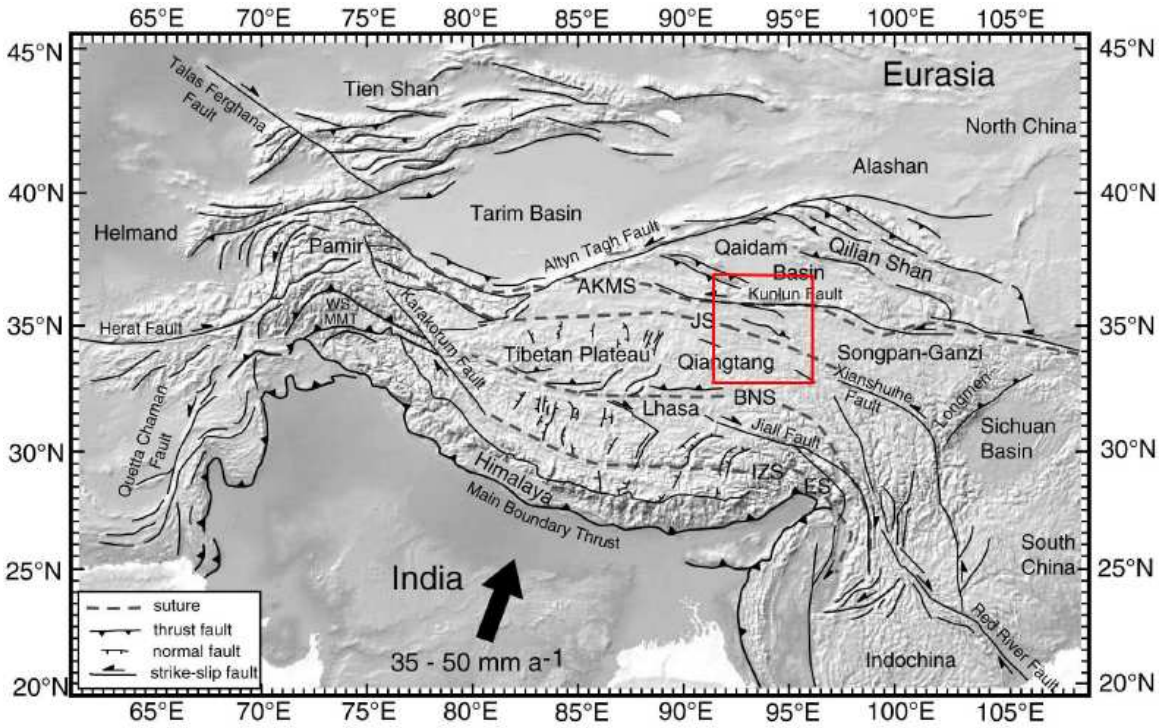

Figure 2.1: The Himalayan-Tibetan orogen. The red square defines the main area investigated in this thesis. WS - Western Himalayan Syntaxis; ES - Eastern Himalayan Syntaxis; MMT - Main Mantle Thrust; AKMS - Anyimaqen-Kunlun-Muztagh Suture; JS - Jinsha Suture; BNS - Bangong-Nujiang Suture; IZS - Indus-Zangbo suture. *from* [*Kearey et al.*, 2009]

2.1 NORTHERN INDIA AND HIMALAYAS

Indian Craton

The Northern Indian sequence includes Neoproterozoic-Cambrian, Carboniferous-Permian, and Mesozoic strata [*Brookfield*, 1993; *Hodges*, 2000; *Myrow et al.*, 2010], overlying the Northern Indian cratonic root. The craton is characterized by a combination of Archean and

Early Proterozoic granitoids and gneisses associated with Lower and Middle Proterozoic sedimentary and metasedimentary assemblages [*Goodwin*, 1996; *Kohn et al.*, 2010]. The Archean-Early Proterozoic gneissic basement of the Indian Shield did not seem to take part in the Late Cenozoic thrusting associated with the rise of the Himalayas [*Parrish and Hodges*, 1996].

Himalayan Sequences

The Himalayas stratigraphy can be separated in three main units: the Lesser Himalayan, the Greater Himalayan and the Tethyan sequences (Fig. 2.3) [*Gehrels et al.*, 2011]. Those three sequences are bounded by three north-dipping Late Cenozoic fault systems: the Main Boundary Thrust, the Main Central Thrust, and the South Tibetan Detachment System [*Yin and Harrison*, 2000]. The Lesser Himalayan sequence (LHS) includes clastic sediments and metasedimentary rocks of passive margin origin [*Gehrels et al.*, 2011]. Whereas the lower LHS includes Paleo- and Mesoproterozoic strata, the upper LHS strata is associated with rifting of Late Proterozoic, Permian, and Cretaceous origin [*Brookfield*, 1993; *Myrow et al.*, 2010]. The LHS southern lower and uppernorthern boundaries are respectively the Main Boundary Thrust (MBT) and the Main Central Thrust (MCT) [*Yin and Harrison*, 2000]. The MCT defines a thick Miocene shear zone (few kilometres to 10 km) [*Yin and Harrison*, 2000; *DeCelles et al.*, 2001] where the Greater (or High) Himalayan units overlie Lesser Himalayan strata. It accommodated at least a displacement of 140 km if not more [*Yin and Harrison*, 2000].

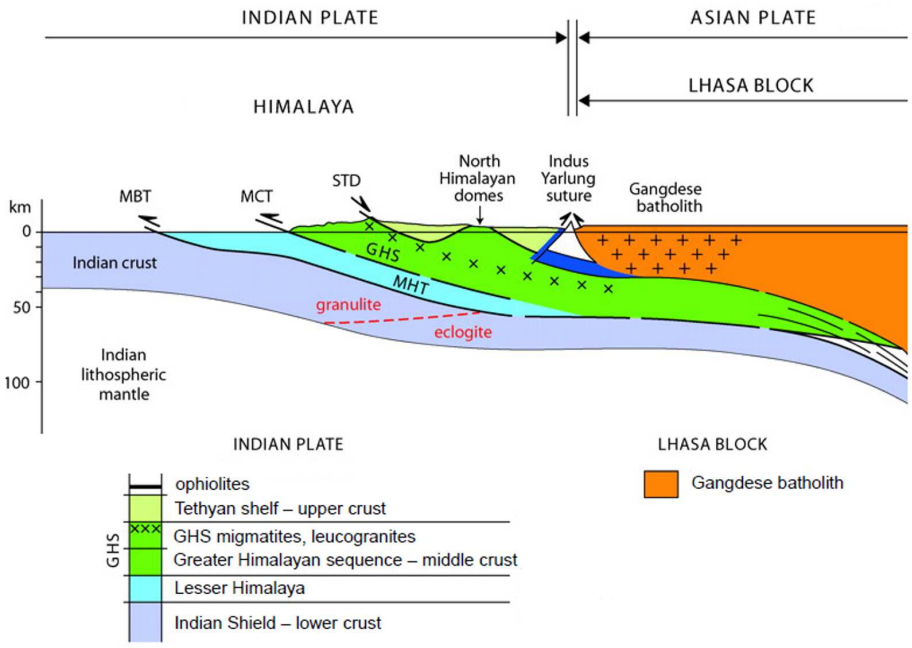

Figure 2.2: Cross-section of the Himalayas and Southern Tibet. *modified from* [*Searle et al.*, 2011]

The Greater Himalayan sequence shows Late Proterozoic to Early Cambrian metasedimentary assemblages [*Yin and Harrison*, 2000], including pelitic to psammitic biotite schist and paragneiss as well as marble and calc-silicate gneiss [*Gehrels et al.*, 2011]. An upper unit is characterized by orthogneiss derived from Ordovician granitic rocks [*Gehrels et al.*,

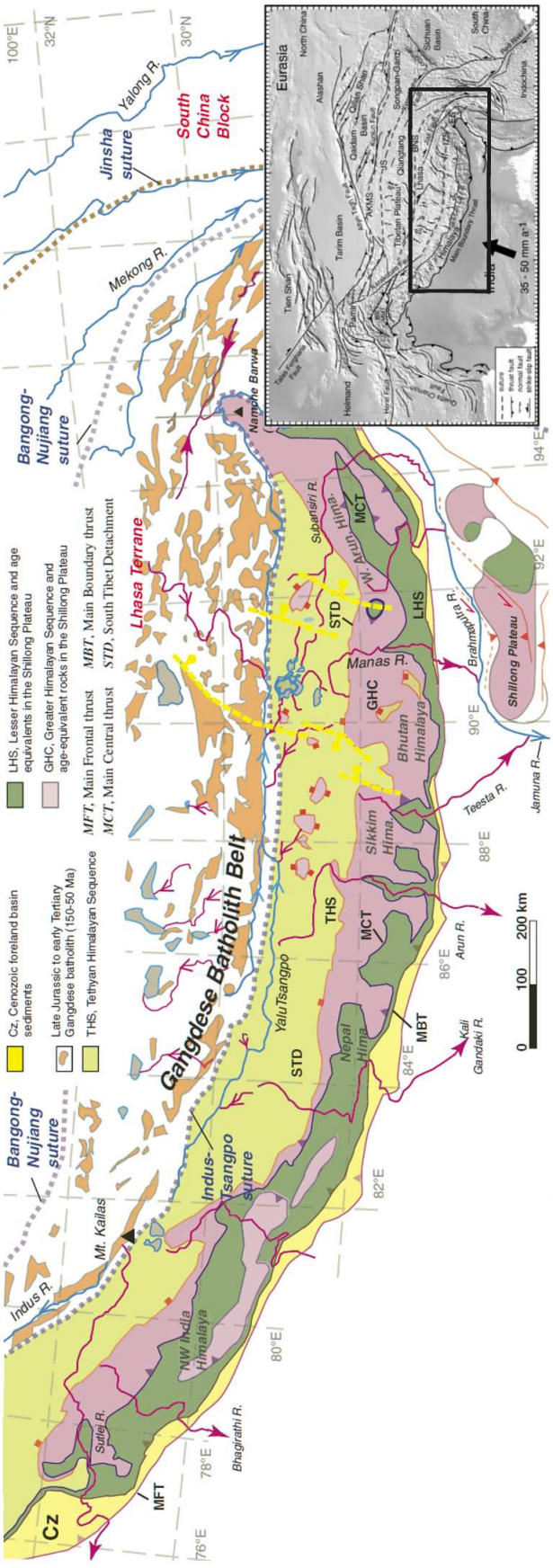

Figure 2.3: Simplified geological map of the Himalayas. *modified from* [*Célérier et al.*, 2009; *Kearey et al.*, 2009]

2011]. The low-angle South Tibetan Detachment (STD) Fault System separates the rear Tethyan sequence from the Greater Himalayan sequence [*Hodges*, 2000]. The hanging wall of the STD presents deformed migmatites and leucogranites (Fig. 2.2) associated with High Himalayan granite series [*Yin and Harrison*, 2000; *Searle et al.*, 2011]. The STD, not active today, has been folded around the North Himalayan gneiss domes exposed in the Tethyan Himalayas (Fig. 2.2) [*Searle et al.*, 2011]. Thus, the Tethyan sequence covers both the frontal and rear portions of the Greater Himalayan metamorphic rocks.

The Tethyan strata is mainly characterized by Late Precambrian to Early Paleozoic sedimentary and metasedimentary rocks associated with thick Permian to Cretaceous continental margin sequences, mainly marine clastic strata and carbonate rocks [*Brookfield*, 1993; *Yin and Harrison*, 2000; *Gehrels et al.*, 2011]. Those may have been deposited along the southern margin of the Tethyan ocean during various rifting events from the Late Proterozoic to Cretaceous [*Brookfield*, 1993]. Younger Tethyan sequences reflect the thrusting of Eocene foreland basin strata [*Gehrels et al.*, 2011]. Inside the Tethyan Himalayan sequence, the shortening is accommodated through folds and thrusts defined as the Tethyan Himalayan Thrust Belt. This fault system is located between the South Tibetan Detachment System and the Indus-Yarlung suture [*Yin and Harrison*, 2000].

Indus-Yarlung Tsangpo Suture Zone

The Indus-Yarlung Suture Zone exhibits local high-pressure metamorphic assemblages associated with deep marine sedimentary rocks, ophiolites and ophiolitic melanges [*Gehrels et al.*, 2011]. The north of the suture highlights the transition into the thick Cretaceous marine clastic strata defined by the Xigaze forearc basin [*Dürr*, 1996]. The Indus-Yarlung suture is bounded by two Cenozoic thrusts (Fig. 2.2) [*Yin and Harrison*, 2000]. The south-dipping Great Counter Thrust defines its southern boundary where the passive continental margin sediments of northern India are underthrusted by the Indus-Yarlung complex. The north-dipping Gangdese thrust is its northern boundary and is characterized by the underthrusting of the Xigaze forearc sequence beneath the Gangdese batholith [*Yin and Harrison*, 2000].

2.2 TIBETAN PLATEAU

Lhasa Terrane

The Lhasa terrane mainly comprises Paleozoic and Mesozoic marine sediments as well as arc-type volcanic rocks (Fig. 2.4) [*Yin and Harrison*, 2000]. Although the terrane is as wide as 300 km near Lhasa, it narrows to less than 100 km to the west, where the active right-slip Karakorum fault defines its transition into the Ladakh-Kohistan arc terrane (northwestern India-Pakistan) [*Pan*, 1996; *Searle*, 1996a]. The Upper Carboniferous to Lower Permian volcaniclastic sediments, as well as the Upper Permian shallow marine sequence in the north, are associated with back-arc extension [*Pearce and Mei*, 1988; *Leeder et al.*, 1988; *Yin and Harrison*, 2000]. The rifting separation of the Lhasa terrane from India is highlighted by the presence of Upper Triassic volcaniclastic sediments and basalts in the southeastern part of the terrane [*Pearce and Mei*, 1988]. Turbidite sequences interlayered with volcanic flows and tuffs characterize the Jurassic deposits mainly exposed in the north of the terrane

[*Yin and Harrison*, 2000]. Whereas, the Lhasa terrane shows widespread limestone and marine deposits from Early to Middle Cretaceous [*Yin and Harrison*, 2000], those appear to be more localized south of the Bangong-Nujiang suture by the end of the Cretaceous [*Liu*, 1988]. The western and eastern Lhasa terrane, south of the BNS, reveal widespread ultramafic rocks [*Liu*, 1988]. Those are interpreted to be either associated with low-angle thrusts that displaced tectonic slices to the north [*Girardeau et al.*, 1984; *Coward et al.*, 1988b] or indicative of suture zones [*Hsu et al.*, 1995; *Matte et al.*, 1996b]. The terrane exhibits two major plutonic sequences. Late Jurrassic granitoids are exposed in the northeastern Lhasa terrane and are probably a signature of the subduction of the Qiangtang block beneath the Lhasa terrane [*Coulon et al.*, 1986]. Along the southern margin of the terrane lies the Cretaceous to Tertiary Gangdese batholith belt, which developed during the north-dipping subduction of the Indian plate [*Allègre*, 1984]. As part of the Cretaceous to Tertiary southern active continental margin of the Lhasa Block, the Xigaze forearc basin, exhibiting mainly flysch deposits [*Wan et al.*, 1998], is exposed south of the Gangdese batholiths [*Yin and Harrison*, 2000]. The southern end of the basin is bounded by the Indus-Yarlung ophiolites [*Wan et al.*, 1998]. The basement of the Lhasa terrane is interpreted to date from Mid-Proterozoic to Early Cambrian times and is defined as the Amdo basement (Fig. 2.4) [*Yin and Harrison*, 2000]. It is exposed predominantly as high-grade orthogneisses intruded by Jurassic granitoids in the northern Lhasa terrane [*Gehrels et al.*, 2011]. As the crystalline Amdo rocks are located within the Bangong suture zone, it makes it difficult to infer their affinity to either Lhasa or Qiangtang terranes or both [*Gehrels et al.*, 2011]. However, prior to the Permian-Triassic rifting, both terranes were likely together [*Yin and Harrison*, 2000]; the Amdo rocks could then be associated to both Lhasa and Qiangtang crystalline crust [*Gehrels et al.*, 2011].

Bangong-Nujiang Suture

The Bangong suture marks the closure of the Mesotethys ocean basin between the Lhasa and Qiangtang terranes (Fig. 2.4) [*Dewey et al.*, 1988; *Yin and Nie*, 1996; *Kapp et al.*, 2003; *Baxter et al.*, 2009]. The suture mainly exhibits Jurassic marine shale, conglomerates, volcanic rocks, rare ophiolitic fragments, and high-pressure complexes [*Gehrels et al.*, 2011]. Directly south of the suture, the Cretaceous marine sediments have been associated with the foreland basin that may have developed in front of the Lhasa block during continuing convergence along the suture, between Lhasa and Qiangtang blocks, in the Late Cretaceous [*Murphy et al.*, 1997; *Yin and Harrison*, 2000]. In the Karakorum region, the Bangong-Nujiang suture is identified as the Shyok suture, or the Main Karakorum Thrust (MKT) [*Yin and Harrison*, 2000].

Qiangtang Terrane

The Qiangtang terrane is bounded by the Bangong-Nujiang Suture to the south and the Jinsha Suture to the north (Fig. 2.4). In central Tibet, the terrane reaches a width of 600 km but narrows both to the west and the east. The terrane meets with the Karakorum terrane to the west in the Karakorum region [*Yin and Harrison*, 2000]. The Qiangtang block consists mainly of Late Proterozoic - Early Paleozoic metamorphic rocks overlain by Carboniferous to Early Mesozoic thick marine strata [*Gehrels et al.*, 2011]. Whereas in the west the terrane

exhibits Carboniferous and Permian shallow marine strata, in the east the terrane is characterized by Triassic-Jurassic shallow marine carbonate rocks interbedded with volcaniclastic strata (Fig. 2.4) [*Liu*, 1988; *Yin and Harrison*, 2000; *Kapp et al.*, 2003; *Pan et al.*, 2004; *Pullen et al.*, 2008]. The widespread Late Triassic to Early Jurassic volcanic records may have re-

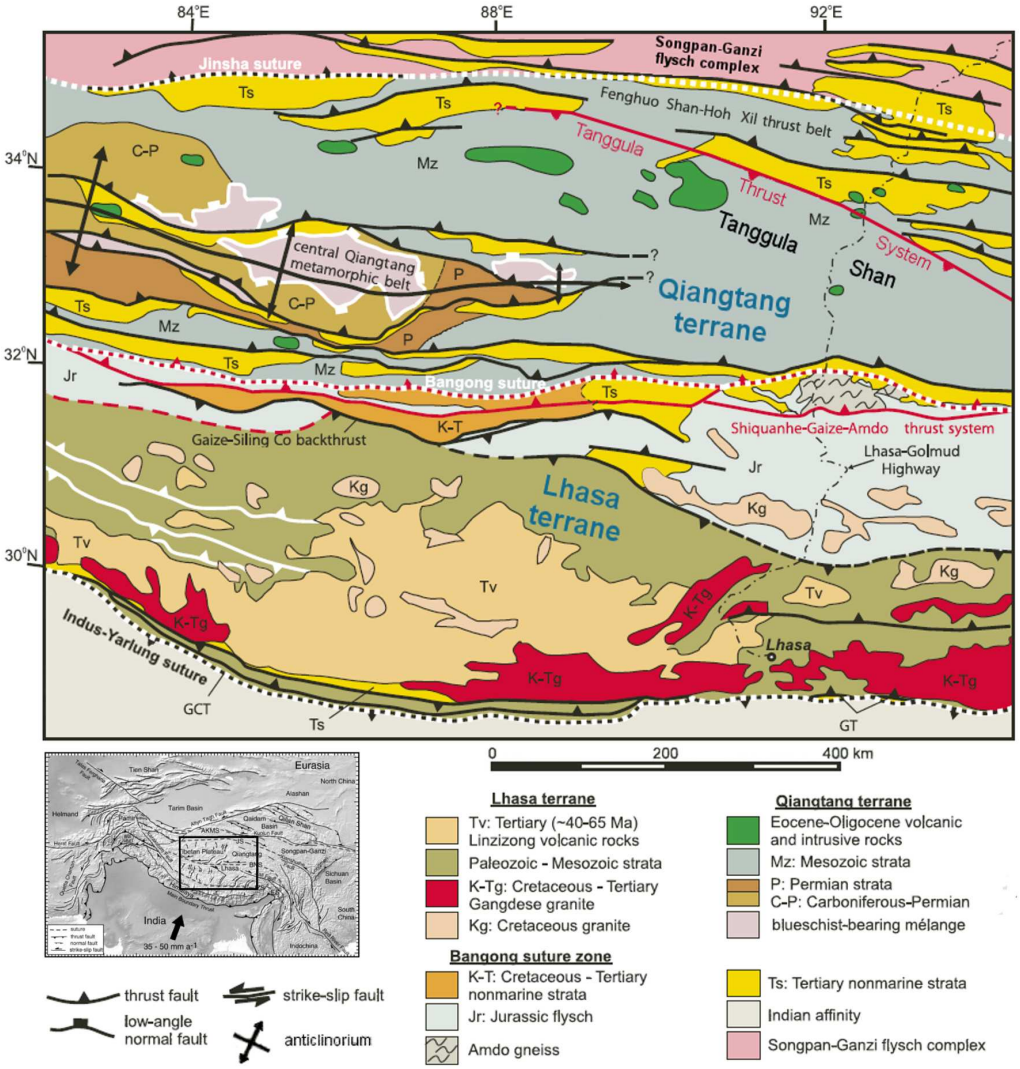

Figure 2.4: Geological map of South and Central Tibet. Tertiary thrust faults are shown in black and major Mesozoic faults are shown in white. GCT = Great Counter thrust; GT = Gangdese Thrust system; Tanggula Thrust trace taken from [*Li et al.*, 2012]. *modified from* [*Kapp et al.*, 2005; *Kearey et al.*, 2009]

sulted from southward subduction of the Songpan-Ganzi flysch complex [*Kapp*, 2001]. One of the particular features of the terrane is the West Qiangtang anticlinorium extending to about 600-km E-W and 150-km N-S (Fig. 2.4) [*Pullen et al.*, 2011]. The anticlinorium metamorphic belt lies on a blueschist and locally eclogite bearing metamorphic rocks melange associated with Upper Paleozoic strata in its core. Both frontal and rear portions are covered by Jurassic to Upper Cretaceous strata [*Yin and Harrison*, 2000; *Pullen et al.*, 2011] (Fig. 2.5). The Qiangtang melange is characterized by a strongly deformed metasedimentary matrix surrounding less deformed formations, such as metasedimentary rocks, mafic amphibolite gneiss, fine-grained metabasites, marble, quartzite and metagranite [*Kapp et al.*,

2003; *Pan et al.*, 2004; *Pullen et al.*, 2011]. Near the Duguer Range, south of the anticlinorium, Qiangtang crystalline basement is exposed at the surface [*Pullen et al.*, 2011] (Fig. 2.5). The metamorphic melange has been interpreted to form a suture zone between the northern and southern blocks of the Qiangtang terrane [*Kidd and Molnar*, 1988; *Sengör et al.*, 1988; *Zhang*, 2001]. However, the melange is more likely to have underthrusted the Qiangtang terrane from the Jinsha suture [*Kapp et al.*, 2000; *Kapp*, 2001; *Pullen et al.*, 2011]. This metamorphic material was identified as parts of the northern Tibetan deeper crust that were exhumed by Late Triassic-Early Jurassic low-angle normal faults. This would mean that much of the deeper crust of northern Tibet is composed of early Mesozoic melange complexes of metasedimentary rocks [*Kapp et al.*, 2000]. According to *Kapp et al.* [2000], this melange may be weaker than the crystalline basement of southern Tibet, and it would explain the major localization of young crustal shortening north of the Bangong-Nujiang suture during the Cenozoic collision compared to southern Tibet, which underwent only minor shortening [*Coward et al.*, 1988a; *Song and Wang*, 1993; *Murphy et al.*, 1997].

To the east of the anticlinorium, the Tanggula ranges (> 6000 m) characterizes mainly Middle to Late Cretaceaous Granites intruding Mesozoic rocks [*Roger et al.*, 2000]. To the north, the Early Tertiary south-dipping Tannggula Trust System (Fig. 2.4) is associated with the formation of the Tuotuohe basin - the southern part of the widespread Hoh Xil basin - and the uplift of the Tanggula mountains in the Paleogene [*Li et al.*, 2010]. According to *Wang et al.* [2008], 40 Ma ago, the Lhasa and southern Qiangtang terranes were close to their modern elevation and formed the proto-Tibetan Plateau. At that time, the Tanggula Thrust and Gangdese Thrust were possibly the northern and southern boundaries of this proto-Tibetan Plateau [*Wang et al.*, 2008]. The Eocene calc-alkaline post-collisional magmatic belt present along the Tanggula mountains [*Roger et al.*, 2000] has been associated with Cenozoic shortening in northern Tibet.

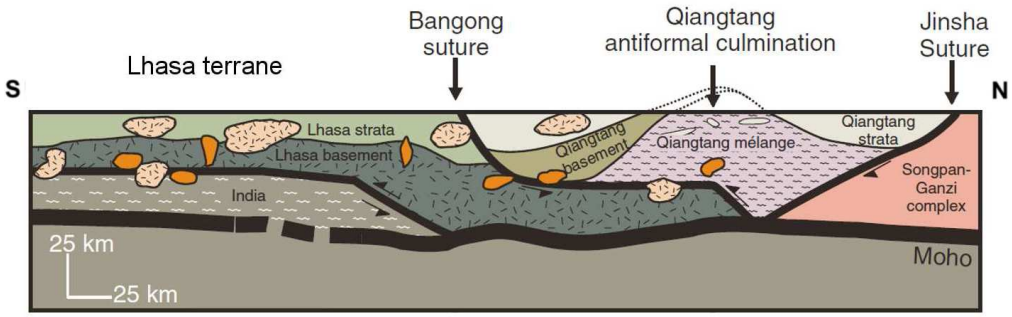

Figure 2.5: Schematic north-south cross-section through the Qiangtang anticlinorium, and the Bangong and Jinsha sutures. *modified from* [*Pullen et al.*, 2011]

Jinsha River Suture Zone

Although well defined in eastern Tibet, with ophiolitic assemblages exposed along a Triassic arc-related narrow belt [*Dewey et al.*, 1988; *Pullen et al.*, 2008], the Late Triassic-Early Jurassic Jinsha suture (Fig. 2.4) appears more scattered to the west [*Gehrels et al.*, 2011]. The eastern part of the suture defines a linear ophiolitic melange zone including peridotites, radiolarites, gabbro and basalts [*Roger et al.*, 2003]. The melange is intruded by granitoids

and exhibits interlayered volcanoclatstic sediments [*Roger et al.*, 2003]. However, the western trace of the suture becomes unclear, with fewer widely dispersed ophiolitic fragments mixed with Tertiary strata, due to the development of the Late Cretaceous to Early Tertiary Fenghuo Shan thrust belt [*Yin and Harrison*, 2000; *Pan et al.*, 2004]. The Jinsha suture is likely to have developed with the soutward subduction of oceanic lithosphere beneath the Qiangtang terrane during the Paleozoic-Mesozoic closure of the Paleotethys ocean [*Pearce and Mei*, 1988; *Yin and Harrison*, 2000; *Pullen et al.*, 2011].

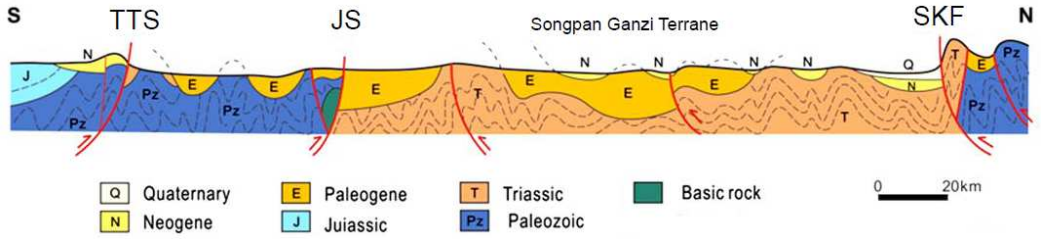

Figure 2.6: Cross-section of Northern Tibet upper crust crossing the Tanggula Trust System (TTS), the Jinsha Suture (JS) and the South Kunlun Fault (SKF). *modified from Wang et al.* [2008]

Songpan-Ganzi Terrane

The Songpan-Ganzi terrane defines a triangular tectonic feature [*Yin and Harrison*, 2000] surrounded by the East Kunlun-Qaidam terrane in the north and the Qiangtang terrane in the south (Fig. 2.6). The terrane narrows to the west, where it is offset by the strike-slip Altyn Tagh fault. In Tibet, the terrane is bounded by the Jinsha suture in the south and the Anyimagen-Kunlun-Muztagh suture in the north. The Songpan-Ganzi terrane consists mostly of Upper Triassic marine strata characterized by several kilometres of a thick sequence of Triassic turbidites (Fig. 2.6), also named the Songpan-Ganzi flysch complex, lying on top of Paleozoic marine sediments belonging to the passive margin of north China [*Yin and Harrison*, 2000; *Gehrels et al.*, 2011]. Southern portions of the terrane exhibit arc-type volcanic rocks [*Yin and Harrison*, 2000; *Weislogel*, 2008]. The terrane also exposes some interbedded lavas and local intrusions of granitoids [*Pearce and Mei*, 1988]. The Songggpan-Ganzi flysch complex underwent intense folding and thrusting during the Triassic collision between the North and South China blocks [*Burchfiel et al.*, 1995; *Yin and Nie*, 1996], forming the Anyimagen-Kunlun-Muztagh suture. In the Eastern part of the terrane, the origin of the significantly thick Songpan-Ganzi flysch complex has been attributed either to the formation of a large accretionary complex resulting, in the off-scrapping of deep marine sediments [*Sengör*, 1990], or to a large erosion flux of sediments from the Qinling-Dabie orogenic belt associated with the Triassic collision between North China and South China [*Yin and Nie*, 1993; *Zhou and Graham*, 1993]. The Songpan-Ganzi flysch complexes are mostly easily deformable pelites, deposited in a deep marine setting. Those sediments may have been underthrust to depths of 60-80 km by Mesozoic thrusting [*Yin et al.*, 1998; *Kapp et al.*, 2000] and thrusting along Cenozoic faults, such as the Fenghuo Shan-Nangqian thrust system (Fig. 2.6) [*Yin and Harrison*, 2000]. The Hoh Xil Basin (HXB) in the eastern part of the terrane covers up to 100,000 km^2, making it the largest Cenozoic sedimentary basin inside Tibet [*Wang et al.*, 2002]. The basin is bounded to the north by the South Kunlun Fault (SKF) and to the south by the Tanggula Thrust

System (TTS), covering the Jinsha Suture (JS) (Fig. 2.6) [*Wang et al.*, 2002]. The HXB may have been bounding the northern edge of the Paleogene proto-Tibetan Plateau, such as the Tarim and Qaidam basin today [*Wang et al.*, 2008]. The Fenghuo Shan-Nangqian Fold and Thrust belt covers the northern edge of the Qiangtang terrane and extends into the Songpan-Ganzi Hoh Xil region, across the Jinsha suture zone [*Yin and Harrison*, 2000]. In response to the shortening associated with the India-Asia collision, the belt is characterized by both north and south dipping thrusts that developed in the Early Tertiary. The Fenghuo Shan-Nangqian thrusting system juxtaposes Permian to Jurassic aged units over Tertiary strata [*Yin and Harrison*, 2000]. East of the Lhasa-Golmud highway in the north of the terrane, the Bayan Har Shan defines the southern branch of the Kunlun mountains. The Bayan Har mountains is characterized by poorly dated low-grade slates belts, which include Triassic sedimentary rocks and Mesozoic plutonic intrusions [*Cowgill et al.*, 2003; *Huang et al.*, 2004].

Kunlun-Qaidam Terrane

The Eastern Kunlun-Qaidam Terrane lies between the Anyimaqen-Kunlun-Muztagh suture in the south and the Qilian suture in the north (Fig. 2.7) [*Yin and Harrison*, 2000]. The terrane is bounded in the south by the Kunlun mountains or Kunlun Shan along the active sinistral Kunlun fault [*Kidd and Molnar*, 1988; *van der Woerd et al.*, 2000]. The Kunlun mountains exhibit mainly Paleozoic and lower Mesozoic rocks intruded by early Paleozoic and Permo-Triassic arc-type magmatism, characterized as the Kunlun batholith [*Yin and Harrison*, 2000]. The Kunlun batholith is the result of the superposition of a broad early Paleozoic arc in the western Kunlun region and a narrower and younger Late Permian to Triassic arc in the eastern Kunlun [*Harris et al.*, 1988; *Jiang et al.*, 1992; *Xu et al.*, 1996]. To the west, the Kunlun region is characterized by Middle to Late Proterozoic gneiss, schist, and marble overlain by Cambrian to Middle Ordovician shallow marine sequences [*Jiang et al.*, 1992; *Huang et al.*, 1996]. To the east, the Proterozoic gneissic basement rocks were overlain by widespread Late Ordovician and Early Carboniferous volcanic deposits (large amounts of basalts, andesites, and rhyolites) interbedded with marine deposits [*Huang et al.*, 1996; *Yin et al.*, 1988; *Pearce and Mei*, 1988]. In the central and northern parts of the East Kunlun-Qaidam block, the Early Paleozoic interruption in volcanic activity is characterized by a widespread deposition of Middle-Upper Carboniferous shallow marine carbonate rocks [*Yin and Harrison*, 2000]. Carboniferous and Early Permian to Middle Triassic ophiolite belts were identified in the eastern Kunlun region [*Yang et al.*, 1996]. Whereas the history of the Qaidam basin basement is relatively complex [*Wang and Coward*, 1990; *Yin and Nie*, 1996], the modern Qaidam basin began to take shape in the Cenozoic [*Song and Wang*, 1993]. The 2800 m high basin is bounded by the Kunlun Shan in the south, the Altun Shan in the northwest and the Qilian Shan-Nan Shan in the northeast (Fig. 2.8) [*Yin et al.*, 2008]. Following the mid-Eocene India-Eurasia collision [*Molnar and Tapponnier*, 1975], significant deposition of sediments began near the end of the Eocene in the Qaidam basin. The thickness of sediments deposited since the Oligocene reaches up to approximately 14 km in the basin [*Wang and Coward*, 1990]. As fold and thrust belts developed along the foreland of the Kunlun Shan mountain belt, the Qaidam basin expanded progressively toward the north and east [*Yin et al.*, 2008]. This eventually lead to pervasive folding in the interior of the basin since the last 10 Ma [*Wang and Coward*, 1990]. In western Tibet, the Qimen Tagh

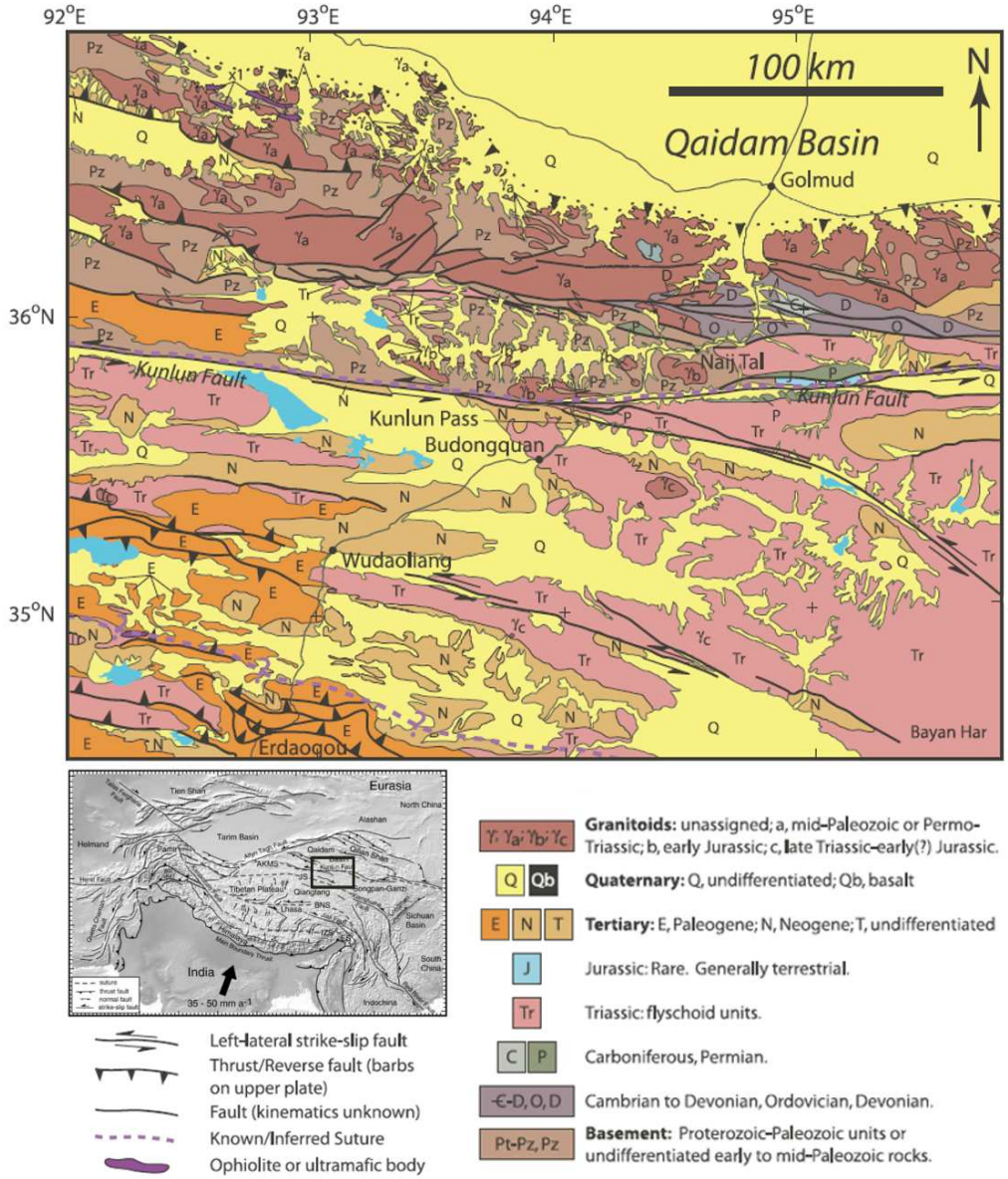

Figure 2.7: Geologic map of the Eastern Kunlun area. *modified from* [*Cowgill et al.*, 2003; *Kearey et al.*, 2009]

thrust system, characterized by north and south dipping thrusts, dies out into the Qaidam basin. Its slip is then transferred to the east through the southeast-dipping North Kunlun Thrust [*Bally et al.*, 1986]. The thrust juxtaposes Proterozoic metamorphic rocks and Paleozoic sedimentary, igneous rocks over the Tertiary strata of the Qaidam basin [*Bally et al.*, 1986; *Song and Wang*, 1993].

2.3 NORTHERN TERRANES AND MARGINS OF THE OROGEN

Nan Shan - Qilian Shan - Altun Shan Terrane

The Nan Shan, the Qilian Shan and the Altun Shan define the three major ranges of the northeastern Tibet boundaries that developed during the Cenozoic. These mountainous

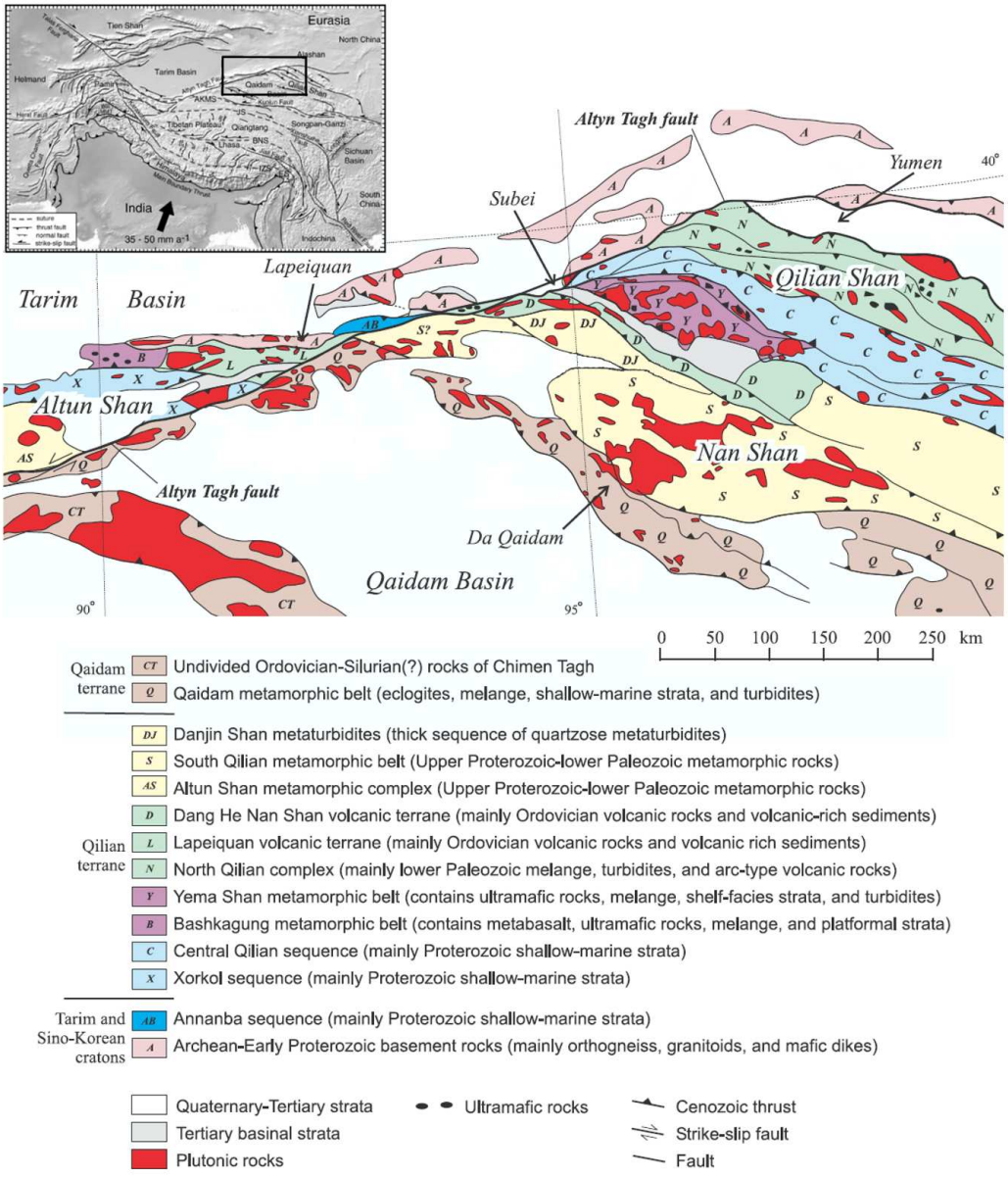

Figure 2.8: Tectonic map of the northeastern boundaries of the Tibetan Plateau. *modified from* [*Gehrels and Yin*, 2003; *Kearey et al.*, 2009]

regions, which expose Tertiary synorogenic series, are characterized by a Proterozoic basement complex overlain by Lower Paleozoic arc-type accreted rocks and Carboniferous to Cretaceous marine and continental platformal sequences [*Yin and Harrison*, 2000; *Gehrels and Yin*, 2003; *Gehrels et al.*, 2011; *Sobel and Arnaud*, 1999]. All three regions are sourced from the same terrane: the Nan Shan - Qilian Shan - Altun Shan terrane (Fig. 2.8) [*Gehrels*

et al., 2011], also called the Qilian terrane [*Yin and Harrison*, 2000], which accreted in the Devonian [*Gehrels and Yin*, 2003]. However, during the Tertiary India-Asia collision, the Nan Shan - Qilian Shan - Altun Shan terrane underwent strong deformation, metamorphism and uplift. Major thrust faults developed and lead to the raise of the Altun Shan, the Qilian Shan and the Nan Shan [*Gehrels and Yin*, 2003]. At the same time, the whole terrane was being offset by the Altyn Tagh fault (Fig. 2.8) [*Gehrels and Yin*, 2003; *Gehrels et al.*, 2011]. Today, the Altun Shan marks the orogen northeastern border between the Qaidam and Tarim basins along the Altyn Tagh fault, and the Nan Shan and the Qilian Shan developed north of the Qaidam basin. The Nan Shan - Qilian Shan - Altun Shan terrane can be divided into three units: the northern, central, and southern Qilian terranes, that accreted between the Ordovician and Devonian [*Yin and Harrison*, 2000]. The northern Qilian terrane developed during the Ordovician as an island arc system along the southern margin of the North China-Tarim cratons, probably the result of a north-dipping subduction [*Yin and Harrison*, 2000; *Gehrels et al.*, 2011]. Following the closure of its associated Late Proterozoic-Cambrian back-arc basin, the northern terrane may have collided with the central Qilian Precambrian gneisses belt [*Xia et al.*, 1996; *Zhang et al.*, 1998]. Ordovician to Silurian highly deformed sequences of marine sediments and volcanic rocks reflect the collision of the central and the southern Qilian terranes [*Cheng*, 1994; *Hsu et al.*, 1995]. However, the accretion of this arcs-complex is still not completely understood [*Gehrels et al.*, 2011]

North China - Tarim Cratons

In the north, the Himalayan-Tibetan orogen is bounded by two major cratonic regions: the Tarim craton to the west and the North China craton to the east [*Gehrels et al.*, 2011], also named as Sino-Korean craton [*Gehrels and Yin*, 2003]. Those two regions, characterized by cold and stable crust, define an Archean and Paleoproterozoic crystalline basement overlain by Proterozoic and Paleozoic sequences [*Pan et al.*, 2004; *Darby and Gehrels*, 2006].

2.4 WESTERN TIBET

To the west, the Tibetan plateau converges to a narrow belt mainly characterized by the Western Kunlun Shan and the Karakorum ranges (Fig. 2.9) [*Yin and Harrison*, 2000]. Beyond these narrow belts, the high elevation extends into the Pamir region to the northwest and into the Hindu Kush ranges to the southwest. In the western part of Tibet, the central Tibetan terranes were offset across the Karakorum and the Altyn Tagh faults. Correlations between the central Tibet and western terranes can be seen in the Western Kunlun - Karakorum region from north to south: North and South Kunlun terranes (Eastern Kunlun-Qaidam terrane), Tianshuihai terrane (Songpan-Ganzi terrane), Karakorum terrane (Qiangtang terrane), Kohistan-Ladakh terrane (Lhasa terrane) (Fig. 2.9) [*Yin and Harrison*, 2000; *Cowgill et al.*, 2003]. The southern boundaries of the North and South Kunlun terranes are respectively the Kudi suture and the Marza suture [*Matte et al.*, 1996a] along the active left-slip Karakash (Karakax) fault. The northern part of the Western Kunlun block highlights a thick Late Devonian to early Permian marine sequence that may reflect possible rifting along the southern margin of the Tarim block [*Yin and Harrison*, 2000].

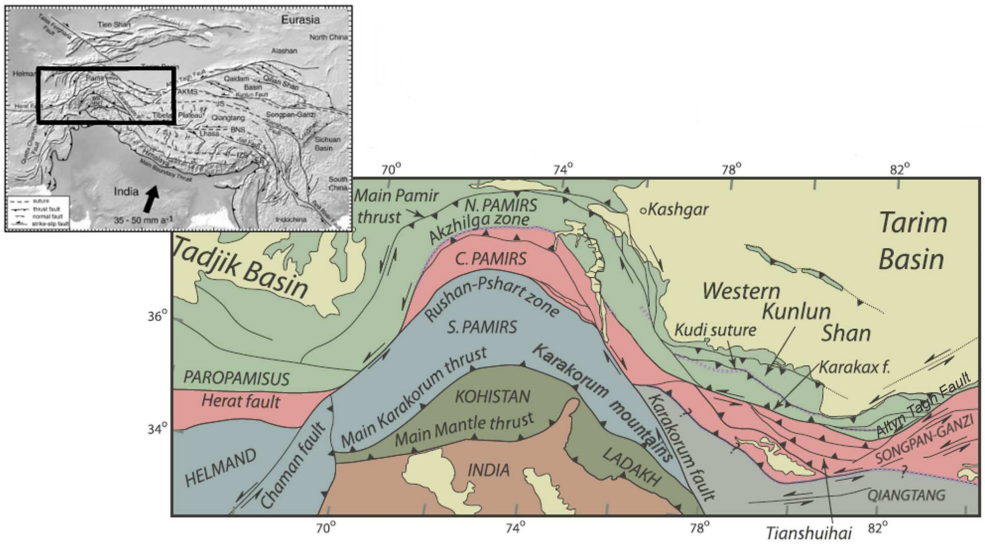

Figure 2.9: Tectonic map of the Western margin of Tibet showing the extension of central Tibet main terranes to the west. *modified from* [*Cowgill et al.*, 2003; *Kearey et al.*, 2009]

Similarly to the development of the Kunlun batholith at the southern margin of the Eastern Kunlun-Qaidam terrane, the western Kunlun ranges are characterized by a two-stage magmatic arcs signature of early Paleozoic and Late Permian-Triassic ages [*Yin and Harrison*, 2000]. The Kunlun arc may have been offset in the Cenozoic by the left-slip Altyn Tagh fault [*Peltzer and Tapponnier*, 1988]. However, the Kudi back arc basin associated with the Triassic Kudi suture and separating the North and South Kunlun terranes did not reach the Eastern Kunlun block [*Yin and Harrison*, 2000]. East of the Pamirs, the northern Karakorum melange complex [*Gaetani and Garzanti*, 1991], along the active right-slip Karakorum fault, defines the boundary between the Tianshuihai terrane and the Karakorum terrane. The Main Karakorum thrust along the Shyok suture separates the Karakorum terrane from the Kohistan-Ladakh arc terrane. The Indus Yarlung suture dissociates Indian sequences from the Kohistan-Ladakh terrane (Fig. 2.9) [*Yin and Harrison*, 2000; *Cowgill et al.*, 2003].

2.5 EASTERN TIBET

To the East, the plateau is characterized as a significant accommodation area, where the deformation is absorbed through different mechanisms involving southeastward extrusion of the Indochina block [*Peltzer and Tapponnier*, 1988; *Leloup et al.*, 1995], block rotation [*Davy and Cobbold*, 1988; *Royden et al.*, 1997] as well as internal deformation [*Wang and Burchfiel*, 1997; *Wang et al.*, 1998]. The eastern end of the plateau is mainly associated with the termination of the Triassic belt defined by the Songpan-Ganzi and the Yidun (Litang-Batang) blocks, bounded by the South-China, the North-China and the Qiangtang blocks since the closure of the Paleotethys ocean [*Yin and Harrison*, 2000; *Roger et al.*, 2008].

The Triassic belt represents a key area in the accommodation of the deformation in eastern Tibet as it involves major strike-slip and dip-slip faults (Fig. 2.10), such as the Longmen Shan thrust belt, the Xiangshuihe-Xiaojiang fault and the Jiali-Gaoligong fault system [*Yin and Harrison*, 2000; *Roger et al.*, 2008]. The Tertiary Longmen Shan thrust belt marks the boundary between the Songpan-Ganzi block and the Sichuan basin. The Anyimaqen-

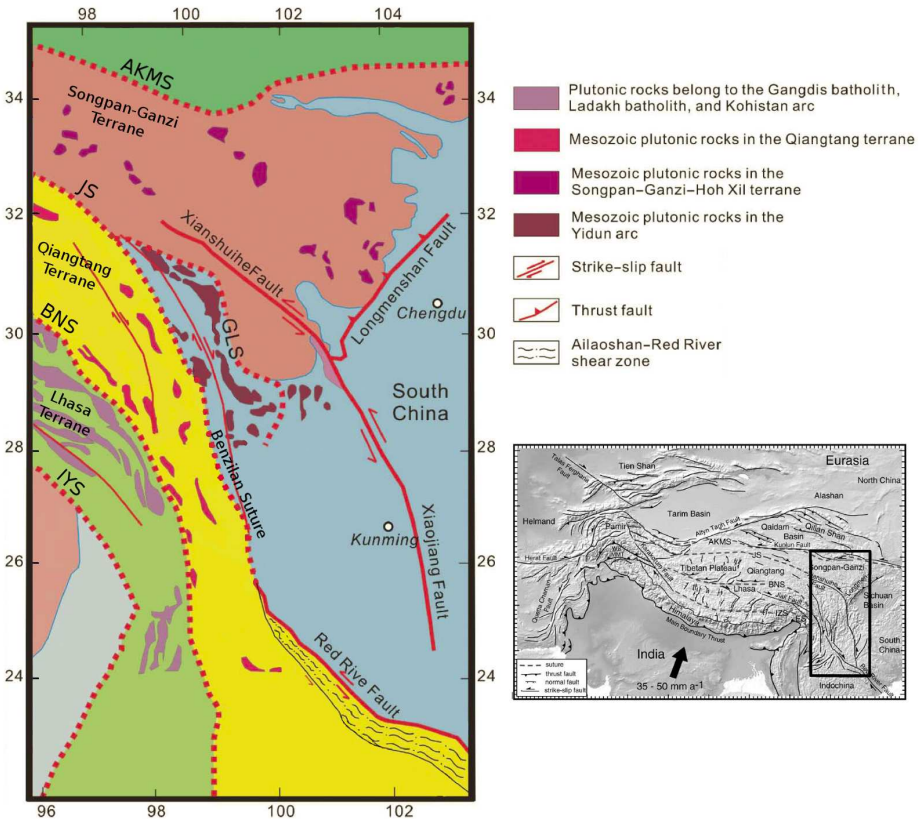

Figure 2.10: Sinplified geological map of the Eastern margin of Tibet. JS = Jinsha suture; IYS = Indus-Yarlung suture; BNS = Bangong-Nujiang suture; GLS = Ganzi-Litang suture; AKMS = Anyimaqen-Kunlun-Muztagh. *modified from* [*Qin et al.*, 2012; *Kearey et al.*, 2009]

Kunlun-Muztagh suture is extending to the east into the Qinling Shan and Dabie Shan belts, which define the boundary between the North-China and the South-China blocks [*Roger et al.*, 2008]. To the southeast, the Jinsha suture zone becomes the Benzilan suture bounding the south of the Triassic Yidun arc. The Ganzi Litang suture defines the northern limit of the Yidun arc and merges with the Jinsha suture to the west (Fig. 2.10) [*Yin and Harrison*, 2000]. The Hf isotope signature of the Yidun calc-alkaline magmas has been associated with the Mesoproterozoic Yangtze craton of the South-China block [*Reid et al.*, 2007]. Therefore, the Yidun arc was likely built on the continental basement of South China [*Burchfiel et al.*, 1995]. The Qiangtang and Lhasa terranes narrow to the southeast (Fig. 2.10), between the Eastern Himalayan syntaxis and the Three Rivers region (South China), and show significant correlation with the pre-Cenozoic continental terranes of the Sundaland region (southeast Asia), such as the Sibumasu blocks [*van Hinsbergen et al.*, 2011].

3 HISTORY AND EVOLUTION OF THE OROGEN

The origin of the collision starts in the Neoproterozoic with the developement of magmatic arcs and accretionary complexes along the northern margin of Gondwana [*Gehrels et al.*, 2011]. The Himalayan-Tibetan orogen is characterized by a relatively juvenile crust [*Dewey et al.*, 1988], as the orogen crust mainly developed during the Neoproterozoic and Early Paleozoic [*Gehrels et al.*, 2011]. From the Late Paleozoic to the Jurassic, the Himalaya-Tibet region experienced some rifting associated with northward displacement of the Tibetan terranes across the Tethyan ocean. The orogen accretion developed progressively at the southern margin of Asia during the Jurassic and Cretaceous, before final collision with India during Latest Cretaceous-Early Tertiary time [*Gehrels et al.*, 2011].

3.1 PRE-TERTIARY HISTORY OF THE OROGEN

Neoproterozoic - Mid-Paleozoic

During the Neoproterozoic, the Himalaya-Tibet region may have been characterized by juvenile magmatic arc terranes that may have developed as a northeast extension of the Arabian-Nubian Shield [*Johnson and Woldehaimanot*, 2003]. Those Neoproterozoic igneous rocks are exposed in the Qilian terranes and the Amdo basement [*Gehrels and Yin*, 2003; *Guynn et al.*, 2006], and could reflect a significant arc-type Neoproterozoic basement in the Himalaya-Tibet region [*Gehrels et al.*, 2011]. The Arabian-Nubian Shield formed the northern part of the East African Orogen that welded the eastern and western parts of the supercontinent Gondwana during the late Neoproterozoic [*Johnson and Woldehaimanot*, 2003]. The Early Paleozoic is characterized by the northern margin of Gondwana undergoing a south dipping subduction (Fig. 3.1). This north-facing system created regional uplift [*Gaetani and Garzanti*, 1991; *Brookfield*, 1993; *Johnson et al.*, 2001], associated with the developement of the Cambrian to early Ordovician granites exposed in the Himalayas, Lhasa, Amdo and Qiangtang terranes [*Guynn et al.*, 2006; *Cawood et al.*, 2007; *Pullen et al.*, 2011]. However, the Himalayan Cambro-Ordovician granites intrusions have also been interpreted to be associated with a pre-orogen rifting event [*Murphy and Nance*, 1991; *Hughes and Jell*, 1999; *Miller et al.*, 2001]. The north-south shortening may have extended across the northern margin of India, leading to the formation of a proto-Himalayan orogen between India and Lhasa in the early Paleozoic (Fig. 3.1) [*Brookfield*, 1993; *Yin and Harrison*, 2000; *Johnson et al.*, 2001; *Cawood et al.*, 2007]. The signature of this event can be seen in the widespread foliation of the Amdo gneiss complex [*Coward et al.*, 1988b; *Dewey et al.*, 1988]. The Qilian terranes may have been welded with the northern Tarim and Sino-Korean cratons along a north-facing subduction system during Ordovician-Silurian times [*Sobel and Arnaud*, 1999; *Gehrels et al.*, 2011]. The accretion of the arcs-complex that characterizes the Qilian terranes is still unclear. However, the Qilian terranes were likely united by the Late Devonian, when they collided with the Eastern Kunlun-Qaidam block along a

south-facing subduction system (Fig. 3.1) [*Cheng*, 1994; *Hsu et al.*, 1995; *Yin and Harrison*, 2000]. Although the Jinsha suture defines the Jurassic boundary between the Cimmerian (Gondwana affinity) and Hunic (Laurasian affinity) terranes, those terranes may have been previously gathered as part of an Early-Mid Paleozoic collisional event (Fig. 3.1) [*Gehrels et al.*, 2011]. The Hunic terranes separated from the Gondwana block in the Silurian with the opening of the Paleotethys ocean between the Qilian-Kunlun terranes and the Qiangtang terrane [*Stampfli and Borel*, 2002; *Gehrels et al.*, 2011]. This event led to the breakup of the proto-Tibetan orogen that developed along Gondwana northern margin [*Metcalfe*, 1996]. To the north, the Rheic ocean closed in the early Carboniferous, when the Hunic terranes welded with the future Laurasia [*Stampfli and Borel*, 2002].

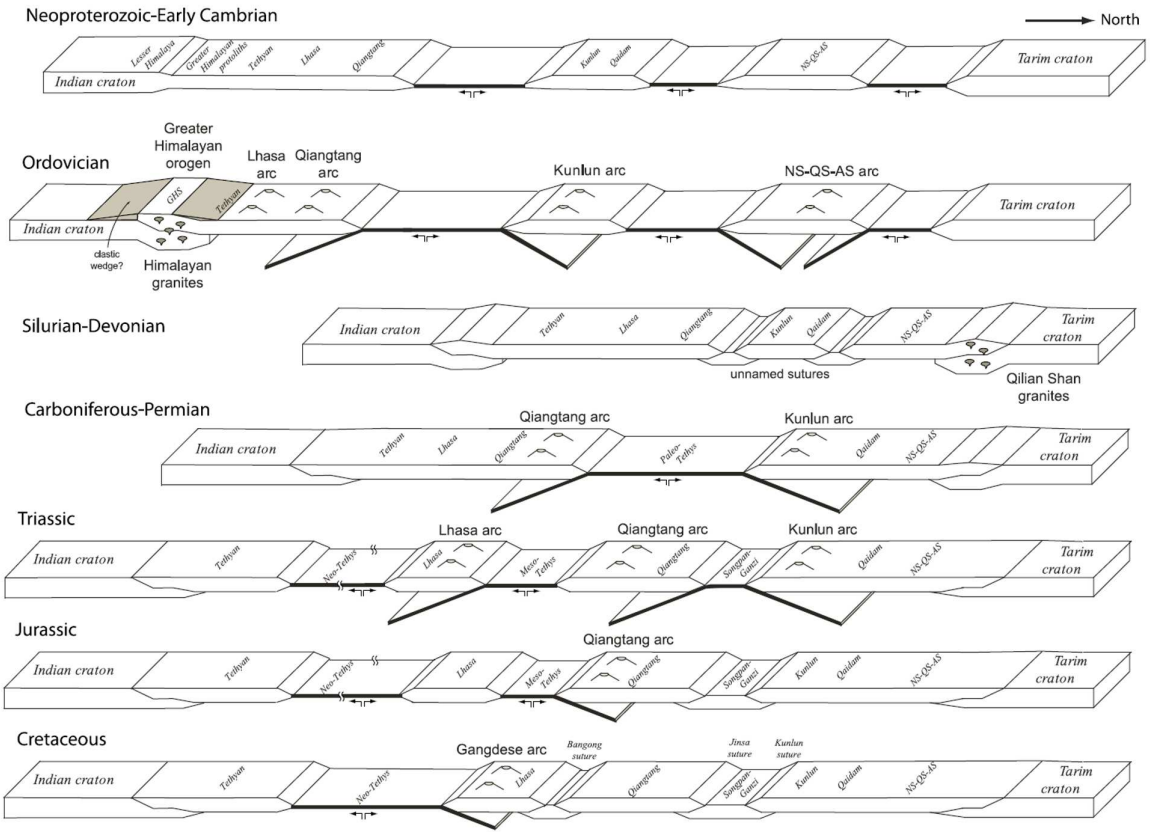

Figure 3.1: Paleozoic-Mesozoic schematic tectonic reconstructions of the Himalayan-Tibetan orogen. *modified from* [*Gehrels et al.*, 2011]

Carboniferous - Permian

About 300 Ma years ago, Gondwana and Laurasia were part of one supercontinent, Pangaea. At that time, the ocean separating Gondwana from Laurasia was the Paleotethys (Fig. 3.2). Both Qiangtang and Lhasa terranes have been characterized to be of Gondwana affinity, and were part of the Cimmerian superterrane along the northern margin of Gondwana [*Pullen et al.*, 2011]. The upper Paleozoic strata, from sequences and terranes located south of the Jinsha suture, highlights similar age groups. Furthermore, those terranes exhibit some glaciogenic sediments, such as diamictite, which likely originated from

a polar ice cap centered on Antarctica, southern Australia, and southern India [*Gehrels et al.*, 2011]. Therefore the terranes were likely located in the vicinity of Gondwana during Carboniferous-Permian time. The broad exhibition of those sediments highlights a more stable tectonic activity in the Himalayan-Tibetan region of Gondwana between the Ordovician and Permian [*Gehrels et al.*, 2011; *Brookfield*, 1993]. In the Late Carboniferous and Early Permian, the northern margin of Gondwana was experiencing some rifting that may have lead to the separation of the Qiangtang terrane from the Lhasa terrane and the opening of the Mesotethys ocean (Fig. 3.1) [*Gehrels et al.*, 2011]. However, it is possible that only a small ocean basin opened and then closed by the end of the Permian [*Zhu et al.*, 2009, 2010]. The separation between the Qiangtang and Lhasa terranes would have then occurred only during the Late Triassic or even Early Jurrassic [*Baxter et al.*, 2009]. By the Late Permian and Early Triassic, the Cimmerian superterrane rifted apart from former Gondwana, creating a new ocean, the Neotethys or Tethys ocean, as both the Qiangtang and Lhasa terranes were starting to drift away from India (Fig. 3.2) [*Gaetani and Garzanti*, 1991; *Brookfield*, 1993; *Metcalfe*, 1996; *Yin and Harrison*, 2000]. At the northern margin of the Qiangtang terrane, the former Jinsha suture was likely characterizing an active subduction zone by the Latest Permian (Fig. 3.1) [*Roger et al.*, 2003]. At the same time, the Paleotethys ocean floor may have started to underthrust the Kunlun batholiths in the north, leading to the superposition of younger magmatism over the older Early Paleozoic arc. This event is likely to have lasted until the Late Triassic [*Yin and Harrison*, 2000].

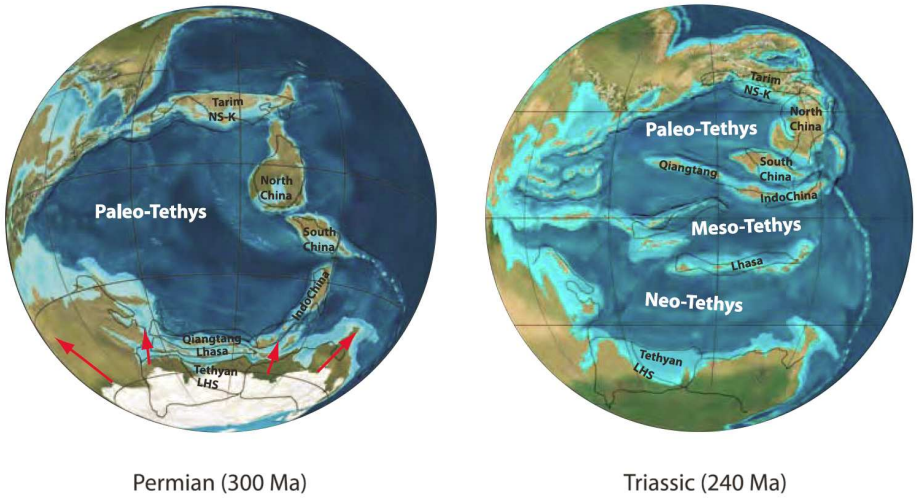

Figure 3.2: Paleogeographic maps of the Himalayan-Tibetan orogen during the Permian and Triassic times. *modified from* [*Gehrels et al.*, 2011]

Triassic

During the Triassic, both oceans, the Neotethys between India and Lhasa and the Mesotethys between Qiangtang and Lhasa were likely open (Fig. 3.2) [*Dewey et al.*, 1988; *Yin and Nie*, 1996; *Metcalfe*, 1996; *Yin and Harrison*, 2000; *Gehrels et al.*, 2011]. The Triassic magmatism signature in the Tibetan region is likely to record the subduction of the Paleotethys ocean floor in north and south dipping systems respectively along the Kunlun and Qiantang

terranes, and the subduction of the Mesotethys ocean floor in a south dipping system along the Lhasa terrane (Fig. 3.1) [*Gehrels et al.*, 2011]. The Triassic Songpan-Ganzi flysch complex is likely to have been deposited mainly as the result of the erosion of the Qinling-Dabie orogen [*Nie et al.*, 1994; *Zhou and Graham*, 1996]. This orogenic belt welded the North China craton with the South China craton during the Triassic [*Yin and Harrison*, 2000]. The Songpan-Ganzi sediments likely filled different tectonic basins [*Yin and Harrison*, 2000]. Another hypothesis supports the notion that the flysch complex originated in a back arc basin, part of a north-dipping subduction system along the Jinsha suture zone [*Hsu et al.*, 1995; *Burchfiel et al.*, 1995]. However, the Triassic volcanic signature of the area does not support this north-dipping subduction assumption [*Zhou and Graham*, 1996]. To the west, magmatic arcs may have been the main suppliers for the Songpan-Ganzi Triassic sediments [*Weislogel*, 2008]. The Cimmerian superterrane collided with Laurasia around 200 Ma ago, creating the Cimmerian orogeny along the suture and closing the Paleotethys Ocean from west to east. The crust of Turkey, Iran, Afghanistan, South-East Asia, and particularly Tibet, has a Cimmerian origin. For the Tibetan Plateau, this signature can be found in the Qiangtang and Lhasa terranes that used to be located along the Paleotethys margin of Gondwana as part of the Cimmerian superterrane [*Pullen et al.*, 2008].

Jurassic

The Jinsha suture started to close in the Early Jurassic (Fig. 3.3) [*Gehrels et al.*, 2011]. However, as the Karakorum batholiths only formed between the Mid-Jurassic and Mid-Cretaceous [*Searle*, 1991], the closure of the Paleotethys ocean was likely diachronous and moved to the west with time [*Yin and Harrison*, 2000]. Furthermore, during the closure of the Paleotethys ocean, the Songpan-Ganzi Triassic flysch must have experienced intense folding [*Burchfiel et al.*, 1995]. In the Middle Jurassic, the Mesotethys ocean was being closed in a south-facing subduction system along the Qiangtang terrane (Fig. 3.1) [*Gehrels et al.*, 2011]. The Bangong suture zone is likely to have closed during the Late Jurassic to Early Cretaceous [*Dewey et al.*, 1988; *Yin and Harrison*, 2000; *Baxter et al.*, 2009; *Gehrels et al.*, 2011]. In Early-Mid Jurassic, Pangaea broke up as the Tethys rift extended to the west and the Atlantic Ocean started to separate the northern supercontinent of Laurasia from the southern supercontinent Gondwana. During the Early Cretaceous, Gondwana rifted apart into multiple continents; Africa, South America, India, Antarctica, and Australia. Western Gondwana (South America and America) broke away from eastern Gondwana (Antarctica, India and Australia) following a major rift event in the Late Triassic. However, the separation occurred in the Middle Jurassic with the formation of young oceanic crust [*Dezes*, 1999].

Cretaceous

During the Early Cretaceous, South America started moving away from Africa due to the opening of the South Atlantic Ocean. Furthermore, at the same time, India rifted from Antarctica, as the Indian Ocean was opening. The magmatism signature of the Himalayan Cretaceous strata reflects this rifting event [*Gaetani and Garzanti*, 1991; *Brookfield*, 1993]. The subduction of the Tethys oceanic lithosphere beneath the Lhasa terrane started in the Middle Cretaceous (Fig. 3.1) and is associated with the formation of the Xigaze forearc basin

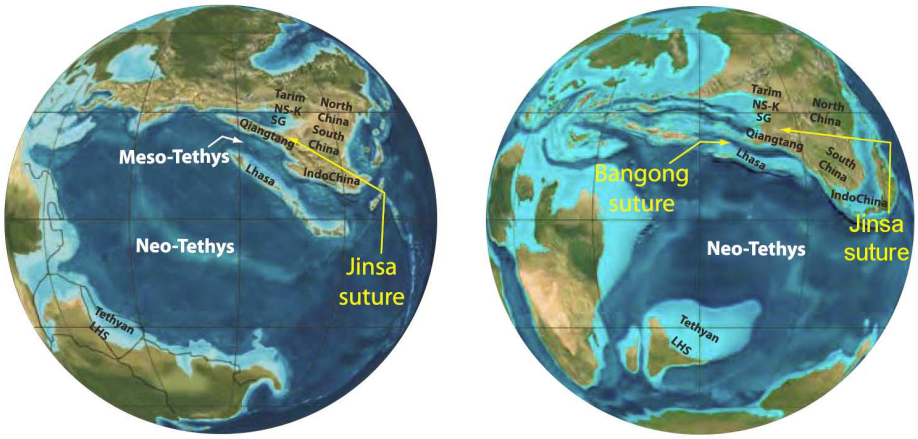

Figure 3.3: Paleogeographic maps of the Himalayan-Tibetan orogen during the Jurassic and Creataceous times. *modified from* [*Gehrels et al.*, 2011]

and Gangdese batholith along the southern margin of the Lhasa terrane [*Yin and Harrison*, 2000]. After starting its northward drifting in the Upper Cretaceous (Fig. 3.3), the Indian plate had covered about 6000 km when it collided with Asia [*Dezes*, 1999]. On a global scale, the closure of the Tethys ocean is characterized by the collision of Africa-Ariabia and India with Laurasia, leading to the buckling and folding of the former Cimmerian continent. This event is identified as the Alpine orogeny. The Alpine orogeny took place in the Late Mesozoic and Cenozoic [*Moores and Fairbridge*, 1998], and includes orogenic belts such as the Alps, the Caucasus, the Iranian Plateau, the Sulaiman Mountains, the Pamir Mountains and the Himalaya-Tibetan orogen.

3.2 CENOZOIC COLLISION BETWEEN INDIA AND ASIA

At about 55-50 Ma, the relative speed between the Indian and Asian plates changed dramatically from 18-19.5 cm/yr to 4.5 cm/yr [*Klootwijk et al.*, 1992], an event interpreted as the beginning of the India-Eurasia collision. However, some see the collision happening as early as the Late Cretaceous [*Yin and Harrison*, 2000] to the Latest Eocene [*Rowley*, 1998] or even much later at around 35 Ma [*Aitchison et al.*, 2007]. Altough it is a continuous process, the India-Asia collision could be set to date from the Late Ypresian (Early Eocene), which characterizes timing of the final marine sedimentation in the Indus-Yarlung Tsangpo suture zone [*Searle et al.*, 2011]. Since the collision, the Himalyan orogeny has accommodated about 2500 km of crustal shortening [*Dezes*, 1999]. *Lee and Lawver* [1995] mentioned a "soft collision" associated with the contact between the Greater India margin and Asia at ~60 Ma followed by a drop in the convergence rate associated with the start of a "hard collision" at ~45 Ma (Fig. 4.5).

The pre-collisional history of the Indian and Eurasian plates defines the strength and rheology of their continental lithospheres. On one hand, millions years of subduction, arc magmatism and terrane accretion have weakened the Eurasian lithosphere allowing broad deformation during the Cenozoic collision between India-Eurasia (Fig. 3.4) [*Yin and Harri-*

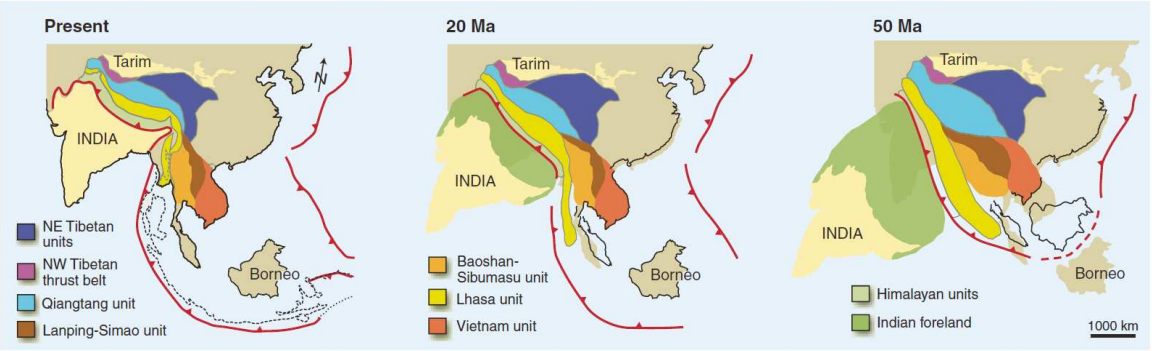

Figure 3.4: Tectonic reconstruction of the Cenozoic collision between India and Eurasia including the major tectonic units of Tibet and Indochina. *from* [Royden et al., 2008]

son, 2000; Tapponnier et al., 2001]. However, on the other hand, the Indian plate defines a strong and deep Precambrian shield that resisted shortening during the collision. Only the Early Proterozoic to Paleocene weak sequences deposited on the northern passive margin of the Indian plate underwent strong deformation in the development of the Himalayan fold and thrust belt [Kearey et al., 2009]. The continental underthrusting of India and its coupling with overriding Eurasia control the shortening across the Himalayan-Tibetan orogen. It has created continental crust as thick as 80 km, weakened by high temperatures and widespread intra-crustal melting, allowing crustal flow and decoupling the Tibetan crust from the underlying convergent motions [Kearey et al., 2009]. The present-day surface deformation within the Tibetan Plateau, with respect to India and stable portions of Asia, is highlighted by GPS measurements [Gan et al., 2007] (Fig. 3.5) The GPS data show a north-south shortening of 40 mm/yr across the plateau, with almost 20 mm/yr east-west motion [Searle et al., 2011]. In addition to the underthrusting of Indian, several lithospheric mechanisms have been proposed to accommodate the shortening during collision, such as downwelling of Indian mantle lithosphere beneath central Tibet [Tilmann et al., 2003], convective removal or delamination of the lithospheric mantle beneath Tibet [England and Houseman, 1988; Molnar et al., 1993] and southward subduction of Asian continental lithosphere [Deng, 1991; Meyer et al., 1998; Tapponnier et al., 2001; Zhao et al., 2011]. It is more than likely that the shortening of Tibetan lithosphere was accommodated through a combination of all those mechanisms [Kearey et al., 2009].

N-S Shortening

Paleomagnetic data suggest a 2600 ± 900 km post-collision shortening for the Himalayan-Tibetan orogen, including 1700 ± 600 km of accommodation in the Tibetan Plateau from north-south shortening and lateral extrusion [Patriat and Achache, 1984; Besse and Courtillot, 1991]. The remaining 900 km would then account for the convergence absorbed in the Himalayan fold-thrust belt [Pichon et al., 1992]. However the geological data predict smaller estimates. The Himalayan fold-thrust belt shortening estimates, based on geological data, vary with the location and thrusts involved in the estimations. In eastern Nepal, the shortening between the South Tibetan Detachment system and the Main Frontal Thrust may be 210 to 280 km [Schelling, 1992]. For western Nepal, DeCelles et al. [2001] mentioned a shortening ranging from 418 to 493 km. In northern Pakistan, the total shortening was es-

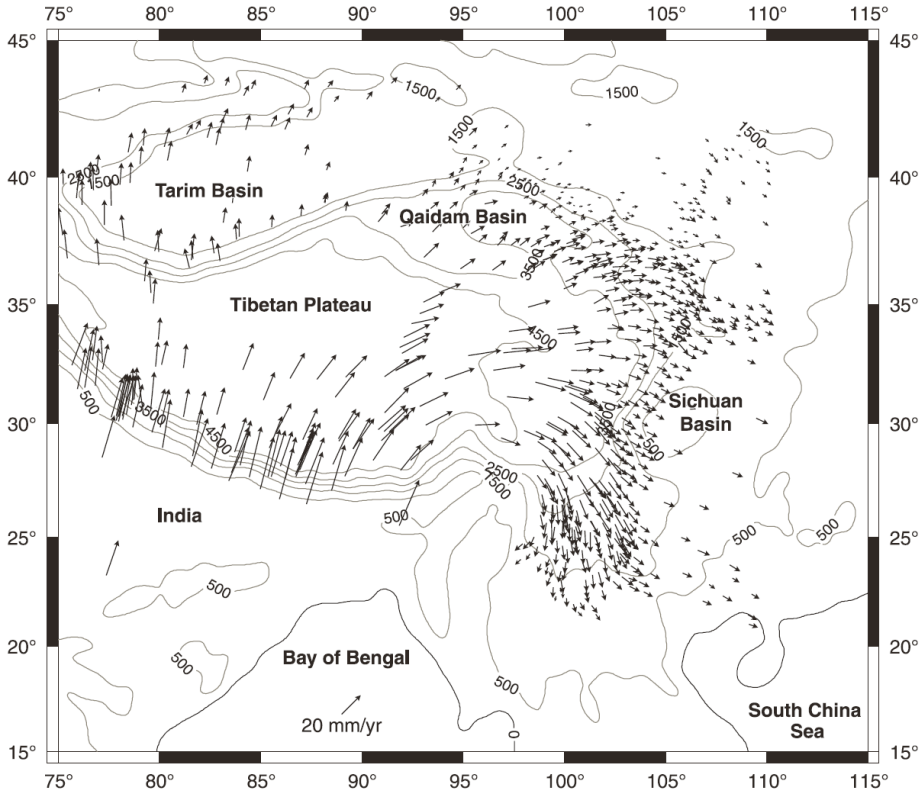

Figure 3.5: Deformation across Tibet highlighted by motion velocities relative to a stable Eurasia. GPS data after [*Gan et al.*, 2007]. The surface elevation is represented by contour lines. *modified from* [*Searle et al.*, 2011]

timated to be 470 km [*Coward and Butler*, 1985]. *Hauck et al.* [1998] estimated a shortening of ~323 km between the Indus-Yarlung suture zone between the Main Frontal Thrust in the eastern Himalaya. It seems that the long-term average rate of shortening in the Himalayan fold-thrust was at its highest in the Neogene and then decreased during Pliocene to Recent times. If the shortening rate has not changed since the Neogene, the total shortening in the Tibetan Himalaya would be on the order of 900 km [*DeCelles et al.*, 2002]. Furthermore, it appears that the shortening estimates prior to the Neogene were quite slow [*Searle and McCarron*, 1997], which characterizes the Himalayan fold-thrust belt as a delayed response in the accommodation of the Cenozoic India-Eurasia collision [*Yin and Harrison*, 2000]. North of the Himalayan fold-thrust belt, geological data highlight 600 to 750 km of N-S Cenozoic shortening across, and north of, the Tibetan Plateau [*van Hinsbergen et al.*, 2011]. In the Lhasa and Qiangtang terranes most of the shortening appears to have occurred prior to the India-Asia collision, as the Lhasa terrane already underwent ~250 km shortening between 100 and 50 Ma [*van Hinsbergen et al.*, 2011] and the Qiangtang terrane underwent ~300 km shortening between 140 and 100 Ma during the Lhasa-Qiangtang collision [*Kapp et al.*, 2005; *DeCelles et al.*, 2007]. During the Cenozoic, the Lhasa and Qiangtang blocks seem to have undergone shortening. Whereas the southern Qiangtang terrane (50-30 Ma) and the Bangong-Nujiang (30-20 Ma) suture zone show a total shortening of ~120 km [*van Hinsbergen et al.*, 2011], the Lhasa terrane presents only ~40 km shortening between 50 Ma and 20 Ma [*He et al.*, 2007; *Kapp et al.*, 2007]. Furthermore, the thrusting associated with the Indus-Yarlung suture highlight a post-collisional

shortening of several tens of kilometres that occurred during the Oligocene and middle Miocene [*Yin et al.*, 1999a]. On the contrary, the Fenghuo Shan-Nanqian thrust likely accommodated up to ~200 km N-S shortening between 50 and 30 Ma in the Songpan-Ganzi terrane [*van Hinsbergen et al.*, 2011]. In total, based on geological data, *van Hinsbergen et al.* [2011] estimated the post-50 Ma shortening in Tibet to be ~450 km. However, the Cenozoic shortening in the Himalayan-Tibetan orogen remains unclear and more work needs to be done.

E-W Extension

In the middle to late Miocene, as the plateau may have reached its present elevation [*Molnar and Tapponnier*, 1978; *England and Houseman*, 1989], southern and central Tibet developed E-W extension characterized by the formation of N-S trending rifts [*Tapponnier and Molnar*, 1977; *Molnar and Tapponnier*, 1978; *Armijo et al.*, 1986; *Burchfiel et al.*, 1991; *Coleman and Hodges*, 1995; *Yin et al.*, 1999b; *Murphy et al.*, 2002; *Taylor et al.*, 2003]. However, *Wang et al.* [2010b] stated the E-W extension could have started earlier in the Mid-Eocene. The igneous activity in Tibet appears to be unrelated to the initiation of rifting, due to its asynchronous and uncorrelated special distribution [*Yin and Harrison*, 2000]. The rifting spacing between the Himalayas and central Tibet decreases systematically to the north and may then characterize a northward decrease of crustal thickness [*Yin*, 2000]. The mode of rifting and the volcanism history (10-30 Ma prior to rifting) in Tibet present strong synchronous similarities with the Baikal rift and Shanxi graben in southeast Siberia and north China [*Yin*, 2000]. As those similar events appear to have covered a broad part of Asia, the rifting in Tibet cannot only be the result of gravitational collapse [*Dewey*, 1988] or convective removal of lithospheric mantle beneath Tibet [*England and Houseman*, 1989]. Instead, *Yin* [2000] mentioned the necessity of a large scale event affecting the entire east of Asia, such as mantle upwelling induced by the 40-35 Ma initiation of the Pacific plate subduction [*Northrup et al.*, 1995]. Mantle upwelling in eastern Asia may have initiated thermal weakening of the lithosphere and, in consequence, triggered the 8-4 Ma rifting episode in Asia [*Yin*, 2000].

When considering only the deformation associated with major fold belts and thrust faults, the India-Eurasia collision presents a shortening deficit [*Dewey et al.*, 1988; *Johnson*, 2002]. Other mechanisms involving large-scale strike-slip faulting and lateral extrusion need then to be taken into account to explain how the convergence was accommodated during Cenozoic collision [*Johnson*, 2002]. For instance, *Armijo et al.* [1989] mentioned that at least 30% of the convergence associated with the ongoing India-Asia collision is absorbed in the eastward extrusion of North Tibet between the dextral Karakorum fault and both sinistral Altyn Tagh and Kunlun faults (Fig. 3.6).

Altyn Tagh Fault

The 1600 km long sinistral strike-slip and lithospheric-scale [*Wittlinger et al.*, 1998] Altyn Tagh fault bounds the northwestern part of the Tibetan Plateau, allowing Tibet to move to the northeast relatively to the Tarim basin (Fig. 3.6) [*Meyer et al.*, 1998; *Cowgill et al.*, 2003]. At its northeastern end, the fault transfers the shortening into the thrust faults of the Nan-

Shan-Qilian Shan thrusts belts (Fig. 2.8) [*Molnar and Tapponnier*, 1975; *Meyer et al.*, 1998]. South of the Tarim Basin, the fault changes its strike as it becomes the Karakax Fault (Fig. 2.9) [*Searle et al.*, 2011]. Minor to medium levels of seismicity have been observed along the entire Altyn Tagh fault system [*CSBS*, 1992]. The last two large earthquakes to date occurred in 1924 near Qiemo in central Altyn Tagh fault, both with a magnitude Mw 7.2 [*CSBS*, 1992]. Palaeoseismic rupture mapping indicates major earthquakes as large as Mw 7.8 in the Holocene [*Washburn et al.*, 2003]. The Altyn Tagh Fault geological offsets have been estimated through a variety of geological constraints and mainly range between 300 and 500 km [*Molnar and Tapponnier*, 1975; *Peltzer and Tapponnier*, 1988; *Ritts and Biffi*, 2000; *Yin and Harrison*, 2000; *Johnson*, 2002; *Cowgill et al.*, 2003].

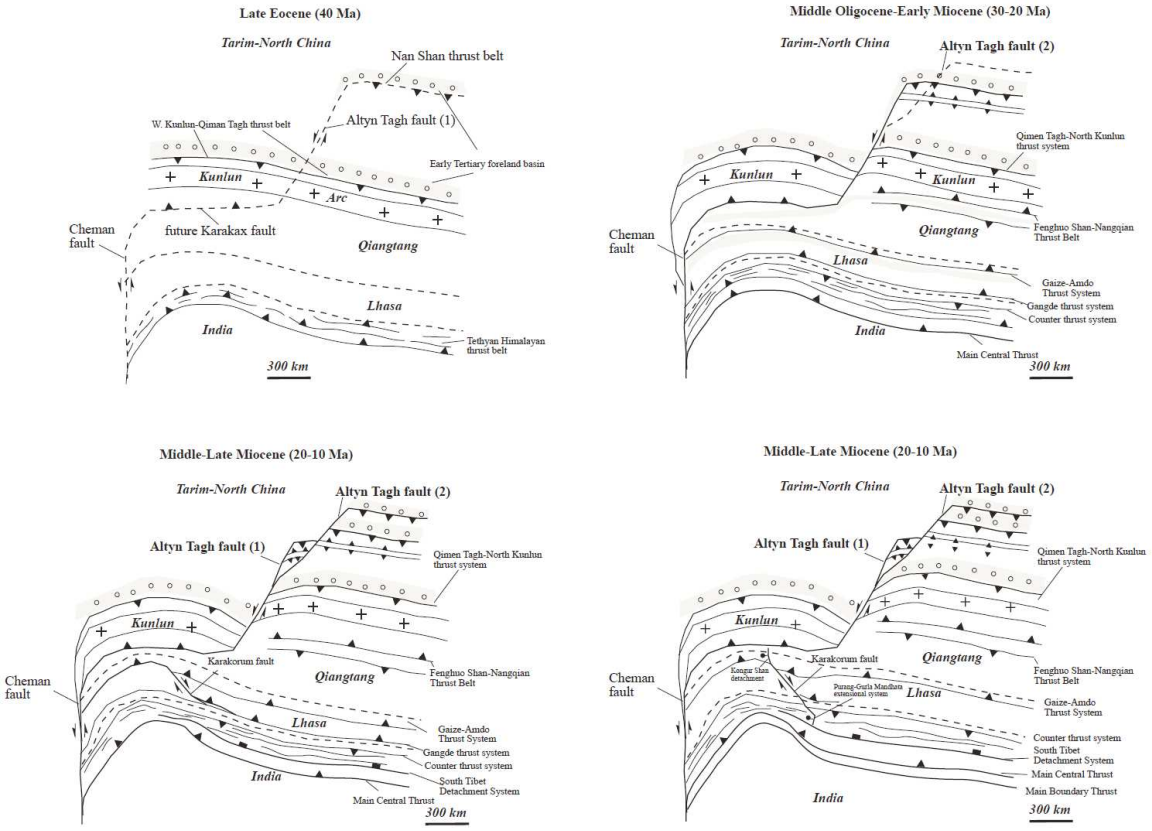

Figure 3.6: Evolution of major Cenozoic structures in the central and northwestern parts of the Himalayan-Tibetan orogen. *from* [*Yin and Harrison*, 2000]

However, the slip rate of the Altyn Tagh Fault is still debated [*Bedrosian et al.*, 2001; *Searle et al.*, 2011] and, in consequence, so is the proportion of crustal extrusion opposite involved in the accommodation of the ongoing north-south convergence in the Tibetan Plateau in opposition to compression [*Bedrosian et al.*, 2001].

Karakorum Fault

The dextral ~700 km long Karakoram Fault extends from the northeastern Pamir to southwestern Tibet, where it merges into the Indus-Yarlung Tsangpo suture zone south of Mount Kailash [*Searle et al.*, 2011]. The Karakorum fault may have developed to accommo-

date the eastward extrusion of northern Tibet (Fig. 3.6) [*Armijo et al.*, 1986] or the oblique convergence between India and Tibet [*McCaffrey and Nabelek*, 1998]. However, the fault could also take part in the Tibet E-W extension and characterize a transfer zone between southern Tibet widely-spaced rifts and northern Tibet closely-spaced rifts [*Yin*, 2000]. In the Pangong Range, the Karakorum fault crosses an exhumed metamorphic complex, including migmatites and abundant leucogranite dykes, however its relation to the fault is still discussed [*Searle et al.*, 2011]. One assumption suggests the metamorphism results from synkinematic shear heating along the Karakoram Fault [*Lacassin et al.*, 2004; *Valli et al.*, 2007; *Weinberg et al.*, 2009], whereas in a second model they may have formed prior to the fault and are unrelated to the shearing motion along the fault [*Searle*, 1996b; *Phillips et al.*, 2004]. The Karakorum Fault seismic activity is an enigma, as for a major tectonic feature of the Himalayan-Tibetan orogen; the fault presents almost no historical earthquake activity [*Searle et al.*, 2011]. This particular feature could be explained by a very large earthquake repetition cycle or elevated temperatures in the middle crust that would prevent earthquakes beneath the Karakorum fault [*Searle et al.*, 2011]. The displacement along the Karakorum Fault and its initiation (the fault either initiated at 25 Ma or more recently 14-12 Ma) are strongly debated [*van Hinsbergen et al.*, 2011]. Whereas some mention a maximum displacement of 150 km [*Searle*, 1996b; *Phillips et al.*, 2004; *Robinson*, 2009], others argue for higher offsets, such as 1000 km [*Peltzer and Tapponnier*, 1988], 600 km [*Lacassin et al.*, 2004] or 280 to 400 km [*Valli et al.*, 2007]. As mentioned before for the Altyn Tagh fault, those uncertainties prevent clear conclusions on the proportion of crustal extrusion associated with the Karakorum fault.

Kunlun Fault

The nearly 1500 km long sinistral east-west trending Kunlun fault generally follows the trace of the Anyimaqen-Kunlun-Muztagh suture and marks the northern boundary of the atypical topography of the Tibetan plateau [*Yin and Harrison*, 2000; *Searle et al.*, 2011]. The total offset along the central segment of the Kunlun fault defines a displacement of 100 $\pm$ 20 km [*van der Woerd et al.*, 2000; *Fu and Awata*, 2007; *Kirby et al.*, 2007]. Similarly to the Altyn Tagh Fault, the Kunlun Fault slip rates vary significantly between short-term geodetic and long-term geological rates. However, the Quaternary slip rates of the Kunlun faults are better constrained, and range around 10 mm/year [*van der Woerd et al.*, 1998; *Zhang et al.*, 2004; *He and Chery*, 2008], although *Kirby et al.* [2007] suggested that slip rates on the eastern portions of the fault decrease eastwards from >10 to <2 mm/year, as the slip is probably transferred northward into the eastern Kunlun Shan [*Kirby et al.*, 2007; *Duvall and Clark*, 2010]. Near the Lhasa-Goldmud highway, the fault splits in two branches, characterizing the Kunlun Fault (KF) and the South Kunlun Fault (SKF). The Kunlun fault may end in the thickened crust of the plateau [*Kirby et al.*, 2007], although *Meyer et al.* [1998] suggested the fault to be a lithospheric discontinuity. The Kunlun fault is likely to be coeval with the Miocene extension [*Jolivet et al.*, 2003] and facilitates the eastward expansion of the Tibetan plateau by linking the north-south trending extensional systems [*Yin and Harrison*, 2000]. Furthermore, the fault accommodates the cumulative slip associated with the eastward motion of the Tibetan Plateau relatively to the Tarim block [*van Hinsbergen et al.*, 2011]. Therefore, the Kunlun fault plays a significant role in the absorption of the convergence between India and Asia by allowing, north of the fault, northeastward motion of northern Tibet in association with the Altyn Tagh fault (Fig. 2.9)

but also, south of the fault, eastward extrusion of the Tibetan plateau [*Lin et al.*, 2002]. In the last century, the central and western segments of the Kunlun fault have experienced some large earthquakes, such as the Mw 8.1 Kokoxili event in 2001 [*Lasserre et al.*, 2005]. However, the eastern segment of the fault seems to present less seismicity [*Kirby et al.*, 2007].

Mid-Cenozoic Extrusion of Sundaland

Based on the modelling of *Molnar and Tapponnier* [1975] and *Tapponnier et al.* [1982], the Mid-Cenozoic extrusion of Indochina from southern Asia (Fig. 3.4) likely accommodated part of the Indo-Asian convergence through major strike-slip faults such as the Red River fault [*Yin and Harrison*, 2000]. The Red River fault, which extends from southeastern Tibet to the South China Sea [*Yin and Harrison*, 2000], has previously been interpreted as a pure Cenozoic right-slip fault [*Dewey et al.*, 1989]. However, the Ailao Shan shear zone, located south of the active Red River fault (Fig. 2.10), defines a major mid-Tertiary left-slip fault zone characterized by a metamorphic belt exposing mylonitic rocks [*Leloup et al.*, 1995]. Therefore, *Leloup et al.* [1993] and *Harrison et al.* [1996] mentioned the Red River fault was likely associated to a left-slip motion during most of the collision and reversed to a right-slip motion at about 5 Ma. The apparent left-lateral offset of the Red River fault has been estimated from ~250 km [*Hall et al.*, 2008; *Fyhn et al.*, 2009] to 700 ± 200 km [*Leloup et al.*, 1995] between ~30-20 Ma. Larger lateral escape estimates have been proposed [*Royden et al.*, 2008], however the resulting geometries and configurations of the different blocks and terranes appear inconsistent with geological observations [*van Hinsbergen et al.*, 2011]. In a review of the Asian Cenozoic deformation, *van Hinsbergen et al.* [2011] highlights that the southeastward extrusion of Sundaland along the Red River fault is likely represented by a displacement of ~250 km. However, the authors did not exclude that value could be slightly underestimated, and mentioned that future kinematic work still needs to be accomplished in eastern Tibet. Furthermore, the surface deformation in Tibet highlights clockwise rotation of eastern Tibet around the eastern Himalayan syntaxis [*Yin and Harrison*, 2000].

4 GEODYNAMIC MODELS AND DEEPER STRUCTURES

In order to account for the significant crustal thickness of Tibet and the uplift of the plateau, *Argand* [1924] proposed a model in which India has been underthrusting the entire plateau. Since then, several studies have been carried out and different models have been proposed to explain the actual continental deformation involved in the Himalayan-Tibetan orogen but also to characterize the lithospheric structure of the Tibetan plateau.

4.1 CRUSTAL DEFORMATION MODELS

Rigid blocks vs Continuum deformation

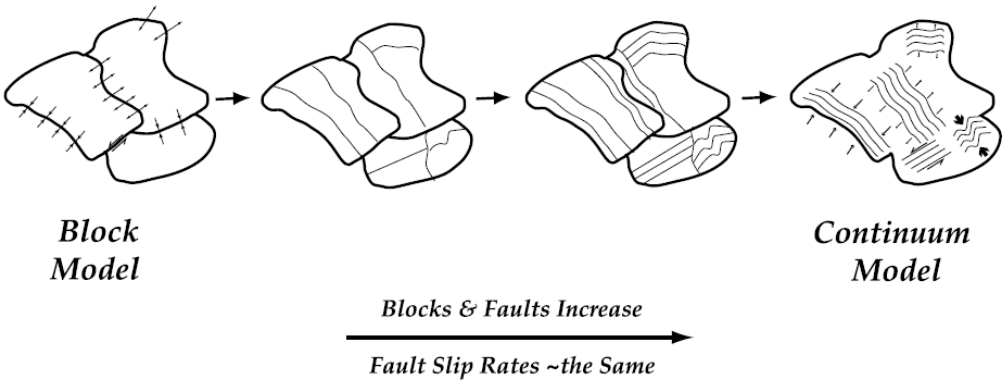

Figure 4.1: Transition from Block to Continuum model. *from Thatcher* [2007]

One of the mechanisms possibly involved in the continental deformation in Tibet is based on the rigid blocks model (Fig. 4.1) [*Tapponnier et al.*, 1982; *Peltzer and Tapponnier*, 1988; *Avouac and Tapponnier*, 1993; *Peltzer and Saucier*, 1996; *Replumaz and Tapponnier*, 2003; *Ryerson et al.*, 2006]. In the rigid blocks model, the deformation resulting from the indentation of India is mainly localized along large-scale, high-slip-rate and deeply rooted strike-slip faults [*Thatcher*, 2007; *Searle et al.*, 2011]. The rigid blocks do not absorb much of the deformation internally. Therefore, in this type of model, the rapid eastward extrusion of Tibet along major strike-slip faults becomes a significant process in the accommodation of the N-S convergence [*Searle et al.*, 2011]. Based on GPS observations, recent approaches of the block model focused on increasing the number of blocks [*Meade*, 2007; *Thatcher*, 2007]. As an alternative to the large blocks models associated with large-slip-rate strike-slip faults [*Peltzer and Tapponnier*, 1988; *Avouac and Tapponnier*, 1993], *Thatcher* [2007] proposed an 11-blocks model for Tibet bounded by lower-slip-rate faults. Furthermore, *Thatcher* [2007] highlights that the model misfits associated with internal deformation of the blocks would characterize the presence of smaller blocks within the larger blocks.

In opposition to the rigid blocks deformation, the continuum deformation model (Fig. 4.1) has been proposed [*England and McKenzie*, 1982; *Vilotte et al.*, 1986; *Houseman and England*, 1996; *England and Molnar*, 1997; *Flesch et al.*, 2001]. In this type of continental deformation, the lithosphere behaves as a continuum medium based on the thin viscous sheet model [*Bird and Piper*, 1980] which allows continuous, distributed crustal deformation driven by more rigid boundaries such as the Tarim block to the north. In the thin viscous sheet model, stresses and strain rates are averaged vertically through the lithosphere (~100 km thick surface layer [*England and Molnar*, 1997, 2005]). In consequence, the deformation associated with the northward indentation of India is mainly accommodated by homogeneous thickening of the crust and only a minor component of the convergence is absorbed by lateral extrusion [*Searle et al.*, 2011]. The continuum deformation model is also characterized by a larger quantity of low-slip-rate faults that delocalize the deformation in the crust [*Shen et al.*, 2005; *Thatcher*, 2007; *Searle et al.*, 2011], in comparison with the rigid blocks model.

Both rigid blocks and continuum deformation models have their limits. For example, the rigid block model does not take into account variations in crustal thickness and therefore possible gravitational collapse of over-thickened continental crust by convective thinning or delamination [*Kearey et al.*, 2009]. Concerning the continuum deformation, *Thatcher* [2007] mentioned that the viscous sheet models smear out the discrete slip occurring across major faults, and therefore affect the kinematic quantification of the surface deformation. Furthermore, the continuum model does not include depth-dependence of crustal viscosity [*Royden et al.*, 1997]. The rigid blocks and viscous sheet models are both quite extreme but, as mentioned by *Thatcher* [2007], the transition from one to another is gradational (Fig. 4.1). Therefore, an intermediate model, which would present a block size decrease (respectively increase of the number of blocks) and low-slip-rate faults compatible with continuum deformation, could be a more appropriate model to describe the observed deformation [*Thatcher*, 2007].

Crustal flow model

An alternative to the homogeneous deformation associated with the continuum model includes vertical stratification of the lithosphere into strong and weak layers, implying decoupling of the deformation and affecting the strain localization during the convergence [*Royden*, 1996; *Ellis et al.*, 1998; *Shen et al.*, 2001]. In this type of model, deformation is dominated by a rapid ductile flow in the middle and/or lower crust [*Bird*, 1991; *Royden et al.*, 1997; *Klemperer*, 2006]. *Royden et al.* [1997] proposed that, due to lower crustal flow, the crustal thickening on the plateau does not involve much upper crustal deformation but rather differential shortening and thickening of the lower crustal. Therefore, the crustal thickening from below [*Royden et al.*, 1997], associated with the viscous lower crust and confined by surrounding rigid blocks such as Tarim, Qaidam and Sichuan blocks [*Clark et al.*, 2005], would explain the formation of the atypical high-elevated and steep-sided Tibetan plateau [*Kearey et al.*, 2009]. Furthermore, in the Tibetan model, crustal flow has been proposed to escape to the east, moving around the eastern Himalayan syntaxis and the rigid Sichuan basin (Fig. 4.2) [*Royden et al.*, 1997; *Clark and Royden*, 2000]. As it encounters the strong crust and upper mantle of the Sichuan basin, the lateral flow of partially

molten lower crust applies dynamic pressure on the upper crust, which responds by dynamic uplift and strike-slip faulting [*Clark and Royden*, 2000; *Clark et al.*, 2005; *Kearey et al.*, 2009].

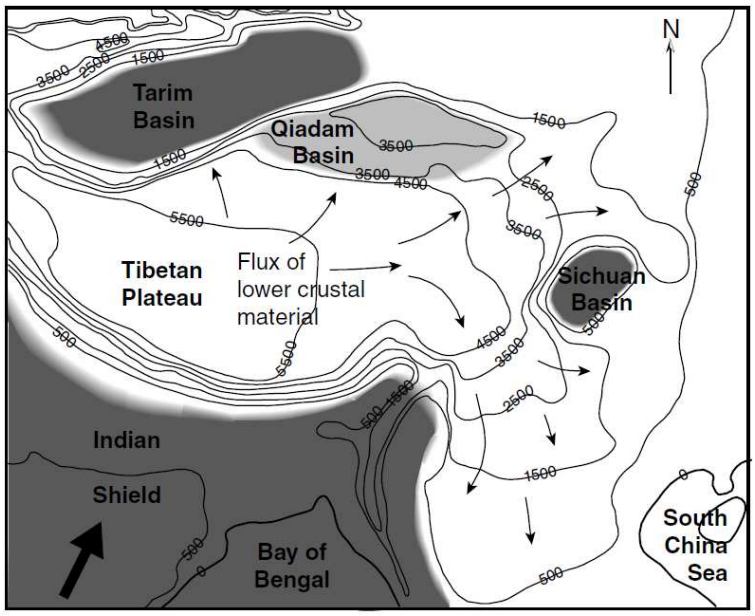

Figure 4.2: Crustal flow in Tibet characterized by the lateral flow of the Tibetan weak lower crust. Areas shaded in dark represent regions of cold, strong, continental material; light grey area represents intermediate strength; white areas represent weak crustal regions. Contour plots represent the smoothed elevations of the Tibetan Plateau and its surrounding regions. *from* [*Clark and Royden*, 2000]

Himalayan channel flow model

The Himalayan channel flow model mainly aims to explain the high-grade metamorphic rocks, leucogranites and migmatite exposed in the Greater Himalayan sequence [*Godin et al.*, 2006]. The channel flow model infers that southern Tibet ductile middle crust was extruded southward in the Greater Himalayas during the Early Miocene [*Searle et al.*, 2011]. This conceptual model was developed as a direct response to the INDEPTH observations [*Nelson et al.*, 1996], particularly the MT results [*Chen et al.*, 1996]. The partially molten crust has been channelled in a narrow zone bounded by low-angle coeval shear zones characterized on the southern flank of the Himalayas by the Main Central Thrust (MCT) at the base of the channel and the South Tibetan Detachment (STD) on top (Fig. 4.3) [*Kearey et al.*, 2009; *Searle et al.*, 2011]. *Beaumont et al.* [2001, 2004] constructed thermo-mechanical models in order to simulate the geological constraints associated with the channel flow and ductile extrusion in the Greater Himalayas. Those models include a seismogenic upper crust, partial melting of the middle crust only and underthrusting of the lower crust by Indian Shield Precambrian granulites [*Searle et al.*, 2011]. *Beaumont et al.* [2001] highlights that the coupling between the low-viscosity crustal channel flow and efficient surface denudation (rapid erosion) not only explains the ductile extrusion observed in the Greater Himalayas but also could predict the formation of the gneiss domes exposed in

the Tethyan Himalayas. Furthermore, this type of channel flow model has also been mentioned to explain the progressive growth of the Tibetan plateau [*Medvedev and Beaumont*, 2006].
In opposition to the Himalayas, there is no direct geological evidence for crustal flow beneath the eastern margin of the Tibetan Plateau, as the Long Men Shan ranges do not show either horizontal extrusion of deep crustal metamorphic rocks or equivalents to the MCT or STD detachments [*Searle et al.*, 2011]. However, *Harris* [2007] mentioned that "channel tunnelling" [*Beaumont et al.*, 2001] could be occurring in eastern Tibet, as the weak crustal layer may not reach the surface.

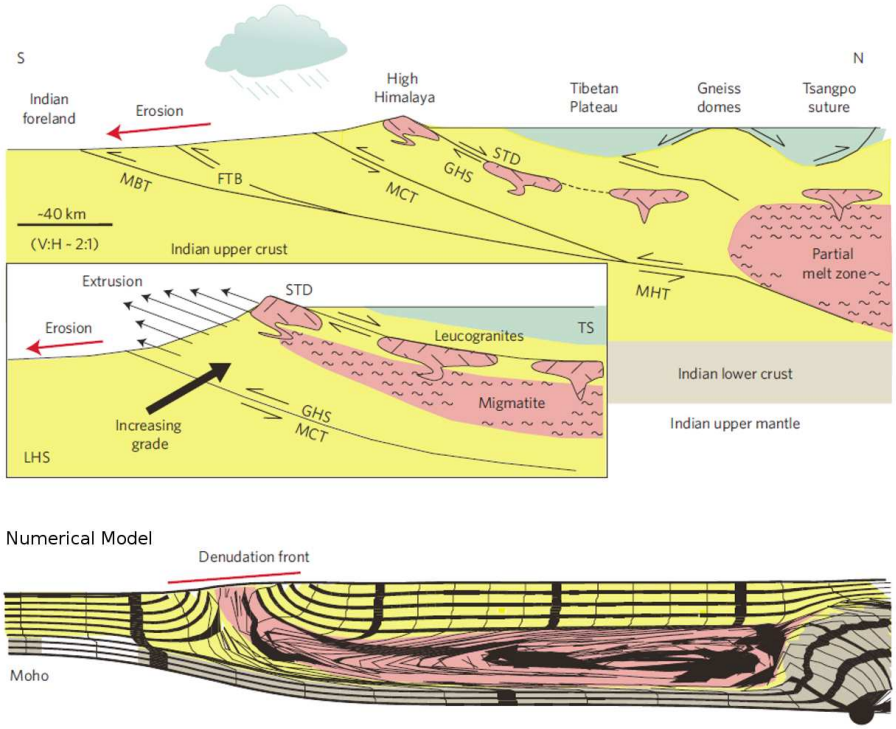

Figure 4.3: Schematic cross-section and numerical model for the Himalayan channel flow; after [*Beaumont et al.*, 2001]. MBT = Main Boundary Thrust; FTB = Fold-Thrust Belt; MCT = Main Central Thrust; STD = South Tibetan Detachment; LHS = Lesser Himalayan Sequence; GHS = Greater Himalayan Sequence. Rapid erosion and removal of material at the southern flank of the Himalayas allow the extrusion of hot, weak ductile rock (pink regions). In the numerical model, the pink zone shows the deformation pattern resulting from channel flow; the black circle shows the position for lithospheric detachement. *modified from* [*Whipple*, 2009]

4.2 POST-COLLISIONAL VOLCANISM AND XENOLITHS

The widespread post-collisional volcanism in Tibet shows systematic variations in space and time (Fig. 4.4 and 4.5) [*Chung et al.*, 2005]. Although it started developing prior to the Indian indentation, the Cretaceous-Eocene Gangdese granitoids and the Paleogene Linzizong volcanic rocks define the voluminous Andean-type magmatic arc signature of southern Tibet (Fig. 4.4). The Gangdese batholith and the Linzizong volcanic rocks high-

light a two-episodes magmatism characterized by a magmatic gap between ~75 and 60 Ma [*Chung et al.*, 2005].

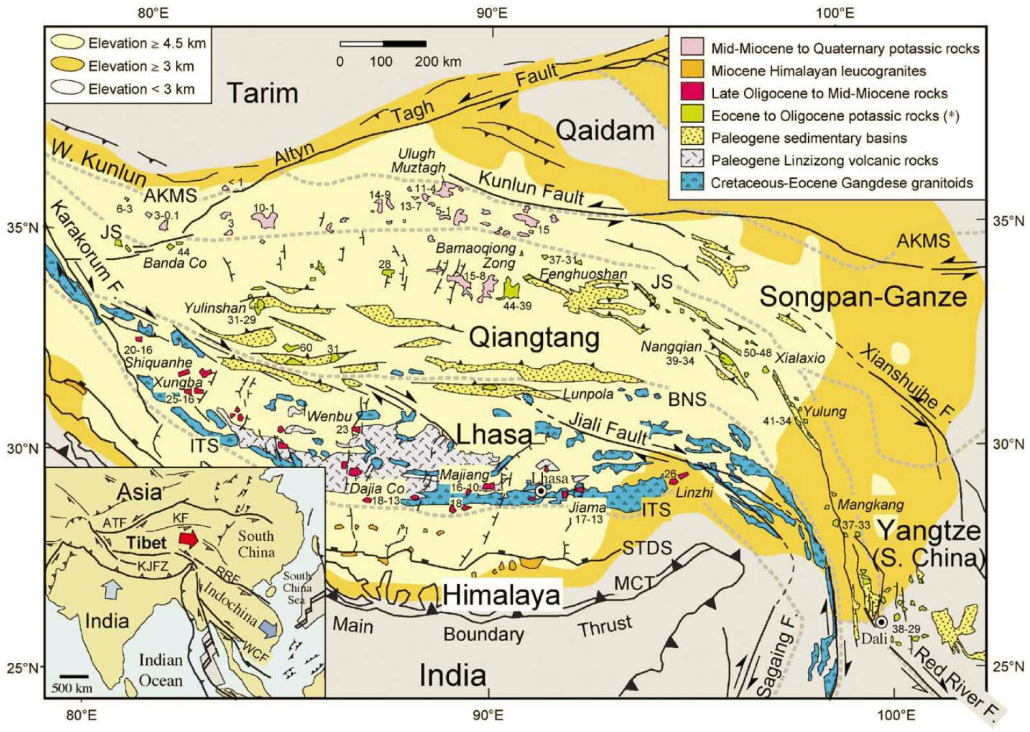

Figure 4.4: Global localization of post-collisional magmatism in Tibet. The asterisk in the legend includes Paleocene (60 Ma) sodium-rich basalts of western Qiangtang. MBT = Main Boundary Thrust; MCT = Main Central Thrust; STDS = South Tibet Detachment System; ITS = Indus-Tsangpo Suture; BNS = Bangong-Nujiang Suture; JS = Jinsha Suture; AKMS = Anyimaqen-Kunlun-Muztagh Suture; ATF = Altyn Tagh Fault; KF = Kunlun Fault; KJFZ = Karakorum-Jiali Fault Zone; RRF = Red River Fault; WCF = Wang Chao Fault. *from* [*Chung et al.*, 2005]

Although those two magmatic phases present mainly a calc-alkaline geochemical signature, the younger magmatic episode shows Sr-Nd isotope ratios suggesting the contribution of a juvenile mantle component [*Wen et al.*, 2003]. This magmatic signature was interpreted as asthenospheric upwelling triggered by the rollback of the subducting Tethyan slab between ~70-60 Ma [*Chung et al.*, 2005]. The Qiangtang terrane presents Eocene to Oligocene (~50-30 Ma) Na-rich calc-alkaline volcanic rocks in the south, whereas the northern part of the terrane highlights coeval potassium-rich shoshonitic lavas [*Chung et al.*, 2005; *Ding et al.*, 2007]. Both suites of lavas were likely derived from a relatively enriched mantle source, and the ultrapotassic signature of the northern Qiangtang lavas may reflect the contamination by partial melts of metasediments in the lower crust [*Ding et al.*, 2007]. In the Lhasa terrane, a new magmatic phase occurred from the late Oligocene to Mid-Miocene (30-10 Ma). This new phase consists in "collision-type" adakites resulting from the melting of thickened garnet-bearing eclogitic lower crust [*Rudnick*, 1995; *Kay and Kay*, 2002; *Searle et al.*, 2011] and ultrapotassic (lamproites) volcanic rocks, requiring a hot enriched lithospheric mantle source, mainly confined to the west of the terrane. Those observations imply significant characteristics for the Lhasa terrane at that time: thick crust, thick enough to develop an eclogitic root, elevated geotherm and hot mantle [*Searle et al.*,

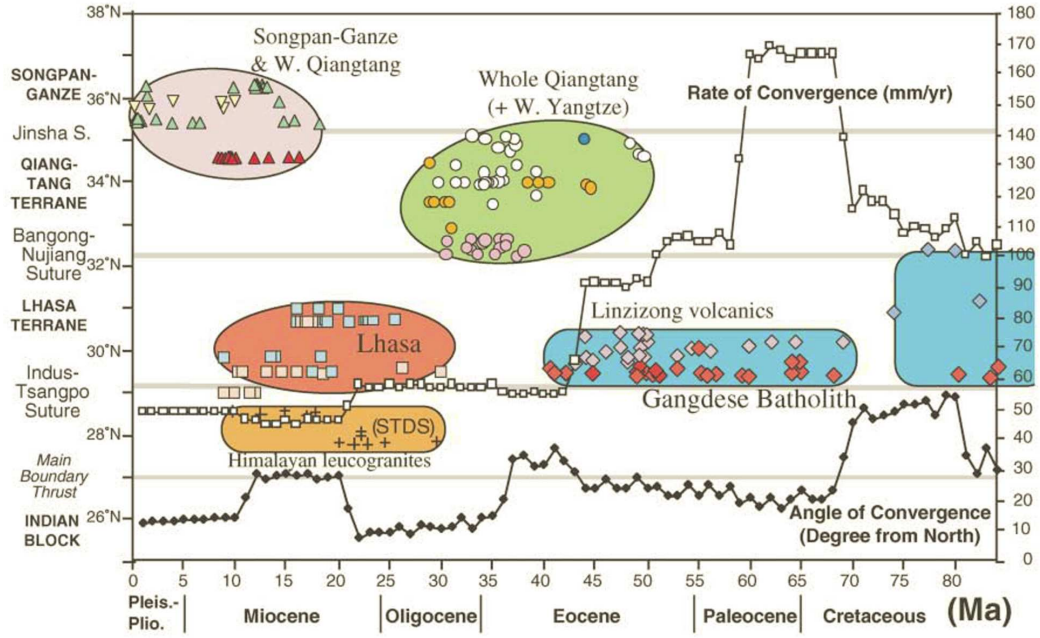

Figure 4.5: Tibetan magmatism spatial and temporal variations associated with estimates for the rate and angle of convergence between India and Asia. For data sources see [*Chung et al.*, 2005]. The data for convergence rates and angles are from [*Lee and Lawver*, 1995]. *from* [*Chung et al.*, 2005; *Searle et al.*, 2011]

2011]. It also suggests that the lower part of the Lhasa lithosphere may have been removed by convective thinning in the late Oligocene, leading to thermal perturbation and therefore the production of both ultrapotassic and adakitic magmas [*Chung et al.*, 2005]. Northern Tibet presents Mid-Miocene to Quaternary widespread potassic magmatism [*Arnaud et al.*, 1992; *Turner et al.*, 1993, 1996], although the younger samples are located only in the western part of northern Tibet. The volcanic rocks are mainly shoshonites [*Chung et al.*, 2005]. They are less K-rich than the Eocene to Oligocene Qiangtang potassic lavas [*Searle et al.*, 2011]. *Turner et al.* [1996] mentioned the shoshonites of northern Tibet likely originate from a lithospheric mantle source, ruling out a subduction origin. Therefore, the temperatures requested to trigger melt within the lithospheric mantle may only be reached with convective thinning [*Turner et al.*, 1993, 1996]. As depleted sub-continental lithospheric mantle would not produce such lavas, *Turner et al.* [1996] proposed that the enriched mantle source for the observed shoshonites involves a multi-stage enrichement of the lithospheric mantle by metasomatism during pre-collisional subduction episodes. Althougth Tibetan potassic lavas have been interpreted to be derived from an ancient, enriched mantle lithospheric source, *Ding et al.* [2007] highlight that potassic lavas could also by produced by melt contaminations from melting of upper crustal rocks that were introduced in the lower crust.

The Ulugh Muztagh (Fig. 4.4) region highlights the presence of leucogranites dated at 11-4 Ma [*Molnar et al.*, 1987; *McKenna and Walker*, 1990], with a geochemical signature that is similar to crustal melts or two-mica (S-type) granites. *Searle et al.* [2011] mentions the possibility that in northern Tibet, the Ulugh Muztagh type of melts are much more abundant at depth and would then characterize the presence of hot and thick crust between the Bangong and Kunlun sutures.

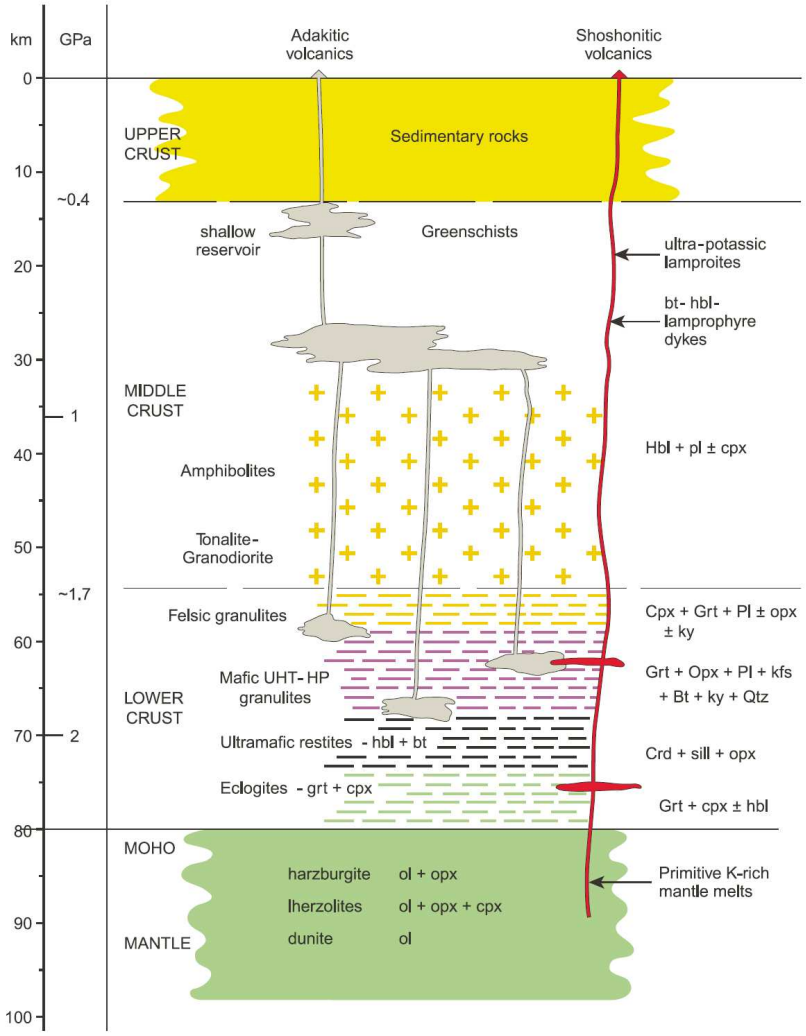

Figure 4.6: Crustal model of southern Tibet including post-collision adakites and shoshonites. Moho depth from [*Owens and Zandt*, 1997; *Schulte-Pelkum et al.*, 2005; *Nábelek et al.*, 2009]; depths of adakite reservoirs and sources from [*Guo et al.*, 2007]; mineral compositions of lower crust granulites and eclogites and ultramafic restites from [*Hacker et al.*, 2000; *Chan et al.*, 2009]. *from* [*Searle et al.*, 2011]

The extracted volcanic rocks entrained xenoliths of granulite, eclogite and ultramafic rocks from the lower crust and upper mantle to the surface, carrying information about Tibet's crustal composition (Fig. 4.6) [*Searle et al.*, 2011]. For instance, granulite xenoliths data from southern Tibet [*Chan et al.*, 2009] suggests the crust was very thick (70-90 km) around 15 Ma ago. Furthermore, *Hacker et al.* [2000] mentioned the absence of hydrous minerals in the lower crust of central Tibet, despite temperatures high enough for dehydration melting of mica. Xenoliths studies across Tibet highlight two different types of structure for the lower crust. The Lhasa terrane and the southern Qiangtang terrane are characterized by crystalline basement possibly extending west into the Pamir, whereas to the north the lower crust is mainly identified as meta-sedimentary rocks [*Hacker et al.*, 2000; *Schwab et al.*, 2004; *Hacker et al.*, 2005; *Chan et al.*, 2009].

4.3 GEOPHYSICAL CONSTRAINTS ON THE DEEP STRUCTURE OF TIBET

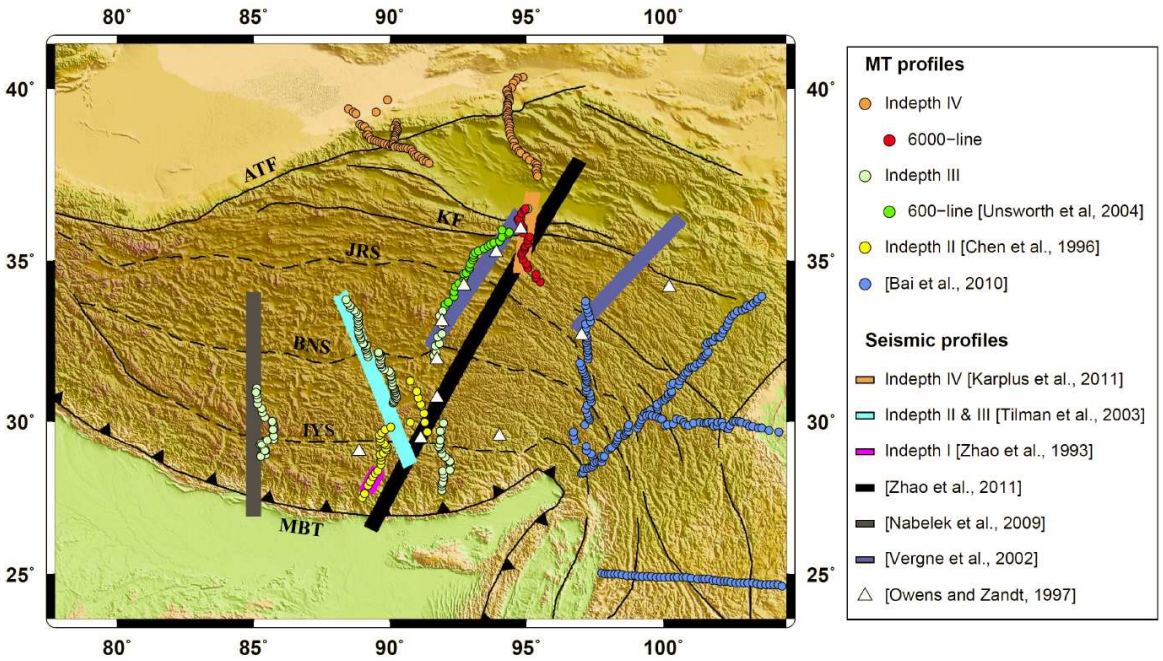

Figure 4.7: Location of the main MT and seismic surveys carried out in Tibet. ATF, Altyn Tagh Fault; KF, Kunlun Fault; JRS, Jinsha River Suture; BNS, Bangong-Nujiang Suture; IYS, Indus Yarlung Sutures; MBT, Main boundary thrust

4.3.1 *Structure and Properties of the Tibetan Crust*

South of the Himalayas, Moho depth is about 40 km [*Mitra et al.*, 2005] and then smoothly increases to about 70-80 km in the Tethyan Himalayas [*Zhao et al.*, 1993; *Nelson et al.*, 1996]. Furthermore, the INDEPTH Phase I seismic reflection investigation (Fig. 4.7) highlighted a strong reflector in the middle crust of the Himalayas interpreted as the active "decollement" beneath India and Asia dipping to the north and characterizing the top of the Indian lower crust [*Zhao et al.*, 1993] (Fig. 4.8). Above the "decollement", a strong seismic anisotropic layer has been identified [*Schulte-Pelkum et al.*, 2005] and may characterize the foliation due to the localized shearing generated by the underthrusting of India. In southern Tibet, the INDEPTH project's seismic reflection surveys revealed the presence of seismic bright spots in the crust at a depth of about 15 km that have been associated with partial melting of the middle and possibly lower crust [*Nelson et al.*, 1996; *Brown et al.*, 1996; *Chen et al.*, 1996]. Partial melting of the middle crust was also proposed following the detection of a mid-crustal low-velocity zone as part of INDEPTH passive-source seismic surveys in southern Tibet [*Kind et al.*, 1996]. However, *Makovsky and Klemperer* [1999] interpreted the seismic bright spots to be associated with the presence of relatively large quantities of free aqueous fluids. INDEPTH magnetotelluric studies in southern Tibet revealed the presence of a strong conductive anomaly in the crust (Fig. 4.8), which confirmed the presence of both melt and aqueous fluids [*Chen et al.*, 1996; *Wei et al.*, 2001; *Li et al.*, 2003; *Unsworth et al.*, 2005; *Spratt et al.*, 2005]. This partially molten layer is likely to extend

along at least 1,000 km of the southern margin of the Tibetan plateau [*Unsworth et al.*, 2005].

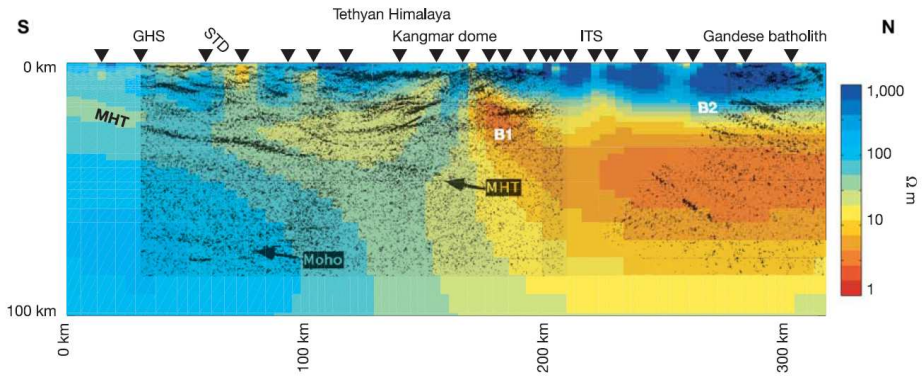

Figure 4.8: Southern Tibet INDEPTH II resistivity model compared with INDEPTH I and II seismic reflection results. B1 and B2 are seismic bright spots (strong reflectors) that indicate zones with high fluid content. MHT = Main Himalayan Thrust ("decollement"); STD = Southern Tibetan detachment. *from* [*Unsworth et al.*, 2005]

Furthermore, *Unsworth et al.* [2005] calculated that the MT data in southern Tibet require a melt fraction of 5-14% in agreement with the presence of a low viscosity layer and therefore crustal flow in southern Tibet. Lateral variations of crustal seismic properties have been investigated through the attenuation of the Lg waves along the INDEPTH profiles [*Xie et al.*, 2004]. The high Lg-wave attenuation observed in southern Tibet has been associated with partially molten middle crust overlain by a layer enriched in aqueous fluids. Such a combination would explain both the MT and seismic data [*Unsworth et al.*, 2005], and can be interpreted by the water-saturated melting of metasediments resulting from dehydration reactions as the Indian lithosphere underthrusts southern Tibet [*Rapine et al.*, 2003; *Xie et al.*, 2004]. Beneath the Lhasa terrane, *Owens and Zandt* [1997] defined high P-wave velocities at the base of the lower crust which were interpreted as the Indian lower crust, underthrusting Tibetan crust. Those high-velocities can be associated with the seismic receiver functions' "Moho doublet" observed beneath the Lhasa terrane and probably characterizing the presence of eclogitized Indian lower crust at the base of the crust of southern Tibet [*Hetényi et al.*, 2007; *Nábelek et al.*, 2009] (Fig. 4.11). In central and northern Tibet, the Lg-wave attenuation and surface wave dispersion analysis infer partial melting of the crust associated with the presence of higher temperatures and probably relatively dry conditions [*Fan and Lay*, 2003; *Rapine et al.*, 2003; *Xie et al.*, 2004]. Low S-wave velocities and a high Poisson's ratio have been observed in the crust of the Songpan-Ganzi and northern Qiangtang terranes, and have been related to partial melting of the crust [*Owens and Zandt*, 1997]. Those observations would be in agreement with the presence of a warmer mantle in northern Tibet, although *McKenzie and Priestley* [2008] suggested that the low-velocity zone in northern Tibet may be associated with radioactive heating of the thickened crust. Another explanation for the presence of crustal melt in northern Tibet involves the Mesozoic and Cenozoic underthrusting of the Songpan-Ganzi flysch complexes, mostly easily deformable pelites, which could have lead to dehydration reactions and produced large quantities of free water in the crust causing extensive partial melting [*Yin and Harrison*, 2000]. Although, the Bangong-Nujiang Suture does not show a significant geo-

physical signature [*Haines et al.*, 2003], unusually high temperatures have been estimated in the crust north of the suture from seismic velocities of the INDEPTH Phase III transect [*Mechie et al.*, 2004]. Furthermore, large conductive anomalies have also been highlighted in the middle-to-lower crust of central and northern Tibet following INDEPTH III surveys [*Solon et al.*, 2005; *Unsworth et al.*, 2004]. As concluded by *Wei et al.* [2007] and *Fan and Lay* [2003], partial melting is likely to be widespread in the Tibetan crust.

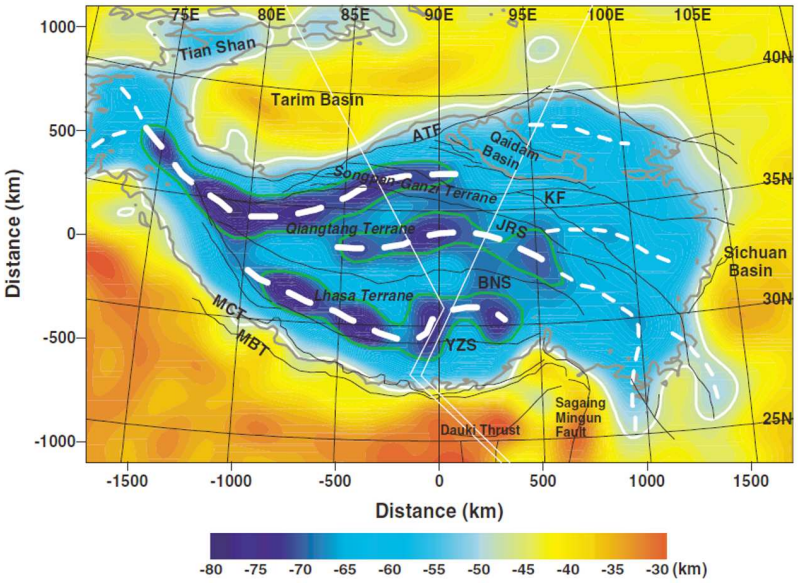

Figure 4.9: Moho depth across the whole Tibetan Plateau inferred from gravity data. The map highlights significant "Moho belts" that show clear E-W trends matching with the border and tectonic sutures of the plateau. *from* [*Shin et al.*, 2007]

As a general trend, *Owens and Zandt* [1997] modelled the crust under northern Tibet to be 10-20 km thinner than in the south. The crust in the south of the Lhasa terrane appears to be the thickest, with an average thickness of 80 km [*Mitra et al.*, 2005; *Zhao et al.*, 2001], and then the crustal thickness reduces in the north of the terrane to about 75 km [*Owens and Zandt*, 1997] or even 65 km [*Zhao et al.*, 2001; *Haines et al.*, 2003]. The crust keeps thinning northward to 60-65 km [*Owens and Zandt*, 1997; *Zhao et al.*, 2001; *Haines et al.*, 2003] up to the middle of the Qiangtang terrane, but the crust thickens again south of the Jinsha suture up to ~80 km [*Vergne et al.*, 2002]. The Jinsha suture highlights a sharp step of a few kilometres in Moho geometry [*Kind et al.*, 2002; *Vergne et al.*, 2002], as the crust thins again further north to about 60-65 km beneath the Songpan-Ganzi terrane [*Owens and Zandt*, 1997; *Zhao et al.*, 2001; *Vergne et al.*, 2002]. Near the northern edge of the plateau, another sharp offset reduces Moho depth up to 50 km [*Vergne et al.*, 2002; *Karplus et al.*, 2011]. The INDEPTH IV seismic surveys confirmed that this Moho offset also characterizes an overlap between the shallower Qaidam Moho and the deeper Tibetan Moho [*Vergne et al.*, 2002; *Shi et al.*, 2009; *Karplus et al.*, 2011]. This particular feature was interpreted as a signature for possible flow of Tibetan crust up to the southern edge of the Qaidam basin [*Karplus et al.*, 2011]. Further north, the crust thickens again to about ~75 km beneath the Qilian Shan but thins down to 50 km beneath the Beishan Basin, north of the Qilian ranges [*Rui et al.*, 1999]. Across the northwestern margins of Tibet, Moho depth shallows to about 50-60 km beneath the Altyn Tagh Fault, and 50 km beneath the Tarim basin [*Wittlinger et al.*,

2004]. The different Moho depths presented here across the Tibetan Plateau represent only an estimation of the north-south trend of the Moho, as the crust thickness will also vary from east to west. Indeed in western Tibet, seismic receiver functions imaged Moho depth at about 75 km beneath the Karakorum fault, but showed a record depth of 90 km beneath the western part of Qiangtang terrane [*Wittlinger et al.*, 2004]. Undulations of the Moho across the whole plateau (Fig. 4.9) have also been highlighted by the gravity models obtained from GRACE-integrated gravity data [*Shin et al.*, 2007].

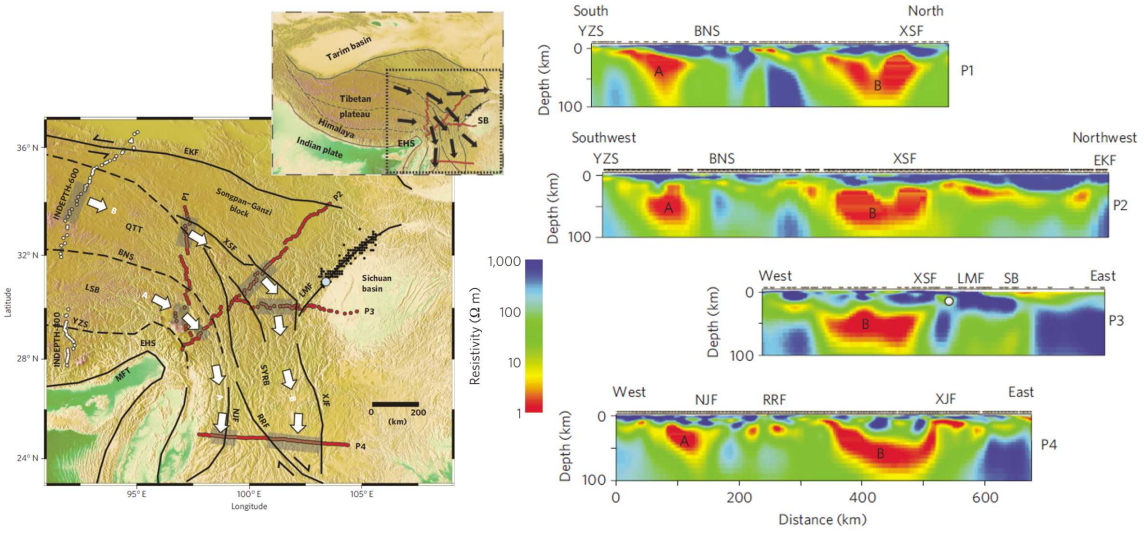

Figure 4.10: High conductivity channels imaged in Eastern Tibet. *modified from* [*Bai et al.*, 2010]

Finally, several geophysical studies agree with the Tibetan crustal flow model. INDEPTH experiments in southern Tibet revealed the presence of a partially molten middle crust [*Nelson et al.*, 1996] which lead to the Himalayan channel flow model [*Beaumont et al.*, 2001]. INDEPTH seismic bright spots and high conductivities of southern Tibet were also interpreted as possible pockets of leucogranite magmas growing today at similar P-T conditions than the Early Miocene leucogranites exposed along the Himalaya [*Gaillard et al.*, 2004]. In central Tibet, *Haines et al.* [2003] mentioned that the loss of lower crust, and therefore the absence of seismic evidence for earlier accretion in the deep crust, is probably due to lateral escape by ductile flow. Furthermore, seismic radial anisotropy observed in the middle-lower crust across Tibet highlights thinning of the crust in a channel manner, consistent with the Tibetan crustal flow model [*Shapiro et al.*, 2004]. Magnetotelluric studies have significantly contributed to the characterization of the Tibetan crustal flow [*Rippe and Unsworth*, 2010; *Bai et al.*, 2010]. For instance, MT studies have highlighted the presence of two mid-crustal channels extending from the Tibetan plateau into southwest China and covering more than 800 km [*Bai et al.*, 2010] (Fig. 4.10). Low shear-wave velocities imaged from surface-wave tomography in southeastern Tibet [*Yao et al.*, 2008] show spatial variations in the strength of the middle and lower crust. *Bai et al.* [2010] and *Yao et al.* [2008] agree that the crustal flow in Tibet may characterize a pattern of deformation more complex than the previously established models *Clark and Royden* [2000].

Several studies suggest the presence of cold, strong mantle beneath southern Tibet and an anomalously warm, weak mantle beneath central and the northern Tibet [*Molnar and*

Chen, 1984; *Lyon-Caen*, 1986; *Molnar*, 1990; *McNamara et al.*, 1997; *Owens and Zandt*, 1997; *Zhao et al.*, 2001; *Tilmann et al.*, 2003]. However, uncertainties remain on the extension and geometry of the underthrusting of the Indian plate but also on the lithospheric structure of northern Tibet, involving either underthrusting of Asia or delamination/convective thinning.

4.3.2 *Underthrusting of India*

Owens and Zandt [1997] interpreted the Indian continental crust and mantle lithosphere to be underthrusting Tibet as far as the Bangong-Nujiang Suture (BNS) (~32°N), where the Indian plate is then likley detached forming a steeply northward-dipping subduction zone. As part of the Hi-CLIMB project, *Nábelek et al.* [2009] presented seismic receiver function observations that defined a 15-km-thick layer ("Moho doublet") above the Moho of the southern Lhasa terrane, interpreted as eclogitized Indian lower crust extending up to 31°N, south of the BNS (Fig. 4.11). Moreover, Pn travel time tomography shows high upper mantle velocities in southern Tibet that have been presented as an evidence for underthrusting of the Indian plate as far as ~32°N [*McNamara et al.*, 1997].

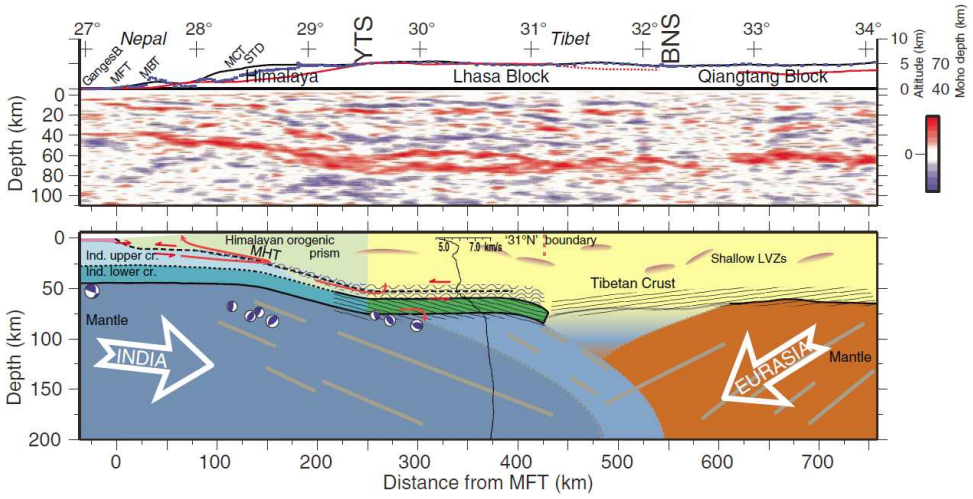

Figure 4.11: Seismic receiver profile and [*Nábelek et al.*, 2009]'s associated interpretation for southern Tibet. YTS = Yarlung Tsangpo Suture, BNS = Bangong-Nujiang Suture. Profile location on (Fig. 4.7). *modified from* [*Nábelek et al.*, 2009]

Following INDEPTH Phase III, the seismic tomography model of *Tilmann et al.* [2003] imaged a subvertical high-velocity zone from 100 to 400 km south of the BNS, interpreted as the downwelling Indian plate (Fig. 4.12). The steep downwelling of the Indian plate at the southern edge of the BNS proposed by *Tilmann et al.* [2003] is in agreement with the subhorizontal underthrusting of India up to the BNS [*Nelson et al.*, 1996; *McNamara et al.*, 1997; *Owens and Zandt*, 1997]. As an alternative to the low angle underthrusting of India proposed by *Owens and Zandt* [1997], seismic receiver function imaged a detached Indian lithospheric mantle dipping northward beneath Tibet up to (33°N), north of the BNS [*Kosarev et al.*, 1999]. Although, the receiver function sections of *Kind et al.* [2002] do not see obvious evidence for a north-dipping interface beneath southern Tibet, *Zhao et al.* [2011] imaged a north-dipping detachement of the Indian lithosphere, but showed

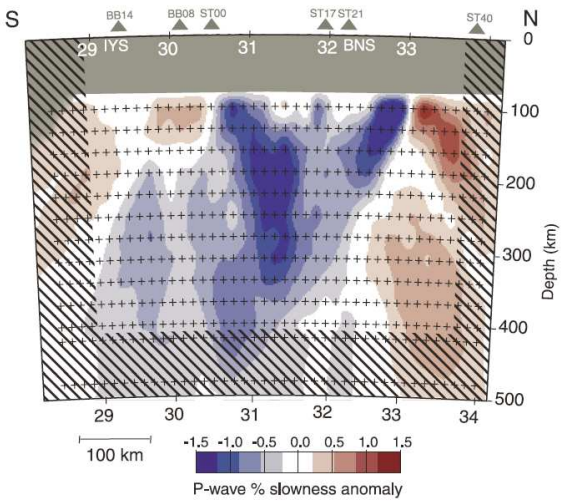

Figure 4.12: P-wave tomography across central Tibet showing a subvertical high-velocity zone interpreted as downwelling Indian lithosphere at the southern edge of the Bangong-Nujiang Suture (BNS). Profile location on (Fig. 4.7). *from* [*Tilmann et al.*, 2003]

the Indian plate does not extent further north than the southern portion of the Lhasa terrane (~30°N) (Fig. 4.13). Furthermore, *Zhao et al.* [2011] interpreted the Indian lower crust - characterized by a Moho doublet [*Kind et al.*, 2002; *Nábelek et al.*, 2009] - is not involved with the dipping Indian mantle lithosphere, but instead extends to the north as a subhozizontal deep crustal layer. The interpretation that the underthrusting of Indian lithosphere only extends to central Tibet, does not agree with post-collisional convergence and shortening estimates [*Johnson*, 2002]. However, the proposed downwelling of the Indian mantle [*Owens and Zandt*, 1997; *Tilmann et al.*, 2003] would help to make up for the global amount of shortening accommodated [*Kearey et al.*, 2009].

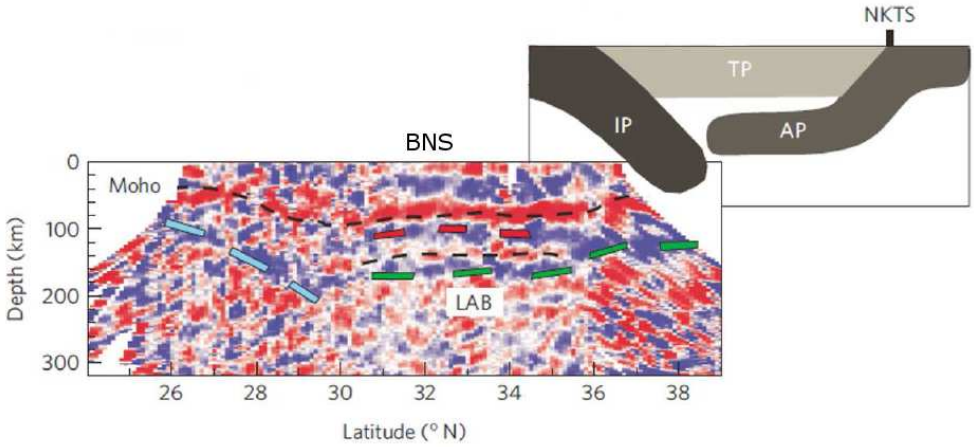

Figure 4.13: S receiver functions profile across Tibet and associated interpretation from *Zhao et al.* [2011]. Moho = black dashed line; lower black dash line = weak indication of Moho of Asian lithosphere. Blue, red and green dashed lines = LAB (Lithosphere Asthenosphere Boundary) of Indian, Tibetan and Asian plates, respectively. IP = Indian, TP = Tibetan, AP = Asian plates, BNS = Bangong-Nujiang Suture, NKTS = North Kunlun Thrust System. Profile location on (Fig. 4.7). *modified from* [*Zhao et al.*, 2011]

Moreover, the downwelling of the Indian lithosphere would be associated with an upward mantle flow beneath Tibet, north of the BNS [*Tilmann et al.*, 2003], in agreement with the low-velocity body imaged by *Wittlinger et al.* [1996] and the presence of a warmer and weaker mantle in northern Tibet [*McNamara et al.*, 1997; *Owens and Zandt*, 1997].
In opposition to a model where the underthrusting of the Indian plate does not extend further north than the BNS, the global seismic tomography model of *Zhou and Murphy* [2005] shows that India is underthrusting nearly the entire Tibetan plateau up to ~36°N . *Zhou and Murphy* [2005] proposed a model where the underthrusting of the Indian plate is characterized by a subhorizontal subduction separated from the Tibetan lithosphere by a thin channel of asthenosphere.

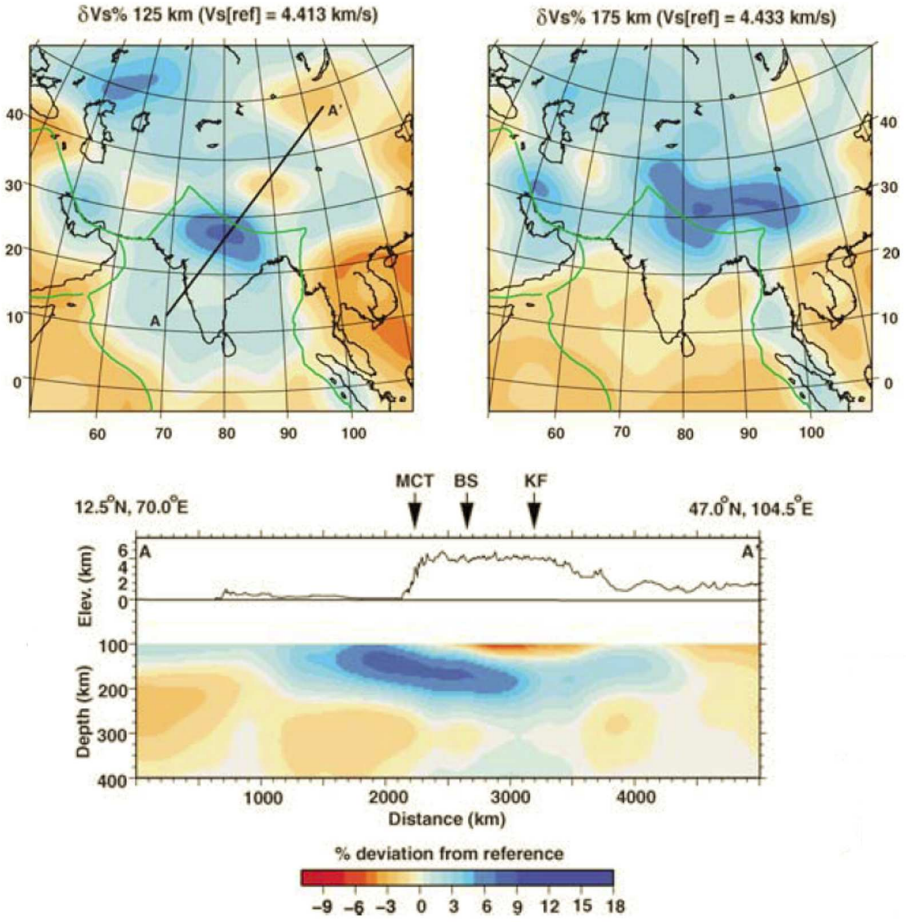

Figure 4.14: High-velocity Tibetan mantle imaged from surface wave tomography. MCT = Main Central Thrust, BS = Bangong Suture, KF = Kunlun Fault. *modified from* [*Priestley et al.*, 2008]

Zhou and Murphy [2005] highlighted a difference between central, western and eastern Tibet, concluding in central Tibet the subduction of India is likely to occur at a steeper angle. Furthermore, the Indian plate, imaged from different receiver functions profiles across the plateau, shows that the underthrusting Indian lithosphere extends progressively further north, from the eastern to western Tibet, as the subducting plate gets less and less steep [*Zhao et al.*, 2010]. Similarly, deep earthquake records suggest that India underlies most of the southeastern and nearly all of northwestern Tibet [*Priestley et al.*, 2008].

Finally, recent surface-wave tomography studies infer that most of, and possibly all, Tibet is underlain by a thick high-velocity lithospheric mantle extending up to 225-250 km at depth (Fig. 4.14) [*Priestley et al.*, 2006, 2008]. Those results suggest that the Indian lithosphere did not sink beneath the plateau [*Priestley et al.*, 2006], and highlights either the near-horizontal underthrusting of Indian lithosphere beneath most of Tibet [*Ni and Barazangi*, 1983; *Zhou and Murphy*, 2005] or the underthrusting of India lithosphere to the south associated, to a lesser extent, with the underthrusting of the high-velocity Asian lithosphere from the north [*Bourjot and Romanowicz*, 1992; *Tapponnier et al.*, 2001].

4.3.3 *Lithospheric Structure of Northern Tibet*

Shear-Wave anisotropy

Several studies have investigated seismic shear-wave anisotropy in order to understand the tectonic behaviour of the Tibetan mantle [*McNamara et al.*, 1994; *Herquell et al.*, 1995; *Hirn et al.*, 1995; *Lavé et al.*, 1996; *Sandvol et al.*, 1997; *Huang et al.*, 2000; *Sol et al.*, 2007; *León Soto et al.*, 2012]. Between the Lhasa terrane and the Kunlun fault, the direction of the fast polarization is mainly E-W to ENE-WSW, and follows the orientation of the major tectonic features [*Yin and Harrison*, 2000; *León Soto et al.*, 2012]. Compared to central and northern Tibet, the Himalayas and the south of the plateau seem to show negligible polarization anisotropy [*Huang et al.*, 2000]. Two processes have been proposed to explain the shear-wave anisotropy observed in central and northern Tibet [*León Soto et al.*, 2012]. On one hand, anisotropy is induced by shearing within the passive asthenosphere as the Tibetan lithosphere moves to the east [*Lavé et al.*, 1996]. On the other hand, anisotropy is a response to N-S shortening, as the asthenosphere is squeezed between the underthrusting Indian lithosphere and the rigid Tarim and Qaidam lithospheric blocks [*Owens and Zandt*, 1997; *Huang et al.*, 2000]. This model would then characterize the presence of an eastward asthenospheric flow and would be in agreement with hot and weak mantle beneath northern Tibet [*Huang et al.*, 2000] (Fig. 4.16).

Underthrusting of Asia vs Convective removal of the lithopshere

Whereas it is quite clear that southern Tibet is underthrusted by India to some extent to the north, the lithospheric structure of northern Tibet remains debated. On one hand, the Asian lithosphere may be underthrusting Tibet from the north [*Bourjot and Romanowicz*, 1992; *Meyer et al.*, 1998; *Tapponnier et al.*, 2001]. Using seismic receiver function techniques, *Kind et al.* [2002] imaged a steep south-dipping interface in northern Tibet, traceable from the Kunlun ranges (at ~100 km depth) down to central Qiangtang (at ~250 km depth), and interpreted as underthrusting Asian lithospheric mantle. Still with seismic receiver functions, *Zhao et al.* [2011] imaged a nearly horizontal Asian lithosphere underthrusting a thin Tibetan lithosphere from the north and extending further south than the BNS (Fig. 4.13). However, compared to the Himalayas, *Kirby et al.* [2002] highlights that eastern Tibet or the Kunlun ranges do not present as much of significant Neogene upper crustal shortening, which opens the debate on the amount of Asian lithosphere underthrusting.

On the other hand, it has been proposed that the lithospheric mantle of northern Tibet is characterized by the removal of gravitationally unstable thickened lithosphere [*England and Houseman*, 1989; *Molnar et al.*, 1993; *Platt and England*, 1994; *Jimenez-Munt et al.*, 2008] by either convective thinning or delamination of the mantle lithosphere [*Burg*, 2011]. Such processes are associated with rapid uplift of the upper part of the lithosphere [*England and Houseman*, 1989; *Molnar et al.*, 1993; *Morency and Doin*, 2004] and could then explain the northward extension of the atypical topography of Tibet [*Jimenez-Munt et al.*, 2008]. In opposition to convective thinning, the delamination mechanism characterizes the removal of the whole mantle lithosphere from the crust as it peels away along the Moho and propagates through a localized shear zone (Fig. 4.15) [*Bird*, 1979; *Bird and Baumgardner*, 1981; *Morency and Doin*, 2004]. In Tibet, convective thinning, with removal of the lower part of thickened lithosphere, appears to be the preferred mechanism [*England and Houseman*, 1989; *Platt and England*, 1994]. As mentioned by *Platt and England* [1994], delamination would lead to direct contact of the astenosphere with the base of the crust and produce volumes and compositions of melts that do not match with the observed volcanism data.

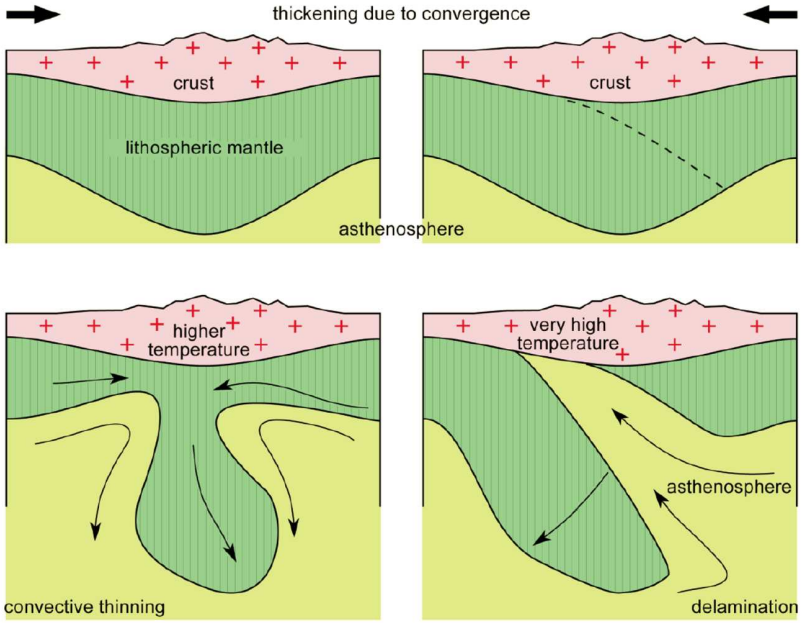

Figure 4.15: Removal of thickened litosphere: Convective thinning vs Delamination. *from* [*Burg*, 2011]

The convective removal of thickened lithosphere inferred for northern Tibet would be in agreement with the observed low seismic velocities. Indeed, Pn and Sn wave observations across the northern Tibetan Plateau exhibit slow mantle velocities [*Ni and Barazangi*, 1983; *McNamara et al.*, 1997] (Fig. 4.16) suggesting the presence of anomalously warm, weak mantle. Furthermore, *Zhao et al.* [2001] inferred that the reduction of crustal thickness in northern Tibet implies a less dense mantle, therefore supporting the presence of hotter mantle. Mantle velocities [*McNamara et al.*, 1997] and geochemical data [*Turner et al.*, 1996] support the presence of lithospheric material (although probably a thin layer) in opposition to material with an asthenospheric origin. Geophysical and geochemical data from northern Tibet would then preclude delamination models, but do not exclude convective thinning or asthenospheric upwelling leading to the presence of a non-eroded thin litho-

spheric mantle lid [*Wittlinger et al.*, 1996; *Turner et al.*, 1996; *McNamara et al.*, 1997; *Tilmann et al.*, 2003]. The convective thinning of the lower part of thickened lithosphere in northern Tibet and the resulting rapid uplift of the lithosphere, may have occurred at ~13 Ma [*Turner et al.*, 1993, 1996]. Because of smoothing issues, *Priestley et al.* [2006, 2008] did not exclude a narrow asthenospheric upwelling beneath northern Tibet [*Tilmann et al.*, 2003] but ruled out a large scale convective thinning due to the presence of a thick high-velocity lithospheric mantle lid beneath Tibet (Fig. 4.14). The latter observation is more in favour of a model in which Asian lithosphere is underthrusting Tibet from the north [*Priestley et al.*, 2006]. As an alternative, complex receiver function conversions observed in northern Tibet [*Kosarev et al.*, 1999] suggest an even more complicated situation than the two models presented previously. Indeed, *Kosarev et al.* [1999] suggested the presence of an ongoing process of destruction and subduction of Asian lithospheric mantle happening in northern Tibet. Furthermore, due the presence of the Tibetan crustal conductor, MT data do not impose much constraint on the upper mantle structures in Tibet. However, north of the Kunlun Fault the Asian upper mantle appears to be relatively resistive and probably characterizes colder conditions compared to the upper mantle of the north Qiangtang and Songpan-Ganzi terranes [*Unsworth et al.*, 2004].

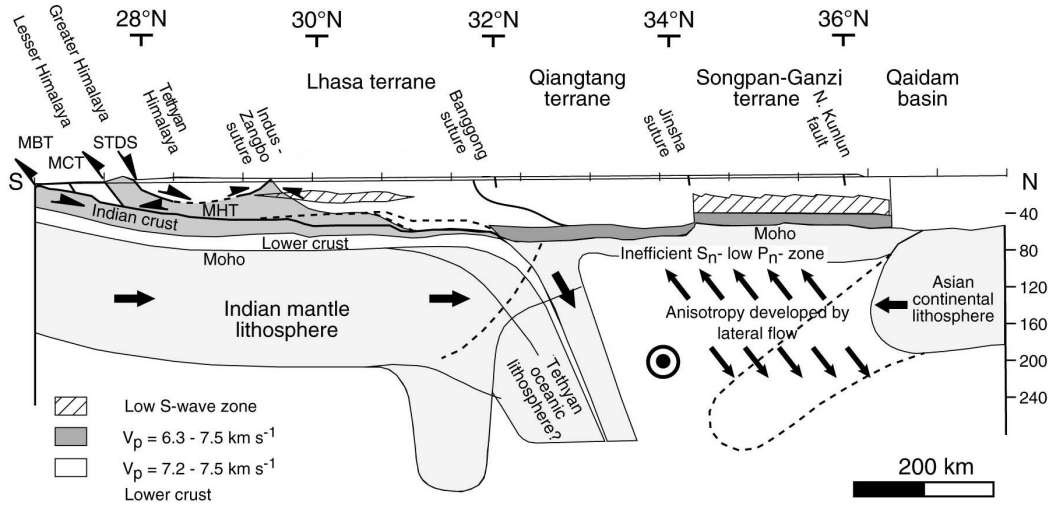

Figure 4.16: Representative N-S cross-section of the Himalayan-Tibetan orogen summarizing some of the major geodynamic processes proposed for the orogen. *modified from* [*Kearey et al.*, 2009]

To conclude, in agreement with the different observations, it appear more than likely that the underthrusting of Asia and convective removal of the thickened lithosphere are both happening in northern Tibet [*Arnaud et al.*, 1992; *Ding et al.*, 2003]. For instance, *Zhao et al.* [2011] imaged the presence of a thin Tibetan lithosphere in central and northern Tibet underlain by the subducting Asian lithosphere (Fig. 4.16). However, the expansion and evolution of those two mechanisms is likely to vary from east to west across northern Tibet [*Zhao et al.*, 2011].

Part II

MAGNETOTELLURICS THEORY

5 ELECTRICAL PROPERTIES OF THE EARTH

5.1 CONDUCTIVITY AND DIELECTRIC PERMITTIVITY

Rock electric properties are defined by their conductivity σ (S/m) (or resistivity $\rho = 1/\sigma$ (Ω.m)) and dielectric permittivity ϵ (F/m). The relative dielectric permittivity ϵ_r or dielectric constant K of a material can be expressed as:

$$K = \epsilon_r = \epsilon/\epsilon_o, \tag{5.1}$$

where $\epsilon_o = 8.854 \times 10^{-12}$ F/m is the free space dielectric permittivity. The interaction of an electric field with a rock will lead to the production of conduction and displacement currents. Both currents are out of phase with each other. Conductivity and dielectric permittivity are complex, frequency dependent ($\omega = 2\pi f$) [*Fuller and Ward*, 1970] and are respectively associated with the conduction density current $\vec{J}$ and the electric displacement $\vec{D}$. In the Fourier domain, electric and displacement currents are expressed as:

$$\vec{J} = [\sigma'(\omega) + i\sigma''(\omega)]\vec{E} = \sigma\vec{E} \tag{5.2}$$

$$\vec{D} = [\epsilon'(\omega) - i\epsilon''(\omega)]\vec{E} = \epsilon\vec{E} \tag{5.3}$$

Whereas conduction currents are due to the motion of charged carriers such as ions and electrons, displacement currents are related to the polarization of the electrical charges under the influence of the electric field.

From Maxwell's equation 7.12, a total density current $\vec{J}_T$ can be defined as:

$$\vec{J_T} = \vec{J} + i\omega\vec{D} = (\sigma + i\omega\epsilon)\vec{E} = \sigma^*\vec{E} \tag{5.4}$$

The complex conductivity σ^* can be associated to the total density current $\vec{J}_T$.

$$\sigma^* = \sigma + i\omega\epsilon, \tag{5.5}$$

$$\sigma^*(\omega) = (\sigma'(\omega) + \omega\epsilon''(\omega)) + i(\omega\epsilon'(\omega) + \sigma''(\omega)) \tag{5.6}$$

The relative amount of conduction current versus displacement current can be expressed as the loss tangent:

$$\tan(\delta) = \frac{\sigma'(\omega) + \omega\epsilon''(\omega)}{\omega\epsilon'(\omega) + \sigma''(\omega)} = \frac{\text{conduction current density}}{\text{displacement current density}} \tag{5.7}$$

In laboratory and field experiments, only *effective* conductivities and permittivities, as highlighted on the equations (5.5) and (5.6), are measured [*Fuller and Ward*, 1970]. Whereas the effective conductivity σ_{eff} is related to the part of the total current density in-phase

with the electric field (Eq. 5.6), the effective dielectric permittivity ϵ_{eff} characterizes the part of the total current density out-of-phase with the electric field (Eq. 5.6).

$$\sigma_{eff}(\omega) = \sigma'(\omega) + \omega\epsilon''(\omega) \tag{5.8}$$

$$\epsilon_{eff}(\omega) = \epsilon'(\omega) + \frac{\sigma''(\omega)}{\omega} \tag{5.9}$$

Those values highlights that the effective parameters are not the conductivity or permittivity but are combinations of them. Furthermore, the effective dielectric constant is defined as:

$$K_{eff}(\omega) = K'(\omega) + \frac{\sigma''(\omega)}{\omega\epsilon_o} \tag{5.10}$$

The effective conductivity gives the real part of the conductivity for low frequencies measurements whereas at high frequencies the effective permittivity becomes the real part of the permittivity. At low frequencies, apart from the dominant conduction currents, a significant dielectric permittivity could also be related to the interfacial polarisation associated with the electrochemical double layer (5.3.1). [*Olhoeft*, 1980; *Keller*, 1989].

5.2 LABORATORY MEASUREMENTS

Laboratory experiments has been reviewed by *Nover* [2005] and *Yoshino* [2010]. In the lab, the physical properties of rocks and minerals can be measured under Earth's surface to mantle and even core pressure and temperature (P,T) conditions. Those measurements are made using laboratory high-pressure high-temperature (HPHT) devices. The HPHT devices can vary depending on special requirements associated with different measurements such as electrical, hydraulic properties or acoustic velocities. Experimental times strongly depend on the cooling systems used with the different devices. Whereas measurements at temperatures >1400°C can last for weeks using the HPHT piston-cylinder, those are limited to a few hours reaction time for temperature around 1900°C using multi-anvil devices. During HPHT measurements, different kinds of electrode arrangements, mainly four or two electrode systems (Fig. 5.1), are used to measure the samples impedances, depending on the temperature and pressure conditions. Various types of electrode materials, such as graphite, platinum, gold, silver and copper, can be used. Under moderate pressure and temperature conditions, non-polarisable electrodes, such as Ag-AgCl or Hg-HgCl can be used on fluid saturated sedimentary rocks. To avoid disturbance in the impedance response due to electrode polarisations, four electrodes measurement systems are employed. In such systems, the current electrodes are located on the sample extremities and the impedance recorded with two ring electrodes applied on the cylindrical sample.

During laboratory studies, an AC electrical current is applied to rock samples to measure the complex response of the electrical charge transport in the material. Rock samples are characterized by an impedance (Eq. 5.11), which is measured at different frequencies,

$$Z(\omega) = Z'(\omega) + iZ''(\omega) \tag{5.11}$$

The impedance frequency dependence of natural materials can be modelled using simple parallel or series combination of RC(resistor/capacitor)-elements (Fig. 5.2) defining a relaxation model [*Debye*, 1927; *Cole and Cole*, 1941; *Huebner and Dillenburg*, 1995]. Whereas the resistors characterize the resistivity or conductivity of the minerals or phases in the

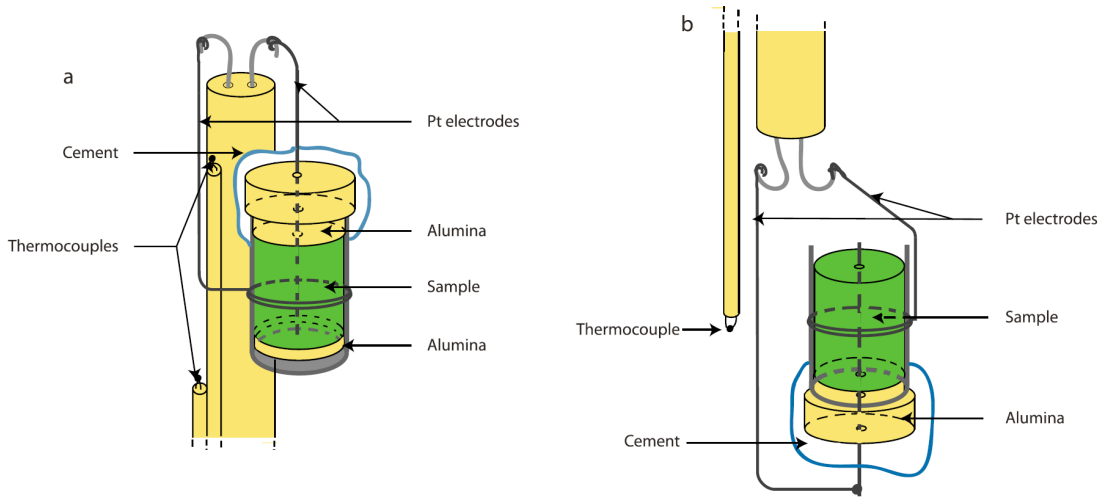

Figure 5.1: Example of laboratory devices used to measure conductivity - *(a)* high pressure experiments (< 0.5 GPa) using a closed cell - *(b)* 1 bar experiments using an open cell. Thermocouples, adjacent to the sample, monitor the temperature. The electrical impedance is measured radially, using an inner platinium (P_t) electrode (1 mm wire) and a Pt tube surrounding the sample as an external electrode. A low thermal expansion inorganic cement fixes the alumina plug onto the Pt external electrode. *from* [*Pommier et al.*, 2008]

rock, the capacitors define the dielectric response of the sample. The measured impedance is usually represented in the complex impedance plane [*Huebner and Dillenburg*, 1995; *Yoshino*, 2010]. The resistance of the rock sample for the RC parallel model can be read as the impedance real part when the impedance phase is 0° (Fig. 5.2).

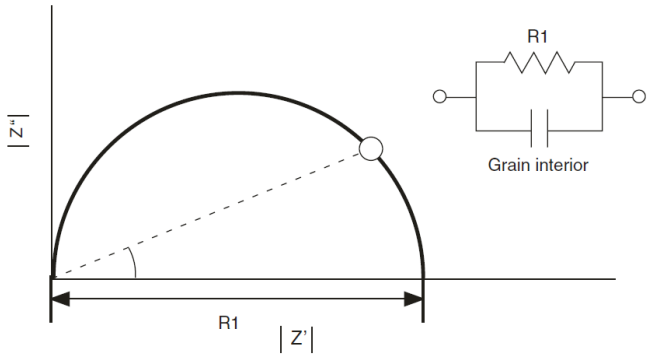

Figure 5.2: Simple impedance spectra where the rock grain interior is the dominant RC system. The semi-circle characterizes the complex impedance at different frequencies. The impedance frequency dependence can also be highlighted by the impedance phase angle. *after* [*Yoshino*, 2010]

However, most of the rocks present more complicated responses. As observed by *Roberts and Tyburczy* [1991] for polycrystalline olivine, three impedance semi-circles infer three different mechanisms affecting the impedance response for various frequencies (Fig. 5.3). Responses characterizing electrodes reaction with the sample appear at the lower frequency side of the impedance plane [*Yoshino*, 2010].

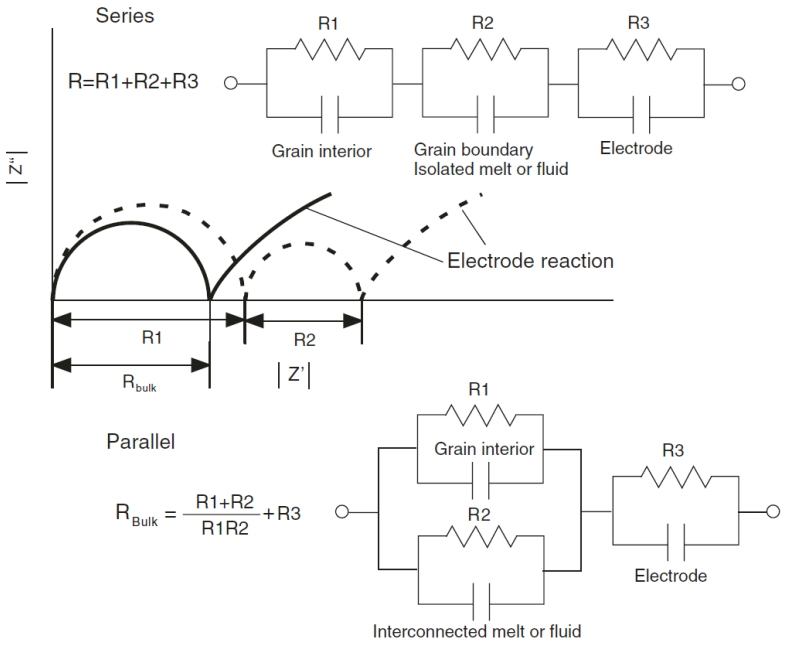

Figure 5.3: Impedance spectra and the associated RC models showing the combination of three dominant mechanisms from high to low frequency (10^4 - 10^{-4} Hz): grain interior, grain boundary or melt/fluid phase and electrode reactions. *Dashed line* - series conduction dominant; *Solid line* - parallel conduction dominant [*Roberts and Tyburczy*, 1999]. *after* [*Yoshino*, 2010]

Using the total resistance R measured, the conductivity of the sample can then be expressed as:

$$\sigma = \frac{\ln(\frac{d_{ext}}{d_{int}})}{2\Pi LR}, \tag{5.12}$$

where L is the sample length (m), d_{ext} and d_{int} are the external and internal (as an electrode is placed in the sample, Fig. 5.1) diameters of the sample (m) and R is the resistance (ohm) measured [*Gaillard*, 2004].

5.3 DIFFERENT CHARGE TRANSPORT SYSTEMS

5.3.1 *Electrolytic Conduction*

Electrolytic conduction in fluid saturated rocks is related to the bulk properties and the geometrical arrangement of the constituents (porosity, permeability, tortuosity, crack orientation, ...) and also to mineral/fluid interactions [*Nover*, 2005]. The latter is mainly characterized by the formation of the electrochemical double layer (DL). This layer can be associated to a surface conductivity σ_s caused by the polarisation of ions or hydrated ions at the inner surface of the pore system. The layer conductivity depends on the electrolyte ionic concentration and also on the surface charges of the minerals interacting with the electrolyte [*Ruffet et al.*, 1995; *Revil et al.*, 1996]. The DL effect on conductivity can be particularly significant in clay bearing rocks (e.g., shale formations) or in low-porous,

low-permeable rocks [*Nover*, 2005]. In such case, the total rock conductivity can be characterized by a general function of three different conductivities:

$$\sigma = f(\sigma_f) + f(\sigma_m) + f(\sigma_s), \tag{5.13}$$

where σ_f is the electrolyte conductivity, σ_m is the rock matrix conductivity and σ_s is the surface conductivity associated to the electrochemical DL. These conductivities are issues from different reactions and charges polarisations, and can in principle be distinguished by studying the frequency dependence of the system rock/pore saturating brine [*Olhoeft*, 1985].

5.3.2 *Electronic Conduction*

Highly conducting phases, such as graphite and ores, can form an interconnected network in the rock matrix increasing the rock conductivity. This system of charge transportation simply obeys Ohm's law and characterizes electronic conduction. The rock conductivity depends on the degree of interconnection and the conductance of the conducting phases [*Nover*, 2005]. The presence of graphite is usually the best explanation for increasing conductivity through electronic conduction. Graphite can be formed through metamorphism of sedimentary carbonaceous material but can also occur in igneous rocks. Particularly high conductivities in crustal shear zones could likely be interpreted as the presence of graphite and might also present electrical anisotropy, dependent on the shearing direction [*Evans*, 2012].

5.3.3 *Semiconduction*

Temperature-induced semiconduction is a major charge transport mechanism for pressure and temperature conditions associated with the lower crust and the mantle. A semiconductor can carry electric current but not as easily as a normal conductor. At room temperature, the conductivity of most rock minerals is relatively low. However, lattice defects and impurities (hydrogen, ferric iron, ...) in the crystal structure of the mineral define charge carriers whose mobility is enhanced with increasing temperature [*Nover*, 2005]. The conductivity of the semiconductor is then dependent on the number and mobility of those charge carriers. At low-temperatures, extrinsic charge transport defines the motion of impurities located on the interstitial crystal lattice positions. At high temperatures, intrinsic conduction or ionic conduction is characterized by the creation of cation (Mg,Fe) vacancies in the crystal lattice [*Yoshino*, 2010], leading to ions motion from regular places to interstitial positions. As an example, extrinsic defects would be the most probable crystal defects for olivine due in part to excess Mg on unoccupied octahedral positions in the crystal lattice. With increasing temperature, olivine intrinsic defects are associated to Mg-Frenkel defects, meaning regular Mg-ions within the lattice moved to interstitial positions leaving negative vacancies in the crystal structure [*Schock et al.*, 1989]. Extrinsic and intrinsic conduction for mantle-relevant mineral phases occur for temperatures between 500 up to 1500°C [*Cemic et al.*, 1980; *Schock et al.*, 1989]. The mobility of charges is mainly linked to the geometry of the crystal lattice, which can then create significant anisotropy

in the conductivity [*Nover*, 2005]. The temperature-dependent conductivity σ ($S.m^{-1}$) is characterized by an Arrhenius equation:

$$\sigma = \sigma_o \exp(\frac{-E_a - P\Delta V}{k_B T}), \tag{5.14}$$

where E_a is the activation energy (J), P is the pressure (MPa), ΔV is the activation volume ($cm^3.mol^{-1}$), k_B is the Boltzmann constant ($1.38 \times 10^{-23} J.K^{-1}$), T is the temperature (K) and σ_o is the conductivity ($S.m^{-1}$) as $T \to \infty$ [*Nover*, 2005; *Pommier et al.*, 2008; *Yoshino*, 2010]. The energy term $E_a + P\Delta V$ relates to the combination of the individual free enthalpies of the charge carriers. Furthermore, whereas the conductivity is weakly affected by the pressure, it is strongly dependent on the oxygen fugacity (effective partial pressure of oxygen). The latter quantity describes the oxidation state of the mantle and has a significant effect on controlling the charge and number of charge carriers, e.g., iron (Fe^{2+}, Fe^{3+}) [*Nover*, 2005; *Evans*, 2012]. The iron content of minerals has a significant impact on their bulk conductivity [*Evans*, 2012].

5.3.4 *Partial Melts*

Charge transport due to partial melt occurs in high temperature gradients areas or at greater depth in the Earth's mantle [*Nover*, 2005]. In amorphous silicates (glasses and melts), electrical conductivity is mainly characterized by ionic conductivity as the charge carriers (ions) are diffused within the melt [*Pommier et al.*, 2008]. In a partially molten rock, the conductivity of the melt phase is much higher than the surrounding solid rock. An interconnected network of melt can then increase the global rock conductivity by several orders of magnitude [*Nover*, 2005; *Partzsch et al.*, 2000]. The conductivity of the melt is the sum of the conductivities σ_i of the different charge carriers. The conductivity of a ion i within the melt can be characterized by the Nernst-Einstein equation:

$$\sigma_i = \frac{D_i q_i^2 N_i}{k_B T H_r}, \tag{5.15}$$

where D_i is the ion coefficient of diffusion ($m^2\ s^{-1}$), q_i is the ion charge (C), N_i is the ion concentration (mol/L), k_B is the Boltzmann constant, T is the temperature (K) and H_r is the Haven ratio (0.2 to 1) characterizing the ion migration mechanisms into the melt [*Pommier et al.*, 2008]. The rock chemistry, the presence of free water, and hydrous mineral phases all affect the temperature at which partial melts form, by moving the solidus in pressure/temperature [*Roberts and Tyburczy*, 1999; *Poe et al.*, 2001]. When water content increases, activation energy and resistivity decrease [*Gaillard*, 2004]. Variations in temperature lead to non-equilibrium conditions between the melt phase and the remaining solid rock, which affects the number of charge carriers in the melt phase and thus complicates laboratory experiments on partially molten rocks [*Nover*, 2005].

5.4 TWO PHASE MIXING MEDIUM

Although multiple phase models have been proposed [*Berryman*, 2006; *Glover*, 2010], in most cases models can be simplified to two phases mixing models. In general, one phase will dominate the conduction and therefore, rock conductivity can be modelled by the

association of a relatively conductive phase representing aqueous fluids or melts within a more resistive matrix. The two phase mixing medium can be assimilated to an homogeneous medium with an effective conductivity σ_{eff}. *Hashin and Shtrikman* [1962] (Tab. 5.1) defined the upper and lower boundaries of the effective conductivity for a two phase medium by:

$$\sigma_f + (1-\phi)\left(\frac{1}{\sigma_m - \sigma_f} + \frac{\phi}{3\sigma_f}\right)^{-1} \geqslant \sigma_{eff} \geqslant \sigma_m + \phi\left(\frac{1}{\sigma_f - \sigma_m} + \frac{(1-\phi)}{3\sigma_m}\right)^{-1}, \quad (5.16)$$

where σ_m is the conductivity of the solid matrix, σ_f is the conductivity of the conductive phase and ϕ is the volume fraction of the conductive material.

Under brittle conditions, rock conductivity will mainly depend on the volume fraction of pore fluid and its degree of interconnectivity [*Evans*, 2012]. One simple formula expressing the electrical conductivity of a aqueous fluid saturated rock is the empirical first Archie's law [*Archie*, 1942]:

$$\sigma_{eff} = \sigma_f \eta^m, \quad (5.17)$$

where η is the porosity, σ_f is the electrolyte conductivity and m is an empirical exponent or cementation factor defining the interconnectivity of the pores (1 for well interconnected pore system and 2 for a poorly interconnected pore system). The conductivity of an electrolyte σ_f is a function of the chemical composition, ion charge and temperature [*Ruffet et al.*, 1995; *Dachnov*, 1975]. Archie's second law added a saturation term to the first equation for partially saturated rocks:

$$\sigma_{eff} = \sigma_f \eta^m S_w^n, \quad (5.18)$$

where S_w is the brine saturation and n is the empirical saturation factor (usually close to 2). Archie's law does not take into account conductivity variations due to the presence of reactive minerals such as clay. In a fluid saturated rock, if the matrix conductivity is still negligible compared to the fluid conductivity, when taking into account the surface conductivity the total conductivity can be defined by the equation:

$$\sigma_{eff} = \sigma_f + m(1+\eta^m)\sigma_s \eta^m, \quad (5.19)$$

where m is the cementation exponent characterizing the pore network and η is the porosity [*Waxman and Smits*, 1968; *Johnson and Sen*, 1988; *Nover*, 2005].
If the porosity is really low, it is necessary to consider the influence of the rock matrix conductivity in those equations [*Hermance*, 1979]

Moreover, a simple model for a two phase mixing medium can represent an equivalent circuit of two resistors which are set in parallel or series depending on the current direction in the medium. Furthermore, the impact of each resistor on the medium effective conductivity will depend on the volume fractions of each phase [*Simpson and Bahr*, 2005; *Evans*, 2012].

$$\sigma_{eff}^{parallel} = \phi\sigma_1 + (1-\phi)\sigma_2 \quad (5.20)$$

$$\sigma_{eff}^{series} = [\frac{\phi}{\sigma_1} - \frac{(1-\phi)}{\sigma_2}]^{-1} \quad (5.21)$$

As an example, this type of model can be applied to model the impact of fractures in a uniform medium [*Yu et al.*, 1997]. In this case, the parallel or series configuration of the equivalent circuit would be characterized by the cracks orientations and the porosity would control the interconnectivity of the fractures. The "parallel" and "series" properties of such model could also be extended to anisotropy studies [*Yu et al.*, 1997]. However, as the conductivity of Earth materials ranges up to 12 orders of magnitude, such a model could quickly lead to biased estimations, such as too high conductivities for the parallel average and too low conductivities for the series average [*Simpson and Bahr*, 2005].

Under brittle conditions, bulk conductivity will be affected by the topology of the fracturation, whereas in partially molten rocks the conductivity depends on the melt interconnection. The latter will be controlled by the volume of melt in the rock and also by the dihedral angle [*Smith*, 1948; *Evans*, 2012]. The melt dihedral angle (Fig. 5.4) associated with a partially molten medium defines the angle made by melt pockets at the grain boundaries and therefore affects the melt interconnectivity through the solid matrix.

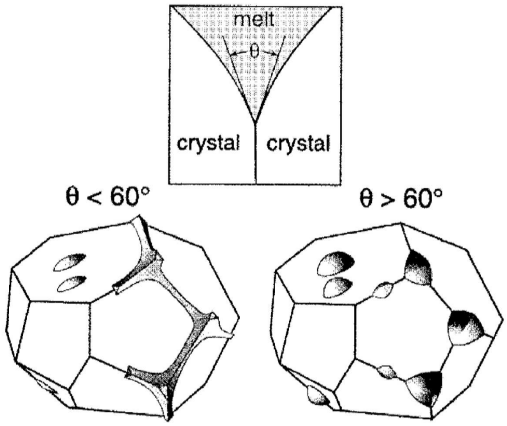

Figure 5.4: Dihedral angle and melt interconnectivity: angles below 60° will define interconnected melt distributions, larger values will characterize isolated pockets of melt [*Evans*, 2012]. *After* [*Righter*, 2003]

Within a partially molten rock, textural or microstructural equilibrium is reached when the surface of the solid phase and the melt define a chemical equilibrium. Moreover, the interfacial-energy-driven equilibration (minimization of the surface energy) between the melt and the solid phase has to be fast enough that it occurs prior to any changes in the pore volume [*Smith*, 1948; *Cheadle et al.*, 2004]. The crystal-melt dihedral angle and microstructural equilibrium within a melt-bearing medium will control melt percolation and therefore the melt segregation and migration behaviour [*Cheadle et al.*, 2004; *ten Grotenhuis et al.*, 2005]. In natural partially molten rock samples, microstructures characterized by variable grain size and various phases will generate anisotropy in the interfacial energies leading to different diheral angles within the rock and disequilibrium in the melt distribution [*Laporte and Provost*, 2000; *Cheadle et al.*, 2004]. Those microstructures will affect the textural equilibrium of the melt-bearing rock, and therefore the porosity-permeability relation in the rock [*ten Grotenhuis et al.*, 2005]. However, with all dihedral angles below 60° (Fig. 5.4), the melt interconnection will reduce those irregularities and lead to textural equilibrium [*Cheadle et al.*, 2004].

Table 5.1: Different geometric models to describe melt distribution; σ_{eff} = effective conductivity, X_m = melt fraction, σ_m = melt phase conductivity, σ_s = solid phase conductivity, C = Archie's law empirical coefficient, n = Archie's law empirical coefficient, β = partitioning between tube and cube distributions. *after* [*ten Grotenhuis et al.*, 2005]

Two Phases Models	Description
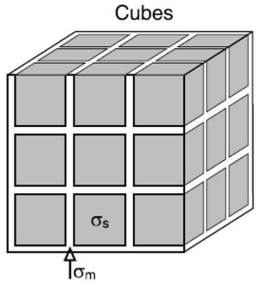	The melt is assumed to be distributed in layers along the grains boundaries and therefore its distribution can be modelled as a layer of uniform thickness surrounding identical cubic grains [*Waff*, 1974]. $\sigma_{eff} = [1-(1-X_m)^{\frac{2}{3}}]\sigma_m$
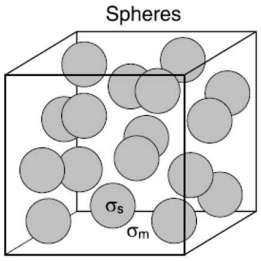	Spherical grains are isolated from each other as the melt phase is distributed along the grains boundaries and has filled the grains' triple junctions [*Waff*, 1974]. The sphere model also characterizes the Hashin-Shtrikman upper bound (HS+) [*Hashin and Shtrikman*, 1962]. $\sigma_{eff} = \sigma_m + \frac{(1-X_m)}{1/(\sigma_s-\sigma_m)+X_m/3\sigma_m}$ The Hashin-Shtrikman lower bound (HS-) is defined the same way, although in this case the spheres would represent melt pockets isolated in the matrix.
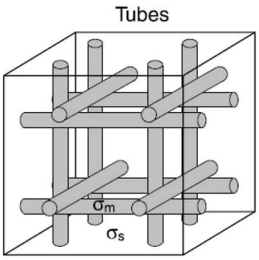	Assuming the melt forms a network along the grains edges (triple junctions), the melt distribution can be assimilated to a network of equally spaced tubes within a rectangular network [*Schmeling*, 1986]. $\sigma_{eff} = \frac{1}{3}X_m\sigma_m + (1-X_m)\sigma_s$
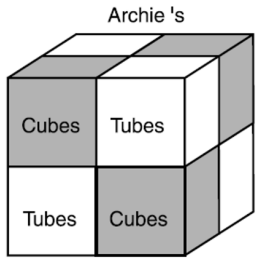	In this model, the melt connectivity changes with the melt fraction [*Watanabe and Kurita*, 1993]. $\sigma_{eff} = CX_m^n\sigma_m$ The melt distribution in the Archie's model can also be characterized by a mixture between the cube and tube models. $\sigma_{eff} = \sigma_{tubes}^{(1-\beta)} * \sigma_{cubes}^{\beta}$

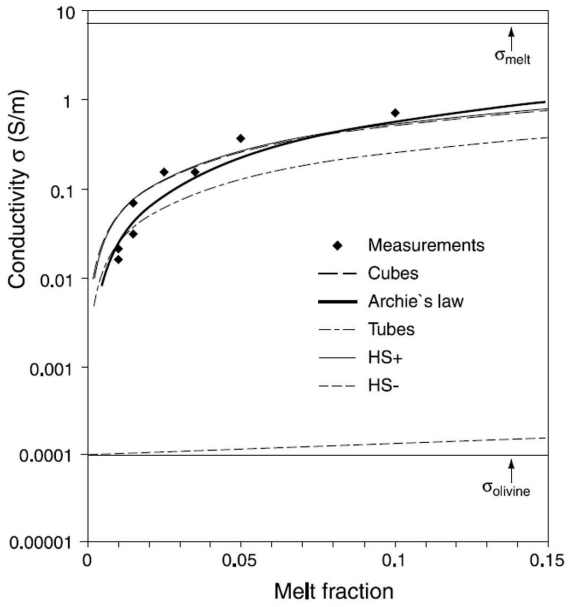

Figure 5.5: Conductivity measurements on partially molten olivine rocks as a function of the melt fraction and compared with the conductivity predictions from different geometric models ($\sigma_{melt} = 7.53$ S/m and $\sigma_{olivine} = 0.0001$ S/m) (Tab. 5.1). *from* [*ten Grotenhuis et al.*, 2005]

Partially molten rocks will present an interconnected melt, and therefore high conductivities, even for low melt fractions [*Partzsch et al.*, 2000]. Furthermore, *Rosenberg and Handy* [2005] highlighted that for a melt fraction of below 7%, melt interconnectivity is already significant enough to dramatically affect the strength of a partially molten rock. As shown in Table 5.1, different geometrical models representing simplified melt distributions can be considered to estimate the effective conductivity of a partially molten rock. The melt fraction in the rock will have a significant impact on which model represents the rock sample the best. For instance, the tube model is more appropriate for low melt fractions, whereas the cube or sphere models would represent high melt fraction samples better. It has been shown for olivine samples that Archie's law (Tab. 5.1) would describe a gradual change in the melt distribution from a tube-type distribution (X_m=0.01) to a cube-type distribution (X_m=0.1) as the melt fraction increases (Fig. 5.5) [*ten Grotenhuis et al.*, 2005].

5.5 RESISTIVITY OF THE EARTH: CRUST AND MANTLE

As most crustal and mantle rocks are relatively poor conductors, the Earth's conductivity is mainly controlled by the occurrence of interconnected highly conductive phases. Figure 5.6 represents a synthesis of the Earth's resistivity covering both MT surveys and laboratory measurements. This summary shows the evolution of crustal and mantle resistivities in different tectonic settings and also highlights the impact of water, saline solutions, melt, graphite and sulfides.

In the crust, porosity and fractures will allow the interconnection of aqueous fluids. The conductivity of those solutions is mainly dependent on particular ionic concentrations (Fig. 5.6), such as NaCl, KCl and dissolved CO_2, and also on temperature, as it will affect

fluid density and charge mobility [*Evans*, 2012]. In the crust, the resistivity of saline and bicarbonate solutions are expected to range between 10 to 0.01 Ω.m [*Nesbitt*, 1993]. In continental sedimentary basins, bulk resistivity will range between 1 to 100 Ω.m depending on the sediments' state of compaction and the pore-fluid salinity [*Evans*, 2012]. The presence of free fluids in the stable lower crust to explain low resistivity anomalies has been strongly debated [*Jones*, 1992; *Yardley and Walley*, 1997; *Wannamaker*, 2000; *Yardley and Walley*, 2000]. From a petrological point of view, the lower crust in stable plate interiors is likely to be characterized by mostly dry granulite rocks as water or saline fluids are not in equilibrium with the high-grade mineral assemblages present in the lower crust [*Yardley and Walley*, 1997]. However, *Wannamaker* [2000] and *Wannamaker et al.* [2008] mentioned that solutions with highly heterogeneous compositions would lower the water fugacity and therefore stabilize those type of fluids in the high-grade metamorphic rocks. In order to prevent fluids to escape, low permeability is needed, however it would also prevent pore interconnection and therefore low resistivity values [*Hyndman et al.*, 1993]. However, the conductivity could be controlled by small cracks and fissures defining a "secondary porosity" that could carry electrical current [*Evans*, 2012]. Furthermore, *Wannamaker et al.* [2008] mentioned that rocks in a ductile regime are likely to favour fluid interconnectivity along mineral boundaries. Therefore, even with low porosity, highly saline fluids could enhance the bulk conductivity. In the oceanic lithosphere, due to their high porosity (saline pore fluid), serpentinized peridotites may represent relatively conductive portions of the oceanic upper mantle (Fig. 5.6).

As an alternative to the presence of free fluids in the lower crust, graphite films located along grain boundaries could significantly enhance the bulk conductivity if interconnected [*Frost et al.*, 1989; *Jones*, 1992; *Hyndman et al.*, 1993]. Graphite originates from films that precipitate during high-grade metamorphism taking place in a CO_2-rich fluid environment (Fig. 5.6). But they can also form in shear zones under mid-crustal P,T conditions [*Glover*, 1996]. The latter context would particularly represent suture zones associated with ocean closures, where the graphite located in shear zones would be produced from metamorphism of organic carbon deposited in marine sediments [*Monteiro Santos et al.*, 2002]. Furthermore, *Glover* [1996] mentioned mechanical deformations are likely to affect graphite connectivity, and therefore the author questioned processes involved in the disconnection and reconnection of graphite films. Recent studies have also highlighted that graphite represents a stabilized step of the carbon cycle through the geological times as it appears

Figure 5.6 *(facing page)*: Overview of the Earth's crust and mantle resistivity. If not specified otherwise most numbers represent log(resisitivity) values in Ω.m [*Evans*, 2012; *Jones*, 1992; *Wannamaker*, 2000; *Pommier et al.*, 2010; *Fullea et al.*, 2011; *Wannamaker et al.*, 2008; *Worzewski et al.*, 2011; *Brasse and Eydam*, 2008]. Oceanic Setting: MT model *from* [*Baba et al.*, 2006] - Subduction Zone: MT model *from* [*Worzewski et al.*, 2011] - Continental Setting: MT model *from* [*Wannamaker et al.*, 2008] - Craton: MT model *from* [*Jones et al.*, 2001] - Melts/Water in the mantle: conductivity of the lithosphere and asthenosphere *from* [*Gaillard et al.*, 2008] - Saline fluids: resistivity as a function of NaCl concentration *from* [*Jones*, 1992] - Partial melts: pressure-temperature diagram *from* [*Hopkins et al.*, 2008], partial melts conductivity as a function of melt fraction *from* [*Schilling et al.*, 2006] - Graphite *after* [*Glover*, 1996] - Sulfides *after* [*Ducea and Park*, 2000].

OCEANIC SETTING

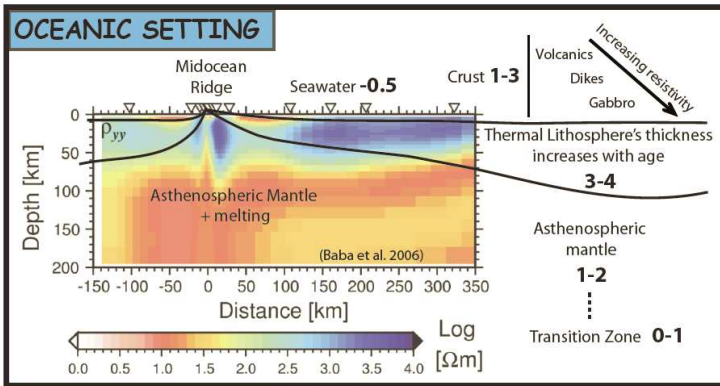

SUBDUCTION ZONE

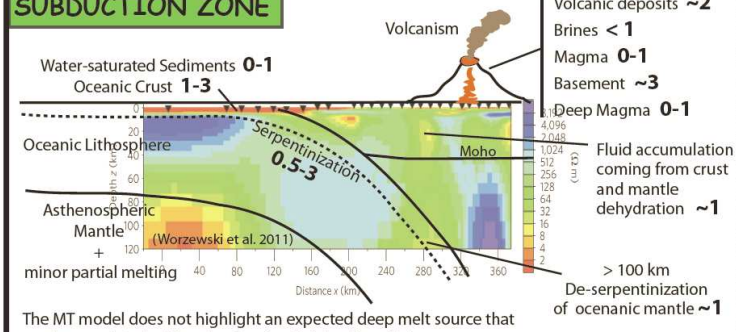

The MT model does not highlight an expected deep melt source that can be associated with volcanism (probably off profile).
Brasse & Eydam 2008 imaged a strong deep magma source in the Bolivian Orocline.

CONTINENTAL SETTING

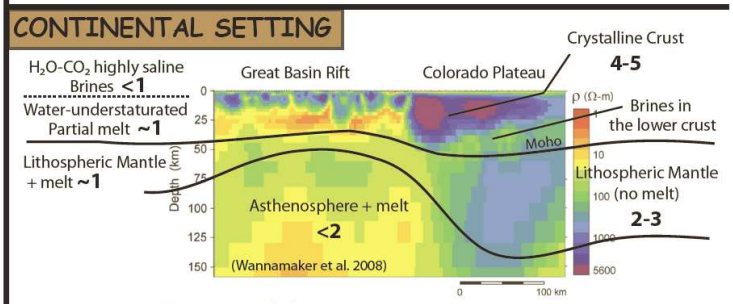

Average Resistivity Model

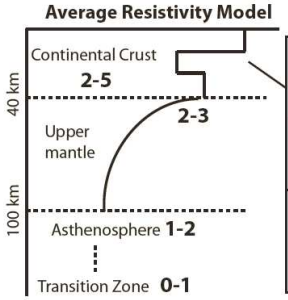

Continental Crust

Upper	+ Fluids <0-2 Dependent on: Fracturation, Porosity, Salinity		+ Sulfides <0-1	+ Graphite <0-1
Mid	Reduction in pore space and interconnectivity	+ Partial Melts <0-2 related to hot geotherm and/or anormal crustal thickness		
Lower	Ductility (T>500°C) can enhance fluids interconnection			

CRATON

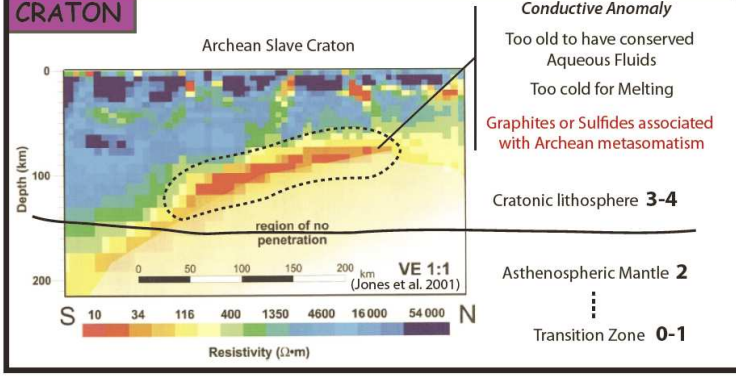

Melts/Water in the Mantle

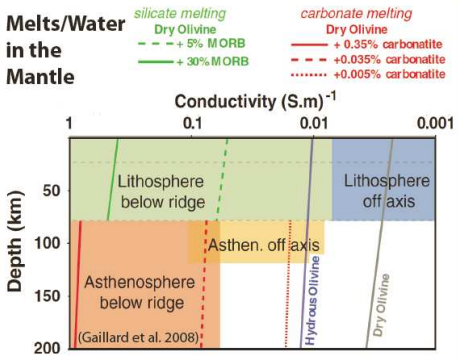

Saline fluids

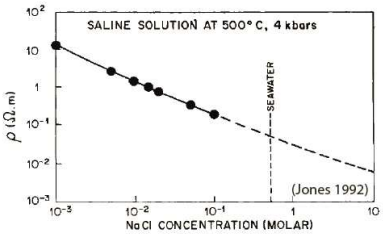

Partial melts

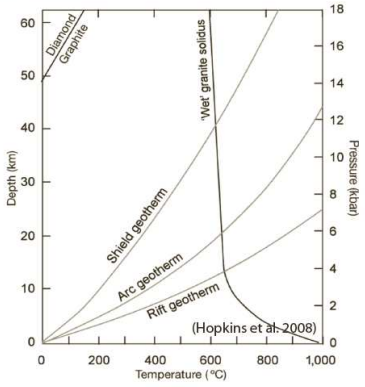

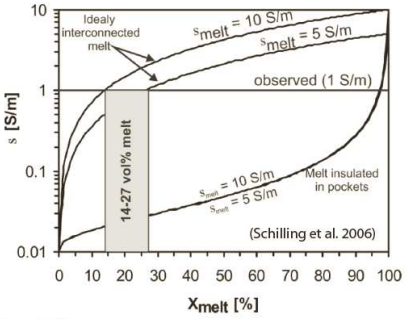

Graphite

Precipitation of stable graphite films associated with deep crustal metamorphim in the presence of CO_2-fluids.
Graphite can also crystallize in strike-slip fault shear zones at mid-crustal P,T.

Sulfides

Sulfide-bearing fluids are usually related to metasomatism.
Sulfide minerals are likely to be trapped in partial molten zones and can explain observed high conductivities even when low melt fractions are expected:
2-5 % Silicate melt ≈ 1% Silicate melt + >0.25% Sulfide melt

Once crystallized, sulfide minerals can still strongly affect the bulk conductivity when forming interconnected networks.

not to be particularly affected by continental weathering [*Galy et al.*, 2008]. Therefore, it is likely that graphite accumulates in the crust and may only recycled through subduction processes [*Galy et al.*, 2008]. In the mantle, deep conductivity anomalies (> ~150-200 km) are unlikely to be related to graphite due to the graphite-diamond phase transition.

In active tectonic regimes, silicate melts are likely to occur in the mantle but also in the crust if elevated geotherms and/or thick crustal conditions are present to enable anatexis. Water would also play a significant role in partial melting by displacing the rock solidus and facilitating partial melting at lower temperatures [*Evans*, 2012]. As temperature will have a strong influence on the melt and crystal conductivities as well as the melt fraction [*Roberts and Tyburczy*, 1999], the conductivity of partial molten rocks will be mainly controlled by temperature and slightly affected by the pressure [*Tyburczy and Waff*, 1983]. Quantifying melt fractions responsible for the observed MT conductive anomalies [*Pommier and Trong*, 2011] is important for understanding the tectonic processes affecting the crust and mantle conductivity. Furthermore, in partial melting areas, the presence of sulfidic melts (Fig. 5.6) could significantly affect the bulk conductivity of a partially molten rock and would lower the silicate melt fraction associated with a particular conductive anomaly [*Ducea and Park*, 2000]. In the deep mantle (> ~100 km), strong conductive anomalies have been associated to carbonatite melts (Fig. 5.6) [*Gaillard et al.*, 2008]. Compared to silicate melts, carbonatite melts are highly conductive (Fig. 5.6). Therefore, due to their large wetting properties [*Gaillard et al.*, 2008], melt fractions as low as 0.01% could significantly enhance the bulk conductivity [*Evans*, 2012]. At the Earth's surface, carbonatites are quite rare and several questions remain concerning their origin and evolution. *Rudnick et al.* [1993] presented the low-viscosity carbonatite melts as effective carriers of incompatible elements through the upper mantle that are likely to take part in mantle metasomatism.

The bulk conductivity of mantle rocks will dependent on parameters such as pressure, composition and oxygen fugacity but particularly on temperature, the presence of hydrous phases and the degree of partial melting [*Karato*, 1990; *Gaillard et al.*, 2008; *Yoshino*, 2010; *Evans*, 2012]. The oceanic lithosphere defines a resistive layer whose thickness increases with its age as the mantle cools down. However, the presence of either water and/or partial melt will increase its conductivity, particularly near mid-ocean ridges and subduction zones (Fig. 5.6). Under most stable continental settings and particularly older cratons (except for the Kaapvaal craton [*Jones et al.*, 2012]), the lithospheric mantle is likely to be dry, although relatively small concentration could be dissolved in the mantle [*Evans*, 2012]. In the presence of wet (hydrogen dissolved) olivine, mantle conductivities are enhanced by hydrogen diffusion (proton conduction) [*Karato*, 1990]. Several laboratory studies have been working on estimating the conductivity of dry and wet mantle rock minerals such as olivine (most common mantle mineral) [*Constable et al.*, 1992; *Hirsch et al.*, 1993; *Xu et al.*, 2000; *Du Frane et al.*, 2005; *Constable*, 1992; *Wang et al.*, 2006; *Vacher and Verhoeven*, 2005; *Yoshino et al.*, 2009; *Poe et al.*, 2010]. However the olivine resistivity estimates can sometime vary by over 1.5 orders of magnitude between different laboratories (Fig. 5.7) [*Jones et al.*, 2012; *Evans*, 2012]. Furthermore, as highlighted by *Jones et al.* [2012], the laboratory studies when associated to MT measurements from the field do not seem to bring clear constraints for conclusions on the water content in the mantle rocks, even when considering stable regions such as cratons.

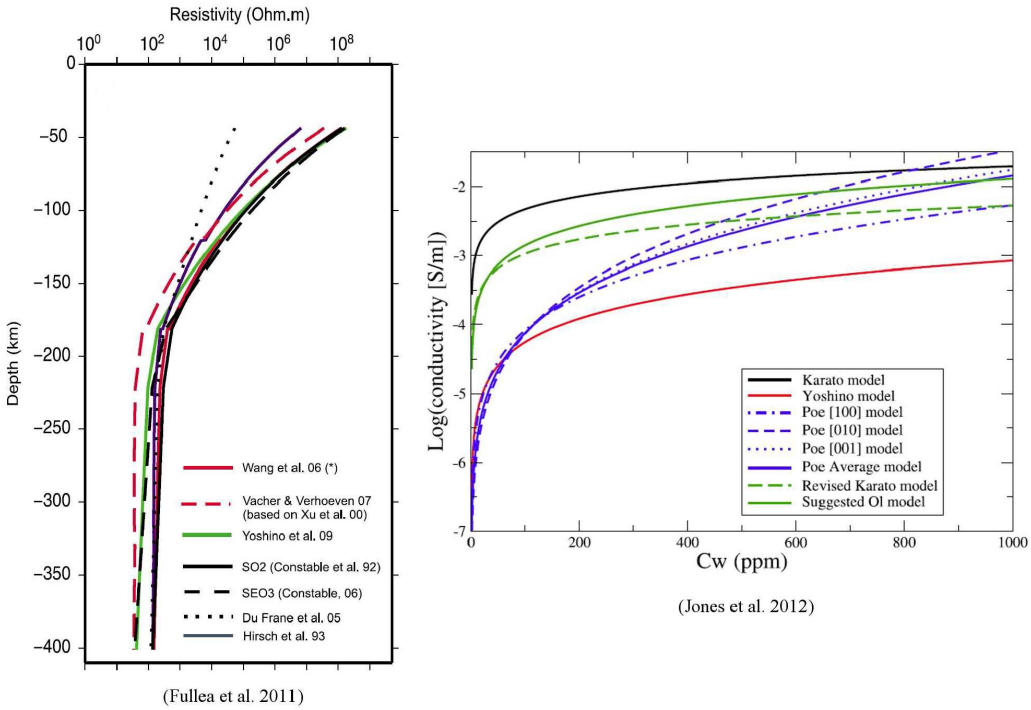

Figure 5.7: Estimations for olivine resistivity - ***On the left*** - Electrical resistivity of dry olivine from different laboratory studies, references: [*Wang et al.*, 2006; *Vacher and Verhoeven*, 2005; *Xu et al.*, 2000; *Yoshino et al.*, 2009; *Constable et al.*, 1992; *Constable*, 1992; *Du Frane et al.*, 2005; *Hirsch et al.*, 1993]; *picture from* [*Fullea et al.*, 2011]. ***On the right*** - Electrical resistivity of olivine with varying water content at a temperature of 800°C from Karato model [*Wang et al.*, 2006], Yoshino model [*Yoshino et al.*, 2009], Poe model [*Poe et al.*, 2010], Revised Karato model and suggested model from [*Jones et al.*, 2012]; *picture from* [*Jones et al.*, 2012]

5.5.1 *Electrical Anisotropy*

Electrical anisotropy observed in magnetotelluric surveys cannot really be differentiated between structural anisotropy related to the particular orientation of macroscopic heterogeneities and intrinsic anisotropy related to the crystal fabric [*Evans*, 2012]. Therefore, interpreting data with apparent anisotropic effects can be quite challenging. Due to the diffusive character of the magnetotelluric method, structures resolution diminishes with depth. Therefore, there is a spatial limit for preferentially oriented heterogeneities below which only equivalent anisotropy can be resolved. This particular issue is discussed in a later chapter through simple 3D synthetic modelling. In those situations, the compositional and tectonic context become quite crucial in guiding the interpretation [*Wannamaker*, 2005]. It is also worth noticing that due to larger scale heterogeneities, a higher degree of anisotropy is more than likely to be expected on MT measurements than it would be for rock samples from laboratory studies [*Simpson and Bahr*, 2005].

In the crust, electrical anisotropy is likely to be mostly macroscopic and would be related to a particular lithologic layering or oriented heterogeneity, cracks, faults, dikes and shear zones containing conductive phases (fluids,melts,graphite) [*Wannamaker*, 2005; *Evans*, 2012]. Furthermore, the observed anisotropy might not necessarily reflect a current

state of stress but could also characterize a signature of past deformation embedded in the rock or an existing fabric that might control fluid distribution [*Wannamaker*, 2005]. Strong foliations associated with metamorphic rocks, particularly carbon-bearing rocks, may also present electrical anisotropy. Graphite films interconnection will increase with pressure [*Glover and Vine*, 1992] and is likely to enhance conductivity along the foliation directions [*Evans*, 2012]. The orientation of the higher conductivities in shear zones would be expected to be parallel to the strike direction [*Wannamaker*, 2005]. Finally, as described in *Jones et al.* [1997], high concentration of sulphides remobilized into fold hinges during deformation can lead to a strong anisotropic signature (Fig. 5.8).

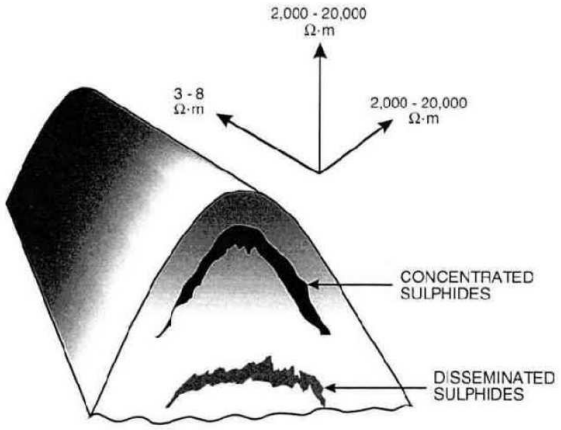

Figure 5.8: Schematic representation of a sulphidic metasediment sample collected in central Trans Hudson Orogen. The rock model is defined by folded layers containing highly concentrated sulphides accumulated near the hinge of the fold, and disseminated sulphides in the rock matrix. The concentrated sulphides are preferentially oriented along strike and therefore can generate electrical anisotropy of several orders of magnitude. *from* [*Jones et al.*, 1997]

In the mantle, some of the situations mentioned for the crust can still account for the presence of anisotropy, but strong electrical anisotropy can also be explained by hydrous defects within shear-aligned olivine crystals [*Wannamaker*, 2005]. As observed in oceanic settings (Fig. 5.6), electrical anisotropy has been attributed to the preferred orientation of hydrogen diffusion in wet olivine in association with the spreading direction of the mid-ocean ridge [*Evans et al.*, 2005]. However, *Yoshino et al.* [2006] argued that the observed anisotropy is more likely to be the result of partial melting interconnected along the plate motion direction.

Seismic anisotropy and electrical anisotropy are not necessarily associated. Compared with SKS seismic studies, magnetotellurics will have a superior resolution of the depth of an anisotropic anomaly [*Evans*, 2012]. It is quite difficult to constrain the exact depth interval of SKS anisotropy [*Savage*, 1999]. However, surface wave tomography can have a good resolution on the depths of S wave anisotropy [*Simons and van der Hilst*, 2003].

More details on the impact of electrical anisotropy on MT data can be found in the next part which focusses on the MT method.

6 NATURAL MAGNETOTELLURIC SOURCES

The fluctuations of the electromagnetic (EM) field at the Earth's surface varies from million of years to microseconds. Whereas the long term variations are linked to changes in the Earth dynamo region, the shorter term variations come from electric currents systems in the upper atmosphere and magnetosphere. In magnetotelluric studies, the period range commonly used ranges from $\sim 10^{-4}$ s (10^{4} Hz) to $\sim 10^{5}$ s (10^{-5} Hz) [*Simpson and Bahr*, 2005]. Natural-source time-varying EM waves observable on the surface of the Earth are generated by distant lightning activity at high frequencies and by the interaction of the Earth's magnetosphere-ionosphere with particles ejected by the Sun (solar plasma) at low frequencies. The *MT dead-band* defines the transition characterized by poor data quality between those two types of fluctuations. In the MT signal power spectrum, the *dead-band* lies in the $0.2 - 7.8$ Hz frequency range [*Schmucker*, 1985; *Vozoff*, 1991; *Simpson and Bahr*, 2005]. The *MT dead-band* poor signal is due to a weak signal to noise ratio. The usual assumption in magnetotelluric studies of the Earth's conductivity structure is that the primary field produced is laterally uniform, i.e. the plane wave criterion is satisfied. Generally this is the case except for areas near the auroral and equatorial electrojets where source distortion effects may sometimes affect the interpretation of data.

6.1 GEOMAGNETIC NATURAL FLUCTUATIONS

The following table (Tab. 6.1) shows a summary of the different geomagnetic variations associated with natural sources, from the sunspots cycles ultra long variations to the sferics VLF variations.

Table 6.1: Classification of geomagnetic fluctuations reproduced from [*Schmucker*, 1985] with ULF part updated from [*McPherron*, 2005]. *A: Peak-to-peak amplitude or maximum departure from undisturbed level; ERC: equatorial ring current in the radiation belt of the magnetosphere; EEJ: equatorial electrojet; PEJ: Polar electrojet; a: auroral zone latitudes; m: mi-latitudes; l: low latitudes; dd: dip equator region on the day-side*

Type	Symbol	Period	A (nT)	Source
Solar cycle variations		11 years	20	ERC modulation by sunspot cycle
Annual variations		1 year	5	Ionospheric sources
Semi-annual variations		6 months	5	ERC modulation within the earth's orbit around the sun
Smoothed storm-time variations				Enhanced ERC after magnetic storms

continued on next page

Table6.1 – continued from previous page

Type	Symbol	Period	A (nT)	Source
storm-time-dependent part	Dst	2 - 27 days	100	
disturbance level time inequality	DS	12 - 24 h	100	
Solar daily variations	S			Ionospheric current
on quiet days	Sq	1 day	30 - 60 (m,l)	loops on day-side
	EEJ	1 day	60 - 120 (dd)	sectors of the both
enhancement on disturbed days	S_D	1 day	10 - 20	hemispheres
Lunar daily variation	L	1 lunar day	1 - 3	Dual ionospheric current loops on both hemispheres
Polar magnetic storms and short-lived substorms	DP			Polar electrojet PEJ in the ionosphere
centre of disturbance in the night-time auroral zone	DP1	10 mn - 2 h	1000 (a) 100 (m,l)	with connecting field-aligned
with correlated irregular variations in low latitudes	DP2	10 mn - 2 h	100 (a) 10 (m,l) 100 (dd)	currents to plasma regions of the magnetosphere
Special effects connected to polar magnetic storms				see DP1
bays = substorms as observed in mid-latitudes	b	30 mn - 2 h	20 - 100 (a,m) 5 - 25 (l)	
Solar flare effect	sfe	10 - 20 mn	10	Short-lived enhancement of Sq currents in the inosphere
Sudden storm commencement	ssc	2 - 5 mn	10 - 100	Impact of intense solar particle stream on magnetopause
Ultra Low Frequency pulsations	ULF	0.2 - 600 s		Standing and propagating
regular continuous pulsations	Pc5	150 - 600 s	100 (a) 10 (m)	hydromagnetic waves in the
	Pc4	45 - 150 s	2	magnetosphere
	Pc3	10 - 45 s	0.5	
	Pc2	5 - 10 s	0.5	
	Pc1	0.2 - 5 s	1	
irregular transient pulsations	Pi2	45 - 150 s	1	
	Pi1	1 - 45 s	1	
Schumann resonance oscillations		1/7.8 s	<0.1	Cavity resonance earth-ionosphere for electromagnetic waves

continued on next page

Table6.1 – continued from previous page

Type	Symbol	Period	A (nT)	Source
Extra Low Frequency emissions	ELF	10^{-3} - 0.2 s	<0.1	Propagating electromagnetic waves in the earth-ionosphere wave guide (ELF) and propagating hydromagnetic waves in the magnetosphere (VLF and ELF)
Very Low frequency Emissions, including whistlers	VLF	10^{-5} - 10^{-3} s		

6.2 SUN INTERACTION WITH THE EARTH

In our solar system, the space between the planets is filled with a fast streaming, magnetized plasma coming from the Sun and is called the solar wind. Terrestrial effects are the result of three general types of conditions on the Sun: eruptive flares, disappearing filaments and coronal holes facing the Earth.

6.2.1 *Sun Activity*

Flares are short term brightenings that last for minutes or hours. They usually occur near active regions of the Sun where strong changes in the magnetic field occur. They are localized on what are called sunspots. Due to the Sun gaseous plasma composition, the solar rotation varies with latitude.

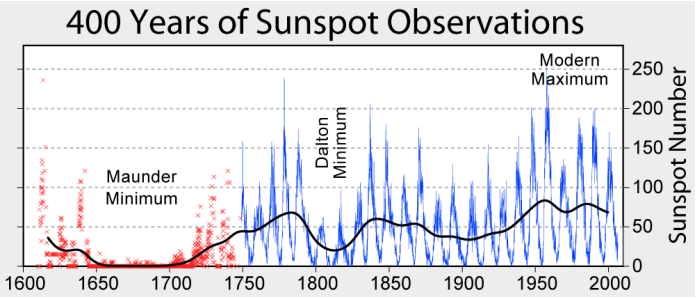

Figure 6.1: The sunspot cycle over the last 400 years revealing the 11 years periodicity of the sun maximum activity. *after* [*Hoyt and Schatten*, 1998a,b; *Stott et al.*, 2003]

At the equator the solar sideral rotation period is 24.47 days [*Snodgrass and Ulrich*, 1990]. However, observed from the Earth, the solar synodic rotation will be 26.24 days. The commonly used definition would be the Carrington rotation (latitude of 26°) characterizing a synodic period of 27.27 days. Sunspots move across the surface of the Sun as the Sun rotates, and can grow as wide as two Earth radii. Sunspots are cooler than the surrounding

photosphere and can be identified as depression areas. Although the lifetime of a typical sunspot is measured in days or even weeks, the solar maximum activity (largest number of sunspots) defines an approximate 11 years period cycle [*Eddy*, 1976] (Fig. 6.1). For reasons not yet understood, solar activity fell to an anomalous minimum in the past between about 1645 and 1715. This period is called the Maunder Minimum, named after Edward Maunder, and it coincided with a very cool period in Europe [*Eddy*, 1976] (Fig. 6.1).

The 11 years sunspot cycle is actually part of a 22 years solar cycle linked to the sunspots magnetic polarity [*Hale*, 1908]. In the early years of a sunspot cycle, sunspots tend to be smaller and to form at higher latitudes, both north and south. As the cycle gets closer to a maximum, the spots generally become larger and form closer to the equator. As the cycle subsides to a minimum, the spots get smaller and appear even closer to the equatorial region. Sunspot migration is highlighted by Maunder's Butterfly Diagram [*Maunder*, 1904] (Fig. 6.2).

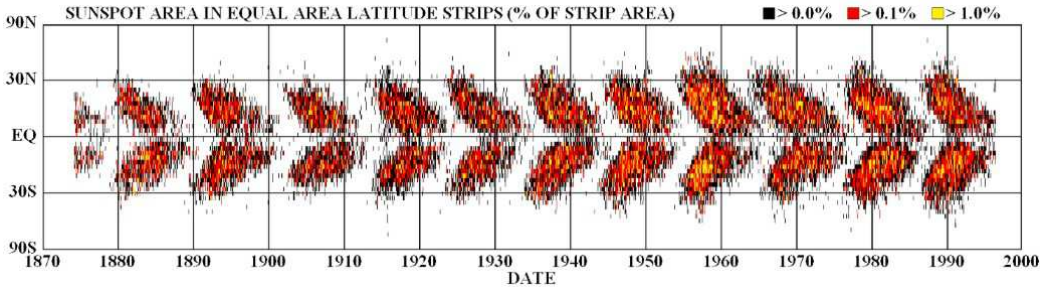

Figure 6.2: Butterfly Diagram: variations in sunspots latitudes between 1870 and 1995. *from* [*NASA*]

The solar cycles have been numbered since 1755 [*spacetoday.org*]. There is usually an overlap between the end of one cycle and the beginning of the next one. This particularity was also observed recently between the protracted end of Cycle 23 and the beginning of Cycle 24. The solar cycle 23 lasted 12.6 years from May 1996 to December 2008. The actual solar cycle 24 started in January 2008 [*Phillips*, 2008] but has been characterized by a strong minimum in the sunspot activity during 2009.

Solar filaments are long string-like features that hang like clouds in the low chromosphere for days or weeks and then disappear. Long-term eruptive activity is usually associated with the disappearance of those filaments. Filaments disappear by forming giant arching prominences that eventually break away from the Sun leading to large bursts of plasma. Three to six days after the disappearance of large solar filaments, the average level of geomagnetic activity is likely to increase [*McNamara and Wright*, 1982].

Although coronal holes are permanently located near the poles of the Sun, sometimes coronal holes may form at lower latitudes during Sun rotations and can then spray the Earth with a high intensity of charged particles. In contrast to other regions of the Sun where field lines arch back to connect, magnetic field lines extend outward from coronal holes.

6.2.2 *The Magnetosphere*

As the solar wind reaches the Earth it interacts with the Earth's inner magnetic field in a region called the magnetosphere [*Gold*, 1959]. The day side of the magnetosphere is

compressed closer to the surface of the Earth and the geomagnetic field fluctuates wildly. The solar wind interacts directly with the magnetosphere in the polar cusp region. Solar wind energy is also transferred to the magnetosphere by magnetic reconnection. The magnetopause is an area of equilibrium between the solar wind's dynamic pressure and the magnetic pressure of the Earth magnetic field. Its surface acts like a shield and varies with solar wind intensity. The magnetosphere is characterized by an assemblage of different current systems (Fig. 6.3). As highlighted on the Table 6.1, ring current modulations, associated with the solar wind, have a significant impact on the longer period geomagnetic fluctuations observed at the Earth's surface. The magnetospheric and ionospheric currents are coupled by the Birkeland (field-aligned) currents [*Alfvén*, 1939] (Fig. 6.3).

Solar wind interaction with the magnetosphere will also produce ultra low fequency (ULF) pulsations characterized as hydromagnetic waves. Many of these waves propagate through the magnetopause and the magnetosphere. Internally they interact with waveguides, cavities, and field lines, creating the pulsations actually seen at the surface [*McPherron*, 2005]. They are classified as regular quasi-sinusoidal Pc pulsations and irregular Pi pulsations [*Schmucker*, 1985; *McPherron*, 2005] (Tab. 6.1).

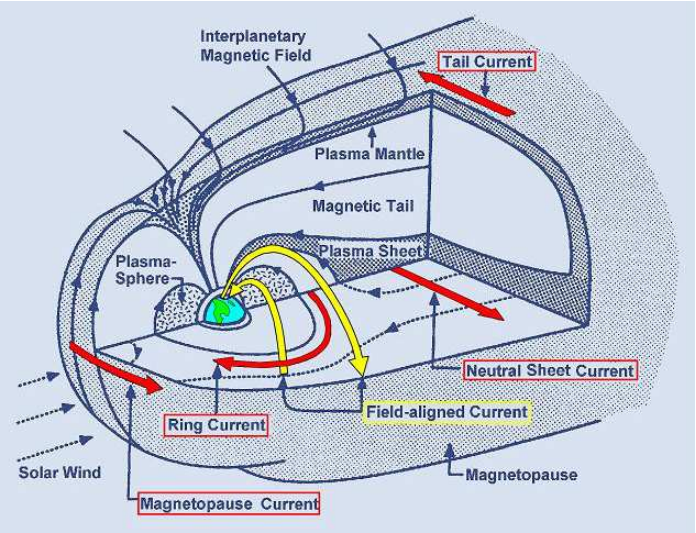

Figure 6.3: Schematic configuration of the magnetospheric currents. *from* [*Lapenta*, 2011]

Geomagnetic activity

The geomagnetic activity on Earth is divided into storms and substorms. Magnetic storms are associated with solar events such as coronal mass ejections [*Tousey*, 1973], solar flares and fast streams. Disturbances associated with geomagnetic storms observed at the Earth's surface are mainly due to modulations of the magnetospheric ring current (Fig. 6.3). The solar maximum increases the intensity and frequency of the geomagnetic storms. The frequency of the geomagnetic storms are characterized by a double peak maxima occuring before and after the highest solar activity (Fig. 6.4).

Magnetic substorms [*Potemra*, 1991] are associated with disturbances in the magnetosphere leading to energy release from the magnetospheric tail (Fig. 6.3) into the high latitude ionosphere. Compared to magnetic storms that take place over a period of several

days, substorms are brief events last only a few hours. Substorms become more frequent during a geomagnetic storm and can even overlap each other.

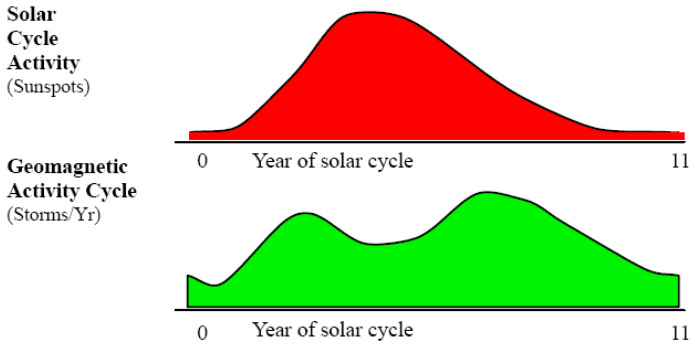

Figure 6.4: Sunspots activity compared with magnetic storms activity during the sun's 11 years cycle. *from* [*NOAA*]

K	nT	a
0	0-5	0
1	5-10	3
2	10-20	7
3	20-40	15
4	40-70	27
5	70-120	48
6	120-200	80
7	200-330	140
8	330-500	240
9	>500	400

Kp-index	NOAA Space Weather Scale Geomagnetic Storm Level
Kp=5	G1
Kp=6	G2
Kp=7	G3
Kp=8	G4
Kp=9	G5

Figure 6.5: Different scales to characterize the intensity of the geomagnetic fluctuations. *from* [*NOAA*]

The **K-index** (Fig. 6.5) is a planetary measure related to the maximum fluctuations (relative to a quiet day) measured on a magnetometer's horizontal components during a three-hour interval [*Bartels et al.*, 1939]. During a quiet day, there is no geomagnetic storm and the intensity of the geomagnetic activity is mainly characterized by the fluctuations associated with the solar daily variations. The critical thresholds leading to customer alerts varies from 6 to 8 following the geomagnetic latitude. However, the K scale has a non-linear relationship with the magnetometer fluctuations. Each K can then be converted back into a linear scale called the equivalent three hourly range **a-index** (Fig. 6.5). The daily **A-index** is merely the average of eight "a" indices to get the daily average. The **Kp-index** is derived by calculating a weighted average of K-indices from a network of mid-latitude geomagnetic observatories [*Bartels et al.*, 1939]. However these observatories do not report their data in real-time. The NOAA **G-scale** focuses on the intensity of proper geomagnetic storm. Kp of 0 to 4 is below the storm level and is labelled Go (Fig. 6.5). Other indices can be considered such as the **DST-index** (index for world wide geomagnetic storm level), the **AE-index** (index for auroral zone geomagnetic substorms activity) and the **PC-index** (index for geomagnetic disturbances at the polar cusp).

6.2.3 *The Ionosphere*

The ionosphere is the key region for MT signals as it is involved in some way in every MT frequency band. The long period MT signal-recorded at the ground originates from ionospheric induced currents [*McPherron*, 2005]. Most of the ionosphere is electrically neutral, however when the solar radiation hits the atmosphere on the sunlit side of the Earth, electrons are dissociated from atoms and molecules to produce ionospheric plasma. The ionosphere lower limit lies between altitudes of 50 to 70 km. The upper limit is undefined but generally fixed to 2000 km. The ionosphere is divided in 4 layers (D, E, F1 and F2) characterized by different electron concentrations increasing with altitude (Fig. 6.6). The sun leads to ionospheric variations over the 24 hour period between daytime and nighttime and over the 11-year cycle of solar activity. At night, the ions and electrons recombine. The D region and the distinction between the two daytime F regions (F1 and F2) disappears. Furthermore, there is a marked decrease in the maximum electron densities in the E and F2 regions by one to two orders of magnitude [*Andersen and Fuller-Rowell*, 1999]. For a sunspot minimum, electron densities are lower by a factor of up to four than at sunspot maximum, especially in the F region.

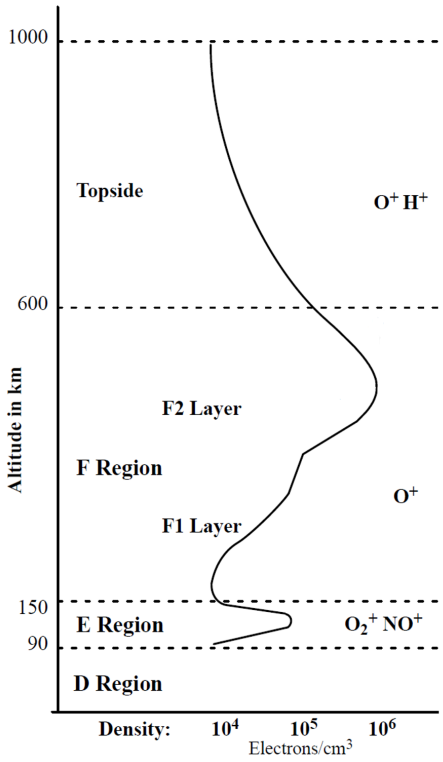

Figure 6.6: Different layers of the ionosphere with the predominant ion populations and electrons density. *after* [*Andersen and Fuller-Rowell*, 1999]

Aurora zone and electrojet

Particules coming from the magnetosphere through the magnetic field lines of the Earth strike the atmosphere at high speed producing ionization. The aurora regions are present

in both hemispheres at geomagnetic latitudes above 60°, and generally is characterized by its oval shape. The Aurora region is bounded by a particular current flowing in the E-region of the ionosphere, named auroral electrojet. There are different types of currents in the ionosphere that can be associated with an ionospheric conductivity tensor [*Mareschal*, 1986]. The Birkeland field-aligned currents [*Alfvén*, 1939] link the magnetosphere and the ionosphere in the auroral zone. They close in the ionosphere through the Pedersen currents and generate Hall currents (Fig. 6.7). These currents produce their own magnetic fields which combine with Earth's magnetic field. The Birkeland currents define two field-aligned current regions characterized as region 1 (high latitude side of the auroral zone) and region 2 (low latitude side) (Fig. 6.7).

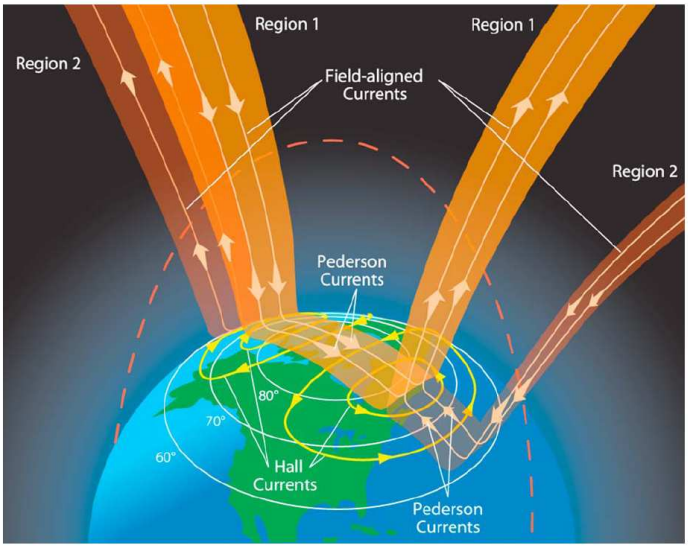

Figure 6.7: Schematic configuration of the Birkeland or field-aligned currents and the associated Pedersen (horizontal bars) and Hall (thin lines) currents. *from* [*Le et al.*, 2010]

The Hall currents in the auroral zone define the polar electrojet (PEJ). The currents are flowing westward in the dawnside of the auroral oval and eastward in its duskside [*Le et al.*, 2010] (Fig. 6.7). The shear zone where both electrojets meet, defines the Harang discontinuity, which occurs at approximately local geomagnetic midnight [*Koskinen et al.*, 1993]. The polar or auroral electrojet is latitudinally defined by the location of region 1/region 2 Birkeland currents. The electrojet central latitude can vary from 68° for quiet times to 58° under disturbed conditions at local midnight, with corresponding noon values ranging from 75° to 65°. Its width varies from 200 km to as much as 2000 km during highly disturbed times.

Sq currents

At mid—latitudes (geomagnetic latitudes below 50°) the major contributor to quasi-regular variations is the S_q (solar quiet) system (Fig. 6.8), which is mainly the result of the effects of atmospheric winds (thermospheric winds) displacing charged particles across geomagnetic field lines [*Mareschal*, 1986]. Electric fields and currents will be generated where ionospheric conductivity is large enough (in the dayside ionosphere). The currents are

concentrated in the ionosphere E−region. Furthermore, changes in thermospheric winds and composition will be related to geomagnetic storms.

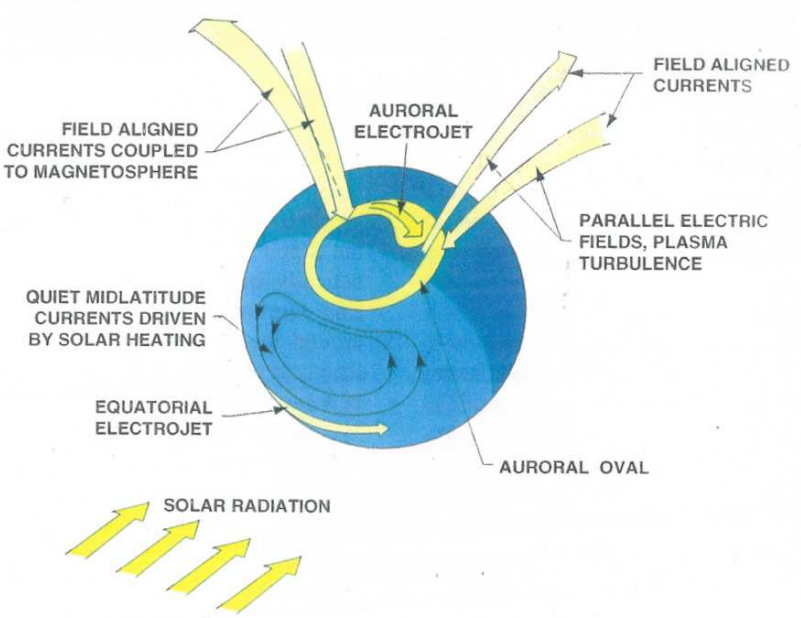

Figure 6.8: Ionospheric current systems. [*Maus*, 2006]

Equatorial electrojet

At low-latitudes, the existence of the daytime equatorial electrojet (EEJ) can essentially be explained by an extension of the Sq electric field to the equatorial regions (Fig. 6.8). In this region, an effective Cowling channel is created along the magnetic dip equator (Fig. 6.9) enhancing conductivity and currents in the E-region of the equatorial ionosphere [*Mareschal*, 1986]. The equatorial electrojet is centred on the magnetic dip equator, but varies in width and intensity with geographical location. Its typical width is around 700 km, with current densities regularly decreasing away from the equator.

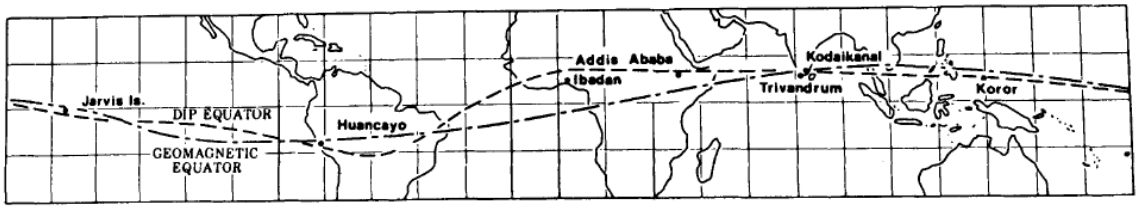

Figure 6.9: The magnetic dip equator loaction across the world. *from* [*Mareschal*, 1986]

6.3 LIGHTNING ACTIVITY

Lightning activity is characterized by cloud-to-ionosphere (sprites), intraclouds and clouds-to-ground electric discharges and are usually divided in two different frequency bands

ranging from 7.8 Hz to 1 kHz and 5 kHz to 30 kHz. The $1-5$ kHz gap in the amplitude spectrum characterizes the *AMT dead band* [*Garcia and Jones*, 2002]. Atmospherics or Sferics are defined as the impulse or wavelet characterizing the return-stroke of lightning. The cavity bounded by the Earth and the ionosphere becomes a waveguide for the propagation of sferics. The Earth–Ionosphere cavity enables electromagnetic resonances called Schumann resonances mainly excited by the lightning discharges. The fundamental mode of the Schumann resonance corresponds to 7.8 Hz [*Garcia and Jones*, 2002] and defines the upper limit of the MT dead band *Vozoff* [1991]. The Schumann resonance's fundamental mode and its multiples belong to the extremely low frequency (ELF) band of the Earth's EM spectrum, and produce characteristic peaks in the ELF responses. The very low frequency (VLF) emissions belong to the highest frequencies spectrum extending up to 30 kHz and covers lightning impulses (sferics) but also wavelets propagating through the magnetosphere and ionosphere [*Schmucker*, 1985]. When sferics travel away from the Earth, they undergo dispersion through the ionosphere and magnetosphere, before returning to the Earth along magnetic field lines. Those dispersed lightning impulses are observed at the Earth's surface as whistlers in the VLF spectrum [*Schmucker*, 1985].

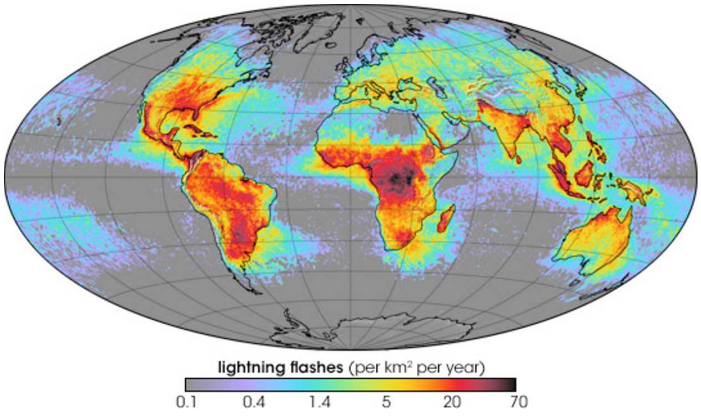

Figure 6.10: Lightning annual flash rates around the world. *from* [*NASA*]

The Sferics propagate from their lightning source in the Earth–Ionosphere waveguide with low attenuation which enables them to travel up to thousands of kilometres away from their source. Lightning flashes occurrence around the world varies between 100 to 1000 per second. The highest lightning activity is localized around the tropics (Fig. 6.10). During the day, sferics tend to be absorbed by the D layer of the ionosphere which disappears at night [*Garcia and Jones*, 2002]. Furthermore, lightning activity will vary from summer (high activity) to winter (low activity) in each hemisphere. Best recording times would then be during nighttime and during the summer months.

6.4 LOCALIZED SOURCE EFFECTS ON MAGNETOTELLURIC RESPONSES

Whereas at mid-latitudes non-homogeneous source effects on long period responses can still be compensated to obtain a quasi-homogeneous MT response, at high and low latitude, the localized currents in the ionosphere, intensified during enhanced magnetospheric activity, bring a non-homogeneous characteristic in the MT source [*Mareschal*, 1986]. The non-uniformity of the magnetic field fluctuations, associated with the com-

plex current systems that are the electrojets, does not agree with the plane assumption anymore. The natural MT sources are defined by really complex current systems and even if in most of the cases the plane wave assumption is correct, sometimes localized sources can lead to erroneous data interpretation. The effect of these sources on MT signal are only understood mainly through studies on source modelling (Tab. 6.2).

Table 6.2: Source field theory for a 1D layered Earth model reproduced from [*Jones and Spratt*, 2001]

Source field geometry	References
Uniform	[*Tikhonov*, 1950] [*Cagniard*, 1953]
Linear	[*Dmitriev and Berdichevsky*, 1979]
Wavenumber (repetitive in space)	[*Price*, 1962] [*Srivastava*, 1965]
Line current	[*Hermance and Peltier*, 1970]
Gaussian	[*Peltier and Hermance*, 1971]
Arbitrary	[*Hibbs and Jones*, 1976a,b]
Dipole	[*Osipova et al.*, 1989]
3D current system	[*Mareschal*, 1981] [*Viljanen et al.*, 1993, 1999] [*Pirjola*, 1998]
Moving Gaussian	[*Hermance*, 1978]

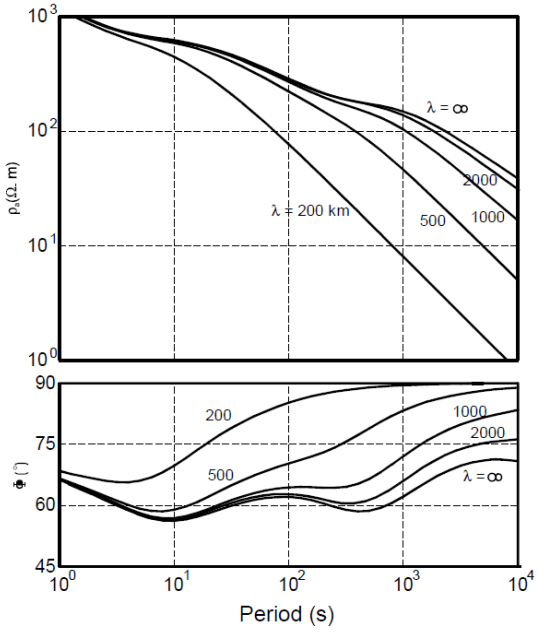

Figure 6.11: 1D apparent resisitivity and phase responses associated with a uniform source field and repetitive wavelength source fields of wavelengths of 2,000 km, 1,000 km, 500 km and 200 km. *from Jones and Spratt* [2001]

Jones and Spratt [2001] described the nature of the source field effect problem by comparing 1D MT responses for a uniform source with different repetitive wavelength source fields (Fig. 6.11), although in reality more complex source field geometry should be considered (Tab. 6.2). Figure 6.11 shows how a 1,000 km wavelength source, if interpreted as

a uniform source, would lead to erroneous interpretations of MT responses. *Viljanen et al.* [1999] highlighted that a more realistic 3D source field leads to more unpredictable effects that are highly location and period-dependent.

Padilha et al. [1997] showed that EEJ source effects, probably present within the $\pm 3^o$ zone [*Padilha*, 1999], would appear at longer periods in conductive regions than for resistive regions (Fig. 6.12). Furthermore, screening effects in the equatorial E-region generate a decrease in amplitude of the magnetic variations near the dip equator during nighttime, so daytime recordings will result in better responses [*Padilha et al.*, 1997; *Padilha*, 1999]. However, *Padilha et al.* [1997] mentioned that in the period band (0.001 to 2000 s) (Fig. 6.12), the MT responses measured are not distorted by the EEJ.

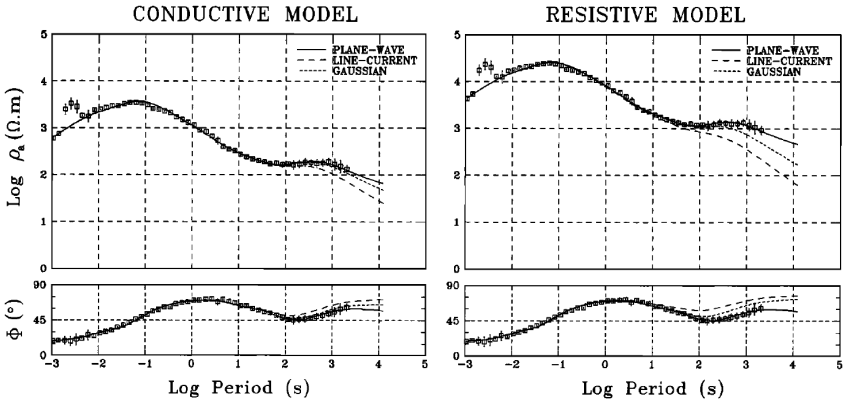

Figure 6.12: Daytime MT responses at one site associated with the most conductive (on the left) and the most resistive 1D models (on the right). For each models, the MT responses highlight different source assumptions: plane-wave (continuous line), gaussian-type electrojet fields (short-dashed line) and line-current-type electrojet fields (long-dashed line). *from* [*Padilha et al.*, 1997]

As highlighted by *Jones and Spratt* [2001], the local source distortion associated with the Polar electrojet can reduce the apparent resistivity and increases the phase values at longer periods (Fig. 6.13). This effect can then cause misinterpretation in the models, such as an underestimated LAB (lithosphere-asthenosphere boundary) depth (Fig. 6.13).

Differences between MT and GDS responses due to source field effects are presented by *Lezaeta et al.* [2007]. MT and GDS responses were measured in the auroral zone over different seasons and showed differences at periods over 4000 s that were associated to source field effects. Compared to MT responses, GDS responses highlighted significant variations in induction vectors following high geomagnetic activity. The study of *Lezaeta et al.* [2007] highlighted variations in the source morphology over the seasons for periods below half a day.

Electrojet effects on a 3D resistivity model response were modelled by *Carrasquilla and Rijo* [1998]. The results on MT responses showed that EEJ effects in MT data at low latitude regions cannot be ignored, but they only occur for periods higher than 10 s resulting in noisier data. Furthermore, the apparent resistivity values depend on the orientation of the principal direction of the 3D conductive structure relative to the direction of the EEJ. Model results from this study showed that the EEJ influence is more important in the host medium than in 3D bodies. The variation in the apparent resistivities were not large but

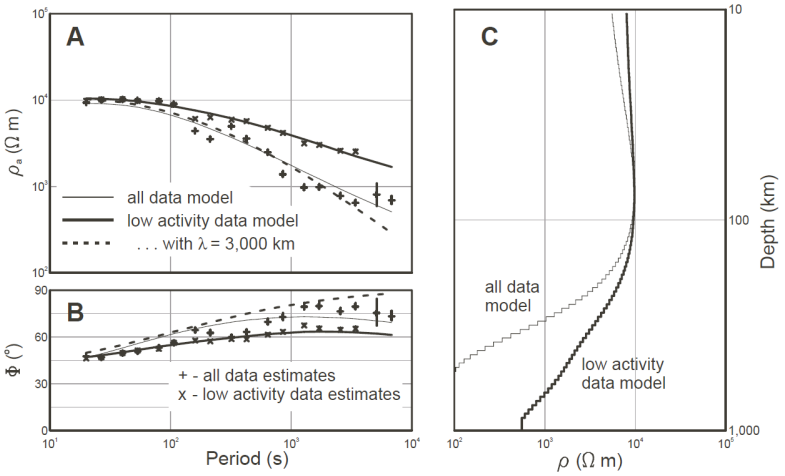

Figure 6.13: Source effect on averaged MT responses and their associated models; A - Observed apparent resistivity and model responses; B - Observed phase data and model responses; C - Associated 1D models. The dashed lines are the theoretical responses for the thick line model in (C) but with a source field with a wavelength of 3,000 km. *from Jones and Spratt* [2001]

the model considered was simple; what would be the EEJ effect on a more complex model or real Earth?

7 THE MAGNETOTELLURIC METHOD

7.1 ASSUMPTIONS

In order to apply electromagnetic (EM) induction to the Earth, the MT theory is based on a few simplifying assumptions [*Cagniard*, 1953; *Keller and Frischknecht*, 1966; *Simpson and Bahr*, 2005]:

- Maxwell's Equations 7.3, 7.4, 7.5 and 7.6 need to be satisfied.
- The EM energy is only dissipated or absorbed by the Earth. The Earth is not an EM source.
- Away from their sources, all fields are conservative and analytic.
- The natural EM source fields need to have been generated relatively far away from the Earth's surface. The fields can then be considered uniform, interacting with the Earth's surface as a plane-polarized wave with a near-vertical incidence. However, the plane wave assumption is not valid anymore for the polar and equatorial regions. This issue was discussed in the previous chapter.
- Although, a simple layered Earth (1D) does not allow accumulation of free charges, in a multi-dimensional Earth charges may accumulate along discontinuities, leading to a non-inductive phenomenon known as static shift.
- The Earth behave as an ohmic conductor ($\vec{j} = \sigma\vec{e}$) and the charge is conserved ($\nabla \cdot \vec{j} = 0$); $\vec{j}$ is the total electric current density ($A.m^{-2}$), σ is the conductivity of the medium ($S.m^{-1}$) and $\vec{e}$ is the electric field ($V.m^{-1}$).
- For the periods used in MT soundings, the quasi-static approximation is valid. The time-varying displacement currents are then neglected compared with the time-varying conduction currents. This approximation defines EM induction in the Earth as a pure diffusion process.
- In comparison with variations in rock conductivities, the electrical permittivities and magnetic permeabilities variations can be neglected. Those can then be respectively identified as ϵ_0 and μ_0.

In the plane wave assumption, the electric ($\vec{e}$) and the magnetic ($\vec{b}$) fields are defined as:

$$\vec{e} = \vec{e_0} e^{i(\omega t - kz)}, \tag{7.1}$$

$$\vec{b} = \vec{b_0} e^{i(\omega t - kz)}. \tag{7.2}$$

where, $\vec{e_0}$ and $\vec{b_0}$ represent the fields amplitude at the origin, ω the angular frequency defined as $\omega = 2\pi/T$ (with T the period), k the wave number defined as $|k| = 2\pi/\lambda$ (with λ the wave length).

Those equations highlight the time invariance of the exciting source in the plane wave assumption. Assuming that the conductivity of the Earth does not change with time at any given site, the impedance tensor calculated from the EM fields should be independent of the time the fields were recorded at. Furthermore, the plane wave assumption is not affected by the Earth's curvature for periods less than a day [*Srivastava*, 1965]. This means that the MT method can rely on a flat Earth model where the EM fields are expressed in Cartesian coordinates.

7.2 MAXWELL'S EQUATIONS

Maxwell united Ampere's and Faraday's work to write four equations that describe the behaviour of the EM fields at any frequency:

Gauss's law: The electric flux across a closed surface is proportional to the enclosed electric charge.

$$\nabla \cdot \vec{d} = q \tag{7.3}$$

Gauss's law for magmatism: There is no free magnetic charges or magnetic monopoles.

$$\nabla \cdot \vec{b} = 0 \tag{7.4}$$

Maxwell-Faraday equation (Faraday's law of induction): A time varying magnetic field will induce an electric current in a closed circuit. The fluctuations of the associated electric field are correlated with the magnetic field variations. The magnetic field or inducing field direction is defined by the circuit or loop axis.

$$\nabla \times \vec{e} = -\frac{\partial \vec{b}}{\partial t} \tag{7.5}$$

Ampere's circuital law (with Maxwell's correction): Any electric current in a closed circuit will produce a magnetic field whose magnitude depends on the current flow. Maxwell's correction of the law is characterized by the term $\frac{\partial \vec{d}}{\partial t}$, meaning that a time varying electric field will generate a magnetic field too. However, according to the quasi-static assumption in the MT theory, this term will be neglected from now on.

$$\nabla \times \vec{h} = \frac{\partial \vec{d}}{\partial t} + \vec{j} \tag{7.6}$$

In the Maxwell equations, $\vec{e}$ defines the electric field ($V.m^{-1}$), $\vec{d}$ the electric displacement ($C.m^{-2}$), $\vec{j}$ the current density ($A.m^{-2}$), $\vec{h}$ the magnetic field ($A.m^{-1}$), $\vec{b}$ the magnetic induction (Tesla) and q the electric charge density ($C.m^{-3}$).

According to the MT assumptions, we have those two simple relationships:

$$\vec{d} = \epsilon_0 \vec{e}, \tag{7.7}$$

$$\vec{b} = \mu_0 \vec{h}. \tag{7.8}$$

Therefore, the Maxwell's equations can then be rewritten as:

$$\nabla \cdot \vec{e} = q/\epsilon_0, \tag{7.9}$$

$$\nabla \cdot \vec{h} = 0, \tag{7.10}$$

$$\nabla \times \vec{e} = -\mu_0 \frac{\partial \vec{h}}{\partial t}, \tag{7.11}$$

$$\nabla \times \vec{h} = \sigma \vec{e}. \tag{7.12}$$

Taking the curl of Maxwell's equation 7.9 and 7.11 leads to the two following equations:

$$\nabla \times \nabla \times \vec{e} + \mu_0 \frac{\partial}{\partial t} \nabla \times \vec{h} = 0, \tag{7.13}$$

$$\nabla \times \nabla \times \vec{h} - \sigma \nabla \times \vec{e} = 0, \tag{7.14}$$

leading to the following relations:

$$\nabla \times \nabla \times \vec{e} + \mu_0 \sigma \frac{\partial \vec{e}}{\partial t} = 0, \tag{7.15}$$

$$\nabla \times \nabla \times \vec{h} + \mu_0 \sigma \frac{\partial \vec{h}}{\partial t} = 0. \tag{7.16}$$

For a vector $\vec{a}$, $\nabla \times \nabla \times \vec{a} = \nabla \cdot (\nabla \cdot \vec{a}) - \nabla^2 \vec{a}$. Considering Maxwell's Equation 7.10, it is quite straight forward to write $\nabla \times \nabla \times \vec{h} = -\nabla^2 \vec{h}$. However, for the electric field, it is a bit more complicated. Assuming no sources exist within the Earth, we saw previously that:

$$\nabla \cdot j = 0 = \nabla \cdot (\sigma \vec{e}) = \sigma \nabla \cdot \vec{e} + \vec{e} \nabla \sigma. \tag{7.17}$$

In theory, the Earth model can be reduced to a homogeneous medium where $\nabla \sigma = 0$, which leads to $\nabla \times \nabla \times \vec{e} = -\nabla^2 \vec{e}$. This consideration enables to simply the classic EM Equations 7.15 and 7.16 without a dramatic effect on their physical meaning. However, it is worth mentioning that in several cases $\nabla \cdot \vec{e} \neq 0$ and the associated σ heterogeneities will act as secondary sources, where free charges tend to accumulate.

For the homogeneous Earth, the EM diffusion equations characteristic of the MT method can then be expressed as:

$$\nabla^2 \vec{e} - \mu_0 \sigma \frac{\partial \vec{e}}{\partial t} = 0, \tag{7.18}$$

$$\nabla^2 \vec{h} - \mu_0 \sigma \frac{\partial \vec{h}}{\partial t} = 0. \tag{7.19}$$

However, the magnetic field $\vec{h}$ cannot be measured directly and only the magnetic induction $\vec{b} = \mu_0 \vec{h}$ is recorded in the field. The diffusion equations for $\vec{e}$ and $\vec{b}$ can then be rewritten as:

$$\nabla^2 \vec{e} - \mu_0 \sigma \frac{\partial \vec{e}}{\partial t} = 0, \tag{7.20}$$

$$\nabla^2 \vec{b} - \mu_0 \sigma \frac{\partial \vec{b}}{\partial t} = 0. \tag{7.21}$$

Assuming the Earth is an homogeneous half-space ($\frac{\partial \vec{e}}{\partial x} = \frac{\partial \vec{e}}{\partial y} = 0$), the solutions of the diffusion equations can be described as:

$$\vec{e}(t, z) = \vec{e}_1 e^{i(\omega t - kz)} + \vec{e}_2 e^{i(\omega t + kz)}, \tag{7.22}$$

$$\vec{b}(t, z) = \vec{b}_1 e^{i(\omega t - kz)} + \vec{b}_2 e^{i(\omega t + kz)}. \tag{7.23}$$

As the Earth is considered to generate no EM energy, $\vec{e}$ and $\vec{b}$ amplitudes cannot be increasing with depth: $\vec{e}_2 = 0$ and $\vec{b}_2 = 0$. In the frequency domain, the electric field and the magnetic induction then become:

$$\vec{E}(w,z) = \int_{-\infty}^{+\infty} e^{i\omega t}\vec{e}_1 e^{i(\omega t - kz)}\, dt, \tag{7.24}$$

$$\vec{B}(w,z) = \int_{-\infty}^{+\infty} e^{i\omega t}\vec{b}_1 e^{i(\omega t - kz)}\, dt. \tag{7.25}$$

The EM fields are described as time dependent harmonic functions (Eq. 7.1 and 7.2) therefore in the frequency domain Equations 7.18 and 7.19 are written as:

$$\nabla^2\vec{E} = i\omega\mu_0\sigma\vec{E}, \tag{7.26}$$

$$\nabla^2\vec{B} = i\omega\mu_0\sigma\vec{B}. \tag{7.27}$$

7.3 BOUNDARY CONDITIONS

When applying the EM equations to model the Earth, the consideration of the basic boundary conditions at the interface between a medium 1 and a medium 2 are essential.

- The normal component of the magnetic induction b_n is continuous at the interface between the two mediums.
$$b_{n1} = b_{n2}. \tag{7.28}$$
- The normal component of the electric displacement d_n is discontinuous at the interface, due to the accumulation of charges on the interface surface, characterized as ρ_s.
$$d_{n1} - d_{n2} = \rho_s. \tag{7.29}$$
- The normal component of the current density j_n is continuous across the interface between the two media. However, this is valid only in the diffusion domain. The relation is not valid anymore when considering the global component of the current density which include the displacement currents.
$$j_{n1} = j_{n2}. \tag{7.30}$$
- The tangential component of the electric field e_t is continuous across the interface.
$$e_{t1} = e_{t2}. \tag{7.31}$$
- The tangential component of the magnetic field h_t can be considered continuous across the interface too.
$$h_{t1} = h_{t2}. \tag{7.32}$$

7.4 TRANSFER FUNCTION AND PENETRATION DEPTH

By combining Equations 7.24, 7.25, 7.26 and 7.27, the following Helmholtz-type relations are defined:

$$\nabla^2\vec{E} + k^2\vec{E} = 0, \tag{7.33}$$

$$\nabla^2\vec{B} + k^2\vec{B} = 0. \tag{7.34}$$

where $k = \sqrt{-i\omega\mu_0\sigma}$ is the wave number.

However in MT, a factor q is usually defined as:

$$q = \sqrt{i\omega\mu_0\sigma} = ik, \tag{7.35}$$

such that:

$$\vec{e}(t,z) = \vec{e}_1 e^{i\omega t - qz}, \tag{7.36}$$

$$\vec{b}(t,z) = \vec{b}_1 e^{i\omega t - qz}. \tag{7.37}$$

This factor q can be rewritten as:

$$q = \sqrt{i\omega\mu_0\sigma} = \sqrt{i}\sqrt{\omega\mu_0\sigma} = \frac{(1+i)}{\sqrt{2}}\sqrt{\omega\mu_0\sigma} = \left(\sqrt{\frac{\omega\mu_0\sigma}{2}} + i\sqrt{\frac{\omega\mu_0\sigma}{2}}\right). \tag{7.38}$$

The *Schumcker-Weidelt transfer function* [*Weidelt*, 1972; *Schmucker*, 1973] C refers to the inverse of q:

$$C = \frac{1}{q}. \tag{7.39}$$

For an homogeneous half-space, the real and imaginary part of the C function are equal.

Considering Equations 7.33 and 7.36, in the frequency domain we can write:

$$\frac{\partial E_x}{\partial z} = -qE_x, \tag{7.40}$$

$$\frac{\partial E_y}{\partial z} = -qE_y. \tag{7.41}$$

Furthermore, the Maxwell-Faraday's Equation 7.5 brings the following relations:

$$\frac{\partial E_x}{\partial z} = -i\omega B_y, \tag{7.42}$$

$$\frac{\partial E_y}{\partial z} = i\omega B_x. \tag{7.43}$$

From Equations 7.40, 7.41, 7.42, 7.43 and 7.39, the C *transfer function* can then be expressed as:

$$C = \frac{E_x}{i\omega B_y} = -\frac{E_y}{i\omega B_x}. \tag{7.44}$$

Equation 7.44 highlights the basics of MT theory: how the electric field characterizes a predictable output in a linear system, where the magnetic field or input interacts with the Earth model through the *transfer function* C.

The transfer function, characteristic of the Earth model, can be directly linked to the resistivity ρ of an homogeneous half-space such that:

$$\rho = \frac{1}{\sigma} = \frac{\mu_0 \omega}{|q|^2} = |C|^2 \mu_0 \omega. \tag{7.45}$$

Furthermore, the *penetration depth* δ or *electromagnetic skin depth* is defined as:

$$\delta = \frac{1}{\mathrm{Re}(q)} = \sqrt{\frac{2}{\omega \mu_0 \sigma}}. \tag{7.46}$$

In order to understand the meaning of the *skin depth*, Equation 7.36 can be rewritten using the Equations 7.38 and 7.46:

$$\vec{e}(t,z) = e^{-z/\delta} \vec{e}_1 e^{i(\omega t - (\sqrt{\omega \mu_0 \sigma/2})z)}. \tag{7.47}$$

Whereas the term $e^{i(\omega t - (\sqrt{\omega \mu_0 \sigma/2})z)}$ is representative of the wave form, the term $e^{-z/\delta}$ highlights the attenuation on the wave amplitude. Therefore, Equation 7.47 shows how the *skin depth* defines the depth where the EM wave amplitude has been attenuated in a homogeneous half-space to $1/e$ of its original amplitude ($\simeq 37\%$).

The EM wave attenuation with depth can also be associated to the *Niblett-Bostick penetration depth approximation* [*Jones*, 1983b] defined as:

$$p = \sqrt{\frac{1}{\omega \mu_0 \sigma}}, \tag{7.48}$$

and representing the depth where the EM amplitude has been reduced to $e^{-1/\sqrt{2}}$ ($\simeq$ 50%) of its original value.

7.5 APPARENT RESISTIVITY AND PHASE

Although the Earth is a more complex model than a simple homogeneous half-space, for each period T, the Earth model can be identified to an equivalent half-space model characterized by the apparent resistivity ρ_a. This concept is representative of the one dimensional (1D) layered Earth model approximation. The apparent resistivity characterizes the average resistivity of an equivalent half-space at the period T (with $\omega = 2\pi/T$). From Equation 7.45, the apparent resistivity can then be defined as:

$$\rho_a(\omega) = |C(\omega)|^2 \mu_0 \omega, \tag{7.49}$$

where $C(\omega)$ is the transfer function corresponding to the equivalent homogeneous half-space at the period T.
A phase ϕ can also be derived from the complex transfer function $C(\omega)$ such that:

$$\phi(\omega) = \tan^{-1}\left(\frac{\mathrm{Im}(C(\omega))}{\mathrm{Re}(C(\omega))}\right). \tag{7.50}$$

The apparent resistivity ρ_a and the phase ϕ are linked entities that can be predicted from each other via the Kramers-Kroening relationship [*Weidelt*, 1972]:

$$\phi(\omega) = \frac{\pi}{4} - \frac{\omega}{\pi} \int_0^{+\infty} \log \frac{\rho_a(x)}{\rho_0(x^2 - \omega^2)} \, dx, \tag{7.51}$$

where ρ_0 represents the high-frequency asymptotic value of $\rho_a(\omega)$. This relation can be approximated [*Weidelt*, 1972; *Kunetz*, 1972] to:

$$\phi(\omega) \simeq \frac{\pi}{4}(1 + \frac{\partial \log(\rho_a(\omega))}{\partial \log(\omega)}). \tag{7.52}$$

The Kramers-Kroening relationship clearly highlights how the phase return to a 45° ($\pi/4$) value, characteristic of an homogeneous half-space, when assuming the apparent resistivity tend to an asymptotic constant for low frequencies.

The skin depth δ (Eq. 7.46) and approximate penetration depth p (Eq. 7.48) can be redefined in function of the apparent resistivity such that:

$$\delta = \sqrt{\frac{T\rho_a}{\pi\mu_0}} \simeq 500\sqrt{T\rho_a}. \tag{7.53}$$

$$p = \sqrt{\frac{T\rho_a}{2\pi\mu_0}}. \tag{7.54}$$

Although less accurate than for 1D problems, those relations can still be used as a primary penetration depth approximation in 2D and 3D situations.

7.6 IMPEDANCE TENSOR

The MT transfer function describes the direct linear relationship between the measured horizontal components of the EM fields. It is defined as an *impedance tensor* $\mathbf{Z}$ characterizing the electrical properties of the Earth for a 3D Earth model.

$$\mathbf{Z} = \begin{pmatrix} Z_{xx} & Z_{xy} \\ Z_{yx} & Z_{yy} \end{pmatrix} \tag{7.55}$$

The impedance tensor $\mathbf{Z}$ links the horizontal components of the electric and magnetic fields in the following relationship:

$$\begin{pmatrix} E_x(\omega) \\ E_y(\omega) \end{pmatrix} = \begin{pmatrix} Z_{xx}(\omega) & Z_{xy}(\omega) \\ Z_{yx}(\omega) & Z_{yy}(\omega) \end{pmatrix} \begin{pmatrix} \frac{B_x(\omega)}{\mu_0} \\ \frac{B_y(\omega)}{\mu_0} \end{pmatrix} = \begin{pmatrix} Z_{xx}(\omega) & Z_{xy}(\omega) \\ Z_{yx}(\omega) & Z_{yy}(\omega) \end{pmatrix} \begin{pmatrix} H_x(\omega) \\ H_y(\omega) \end{pmatrix}. \tag{7.56}$$

The impedance tensor $\mathbf{Z}$ is complex and by analogy with the Schmucker-Weidelt transfer function (Eq. 7.49 and 7.50), it can be associated to the apparent resistivity and phase.

$$\rho_{a,ij}(\omega) = \frac{1}{\mu_0\omega}|Z_{ij}(\omega)|^2 \tag{7.57}$$

$$\phi_{ij}(\omega) = \tan^{-1}(\frac{Im(Z_{ij}(\omega))}{Re(Z_{ij}(\omega))}) \tag{7.58}$$

As an alternative, *Weaver et al.* [2000] defines the MT tensor $\mathbf{M}$ by considering the magnetic induction $\vec{B}$ instead of the magnetic field $\vec{H}$.

$$\begin{pmatrix} E_x(\omega) \\ E_y(\omega) \end{pmatrix} = \begin{pmatrix} M_{xx}(\omega) & M_{xy}(\omega) \\ M_{yx}(\omega) & M_{yy}(\omega) \end{pmatrix} \begin{pmatrix} B_x(\omega) \\ B_y(\omega) \end{pmatrix} \tag{7.59}$$

7.7 GEOMAGNETIC TRANSFER FUNCTION

The geomagnetic transfer function or tipper vector characterizes the linear relationship between the vertical component and the horizontal components of the magnetic field.

$$H_z(\omega) = \begin{pmatrix} T_x(\omega) & T_y(\omega) \end{pmatrix} \begin{pmatrix} \frac{B_x(\omega)}{\mu_0} \\ \frac{B_y(\omega)}{\mu_0} \end{pmatrix} = \begin{pmatrix} T_x(\omega) & T_y(\omega) \end{pmatrix} \begin{pmatrix} H_x \\ H_y \end{pmatrix} \tag{7.60}$$

As for the impedance tensor $\mathbf{Z}$, the tipper vector $\vec{T}$ is complex. The geomagnetic transfer function is usually represented by the real and imaginary induction arrows defined on the xy plane as:

$$\vec{T}_{Re}(\omega) = \begin{pmatrix} Re(T_x(\omega)) & Re(T_y(\omega)) \end{pmatrix}, \tag{7.61}$$

$$\vec{T}_{Im}(\omega) = \begin{pmatrix} Im(T_x(\omega)) & Im(T_y(\omega)) \end{pmatrix}. \tag{7.62}$$

The vertical magnetic field amplitude increases with lateral resistivity gradients [*Jones and Price*, 1970; *Jones*, 1986; *Simpson and Bahr*, 2005]. The real induction arrows usually indicate significant lateral contrasts in the resistivity, by pointing towards (**Parkinson's convention** [*Parkinson*, 1959]) or away from (**Wiese's convention** [*Wiese*, 1962]) the anomalous current concentration characterized by the presence of a conductive anomaly. The Parkinson's convention, pointing towards the conductive anomalies, is usually preferred when mapping induction arrows [*Jones*, 1986; *Simpson and Bahr*, 2005].

7.8 DIMENSIONALITY CONCEPTS

In MT data analysis, it is important to assess the right dimensionality of the subsurface in order to avoid erroneous interpretations. Some parameters such as the *Swift skew* [*Swift*, 1967] or the *Impedance polar diagrams* [*Vozoff*, 1991] can be considered to determine the dimensionality of the data at different frequencies. However as mentioned by [*Jones*, 2012], those dimensionality tools are amplitude-based and can then be severely affected by distortion. However, as presented later, other tools can provide a more robust estimation of the dimensionality of the data.

7.8.1 *1D Earth*

In the 1D Earth model or layered Earth model, the conductivity only varies with depth. The diagonal elements of the impedance tensor $\mathbf{Z}$ are zero. The absolute values of the off-diagonal elements are equal as there is no lateral variations in the conductivity:

$$\mathbf{Z_{1D}} = \begin{pmatrix} 0 & Z_{xy} \\ Z_{yx} & 0 \end{pmatrix}, \tag{7.63}$$

with:

$$Z_{xy} = -Z_{yx}. \tag{7.64}$$

The analogy with the *Schmucker-Weidelt* transfer function (Eq. 7.39, 7.49 and 7.50) brings the following relations:

$$Z_{1D} = Z_{xy} = -Z_{yx} = i\mu_0\omega C, \tag{7.65}$$

$$\rho_{a_{1D}}(\omega) = \frac{1}{\mu_0\omega}|Z_{xy}(\omega)|^2 = \frac{1}{\mu_0\omega}|-Z_{yx}(\omega)|^2 = \mu_0\omega|C(\omega)|^2, \tag{7.66}$$

$$\phi_{1D}(\omega) = \tan^{-1}\left(\frac{Im(Z_{xy}(\omega))}{Re(Z_{xy}(\omega))}\right) = \tan^{-1}\left(\frac{Im(-Z_{yx}(\omega))}{Re(-Z_{yx}(\omega))}\right) = \tan^{-1}\left(\frac{Im(C(\omega))}{Re(C(\omega))}\right). \tag{7.67}$$

Assuming that the MT data are error and noise free, and sampled continuously at all frequencies, the 1D MT inverse problem has a unique solution [*Tikhonov*, 1965; *Bailey*, 1970].

7.8.2 *2D Earth*

In a layered Earth model, lateral variations in one single direction, such as a vertical contact between two zones of different conductivity (Fig. 7.1), define the 2D Earth. The orientation of such contact is identified as the geolelectric strike or strike direction. In an ideal 2D case, any MT data can be rotated around a vertical axis to a certain angle θ (strike azimuth) where the diagonal elements of the impedance tensor become null. The impedance tensor is then described as:

$$\mathbf{Z_{2D}} = \mathbf{R}\mathbf{Z_{obs}}\mathbf{R}^T = \begin{pmatrix} 0 & Z_{xy} \\ Z_{yx} & 0 \end{pmatrix} = \begin{pmatrix} 0 & Z_{\parallel} \\ Z_{\perp} & 0 \end{pmatrix} = \begin{pmatrix} 0 & Z_{TE} \\ Z_{TM} & 0 \end{pmatrix}, \tag{7.68}$$

with $Z_{xy} \neq -Z_{yx}$ and $\mathbf{R} = \begin{pmatrix} \cos(\theta) & \sin(\theta) \\ -\sin(\theta) & \cos(\theta) \end{pmatrix}$ the rotation matrix.

The strike azimuth defines a new coordinate system (x,y,z) where the off-diagonal elements of the impedance tensor characterize electric currents either parallel (along-strike E_x component) or perpendicular (across-strike E_y and E_z components) to the strike direction. Therefore, the Maxwell equations can be decoupled into two modes: the Transverse Electric (TE) or E-polarisation mode and the Transverse Magnetic (TM) or B-polarisation mode. By definition, in a 2D situation the resistivity and the fields do not vary along the strike direction ($\frac{\partial}{\partial x} = 0$). The two polarisations are then described by the following equations [*Simpson and Bahr*, 2005]:

TE mode (E_x,B_y,B_z):

$$\begin{aligned} \frac{\partial E_x}{\partial y} &= i\omega B_z, \\ \frac{\partial E_x}{\partial z} &= -i\omega B_y, \\ \frac{\partial B_z}{\partial y} - \frac{\partial B_y}{\partial z} &= \mu_0\sigma E_x, \end{aligned} \tag{7.69}$$

TM mode (E_y,E_z,B_x):

$$\begin{aligned} \frac{\partial B_x}{\partial y} &= \mu_0 \sigma E_z, \\ -\frac{\partial B_x}{\partial z} &= \mu_0 \sigma E_y, \\ \frac{\partial E_z}{\partial y} - \frac{\partial E_y}{\partial z} &= -i\omega B_x. \end{aligned} \tag{7.70}$$

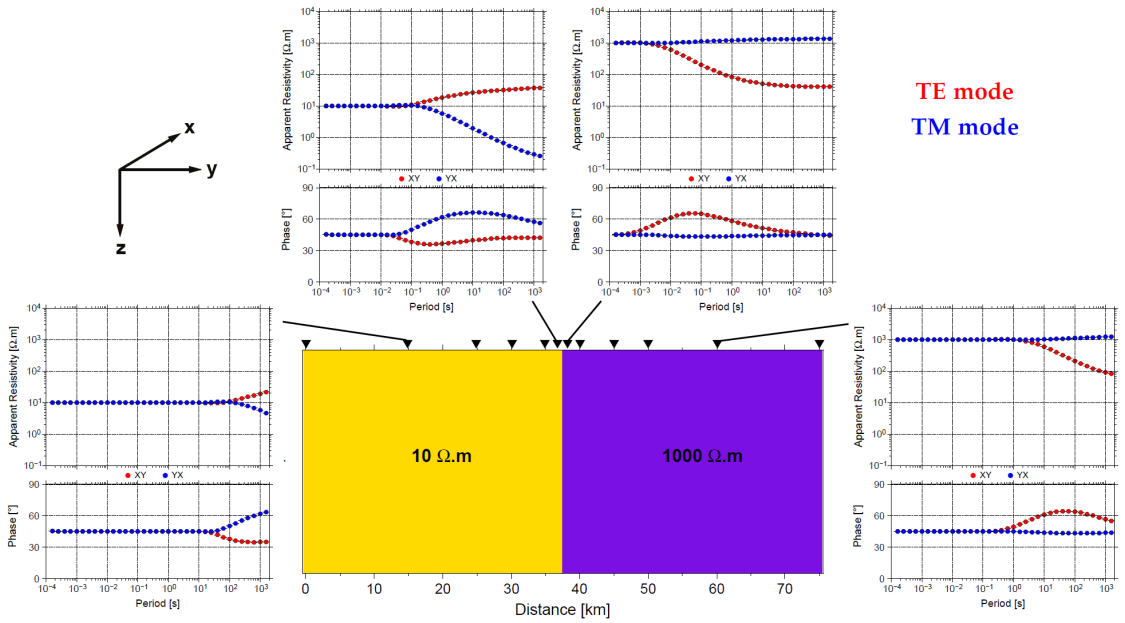

Figure 7.1: MT responses associated with a sharp 2D resistivity transition.

One can notice that the vertical magnetic field in only associated with the TE mode. In the 2D case, the relation between the vertical and horizontal components of the magnetic field (Eq. 7.60) will be simplified to the following expression [*Vozoff*, 1991]:

$$H_z = T_y H_y. \tag{7.71}$$

Figure 7.1 shows an example of a 2D contact and the associated behaviour of the TE and TM modes responses depending on the recording distance from the vertical contact. For two sites located on each side of the contact, the TE mode responses tend to the same values at longer periods (Fig. 7.1): the TE mode is continuous through the contact. On the contrary, the TM mode is discontinuous across the resistivity sharp transition. Those particularities are the direct illustration of the EM boundary conditions discussed previously. At the shortest periods, the two modes are not dissociated as they both sense a simple half-space characterized by a 45° phase. As the distance of the recording stations from the 2D contact increases, the split between the two modes will occur for longer periods (Fig.

7.1).

Quasi 2D Approach

One common approach is to approximate the Earth as a combination of a regional 2D structure including embedded small-to-medium scale 3D bodies. This quasi 2D configuration is particularly appropriate in geological setting where the MT transect crosses large scale fault or sutures. Such approximation is mainly dependent on the lateral extend of the pseudo 3D structures along strike, their conductivity and the associated skin depth at the period of interest [*Jones*, 1983a]. In those quasi 2D situations, the rotation of the impedance tensor $\mathbf{Z_{obs}}$ to the strike azimuth coordinate system (often in agreement with the surface geology) will minimize the tensor diagonal elements to a negligible level. However, distortion apart, the quasi 2D assumption could lead to erroneous interpretations resulting from the presence of artefacts associated to 3D effects. The 3D effects affecting the TM and TE modes in function of the orientation of the 3D structures relatively to the 2D regional strike direction have been discussed in *Ledo* [2006]. Furthermore, *Berdichevsky* [1999] highlighted that the TM mode is more affected by 3D effects related to resistive structures whereas the TE mode will be more affected by 3D effects associated with conductive structures. The distortion effects of near-surface small scale 3D bodies and their removal are discussed in the following distortion section.

7.8.3 *3D Earth*

When the conductivity changes in all three directions with depth on a regional scale, the MT impedance tensor can no longer be simplified by rotation: the Earth is 3D. Therefore, the TE and TM modes discussed above are not valid in the 3D Earth. The impedance tensor $\mathbf{Z}$ is then characterized in its general form (Eq. 7.55) by 8 unknown parameters (real and imaginary parts of the four elements tensor) at each frequencies.

7.8.4 *Anisotropy*

Situations where electrical anisotropy may be observed in magnetotelluric surveys has been presented previously in the *Electrical properties of the Earth*'s chapter. For the anisotropic problem, the resistivity (or conductivity) usually considered to be a scalar becomes a symmetric and positive-definite tensor [*Weidelt*, 1999]. The resistivity tensor $\boldsymbol{\rho}$ can be simplified to a diagonal matrix following a combination of rotations (Eq. 7.72 and Fig. 7.2) [*Pek and Verner*, 1997; *Pek and Santos*, 2002]:

$$\boldsymbol{\rho} = \begin{pmatrix} \rho_{xx} & \rho_{xy} & \rho_{xz} \\ \rho_{yx} & \rho_{yy} & \rho_{yz} \\ \rho_{zx} & \rho_{zy} & \rho_{zz} \end{pmatrix} = \mathbf{R}_{\mathbf{z}}^{\mathsf{T}}(\alpha_S)\mathbf{R}_{\mathbf{x}'}^{\mathsf{T}}(\alpha_D)\mathbf{R}_{\mathbf{z}'}^{\mathsf{T}}(\alpha_L) \begin{pmatrix} \rho_1 & 0 & 0 \\ 0 & \rho_2 & 0 \\ 0 & 0 & \rho_3 \end{pmatrix} \mathbf{R}_{\mathbf{z}'}(\alpha_L)\mathbf{R}_{\mathbf{x}'}(\alpha_D)\mathbf{R}_{\mathbf{z}}(\alpha_S), \tag{7.72}$$

with $\mathbf{R_z}(\alpha_S)$, $\mathbf{R_{x'}}(\alpha_D)$ and $\mathbf{R^T_{z'}}(\alpha_L)$ the rotation matrices respectively associated with the strike, the dip and the slant angles (Fig. 7.2).

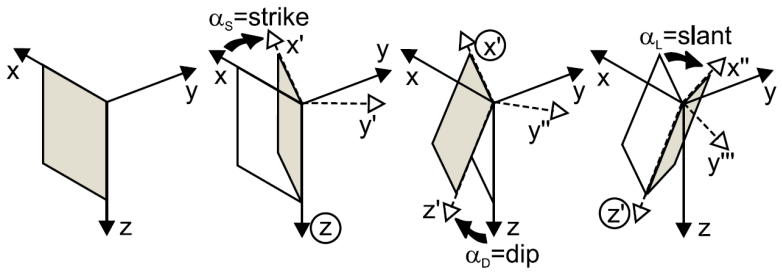

Figure 7.2: Anisotropy parameters associated with the general orientation of a thin conductive dike. *from Pek and Santos* [2002]

By definition the MT method is only associated to the horizontal components of the primary current induced in the Earth. Therefore, the anisotropy parameters cannot be fully recovered but rather their projection onto an horizontal plane [*Heise et al.*, 2006]. Furthermore, the MT method is sensitive to the conductivity of a volume whose resolution will decrease with depth and it cannot distinguish microscopic anisotropy from macroscopic anisotropy [*Weidelt*, 1999; *Wannamaker*, 2005]. Therefore, the resistivity tensor will only represent the effective bulk resistivity of a particular volume [*Heise et al.*, 2006].

What are the effects of anisotropy on the MT responses?

Figure 7.3 presents an example of anisotropic responses for a simple 1D case. The xx and yy components of the MT response are null. Whereas the yx component is constant over the periods (no conductivity changes in this polarization), the xy component of the MT response reveals the vertical transitions between 1000 Ω.m and 20 Ω.m layers [*Heise et al.*, 2006]. A 1D anisotropic model will likely generate responses which could equally fit a 2D isotropic model (Fig. 7.3). The main difference would come from taking into consideration the magnetic transfer function, which is null in the 1D case [*Martí*, 2012]. It is also worth to check for consistency in the MT responses between different sites in a survey [*Martí et al.*, 2010]. Therefore, in some situations the combination of the spatial uniformity in the responses and the absence of induction vectors at longer periods may reveal the presence of an anisotropic layer at depth. Unfortunately, such conclusion is not straightforward as in most cases overlying 2D and 3D structures will likely increase the ambiguity between anisotropic and isotropic 2D, 3D bodies [*Heise et al.*, 2006]. Furthermore, as pointed out by *Heise et al.* [2006] phase splits will identify lateral and vertical conductivity gradients (Fig. 7.3) but may not necessarily characterize anisotropy.

In situations of strong anisotropy, *Martí* [2012] mentioned that phases out of quadrant (> 90°) but also apparent contradictions between the induction arrows and the structural strike should be expected. [*Heise and Pous*, 2003] presented how anisotropy could lead to phase out of quadrant in the MT responses and mentioned situations involving high

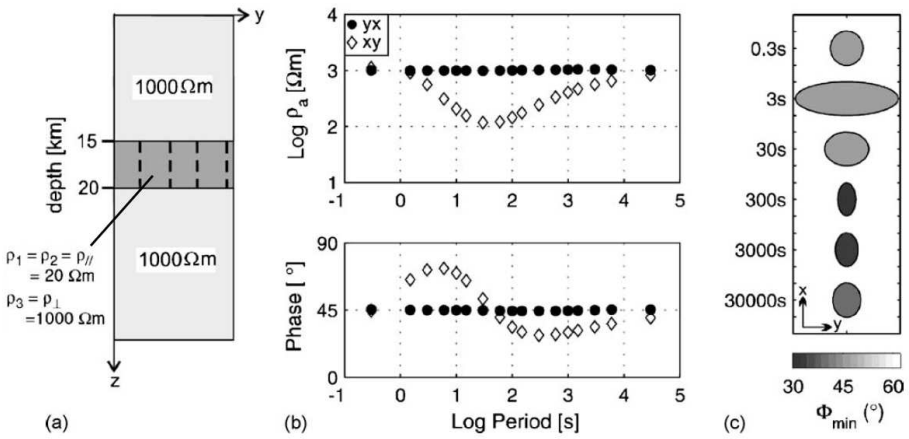

Figure 7.3: a) 1D model including an anisotropic layer. b) xy and yx apparent resistivities and phases. c) Phase tensor ellipses at different periods. *modified from Heise et al.* [2006]

anisotropy ratios or high differences between the anisotropy strike azimuth. Furthermore, the presence of different anisotropy strikes could lead to quasi 3D situations where the impedance tensor is not diagonalizable for some periods and the Maxwell equations cannot be decoupled [*Martí*, 2012].

Martí [2012] highlighted that the conductivity tensor involves such a number of parameters that the MT responses may not even fully characterize the resistivity tensor, expending the non-uniqueness of the inverse problem. For example, *Jones* [2006] presented two 2D models, one isotropic and the other one anisotropic, both generating the same MT responses. In the same paper, the author also mentioned how an upper anisotropic layer could act as a polarizing filter such that only one of the two 2D mode would penetrate through it, inhibiting the 2D structural resolution of the lower layers.

7.8.5 *Impedance Invariants*

In order to identify the impedance tensor dimensionality, [*Weaver et al.*, 2000] presented a way to characterize the MT tensor $\mathbf{M}$ (Eq. 7.59) with seven independent parameters invariant under rotation of the reference system. They are defined as the WAL invariants. *Martí et al.* [2010] extended the WAL dimensionality criteria to distinguish anisotropic media from 2D isotropic media.

Furthermore, it is worth mentioning two particular rotational invariants that are commonly considered. Those are the Berdichevsky average, Z_B [*Berdichevsky and Dimitriev*, 1976a] and the determinant average Z_{det}, the square root of the impedance tensor's determinant.

$$Z_B = \frac{Z_{xy} - Z_{yx}}{2} \tag{7.73}$$

$$Z_{det} = Z_{xx}Z_{yy} - Z_{xy}Z_{yx} \tag{7.74}$$

One major advantage in considering those two parameters is that not only they characterize meaningful averages of the impedance tensor but they are also independent on the regional strike direction. *Pedersen and Engels* [2005] presented the 2D inversion of the

impedance determinant in order to include information from the diagonal elements. This method has some advantages, particularly when the strike direction is expected to vary significantly with depth or along the profile. However, such method must be considered with care.

7.9 DATA ACQUISITION AND PROCESSING

7.9.1 *Magnetotelluric Data Acquisition*

Good overviews on the MT fieldwork procedures and associated instrumentation can be found in *Simpson and Bahr* [2005] and *Ferguson* [2012]. The MT sites should be located as far as possible from any source of electromagnetic (EM) noise. Although, the MT recording equipments and processing methods have improved, high level of EM noise will degrade the responses. The main sources of artificial EM noise usually include power lines, railways, pipelines and electric fences. Furthermore, any apparent geological perturbation such as swamps, saline aquifers, salt lakes, topography and coastlines that could affected the responses need also to be taken into account when choosing sites locations.

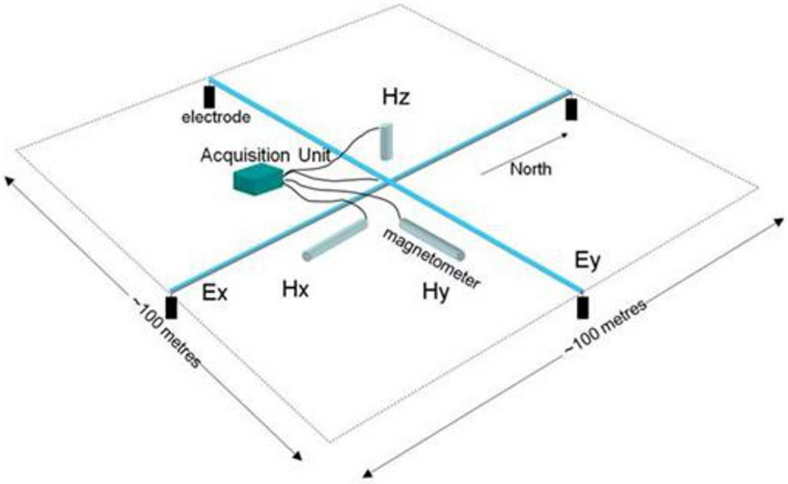

Figure 7.4: Typical layout for a BBMT site. *from Moombarriga Geoscience*

For natural-source land MT surveys, there are three different categories of MT recording systems, each of them covering different period ranges. The long-period magnetotelluric (LMT) instruments will usually be used to record data from 1s to >10000s. The broadband MT (BBMT) instruments will measure data over periods of 0.001s to 1000s. Audio-frequency MT (AMT) instruments will cover the period band of 0.0001s to 1s. For each systems, the electric field horizontal components are measured with four electrodes defining two electric dipoles (usually 100m long) that are orientated along the geographic north-south and east-west directions (Fig. 7.4). A ground electrode is also placed near the intersection of the two dipole lines. With the LMT system, the magnetic field components are measured with a fluxgate magnetometer. For the BBMT and AMT instruments, the magnetic components are recorded using induction coil sensors whose size will vary with the instruments (BBMT system uses longer coil sensors). The common station layout of a broadband MT station can be seen on Figure 7.4. The magnetometers needs to be placed

few meters away from the electric lines (E-lines) in order to minimize inductive coupling. The induction coil sensors are aligned with respect to the E-lines orientations (horizontal sensors only) and need to be levelled (all sensors). The AMT and LMT instruments will have a similar layout. For the AMT system, the E-lines may be shorter, whereas for the LMT system, all magnetic components are recorded by one single fluxgate magnetometer which is placed in one of the quadrants (preferably not the same as the acquisition unit) defined by the E-lines.

Usually, to lower the contact resistance and to enhance the electrodes moist, each electrode is placed slightly tilted in a bucket filled with mud made from local soil and salt water if using Ag-AgCl electrodes ($CuSO_4$ solutions if using $Cu - CuSO_4$ electrodes). The bucket containing the electrode is then completely buried. The magnetic sensors and the acquisition unit are also usually buried in order to protect them from human and animal interference, avoid noise from the wind and to minimize temperature effects. Burying the equipment is particularly important if the instruments will stay on site for more than a day (BBMT and LMT surveys). For the same reasons as the sensors, it is also worth burying the cables during long period recordings.

Before starting the survey, the magnetometers need to be calibrated. For BBMT and AMT induction coil sensors, it is necessary to conduct a frequency-dependent calibration. However the LMT system response can be considered frequency-independent and the calibration can be done from a simple DC response. The noise and the quality of the contact at the electrodes is usually evaluated by simple DC measurements of the voltage and resistance between each electrodes and the ground electrode before starting recording.

The fluctuations of H_x, H_y, H_z, E_x and E_y are recorded as a set of time series whose sampling rate will vary with the system used. The recording times can vary from hours to weeks, depending on the period range investigated but also on the local noise as in such situations longer records will lead to more robust estimates of the transfer functions.

In practice, all MT stations are not recorded simultaneously. This is mainly due to the time necessary to lay out each stations, the accessibility of the sites and of course it also depends on the number of instruments available. Stations are moved along the profile over the recording time necessary to complete the transect. BBMT stations are usually left 3 to 6 days in the ground. LMT stations have to be left in the ground for at least a week, but usually 2 to 3 weeks of data are recorded in order to get more robust estimates at the longer periods.

INDEPTH III: In April-June 1999, MT data were collected in northern Tibet along the Lhasa-Golmud highway as part of INDEPTH III. The resulting 600 profile consists on 19 long-period magnetotelluric (LMT) and 35 broadband magnetotelluric (BBMT) stations. The LMT data were recorded with the LIMS instruments developed by the *Geological Survey of Canada*. The broadband MT data were acquired with two Electromagnetic Instruments Incorporated (EMI)MT-24 systems [*Unsworth et al.*, 2004]. Stations were deployed every 15 km in average for the BBMT sites and every 25 km for the LMT sites. The stations were laid out following the classic MT configuration presented on Figure 7.4. INDEPTH III data were recorded during the solar cycle 23 when the sun activity was quite strong (Fig. 7.5).

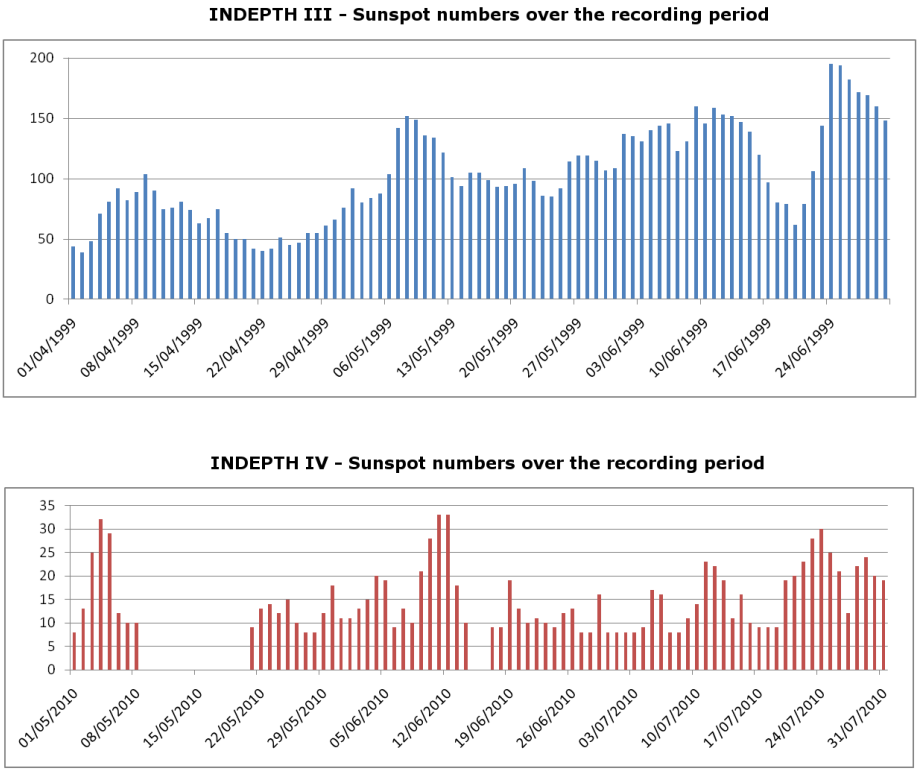

Figure 7.5: Sunspot activity during the Indepth III and IV MT recordings. The data was taken from the Solar Influences Data Analysis Center's website [*SIDC*].

INDEPTH IV: Due to a low signal period in 2009, INDEPTH IV MT fieldwork was delayed. The MT fieldwork took place between May and July 2010. The data were recorded at the beginning of Cycle 24 when the sunspot numbers started to increase again. Although the sun activity was not as significant as for INDEPTH III recordings, the sunspot numbers improved significantly from 2009, with some really nice peaks in early-mid June (Fig. 7.5). LMT data were acquired using *LEMI-417M* [2009] systems across the northern margins of the Tibetan plateau in collaboration with the China University of Geosciences, Beijing (CUGB) and the University of Alberta, Canada. Most of LMT stations were left recording for approximately two weeks. The Indepth IV MT survey is characterized by two profiles crossing the Altyn Tagh fault and one profile crossing the Kunlun fault (DIAS main focus) located on the same line as the Indepth IV seismic data which were already acquired in the area [*Karplus et al.*, 2011]. As broadband magnetotelluric data but only few LMT sites were collected along the INDEPTH IV lines by the CUGB group in 2009, the new Kunlun profile or 6000-line was completed by LMT stations. The BBMT data collected in 2009 by CUGB was recorded using *Phoenix MTU* [2010] systems. The locations of the LMT sites were constrained by the broadband sites with good data quality. Unfortunately, during the deployment, some planned locations had to be modified due to some flooding. The 6000 profile consists on 13 long-period magnetotelluric (LMT) stations and 38 broadband magnetotelluric (BBMT) stations. Stations were deployed every 5 to 10 km for the BBMT sites and every 10 to 25 km for the LMT sites. Both instruments and cables were buried.

Figure 7.6: Electrodes layout scheme characterizing the *star* configuration.

During the INDEPTH IV survey, the LMT sites were laid out in a *star* configuration consisting on adding two more electric dipoles along the NW-SE and NE-SW directions (Fig. 7.6). In addition to the conventional N-S and E-W dipoles layout (Fig. 7.4), a second set of two dipoles are deployed with a 45° rotation from the classic setup. Before processing the data, the electric field components recorded by the second set of dipoles need to be rotated back by 45° to the Cartesian coordinate system defined by the north and east directions. Although the star layout is a lot more work in the field, it has several advantages. The electric field horizontal component (E_x, E_y) are recorded twice from different electrodes leading to two data sets for one single location. Therefore, if the contact quality at some electrodes decreases or if some connection get biased for one set of dipoles, there is still a chance to get decent responses from the second set of E_x, E_y components. Furthermore, such system may give a better control on removing distortion effects associated with surficial 3D anomalies. For all processed sites, the responses generated from the two sets of dipoles were almost identical and the data less affected by noise was chosen to be merged with the corresponding BBMT data. Due to time issues, but also as both processed sets of data did not present any shifts between their apparent resistivity curves, the distortion removal associated with the star layout was not investigated further. However, as part of future work, it would be interesting to test this particular configuration using 3D distorted synthetic data.

7.9.2 *Processing the Time Series*

Processing MT data consists mainly on reducing the significant size of the digital time series to a more compact format characterized by the frequency-dependent transfer functions. However, data processing is a critical stage for the further interpretation of the data since a bad signal to noise ratio in the time series can lead to biased estimates of the MT response functions. If low enough or Gaussian distributed, the noise affecting the time series can be removed by a simple least-square scheme implemented in the estimation of the transfer functions. However, when the data is strongly affected by *outliers* and correlated noise, a more *robust* processing scheme needs to be applied on the data [*Jones et al.*, 1989; *Vozoff*, 1991; *Simpson and Bahr*, 2005]. A comparison of different methods used for MT transfer functions estimation was presented in *Jones et al.* [1989]. Furthermore, a more recent overview of the processing techniques can be found in *Chave* [2012]. Although their

implementation will vary with the different schemes involved in robust processing, the general concepts of MT data processing usually remain the same.

As part of the pre-conditioning of the data, it is necessary to reduce the effects of trends and to remove severe noise (spikes) affecting the time series. Furthermore, before transforming the data into the frequency domain, the time series are separated into segments usually using a Hamming window to avoid spectral leakage. The length of each segment will depend on the period calculated (evaluation frequency). A large number of segments will lead to better statistical results. *Simpson and Bahr* [2005] highlighted there should be 6 to 10 evaluation frequencies per decade. A higher number of frequencies is unnecessary as *Weidelt* [1972]'s dispersion relation predicts similar results for neighbouring frequencies. A lower number of frequencies could lead to aliasing in the frequency domain. Furthermore, the evaluation frequencies will need to be equally spaced on a logarithmic scale. Each data segments are then converted into the frequency domain using a (Discrete or Fast) Fourier Transform or a wavelet transform. It is worth mentioning that if frequency-dependent (the case for AMT and BBMT systems), the calibrations can only be applied on the measured field components at this stage [*Simpson and Bahr*, 2005].

In the frequency domain, the raw power spectra of each channel for each time segment are used to calculate the auto and cross spectra (defined by the products of the field components and their complex conjugates) that are stored in the following spectral matrix for each evaluation frequency (ω):

B_x	B_y	B_z	E_x	E_y	
$B_x.B_x^*$	$B_y.B_x^*$	$B_z.B_x^*$	$E_x.B_x^*$	$E_y.B_x^*$	B_x
$B_x.B_y^*$	$B_y.B_y^*$	$B_z.B_y^*$	$E_x.B_y^*$	$E_y.B_y^*$	B_y
		$B_z.B_z^*$			B_z
			$E_x.E_x^*$	$E_y.E_x^*$	E_x
				$E_y.E_y^*$	E_y

A same evaluation frequency is associated with a number of spectral matrices issued from different time windows. Therefore, the spectral matrices can be stacked for each evaluation frequency. This procedure can either be done by hand by selecting noise-free time windows or weighted by using statistical techniques.

The equations characterizing the impedance tensor (Eq. 7.56) and the tipper vector (Eq. 7.60) can be extended to:

$$E_x(\omega) = Z_{xx}(\omega).H_x(\omega) + Z_{xy}(\omega).H_y(\omega) + \delta Z(\omega), \tag{7.75}$$

$$E_y(\omega) = Z_{yx}(\omega).H_x(\omega) + Z_{yy}(\omega).H_y(\omega) + \delta Z(\omega), \tag{7.76}$$

$$H_z(\omega) = T_x(\omega).H_x(\omega) + T_y(\omega).H_y(\omega) + \delta T(\omega), \tag{7.77}$$

where the terms $\delta Z(\omega)$ and $\delta T(\omega)$ represent uncorrelated noise. As the data is not noise free, a statistical solution is required in the determination of the MT response functions. In both least-squares and robust processing methods, the equations 7.75, 7.76 and 7.77 are solved as a *bivariate linear regression* problem (Eq. 7.78, 7.79, 7.80, 7.81, 7.82 and 7.83) [*Simpson and Bahr*, 2005].

The conventional way to estimate the impedance tensor and tipper vector elements is to take the crosspower of the equations 7.75, 7.76 and 7.77 with H_x and H_y, usually less noisy (except for frequencies within the MT dead-band) than the electric components [*Vozoff*, 1991]. However, any noise present in each component will be amplified by their autopowers, leading to biased impedance estimates [*Simpson and Bahr*, 2005]. The *remote reference* processing method was introduced by *Goubau et al.* [1978] and *Gamble et al.* [1979] to avoid this problem. This particular processing method consists on using two remote channels in the processing. Since those are taken from a neighbouring remote site, the remote reference technique enables to remove uncorrelated noise between the stations. However, the correlated noise will remain. As they are more homogeneous and usually less affected by noise, the magnetic rather than electric horizontal components of the remote site are usually considered. Similarly to the conventional local processing technique, the impedance tensor and tipper vector components can be determined by taking the crosspower of the equations 7.75, 7.76 and 7.77 with the remote horizontal magnetic field complex conjugates (R_x^* and R_y^*) leading to the following equations:

$$Z_{xx} = \frac{\langle E_x R_x^* \rangle \langle H_y R_y^* \rangle - \langle E_x R_y^* \rangle \langle H_y R_x^* \rangle}{DET}, \tag{7.78}$$

$$Z_{xy} = \frac{\langle E_x R_y^* \rangle \langle H_x R_x^* \rangle - \langle E_x R_x^* \rangle \langle H_x R_y^* \rangle}{DET}, \tag{7.79}$$

$$Z_{yx} = \frac{\langle E_y R_x^* \rangle \langle H_y R_y^* \rangle - \langle E_y R_y^* \rangle \langle H_y R_x^* \rangle}{DET}, \tag{7.80}$$

$$Z_{yy} = \frac{\langle E_y R_y^* \rangle \langle H_x R_x^* \rangle - \langle E_y R_x^* \rangle \langle H_x R_y^* \rangle}{DET}, \tag{7.81}$$

and for the tipper elements,

$$T_x = \frac{\langle H_z R_x^* \rangle \langle H_y R_y^* \rangle - \langle H_z R_y^* \rangle \langle H_y R_x^* \rangle}{DET}, \tag{7.82}$$

$$T_y = \frac{\langle H_z R_y^* \rangle \langle H_x R_x^* \rangle - \langle H_z R_x^* \rangle \langle H_x R_y^* \rangle}{DET}, \tag{7.83}$$

with

$$DET = \langle H_x R_x^* \rangle \langle H_y R_y^* \rangle - \langle H_x R_y^* \rangle \langle H_y R_x^* \rangle. \tag{7.84}$$

If there is no remote site available for the processing, the data can be processed only locally by replacing R_x^* and R_y^* by the local H_x and H_y components. In order to determine the impedance tensor and the tipper vector at a particular frequency, the autopowers and crosspowers in Equations 7.78, 7.79, 7.80, 7.81, 7.82 and 7.83 are substituted by the appropriate elements of the spectral matrix described above [*Simpson and Bahr*, 2005].

Different processing codes have been developed in order to improve the quality of the transfer functions estimations in noisy environments [*Jones and Jödicke*, 1984; *Egbert and Booker*, 1986; *Chave et al.*, 1987; *Egbert*, 1997; *Chave and Thomson*, 2004; *Smirnov*, 2003]. Those may perform differently depending on the nature and degree of noise contamination. Commonly used robust processing schemes are based on M-estimators [*Huber*, 1981]. The Indepth phase IV long period data was processed using *Smirnov* [2003]'s processing code which is based on *Siegel* [1982]'s repeated median algorithm. The robustness of an estimator is characterized by its breakdown point or fraction of outlying data points that can

corrupt the estimator [*Hampel et al.*, 1986]. The code of *Smirnov* [2003] provides a robust statistical procedure with a high breakdown point.

7.10 THE DISTORTION PROBLEM

7.10.1 *Distortion Effects*

Distortion issues are a major problem in magnetotellurics as they can lead to erroneous interpretations. *Berdichevsky et al.* [1973] separated the MT distortion processes into two major effects: the galvanic and inductive effects. As a simple example, when considering a relatively conductive (or resistive) 2D or 3D surficial body embedded in an homogeneous media, the primary electric field will produce charges accumulation in the areas of resistivity contrasts. Those charges will generate a secondary electric field that distorts the primary electric field (Fig. 7.7). This phenomenon is defined as galvanic distortion and its behaviour will mainly depend on the resistivity of the anomaly [*Jiracek*, 1990]. The galvanic effects are also commonly identified as vertical and horizontal current gathering, current channelling, current concentration into conductive zones, current deflection around resistive bodies and current leakage [*Jones*, 1983a; *Park*, 1985]. At a resistivity contrast, the current flow will be perturbed by the surface charges within *adjustment distances* or *equilibrium distances* [*Jones*, 1983a]. The galvanic distortion could also be generated by topography effects. In 2D, the galvanic topography effects mainly affects the TM mode as perpendicular to the strike of the topography and the maximum charge concentration will occur for the steepest topography [*Jiracek*, 1990].

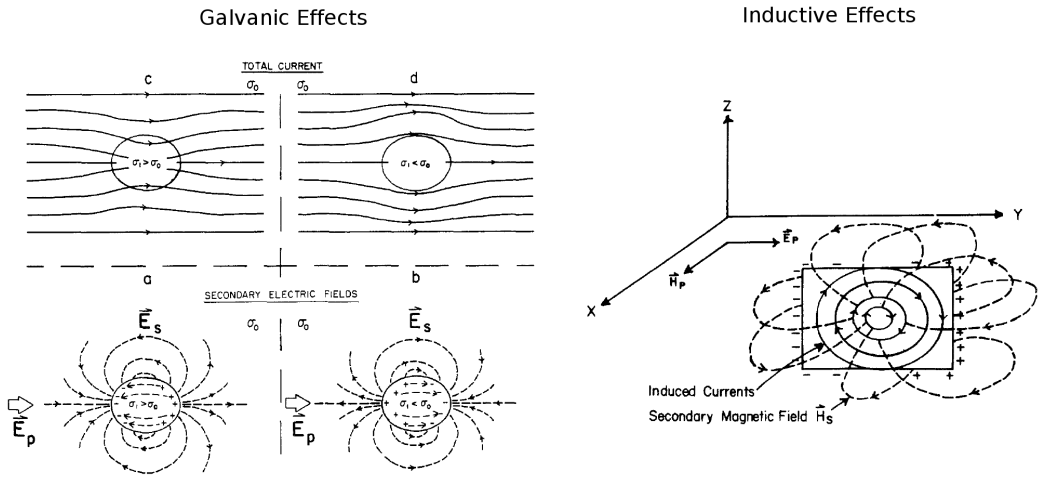

Figure 7.7: **Galvanic Effects** - Charges accumulation around conductive (a) and resistive (b) structures creates a secondary electric field $\vec{E}_s$ (dashed) that will add to the primary electric field $\vec{E}_p$. The secondary electric field $\vec{E}_s$ produced by a conductive inhomogeneity is opposed to the primary field $\vec{E}_p$ (a) which will lead to current channelling (c). However, if the inhomogeneity is resistive (b), the galvanic effect will be characterized by current deflection (d). **Inductive Effects** - Induced vortex currents producing a secondary magnetic field $\vec{H}_s$. *modified from Jiracek* [1990]

Furthermore, in agreement with the Faraday's law the time-varying magnetic field induces currents in the embedded body. Those induced currents produce a secondary magnetic field that will distort the primary magnetic field (Fig. 7.7). This phenomenon characterizes the inductive distortion. Those induction effect can be particularly significant on the TE mode when modelling soundings over a resistive block adjacent to a surficial conductive zone [*Jiracek*, 1990]. Such situation could for example result in the modelling of a *false conductive layer* [*Berdichevsky and Dimitriev*, 1976b] when using the TE mode only for 1D modelling. This particular induction effect is also called *coast effect* [*Parkinson and Jones*, 1979] when the surficial conductive zone characterizes an ocean .

Whereas the inductive effects will increase to saturation as the frequency increases, on the contrary the galvanic effects will increase to saturation as the frequency decreases *Jiracek* [1990]. Therefore, the galvanic distortion affecting the electric field persists at longer periods which is a serious problem for the overall interpretation of MT data. Furthermore, in addition to the galvanic electrical distortion, [*Chave and Smith*, 1994] presented that galvanic effects will also affect the magnetic field. The authors demonstrated that for some particular data sets such as MT data collected on the seafloor or in crystalline environments, the galvanic distortion can be important even at long periods. However, in comparison to the electric galvanic effects, it has been considered that in general the magnetic galvanic effects will mainly occur for a limited frequency range [*Chave and Jones*, 1997]. Therefore, similarly to the induction distortion, the galvanic magnetic distortion is usually considered secondary [*Groom et al.*, 1993].

Static Shift

As seen on Figure 7.7, the total electric field over an anomalous body gets distorted due to galvanic effects. For a conductive anomaly, the total electric field is reduced directly on top of the body. Depending on the orientation of the primary electric field, the total $\vec{E}$ field will be enhanced off the end of the body and diminished along its side. Opposite effects will affect the total $\vec{E}$ field over a resistive body (Fig. 7.7). Such effects will affect the MT apparent resistivities which will be shifted upwards when the total $\vec{E}$ field increases and shifted downwards as the total $\vec{E}$ field decreases [*Jiracek*, 1990]. For a surficial body, when the skin depth in the host becomes bigger that the dimensions of the body (not true at the highest frequencies), the quasiuniform charging electric field will remain DC as the frequency decreases and the impedance phase will remain undistorted. Therefore, the shift on the MT apparent resistivities becomes frequency independent [*Berdichevsky and Zhdanov*, 1984; *Jiracek*, 1990]. This particular phenomenon is identified as *static shift* [*Simpson and Bahr*, 2005]. Static shifts are particularly an issue in 1D and 2D modelling, when the stations are placed over small 3D surficial bodies. Those small anomalies may not affect the global dimensionality of the data but may shift the apparent resistivity curves significantly. Furthermore, [*Jones*, 1983a] highlighted that compared to its length-to-width ratio, the *length-to-skin-depth-in-host* ratio of a 3D body is far more critical in the interpretation of the data using a 2D solution.

In order to illustrate the distortion effects generated by a small scale 3D body in a 2D environment, a synthetic model (Fig. 7.8) and associated responses were created using WinGLink's 3D forward modelling code [*Mackie et al.*, 1994]. The data presented on Figure 7.8 was decomposed using the *Strike* program [*McNeice and Jones*, 2001]. An example of

fully distorted data can be seen on Figure 7.10. The distortion removal process will be discussed in details below. However, as mentioned later the static shift effects cannot be corrected and then will remain affecting the apparent resistivity curves (Fig. 7.8). Different particular observations can be highlighted here. First, although they affect significantly the data, the distortion and static shift effects will be cancelled within a short distance to the anomaly. This can be seen on the curves and on the modelling of the current behaviour around the anomaly (Fig. 7.8). Secondly, the behaviour of the TE mode shifts around the anomaly can be well predicted by the modelling of the EM energy (decrease on the sides of the anomaly and increase at the ends). This observation is valid for the TM mode but is not presented here. Furthermore, Figure 7.8b also highlights how the distortion effects reach saturation with increasing periods. Finally, it is also worth noticing that the two modes completely vanish directly on top of the 3D body. For a site deployed near such anomaly in a real context (comparable dimensions with the E-lines length), the star layout mentioned previously in the acquisition section could be really helpful for static shifts correction.

Whereas the electric galvanic distortion is frequency-independent (under the conditions mentioned above), the magnetic galvanic distortion effects are frequency-dependent and will decrease with the frequency [*Groom et al.*, 1993; *Chave and Smith*, 1994]. For this reason, the determination of the magnetic galvanic distortion parameters can lead to instabilities and must be taken with care [*McNeice and Jones*, 2001]. When the inductive and magnetic galvanic distortion effects are neglected and when the dimensionality can be considered quasi 2D (small scale 3D bodies embedded in a regional 2D environment) [*Groom and Bahr*, 1992], the measured impedance tensor can be described by the equation:

$$\mathbf{Z_{obs}} = \mathbf{R}(\theta)\mathbf{C}\mathbf{Z_{2D}}\mathbf{R}^{\mathsf{T}}(\theta) = \mathbf{R}(\theta)\mathbf{C}\begin{pmatrix} 0 & Z_{\parallel} \\ Z_{\perp} & 0 \end{pmatrix}\mathbf{R}^{\mathsf{T}}(\theta), \tag{7.85}$$

with $\mathbf{C}$ the telluric distortion tensor and $\mathbf{R}(\theta)$ the rotation tensor to the regional 2D strike coordinates. The distortion effects on the electric field are characterized by the tensor $\mathbf{C}$, whose elements are real and frequency-independent [*Groom et al.*, 1993]:

$$\mathbf{C} = \begin{pmatrix} C_{xx} & C_{xy} \\ C_{yx} & C_{yy} \end{pmatrix}. \tag{7.86}$$

Different methods have been considered to evaluate the directionality of the data in quasi 2D situations and to remove the distortion effects present in the tensor $\mathbf{C}$. In the next two sections, the main focus will be on the Groom-Bailey decomposition [*Groom and Bailey*, 1989] and on the phase tensor [*Caldwell et al.*, 2004] as those two techniques have been applied later on the Tibet MT data. However, it is worth mentioning the phase tensor is not a decomposition technique but can be very useful for the characterization of the dimensionality and directionality of the regional conductivity structures. Other distortion tools no discussed here include the methods of *Swift* [1967], *Bahr* [1988] and *Weaver et al.* [2000]. The distortion problem has also been considered for 3D situations. For example, [*Garcia and Jones*, 2001] attempted to extend the MT tensor decomposition scheme to a regional 3D environment.

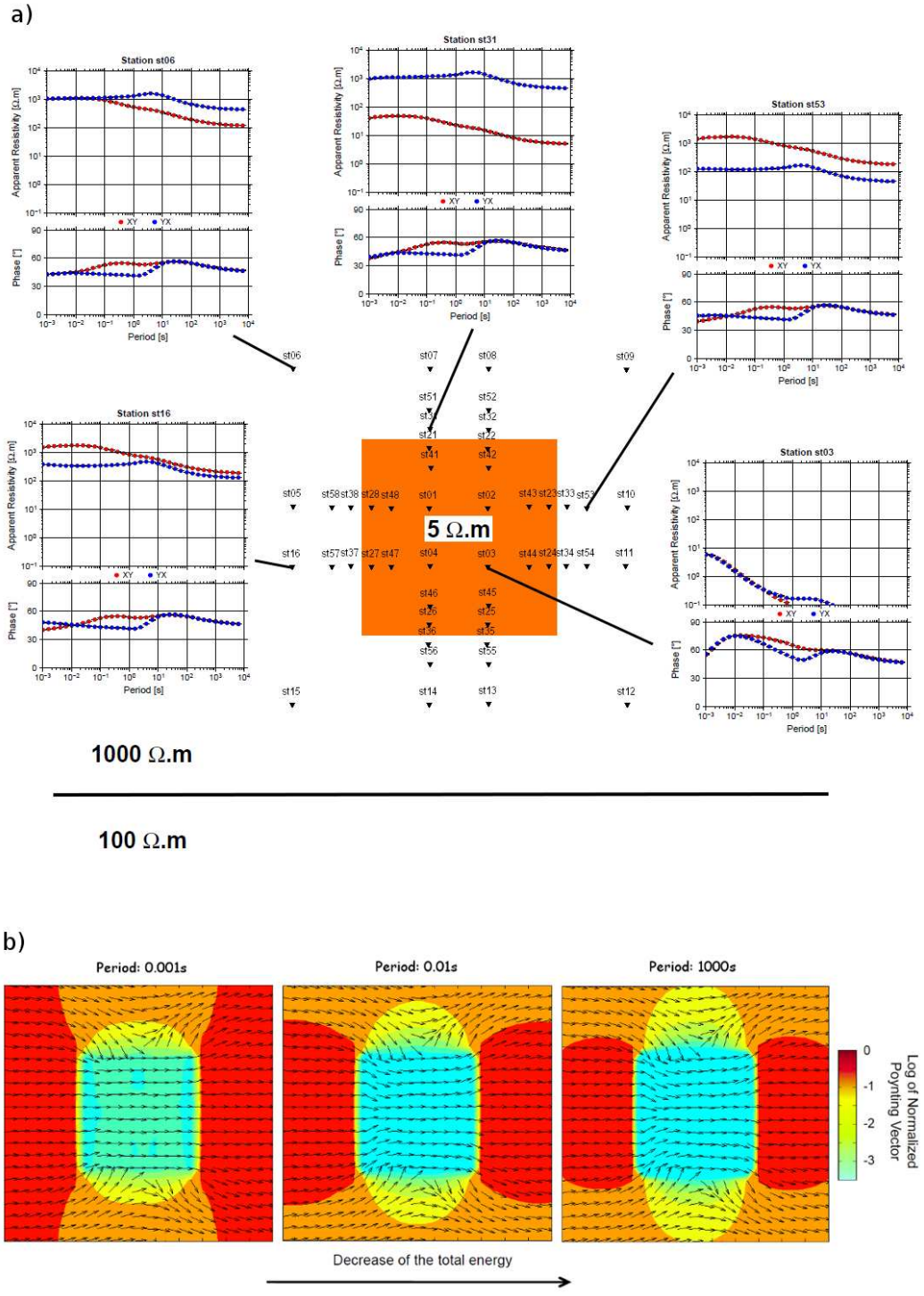

Figure 7.8: The distortion problem. a - 3D synthetic model and associated responses (decomposed to 45° using *Strike* [*McNeice and Jones*, 2001]). The 2D background is characterized by a contact of 45° azimuth between a 100 Ω.m medium and a 1000 Ω.m medium. At 30km, the model becomes 1D with a half-space of 100 Ω.m. A surficial 3D body of 100 m width and 200 m depth is introduced at 3km from the 2D contact. Only the distance of the contact from the anomaly is out of proportion on the picture. b - Current and EM energy modelling around the anomaly for different periods. It is worth noticing the polarisation of the currents is paralell to the strike direction, therefore it mainly characterizes the distortion effects on the TE mode

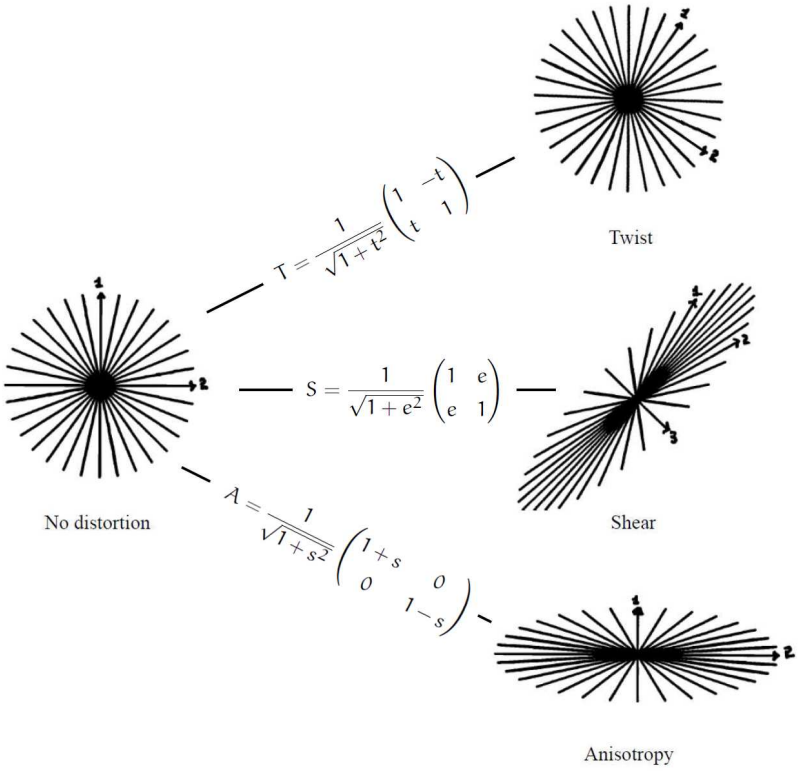

Figure 7.9: The different distortion effects that characterize the Groom-Bailey decomposition applied on the electric field. The equations characterizing the twist, shear and anisotropy are also highlighted where t, e, and s are real values. *modified from Groom and Bailey* [1989]

7.10.2 *Groom-Bailey Decomposition*

The solution to Equation 7.85 is non-unique and then cannot be solved directly. *Groom and Bailey* [1989] proposed a decomposition of the distortion tensor **C** into determinable and indeterminable parameters with a physical meaning. The parametrisation of the distortion matrix **C** (Eq. 7.87) is characterized by a scalar or *gain* g and three tensors: the *twist* **T**, the *shear* **S** and the *anisotropy* **A**.

$$\mathbf{C} = g\mathbf{TSA} \tag{7.87}$$

Figure 7.9 illustrates the physical effects of each tensor on the horizontal components of the electric field. The twist tensor **T** rotates the electric field vectors through a clockwise angle $\phi_{twist} = \tan^{-1}(t)$ (Fig. 7.9). The shear tensor **S** develops anisotropy on axes which bisect the principal axes of the regional induction. For example, in a Cartesian coordinate system a vector on the x axis is deflected clockwise by an angle $\phi_{shear} = \tan^{-1}(e)$, and a vector along the y axis is deflected counter-clockwise by the same angle (Fig. 7.9). Therefore, for meaningful reasons the shear angle cannot exceed 45°. The anisotropy tensor **A** stretches the two field components by different factors and then generate anisotropy.

The decomposition is characterized by nine unknown (the regional strike θ, g, t, e, s, and the real and imaginary parts of the regional 2D impedance tensor) and eight known parameters (real and imaginary parts of the measured impedance tensor). However, the distortion anisotropy is indistinguishable experimentally from the inductive anisotropy

except if the anisotropy from $\mathbf{Z_{2D}}$ (Eq. 7.85) is known independently. Neither g nor $\mathbf{A}$ can be determined separately since the tensor resulting from the product $g\mathbf{AZ_{2D}}$ is a valid 2D impedance tensor. Therefore, the Groom-Bailey decomposition cannot remove static shifts. The accuracy of the distortion model is characterized by the misfit (weighted by the data errors) between the observed data and the data modelled by the decomposition [*Groom and Bailey*, 1989].

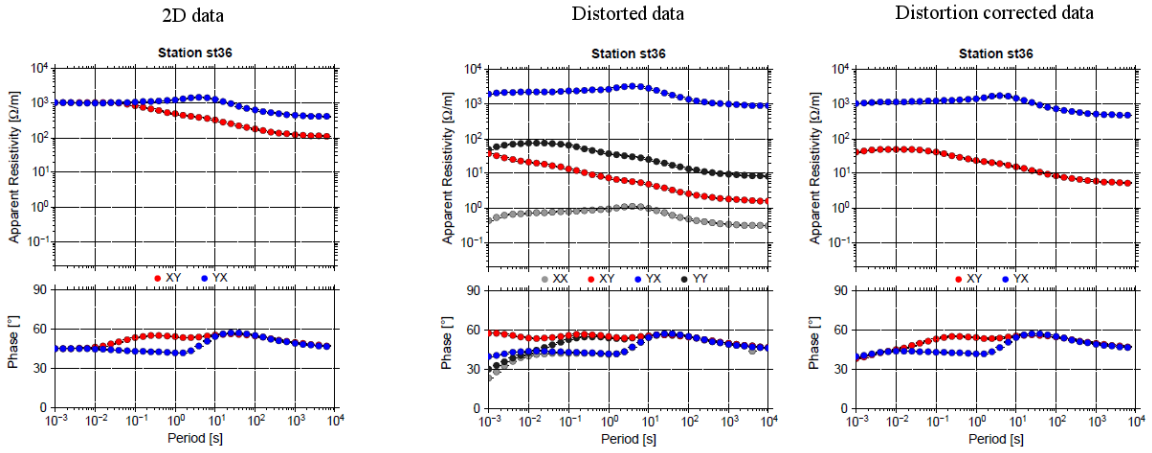

Figure 7.10: Distortion correction for site st36 from the 3D synthetic model presented in Figure 7.8. For all the three plots, the data have been rotated to the regional strike 45°. The *2D data* were modelled without the 5 Ω.m 3D anomaly. The *distorted data* was modelled with the presence of the 3D anomaly (Fig. 7.8) and the *distortion corrected data* is the result of the decomposition of the distorted data after using the *Strike* program from *McNeice and Jones* [2001].

The Groom-Bailey decomposition was extended by *McNeice and Jones* [2001] to compute the distortion model and determine the geoelectric strike over a range of frequencies and sites. This multifrequency, multi-site approach is particularly useful to identify the geoelectric of an MT profile and then for 2D modelling. The method has been developed as a freely available program called *Strike* [*McNeice and Jones*, 2001]. Considering particular segments of the profile and different frequency (depth) ranges will help for a more robust estimation of the regional 2D strike direction. Figure 7.10 presents how the decomposition is quite efficient in recovering the MT responses of the regional 2D model, even when the phase is distorted at the higher frequencies (not always the case as seen on Figure 7.8). However, although the shape of the MT resistivity curves are recovered, the static shift effects remain. Figure 7.8 highlights clearly that the distortion problem, although very localized, can significantly affect the data and that even when considering a simple model, the decomposition cannot fix everything. However, it is worth mentioning that for the presented model, perhaps numerical problems cannot be excluded, particularly at the highest frequencies.

Although *Berdichevsky* [1999] highlighted that there is no "standard remedy" for static shift removal, different correction methods have been described by *Jones* [1988], *Berdichevsky et al.* [1989] and *Pellerin and Hohman* [1990]. One important step in static shift correction would be to compare the apparent resistivity curves between neighbouring sites along

the 2D profile. The apparent resistivity shifts should be corrected in the frequency range corresponding to small phases variations along the profile [*Berdichevsky*, 1999]. Another method would be to shift the apparent resistivity curves to the arithmetic average of the two modes *Vanyan et al.* [1989]. The correction for static shifts can also be introduced in the inversion procedure [*deGroot-Hedlin*, 1991].

7.10.3 *Phase Tensor*

The MT phase tensor $\mathbf{\Phi}$ was first proposed by *Caldwell et al.* [2004]. The tensor is defined as the ratio of the real part $\mathbf{X}$ and imaginary part $\mathbf{Y}$ of the complex impedance $\mathbf{Z}$ such that $\mathbf{Z} = \mathbf{X} + i\mathbf{Y}$ and $\mathbf{\Phi} = \mathbf{X}^{-1}\mathbf{Y}$. As mentioned previously, when affected by galvanic distortion, the observed impedance can be expressed as $\mathbf{Z} = \mathbf{C}\mathbf{Z}_\mathbf{R}$, where the complex regional impedance can also be characterized as $\mathbf{Z}_\mathbf{R} = \mathbf{X}_\mathbf{R} + i\mathbf{Y}_\mathbf{R}$. The following equation demonstrates that the phase tensor is independent of the distortion tensor $\mathbf{C}$.

$$\begin{aligned} \mathbf{\Phi} &= \mathbf{X}^{-1}\mathbf{Y} \\ &= (\mathbf{C}\mathbf{X}_\mathbf{R})^{-1}(\mathbf{C}\mathbf{Y}_\mathbf{R}) \\ &= \mathbf{X}_\mathbf{R}^{-1}\mathbf{C}^{-1}\mathbf{C}\mathbf{Y}_\mathbf{R} \\ &= \mathbf{X}_\mathbf{R}^{-1}\mathbf{Y}_\mathbf{R} \\ &= \mathbf{\Phi}_\mathbf{R} \end{aligned} \tag{7.88}$$

In the Cartesian coordinate system (x,y) (Fig. 7.11), the phase tensor can be expressed as:

$$\mathbf{\Phi} = \begin{pmatrix} \Phi_{xx} & \Phi_{xy} \\ \Phi_{yx} & \Phi_{yy} \end{pmatrix} = \frac{1}{\det(\mathbf{X})} \begin{pmatrix} X_{yy}Y_{xx} - X_{xy}Y_{yx} & X_{yy}Y_{xy} - X_{xy}Y_{yy} \\ X_{xx}Y_{yx} - X_{yx}Y_{xx} & X_{xx}Y_{yy} - X_{yx}Y_{xy} \end{pmatrix} \tag{7.89}$$

with $\det(\mathbf{X}) = X_{xx}X_{yy} - X_{yx}X_{xy}$ the determinant of $\mathbf{X}$ [*Caldwell et al.*, 2004].

The tensor $\mathbf{\Phi}$ is characterized by three scalar quantities Φ_{max}, Φ_{min} and β, that are independent of the coordinate system in which the tensor is expressed [*Caldwell et al.*, 2004]. Those coordinate invariants are defined as:

$$\Phi_{max} = (\Phi_1^2 + \Phi_3^2)^{1/2} + (\Phi_1^2 + \Phi_3^2 - \Phi_2^2)^{1/2}, \tag{7.90}$$

$$\Phi_{min} = (\Phi_1^2 + \Phi_3^2)^{1/2} - (\Phi_1^2 + \Phi_3^2 - \Phi_2^2)^{1/2}, \tag{7.91}$$

$$\beta = \frac{1}{2}\tan^{-1}\left(\frac{\Phi_3}{\Phi_1}\right), \tag{7.92}$$

with $\Phi_1 = (\Phi_{xx} + \Phi_{yy})/2$, $\Phi_2 = (\det(\Phi))^{1/2}$ and $\Phi_3 = (\Phi_{xy} - \Phi_{yx})/2$.

The phase tensor is usually written as a function of its invariants and can be represented as an ellipse in the horizontal plan of the Cartesian coordinate system (x,y,z) for each

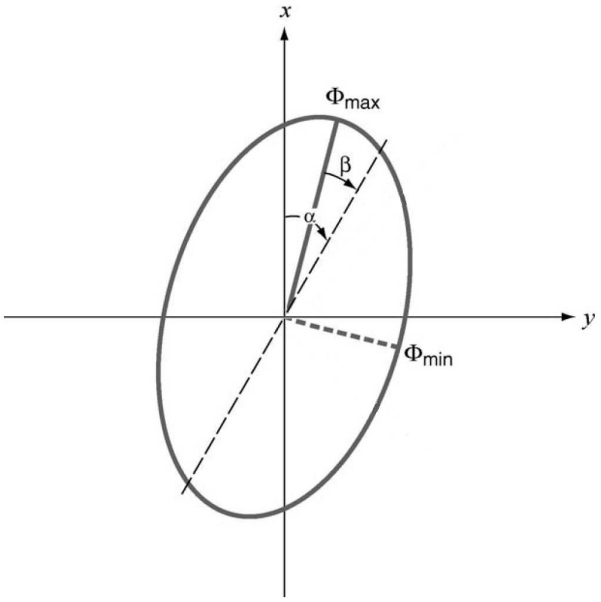

Figure 7.11: The phase tensor is commonly represented as an ellipse. *from Heise et al.* [2006]

frequency of each site (Fig. 7.11). As presented by *Caldwell et al.* [2004], the phase tensor can be decomposed as:

$$\mathbf{\Phi} = \mathbf{R}^{T}(\alpha-\beta)\begin{pmatrix}\Phi_{max} & 0\\ 0 & \Phi_{min}\end{pmatrix}\mathbf{R}(\alpha+\beta) \tag{7.93}$$

where $\mathbf{R}(\alpha+\beta) = \begin{pmatrix}\cos(\alpha+\beta) & \sin(\alpha+\beta)\\ -\sin(\alpha+\beta) & \cos(\alpha+\beta)\end{pmatrix}$ is the rotation matrix and with:

$$\alpha = \frac{1}{2}\tan^{-1}\left(\frac{\Phi_{xy}+\Phi_{yx}}{\Phi_{xx}-\Phi_{yy}}\right) \tag{7.94}$$

$$\beta = \frac{1}{2}\tan^{-1}\left(\frac{\Phi_{xy}-\Phi_{yx}}{\Phi_{xx}+\Phi_{yy}}\right) \tag{7.95}$$

In 1D and 2D scenarios, the phase tensor is symmetric and the angle α, which is dependent on the coordinate system, will define the orientation of the main axis of the phase tensor's ellipse ($\beta = 0$). However, in 3D cases, the phase tensor will be non-symmetric and needs to be characterized by the skew angle β which measures the tensor's asymmetry [*Caldwell et al.*, 2004]. Therefore, the ellipse's major axis will be oriented in the direction $\alpha-\beta$ (Fig. 7.11). The coordinate-invariant skew angle β defines the deviation of the phase tensor principal axes from an equivalent symmetric configuration resulting from the asymmetry of the phase responses produced by 3D structures [*Heise et al.*, 2006].

In the isotropic 1D case, $\Phi_{max}-\Phi_{min}$ will be zero and the phase tensor is then represented as a circle whose radius will increase with period if the conductivity increases with depth [*Caldwell et al.*, 2004]. When considering an uniform half-space, the phase tensor becomes the identity matrix ($\phi_{max} = \phi_{min} = 1$) due to the phase difference of 45°

between $\vec{H}$ and $\vec{E}$ [*Heise et al.*, 2006]. In the isotropic 2D case, the ellipse axes are parallel and perpendicular to the 2D strike direction. Furthermore, the phase tensor's main components will characterize the TE and TM mode phases such that [$\phi_{xy} = \tan^{-1}(\Phi_{max})$ and $\phi_{yx} = \tan^{-1}(\Phi_{min})$] or [$\phi_{xy} = \tan^{-1}(\Phi_{min})$ and $\phi_{yx} = \tan^{-1}(\Phi_{max})$]. The phase tensor ellipse will then have either its major or minor axes aligned with the geoelectric strike direction. In 3D, the skew angle β is non-zero. Furthermore, *Caldwell et al.* [2004] highlighted that a small value for β ($< 3°$) is not necessary an indication for an approximate 2D configuration which is rather highlighted by the consistency in the ellipse principal axes directions over several periods and stations. On the contrary, a rapid change in the direction of the ellipse's principal axes would indicate the presence of a regional 3D structure.

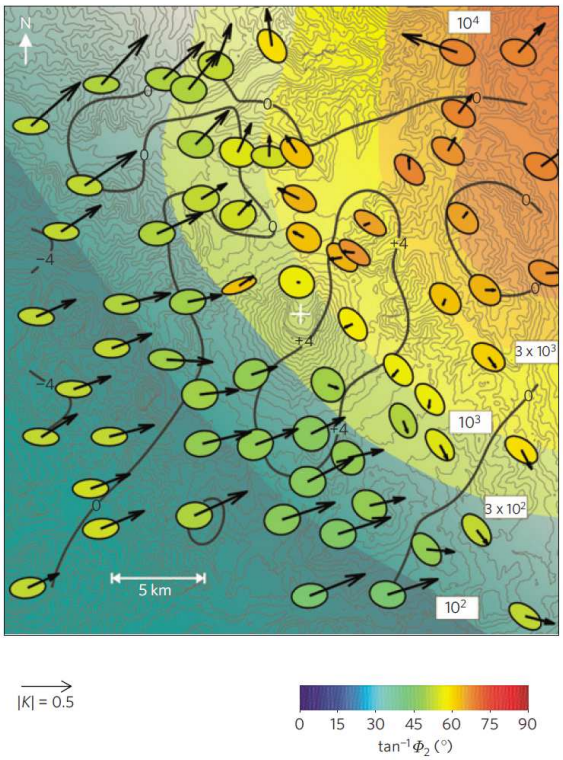

Figure 7.12: Phase tensor ellipses and induction vectors (real parts) at a period of 85 s for a survey taking place in the Mount St Helens area. The background colour represents the regional conductance anomaly (red colours are associated with high conductance areas). The ellipses are normalized by ϕ_{max} and their colour characterize the geometric mean Φ_2 ($\sqrt{\phi_{max}\Phi_{min}}$). The skew angle is defined by the contour lines. *from Hill et al.* [2009]

The phase tensor major axis will usually align with the direction of the maximum inductive current flow. The orientation of the tensor's principal axes will either be parallel or perpendicular to the steepest horizontal conductivity gradients characterizing the regional conductivity structure [*Caldwell et al.*, 2004; *Hill et al.*, 2009]. Therefore, the phase tensor provides a good first interpretation of the regional conductivity distribution in a particular area and is often associated with the induction arrows, also unaffected by distortion. As an example, Figure 7.12 presents a mapped representation of the phase tensor

and induction arrows plotted as a single period for a MT study of Mount St Helens [*Hill et al.*, 2009]. In the eastern part of the studied area, the mapped representation of the phase tensor ellipses (Fig. 7.12) highlights the radial alignment of the major axes towards the high conductance area in agreement with the induction arrows directions. However, for sites located in the high conductance zone, the induction vectors become really small and the major axes of the phase tensor ellipse are mainly orientation tangentially to the conductance contrast. However, since they do not sample the same volume, phase tensor and induction vectors may not be always comparable. Furthermore, as mentioned by [*Caldwell et al.*, 2004], any misalignment between the ellipse's principal axes and the induction arrows may result from the asymmetry ($\beta \neq 0$) produced by the presence of 3D structures.

The phase tensor appears as a really useful tool to obtain a primary information about the dimensionality and distribution of the regional conductivity structures in a 3D environment but it must not be forgotten that its efficiency also rely on the estimation of the uncertainties on its own parameters.

7.11 MODELLING AND INVERSION

Before modelling or inverting any MT data, a last test known as D^+ or ρ^+ consistency check can be performed. The D^+ model defined by *Parker and Booker* [1980] and *Parker and Whaler* [1981] describes a series of delta functions (infinitesimally thin sheets of finite conductance) that minimizes the χ^2 misfit for 1D MT data [*Parker and Booker*, 1996; *Simpson and Bahr*, 2005]. The determination of the D^+ solutions can be used as a simple test that verifies the accuracy of the 1D modelling assumption on a particular data set. In their ρ^+ code, *Parker and Booker* [1996] extended the D^+ approach to test the mutual consistency between the apparent resistivity and phase by predicting one from the other. This particular consistency test can be applied on 1D and 2D data and can solve for missing, corrupted data, since the ρ^+ program can define bounds on missing phase or resistivity data. An example of this consistency approach can be found in *Spratt et al.* [2005].

Once the data has been decomposed and fully analysed, the final step is to model the Earth resistivity structures characteristic of the measured data. Depending on the dimensionality of the data, 1D, 2D or 3D models can be considered. *Forward modelling* will enable to generate synthetic responses from a 1D or multi-dimensional model. Whereas, the 1D forward modelling remains relatively simple, in multi-dimensional cases the model needs to be discretised through different methods such as Finite Elements (FE) [*Wannamaker et al.*, 1987], Finite Differences (FD) [*Mackie et al.*, 1994; *Pek and Verner*, 1997] or Integral Equations (IE) [*Avdeev et al.*, 2002] in order to define the model mesh. The Maxwell's equations and boundary conditions presented previously are then solved for each cell of the mesh. The formulation of the corresponding equations system will then depend on the approximation used (FE, FD or IE). The synthetic data generated by forward modelling are compared with the measured data and the misfit between the observed and model responses is usually presented as an RMS misfit. Inversion programs will try to find the "best" model that fits the data by adjusting the forward model in association with the minimisation of the misfit between the observed and model responses. Choosing to minimize the misfit between modelled and measured responses by increasing the roughness of a

model is not necessarily justified [*Simpson and Bahr*, 2005]. In the Occam approach, *Constable et al.* [1987] presented an inversion scheme to generate *smooth models* by introducing gradational conductivity contrasts as a regularization operator.

There are a variety of inversion codes available that are commonly used for 1D and 2D inversions. Those include REBOCC [*Siripunvaraporn and Egbert*, 2000], OCCAM 1D [*Constable et al.*, 1987] and 2D [*deGroot-Hedlin and Constable*, 1990], RLM2DI [*Rodi and Mackie*, 2001] (implemented in the Geosystem's software, WinGLink). The 2D resistivity models presented later were mainly generated using the program by *Mackie* [2002] and *Baba et al.* [2006] which is an anisotropic version of the Non-Linear Conjugate Gradients (NLCG) algorithm by *Rodi and Mackie* [2001]. The program by *Rodi and Mackie* [2001] is a finite-difference code that uses the NLCG method to minimize the objective function associated with the 2D isotropic inverse problem in order to find *regularised solutions* [*Tikhonov and Arsenin*, 1977]. The 2D anisotropic approximation presented by *Baba et al.* [2006] operates similarly to the isotropic approximation, but assumes the resistivity varies along anisotropy axes defined as parallel and perpendicular to the main axis of the regional geoelectric strike. Therefore, the resistivity matrix (Eq. 7.72) is characterized by a diagonal tensor and the anisotropic modelling is defined by three models; *xx* - horizontal resistivity across profile, *yy* - horizontal resistivity along profile, and *zz* - vertical resistivity. The TE and TM modes are now associated with the following equations:

$$\frac{\partial^2 E_x}{\partial^2 y} + \frac{\partial^2 E_x}{\partial^2 z} + i\omega\mu\frac{E_x}{\rho_{xx}} = 0, \tag{7.96}$$

$$\frac{\partial}{\partial y}(\rho_{zz}\frac{\partial H_x}{\partial y}) + \frac{\partial}{\partial z}(\rho_{yy}\frac{\partial H_x}{\partial z}) + i\omega\mu H_x = 0, \tag{7.97}$$

as the anisotropic inversion algorithm aims to solve for the following model vector [*Baba et al.*, 2006]:

$$\mathbf{m}(y,z) = \ln\begin{pmatrix}\rho_{xx}(y,z)\\ \rho_{yy}(y,z)\\ \rho_{zz}(y,z)\end{pmatrix}. \tag{7.98}$$

Furthermore, two types of regularizations are imposed on the objective function (Eq. 7.99). As for *Rodi and Mackie* [2001]'s program, the second term of the objective function define the smoothness of the final model. In the anisotropic version of the code [*Mackie*, 2002], a third term, which characterizes the closeness between the ρ_{xx}, ρ_{yy} and ρ_{zz} models, is added to the objective function. In this particular anisotropic inverse problem, the objective function is characterized by the following equation:

$$\phi(\mathbf{m}) = (\mathbf{d} - F(\mathbf{m}))^t\mathbf{V}^{-1}(\mathbf{d} - F(\mathbf{m})) + \tau_s(\mathbf{m} - \mathbf{m}_0)^t\mathbf{L}_s^t\mathbf{L}_s(\mathbf{m} - \mathbf{m}_0) + \tau_c\mathbf{m}^t\mathbf{L}_c^t\mathbf{L}_c\mathbf{m}. \tag{7.99}$$

where $\mathbf{d}$ is the data, F is the forward modelling operator, $\mathbf{m}$ is the unknown model, $\mathbf{m_0}$ is the a priori model and $\mathbf{V}$ is the covariance matrix. The terms $\mathbf{L_s}$ and $\mathbf{L_c}$ are the regularization operators expressing the imposed constraints respectively associated with the

smoothness and *closeness* regularizations. As seen on the objective function (Eq. 7.99), those two regularizations are parametrized by the smoothness parameter τ_s and the closeness parameter τ_c [*Baba et al.*, 2006]. Therefore, the anisotropic inversion code seeks suitable models with an imposed regularization constraint on the closeness of the three models in the three directions (xx horizontal resistivity across-profile, yy horizontal resistivity along-profile, and zz vertical resistivity). For an isotropic inversion, the closeness is set to a high value ($\tau_c = 100,000$) resulting in three models that are identical. When the closeness τ_c is set to 0, the three models become completely independent.

The 3D inversion results presented later were obtained using the 3D code WSINV3DMT [*Siripunvaraporn et al.*, 2005]. The code uses the *data space* approach presented by [*Parker*, 1994] and also used in the 2D inversion program REBOCC [*Siripunvaraporn and Egbert*, 2000]. The main advantage of the data space approach compared with the *model space* method [*Constable et al.*, 1987] is the reduction of memory usage. More details about the common inversion schemes used in MT can be found in *Siripunvaraporn* [2012]. For 3D synthetic modelling, the models shown later and associated synthetic data were generated from [*Mackie et al.*, 1994]'s 3D forward modelling algorithm as part of the Geosystem's commercial software WinGLink.

Part III

MODELLING OF NORTHERN TIBET

8 REVISED INDEPTH III 2D MODELLING

8.1 GLOBAL SETTINGS

In 1999, long period MT (LMT) and broadband MT (BBMT) data were collected in the north of the Tibetan Plateau. The INDEPTH phase III 600-line magnetotelluric profile [*Unsworth et al.*, 2004] crosses three major tectonic terranes of the northern Tibetan plateau: the Qiangtang terrane, the Songpan-Ganzi terrane and the eastern Kunlun-Qaidam terrane, respectively separated by the Jinsha River Suture and the Kunlun Fault (Fig. 8.1). Previous inversions [*Unsworth et al.*, 2004] of the 600-line data used both magnetotelluric modes (TE and TM) and vertical magnetic field data to derive a highly smoothed model (Fig. 8.2) that is characterized by a relatively laterally uniform, mid-crustal conductor extending from the southern end of the 600-line profile to the Kunlun Shan and interpreted to end abruptly at the Kunlun Fault. As a consequence, the fault which accommodates

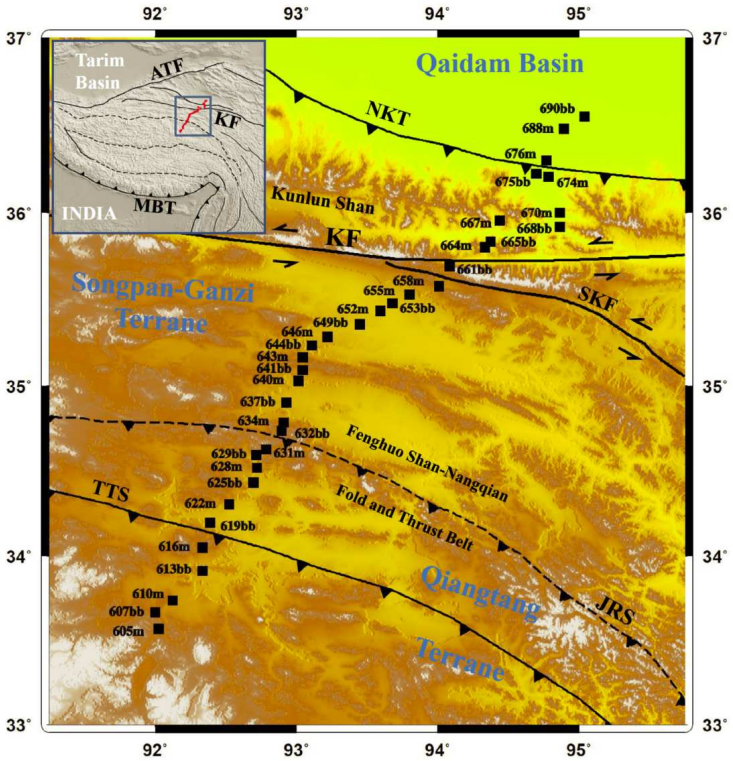

Figure 8.1: Location of the 600-line magnetotelluric stations associated with the regional tectonic settings. The map shows the locations of the long-period and broadband merged stations (m) as well as broadband-only stations (bb). ATF, Altyn Tagh Fault; KF, Kunlun Fault; MBT, Main boundary thrust; NKT, North Kunlun Thrust; SKF, South Kunlun Fault; JRS, Jinsha River Suture; TTS, Tanggula Thrust System.

the plateau's eastward extrusion, has been identified as a significant rheological boundary [*Unsworth et al.*, 2004] between weak, warm Tibetan crust [*Klemperer*, 2006] and the rigid eastern Kunlun-Qaidam block. The high conductivity of the middle and lower crust south of the Kunlun Shan was interpreted as partial melt [*Unsworth et al.*, 2004], consistent with previous interpretations of INDEPTH phase II magnetotelluric data farther south [*Chen et al.*, 1996; *Wei et al.*, 2001]. In anticipation of the INDEPTH IV magnetotelluric field campaign, a subset of 19 long-period magnetotelluric (LMT) stations and 35 BBMT stations from the 1999 INDEPTH III MT survey in northern Tibet were reanalysed and remodelled using modern techniques previously unavailable. In the revised study of the 600-line data, time series were not reprocessed. According to [*Unsworth et al.*, 2004], the time series were processed with processing codes from [*Egbert*, 1997; *Jones et al.*, 1989] using remote reference data when available. At common locations, the BBMT and LMT data were remerged considering the LMT data as the shifting reference for statics control.

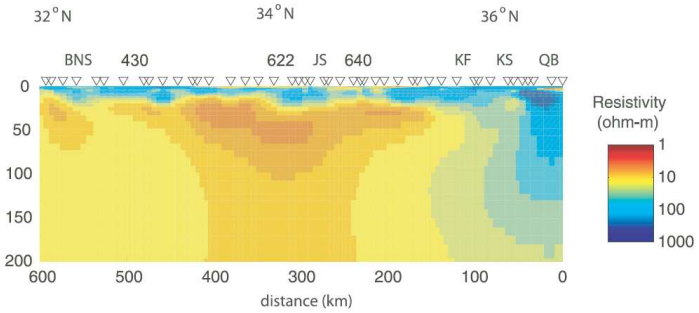

Figure 8.2: Previous MT model of the 600-line from *Unsworth et al.* [2004].

8.2 DATA ANALYSIS

The apparent resistivities and phases for each site are plotted for all components XX, XY, YX and YY in the appendix on INDEPTH III - SUPPLEMENTARY FIGURES (Fig. A.1).

8.2.1 *Phase Tensor and Induction Arrows*

As mentioned previously, the phase tensor is a good tool to characterize the dimensionality and distribution of regional conductivity structures. The phase tensor ellipses calculated from the INDEPTH III data show a relatively strong consistency between neighbour sites and periods revealing significant features of northern Tibet geology.

The skew angle β is reasonably low except for some longest periods. For those periods, the direction and shape of the ellipses can be quite chaotic (Fig. 8.3), revealing either the presence of significant 3D structures or bad data quality. For some sites, few long period data points had to be removed from the final decomposed data as they were inconsistent with the rest of the data. The mid-period ranges of few sites located in the Kunlun ranges also show some high skew angle values that are probably associated with small- to middle-scale 3D structures located beneath the Kunlun mountains.

There are different trends that can be highlighted from the phase tensor ellipses Φ_2. First, from the southern end of the profile to station number 22, the phase tensor geometric

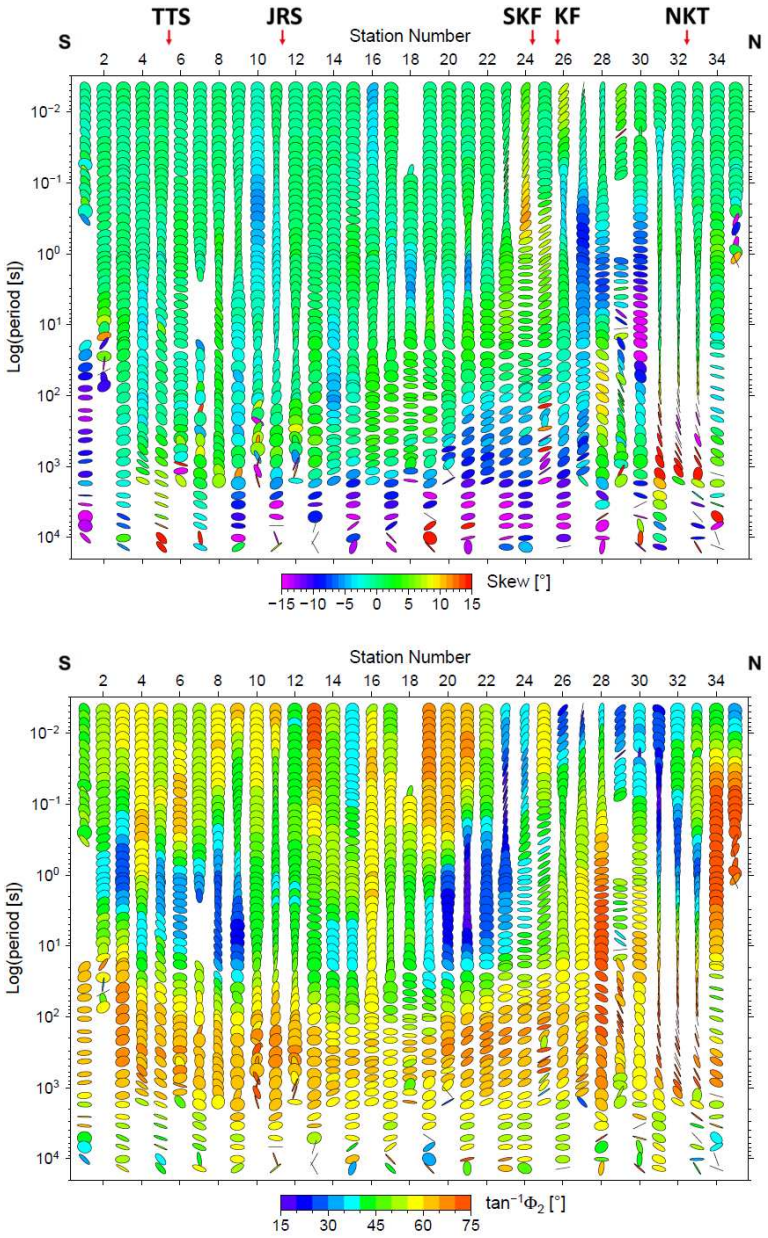

Figure 8.3: Phase tensor ellipses for each periods of each INDEPTH III sites. The ellipses are normalized by ϕ_{max} and filled with the **skew angle** β and the **geometric mean** Φ_2 ($\sqrt{\phi_{max}\Phi_{min}}$). The ellipses are plotted so that the horizontal axis corresponds to an east-west orientation.

mean Φ_2 is quite high between 0.001 s and 0.1 s and probably characterizes the shallow sediments of the Songpan-Ganzi terrane. This particular feature is likely to be shallow enough that it does not appear on the plot of the phase tensor ellipses with depth (Fig. 8.4). In the same station range, although Φ_2 was lower between 0.1 s and 10 s, it increases again for periods below 10 s. The high phases values at those periods likely characterize the substantial middle-to-lower crust conductor of northern Tibet modelled by [*Unsworth et al.*, 2004].

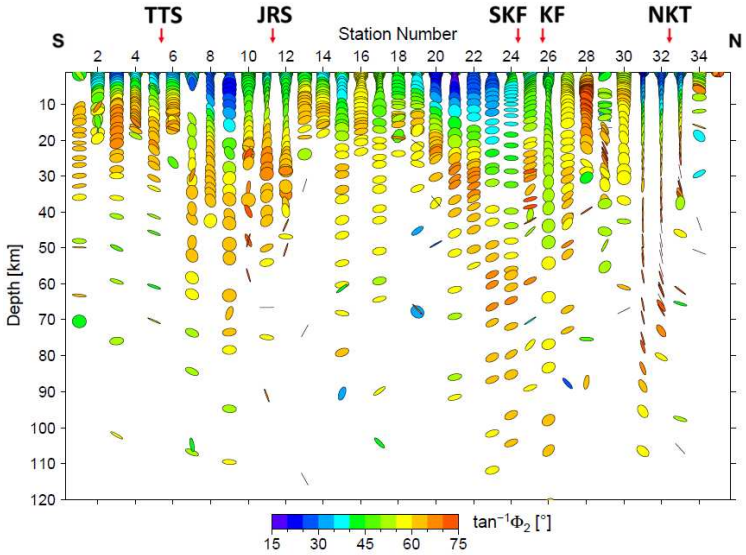

Figure 8.4: Phase tensor ellipses for each INDEPTH III sites and approximated penetration depths derived for each period from the impedance determinant. The ellipses are normalized by ϕ_{max} and filled with the **geometric mean** Φ_2 ($\sqrt{\phi_{max}\Phi_{min}}$). The ellipses are plotted so that the horizontal axis corresponds to an east-west orientation.

To the north, the effects of the high conductive Qaidam basin related to extensive salt deposits [*Kezao and Bowler*, 1986], are seen on stations 31, 32 and 33 as the major axes of the flattened ellipses point towards the north, whereas the sites 34 and 35 located right on top of the basin show strong Φ_2 values for periods below 0.02 s. The closer to the Qaidam salt layer the sites get, the less deep they sense (Fig. 8.4). Therefore, poor resolution for lower crustal structures can be expected in the northern end of the profile. Furthermore, for some sites, the depth penetration of the signal seems to vanish as it hits the crustal conductor located in the crust of the Qiangtang and Songpan-Ganzi terranes (Fig. 8.4). It is worth noticing that using the impedance tensor determinant to evaluate the penetration depth of the signal is only a first approximation as it defines some kind of average of all tensor's component. However, each component has a different penetration depth and it is shown later that in the quasi-2D case, the TE and TM mode will sense different depths and can sometimes complement each other in the modelling of deeper structures.

The real induction arrows can be useful in characterizing the presence of conductive structures. The pointing part of the arrows were omitted as Figure (A.3) was getting to complex and the focus here is mainly to check for the consistency in the orientations of the vectors rather than their sense. Furthermore, the main focus being on large scale conductive structures, the induction arrows were only plotted from 10 s to longer periods for more clarity in the plot. North of the profile, the induction vectors are orientated towards the conductive Qaidam basin. In the central and southern part of the profile, the real induction vectors are oriented more or less north-south as they are probably sensing the northern Tibet crustal conductor imaged previously by *Unsworth et al.* [2004]. Furthermore, the global orientation of the strongest real induction arrows suggests an east-west direction for the strike of the quasi-2D profile in agreement with the phase tensor and the surficial geology. Error estimates on the phase tensor parameters and on the length and orientations of the real induction arrows can be found in the appendix on INDEPTH

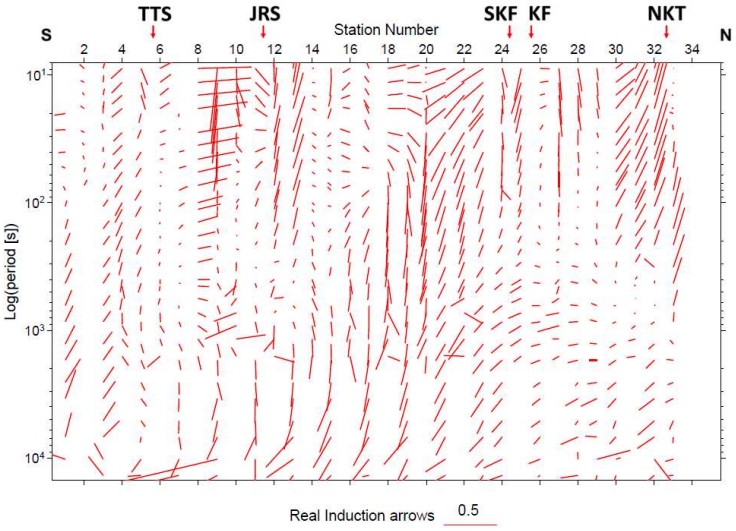

Figure 8.5: Real induction arrows directions for each periods (> 10 s) of each INDEPTH III sites. The arrows are plotted so that the horizontal axis corresponds to an east-west orientation. Only the direction but not the sense of each vector is plotted here in order to show a clearer trend of the distribution of the vectors' direction.

III - SUPPLEMENTARY FIGURES (Fig. A.2 and A.3). Those are relatively low except for few sites, particularly for some longer period sections associated to the tipper data. In consequence, during the modelling the error floor associated to the geomagnetic transfer function was set to a relatively high value of 0.1.

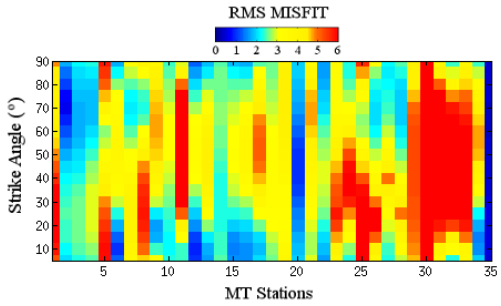

Figure 8.6: Multi-frequency (< 100 Hz), single site Groom-Bailey decomposition misfit associated with different strike angles. Station numbers increase to the north.

8.2.2 *Strike Analysis and Distortion decomposition*

The strike analysis and distortion decomposition was applied on the 600-line data using the program *Strike* by *McNeice and Jones* [2001] in order to determine the most appropriate strike direction and correct the data from galvanic effects. As presented in the MT method Chapter, the *Strike* algorithm extends the Groom-Bailey distortion decomposition [*Groom and Bailey*, 1989] to a multi-site and multi-frequency approach. Furthermore, the Niblett and Bostick depth approximation [*Jones*, 1983b] can also be used with the *Strike* program to investigate the variations in the geolectric strike orientation for different depth bands.

The strike analysis was applied in three different configurations for a better understanding of the geoelectric strike behaviour with depth and frequency.

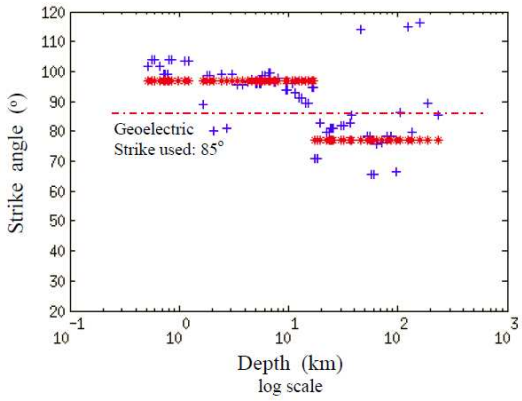

Figure 8.7: Multi-site, multi-depth strike analysis applied on several depth bands. Station Numbers increase to the North.

In order to check for the dependence on the geoelectric strike for each site of the 600 profile, a multi-frequency, single-site analysis was done by constraining the analysis to strike angles ranging from 5° to 90° and taken every 5° (Fig. 8.6). This range of strike azimuth covers all possible orientations for the geolectric strike azimuth direction due to the 90° ambiguity in its determination. Most sites seem to present a better fit to the distortion model for strike angles of $90° \pm 20°$. This trend appears to be even more restricted to the north, as the lowest RMS can only be reached for azimuths of $90° \pm 5°$. Outside this range the distortion model is badly fitted, making the 2D approximation more difficult.

Another approach in the evaluation of the strike azimuth was done by multi-site analysis applied on small depth bands to check the evolution of the whole profile's geoelectric strike with depth (Fig. 8.7). In this particular case, the strike analysis reveals two major trends in the estimates: an azimuth of N95°E characterizing mainly the upper crust [100 m - 15 km] and an azimuth of N75°E for the deeper crust and mantle structures [15 km - 300 km]. A strike angle of N85°E appears as a good compromise between the shallow and deeper parts of the profile. A similar study considering small frequency bands instead, showed the same behaviour.

Finally, *uncontrained* and 85°-*constrained* strike single-site, multi-depth decompositions were performed for both depth bands presented above. By comparing the associated Groom-Bailey decomposition misfits, Figure 8.8 highlights that the bad misfits present in the stations of the northern part of the profile are mainly restricted to shallower depth or high frequencies. The results show that a strike azimuth of N85°E confirm to be a good trade-off value for the geoelectric strike, particularly for the modelling of mid-crustal to upper mantle structures: the main areas of interest in this study. Therefore, those different approaches in the strike analysis led us to adopt a strike orientation of N85°E, in agreement with the east-west trend of the main geological structures and with the phase tensor ellipses and induction vector results.

Figure 8.9 presents the decomposed TE and TM responses of some sites representative of the 600 profile. Although some bad data points had to be removed before the modelling,

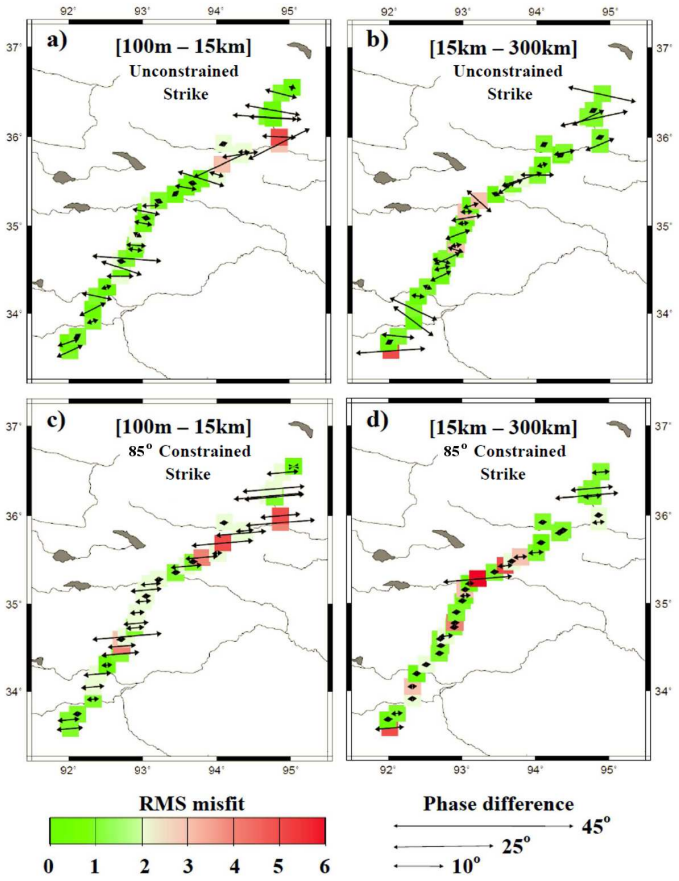

Figure 8.8: Comparison between Groom-Bailey decomposition misfits associated with unconstrained and 80°-constrained multi-frequency (< 10 Hz), single-site strike analyses for two particular depth bands.

most sites present reasonable data quality. In the southern and middle part of the profile, the responses are quite similar up to station 652m, except for a few sites such as site 631m, which could be affected by static shifts. Overall, those responses present a similar behaviour in the phase: high phases at short periods, then low phases between 1 s and 100 s before increasing again at longer periods. This behaviour was also well illustrated by the phase tensor pseudo-sections (Fig. 8.3). Furthermore, north of the station 652m, the resistivity levels associated with the apparent resistivity curves become higher. However, it is interesting to notice the particular behaviour of the phases as those remain substantially high (particularly the TM phase) and present a significant split between the TM and TE phases at longer periods consistent over a couple of neighbour sites (655m, 658m and 664m). On site 674m the huge difference in the apparent resistivity curves is likely due to the proximity of the Qaidam basin's salt deposits mentioned previously. This effect can also be seen on the TE phase response which shows a steep increase in the phase. Therefore, before the final modelling, some longer periods of the TE mode were removed at some sites as they were more affected by noise and distortion owing to the effect of the highly conductive Qaidam Basin bounding the northern edge of the profile [*Unsworth et al.*, 2004]. Furthermore, as it appeared the data for station 668bb was badly fitted by

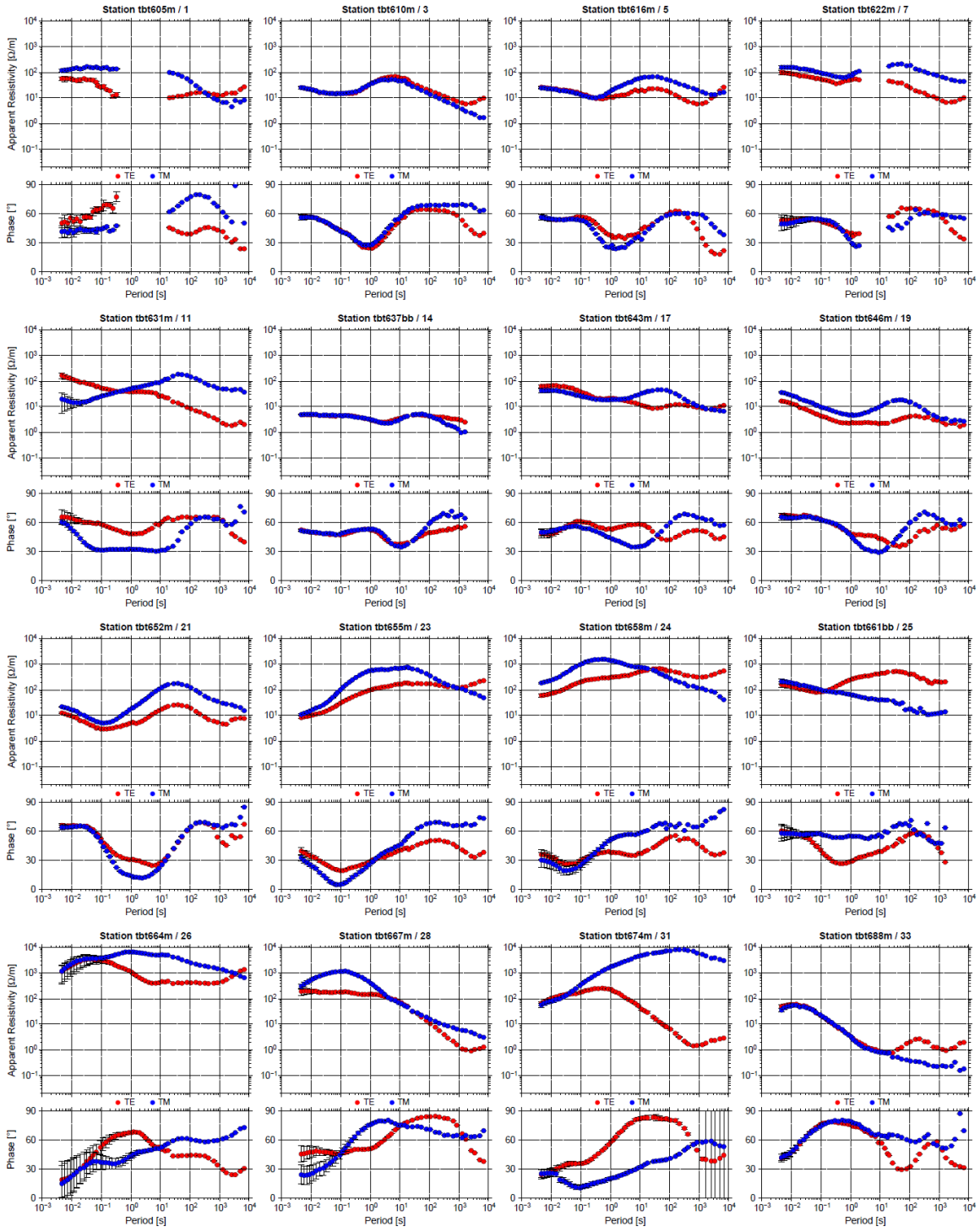

Figure 8.9: Comparison between the TE and TM responses of sites from the 600-line which have been decomposed to the N85°E strike direction using the *Strike* program [*McNeice and Jones*, 2001].

preliminary models, this station was not used for the final modelling of the data. Therefore, only 34 stations are used in the 2D modelling presented in the next section.

8.3 2D MODELLING

8.3.1 *Inversion Results*

Two models are presented in this section: global isotropic and anisotropic models of the 600 line (Fig. 8.10 and 8.12). Furthermore, a local anisotropic crustal model obtained using fewer stations and focusing on the upper to middle crust around the Kunlun Shan (Fig. 8.16) will be described in a later section. The models were obtained using the modified version of *Rodi and Mackie* [2001]'s 2D magnetotelluric inversion algorithm incorporating a trade-off parameter (closeness τ_c) for electrical anisotropy [*Mackie*, 2002; *Baba et al.*, 2006]. As mentioned in the MT method chapter, the 2D anisotropy problem is restrictively solved by assuming that the anisotropy axes are parallel and perpendicular to the main axis of regional geoelectric strike, an assumption valid for this region but not generally applicable. Anisotropic modelling defines three models; xx-horizontal resistivity across-profile, yy-horizontal resistivity along-profile and zz-vertical resistivity. It is worth mentioning the MT method is less sensitive to vertical conductive features than to horizontal ones. Furthermore, both TE and TM magnetotellurics modes are sensitive to different horizontal conductivities. Whereas the TE mode is mainly dependent on the along-strike conductivity, the TM mode is more sensitive to both across-strike and vertical conductivity [*Baba et al.*, 2006]. Therefore, the yy and zz models are usually quite similar.

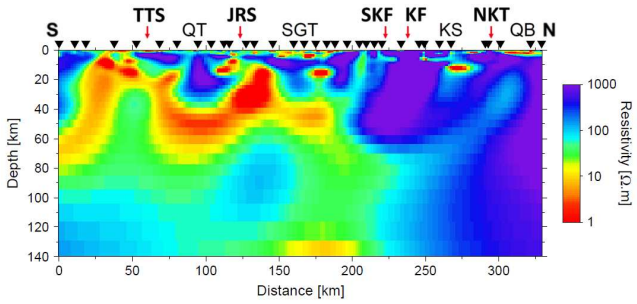

Figure 8.10: Global isotropic 2D resistivity model of the 600-line. TTS, Tanggula Thrust System; QT, Qiangtang Terrane; JRS, Jinsha River Suture; SGT, Songpan-Ganzi terrane; SKF, South Kunlun Fault; KF, Kunlun Fault; KS, Kunlun Shan; NKT, North Kunlun Thrust; QB, Qaidam Basin.

The data were inverted simultaneously for both TE and TM modes and also the geomagnetic transfer function. For the main isotropic and anisotropic models, the data were inverted for TM, TE modes and the vertical magnetic field (Hz) transfer function, allowing the inversion for static shifts for few selected sites. Error floors of $8\% - 3\%$ and $10\% - 3\%$ were respectively applied for TM and TE apparent resistivity and phase, as well as 0.1 for the geomagnetic transfer function. The smoothness trade-off τ_s used was 1 and the models closeness τ_c was set to 100000 for the isotropic inversion and to 1 for the anisotropic case. More details on the misfit of the TE and TM apparent resistivity and phase can be found for the anisotropic model in the appendix on INDEPTH III - SUPPLEMENTARY FIGURES in Figures A.4 and A.5. Both isotropic and anisotropic models are consistent on a

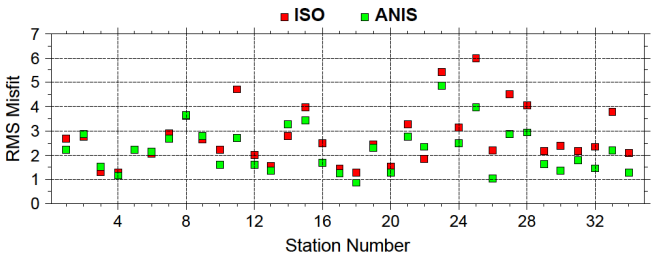

Figure 8.11: Difference between the anisotropic (green) and isotropic (red) RMS misfits. Station numbers increase to the north.

lithospheric scale and exhibit several robust features that were not evident in the previous isotropic solutions [*Unsworth et al.*, 2004], but show significant differences in the middle-lower crust of the Kunlun Shan area. This is particularly reflected in the net improvement of the RMS misfit for a number of sites located in the northern part of the profile (Fig. 8.11), when the extension of the crustal conductor is allowed in the profile direction only (yy model). From now on, when referring to the 600-line model in further discussions, only the anisotropic model is considered. The previous inversions of the data from the 600-line presented in *Unsworth et al.* [2004] used both magnetotelluric modes and vertical magnetic field data to derive highly smoothed models that were all characterized by a relatively laterally uniform, mid-crustal conductor extending from the southern end of the 600-line profile to the Kunlun Shan and ending abruptly at the Kunlun Fault. The new 2D anisotropic revised resistivity model for the INDEPTH III 600-line fits the data better (both in global root-mean-square (RMS) misfit and in local misfits) than the previous model, is more focussed, less smooth, exhibits greater lateral variability and particularly highlights electrical anisotropy in the northern part of the profile (Fig. 8.12).

As mentioned in the MT method chapter, simple small-scale 3D structures present in the subsurface can lead to the shifts of the apparent resistivity curves up to one order of magnitude. However, the correction for statics shifts is not straightforward. In order to solve for the static shifts, the data was first inverted for the phase only. Observed and calculated responses were then compared between each other but also with the responses of neighbour sites. When significant shifts in the responses between two neighbour sites were observed in both measured and calculated responses, the data was set to be corrected for static shifts in the final inversions. The strongest static shifts corrections are mainly found in the TE responses of sites located in the Kunlun Shan and the TM responses of sites located just north of the Jinsha suture (Fig. 8.13).

A first evaluation of the sensitivity associated with the different model structures can be plotted in the form of sensitivity maps (Fig. 8.14). The sensitivity matrix is computed from the Jacobian matrix during the inversion [*Baba et al.*, 2006] and can then be plotted as sensitivity maps which highlight the structures of strong influence on the perturbation of the data [*Ledo et al.*, 2004]. Using sensitivity maps, deeper structures can be ruled out considering a sensitivity threshold. Although [*Schwalenberg et al.*, 2002] mentioned the choice of that limit remains an open question, [*Brasse et al.*, 2002; *Ledo et al.*, 2004] used a sensitivity threshold of 10^{-4} below which, model structures can be ruled out. Both

xx and yy sensitivity maps have a good coverage of the models (Fig. 8.14). The areas of high sensitivity are mainly associated with the main crustal conductive anomaly, as well as the anisotropic feature observed beneath the north of the profile. Therefore, the extension of the crustal conductor to the north only observed on the yy model is not an artefact. Furthermore, for deeper structures, whereas the xx model looses sensitivity

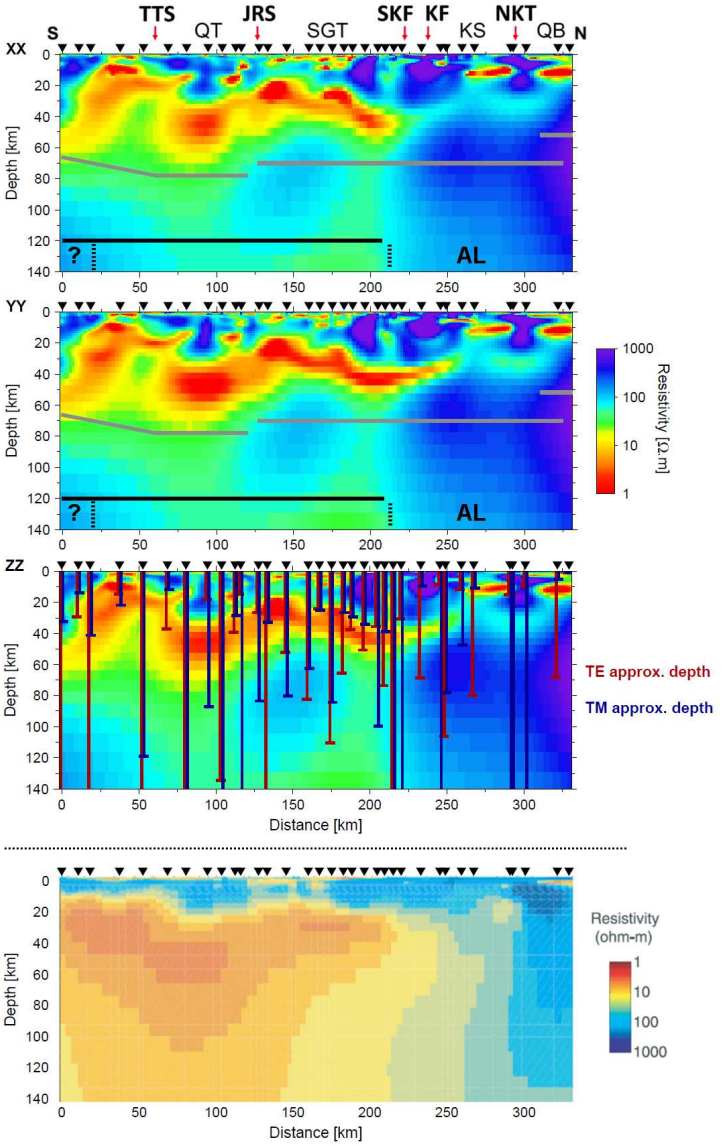

Figure 8.12: Global anisotropic 2D resistivity model of the 600-line. The approximate Niblett-Bostick penetration depths [*Jones*, 1983b] of TE and TM modes are plotted on top of the zz model. The Moho depth [*Vergne et al.*, 2002; *Karplus et al.*, 2011] is highlighted by the grey lines. The black line shows the lithosphere-asthenosphere boundary location for a thin Tibetan lithosphere in the north part of the plateau imaged by seismic receiver functions [*Zhao et al.*, 2011]. TTS, Tanggula Thrust System; QT, Qiangtang Terrane; JRS, Jinsha River Suture; SGT, Songpan-Ganzi terrane; SKF, South Kunlun Fault; KF, Kunlun Fault; KS, Kunlun Shan; NKT, North Kunlun Thrust; QB, Qaidam Basin; AL, Asian lithosphere. The previous isotropic model of the 600-line from *Unsworth et al.* [2004] is also highlighted.

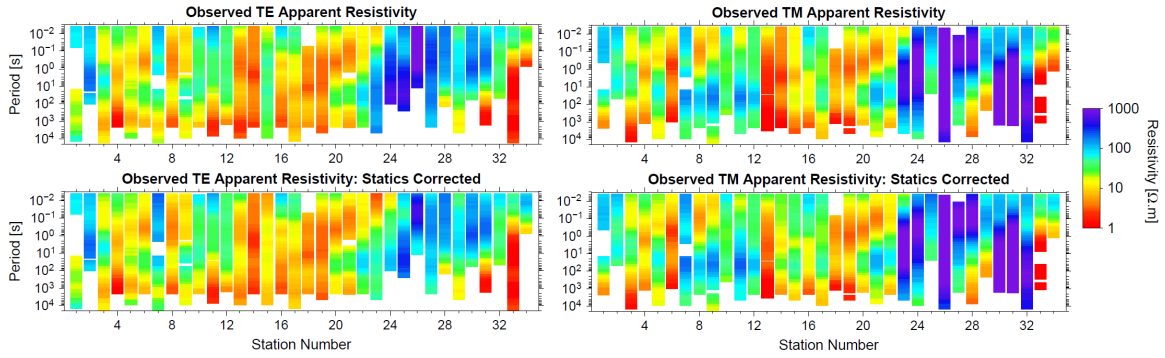

Figure 8.13: Comparison between the TE and TM apparent resistivities before and after static shift correction using the coefficients determined for selected sites during the inversion of the 600-line data. Station numbers increase to the north.

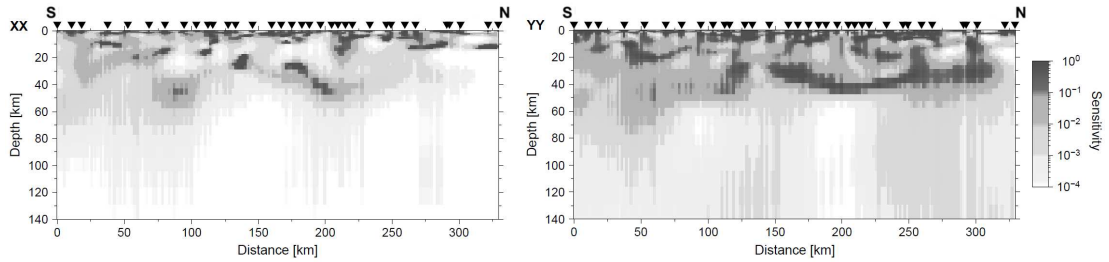

Figure 8.14: Sensitivity maps associated with the 600-line global anisotropic model. The white areas reflect the lack of sensitivity on the corresponding model structures due to sensitivity values below 10^{-4}.

for the central and northern structures below 60 km, the yy maps show a relatively strong sensitivity. This observation reflects the complementarity of both TE and TM modes which is also characterized by the variations in the penetration of the signals associated with both modes (Fig. 8.12). Further investigations on the resolutions of the deeper structures are also highlighted from the forward modelling resolution tests presented on Figures 8.17 and 8.18, which are discussed in a later section.

Figure 8.15 shows the main along-strike and across-strike anisotropic structures characterizing the 600-line model. It appears from the global anisotropic inversion that all anisotropic anomalies are located in the crust. The anisotropic INDEPTH III model particularly highlights an extension of the main conductive crustal anomaly to the north past the Kunlun fault in the yy direction, that is, the profile direction perpendicular to the fault. This particular feature is more explicit in the focussed inversion of few sites located only around the Kunlun Shan area presented in a later section.

8.3.2 *Main Crustal Anomaly*

As mentioned previously, conductive materials found in the Earth include metallic minerals, graphite, molten rocks and aqueous (ionic) fluids [*Jones*, 1992]. It is possible that metallic minerals and graphite exists locally in Tibet [*Li et al.*, 2003]. However, since the main crustal anomaly beneath the Qiangtang and Songpan-Ganzi terranes (Fig. 8.12) crosses

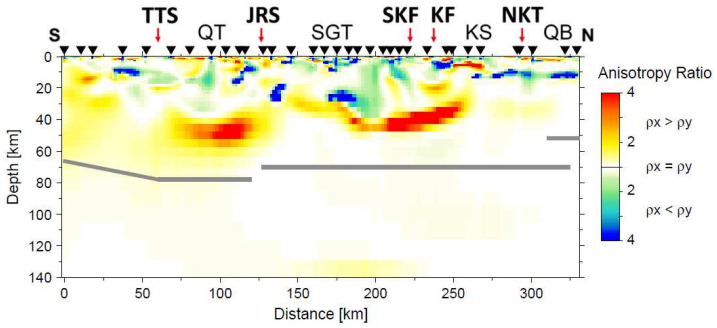

Figure 8.15: Anisotropic differences between the xx and yy models. The resistivity ratio between the xx and yy models are also highlighting the areas of crustal anisotropy: blue areas correspond to structures which are more conductive along-strike whereas the red areas show the anisotropic structures which are more conductive across-strike (profile direction). The Moho depth [*Vergne et al.*, 2002; *Karplus et al.*, 2011] is highlighted by the grey lines. TTS, Tanggula Thrust System; QT, Qiangtang Terrane; JRS, Jinsha River Suture; SGT, Songpan-Ganzi terrane; SKF, South Kunlun Fault; KF, Kunlun Fault; KS, Kunlun Shan; NKT, North Kunlun Thrust; QB, Qaidam Basin.

major terrane boundaries as it extends further south in the Lhasa terrane [*Wei et al.*, 2001], graphite and metallic minerals are more than likely not responsible for the observed large spatial extend of the crustal conductive anomaly. Furthermore, whereas in southern Tibet the observed conductive anomaly was interpreted as a combination of melt and aqueous fluids [*Unsworth et al.*, 2005], the crust of northern Tibet is likely to present no widespread concentrations of aqueous fluids [*Rapine et al.*, 2003]. Therefore, due to the presence of temperature high enough to generate partial melting of crust in northern Tibet [*Owens and Zandt*, 1997; *Mechie et al.*, 2004], the main crustal anomaly observed on the resistivity models is more than likely mainly related to widespread partial melting of the middle-to-lower crust.

The crustal conductivity structure in the model exhibits marked vertical offsets beneath the surface traces of the Tanggula thrust system (TTS) and the Jinsha River suture (JRS), show convincing spatial correlations with locally mapped tectonic features (Fig. 8.12). Lateral variation in conductivity observed in the conductive layer can be the result of changes in porosity within the layer, in layer thickness, in the degree of melting and in the degree of interconnectivity of the melt phase [*Li et al.*, 2003]. Receiver function analysis on teleseismic data [*Vergne et al.*, 2002] highlights Moho steps located beneath the main reactivated sutures. Although, *Kind et al.* [2002] imaged a displacement in the Moho of 2 to 3 km associated with the Cenozoic reactivation of the Jinsha River suture, according to *Wittlinger et al.* [1996] the Jinsha suture Moho offset could be as big as 15 km to account for the variations in the seismic time delays observed between both side of the suture. Surface-elevation homogeneity across the JRS, in contrast to observed irregular Moho geometry [*Wittlinger et al.*, 1996; *Vergne et al.*, 2002] is explained by weak middle-lower crust, mapped by the magnetotelluric model, that decouples crust-mantle boundary deformation. This decoupling is characterized by the offset observed in the conductive layer across the suture (Fig. 8.12). North of the Tanggula Shan, a similar behaviour is observed across the TTS.

8.3.3 *Upper Mantle*

Due to the presence of strong crustal conductors, particularly in the southern and middle sections of the 600 profile, obtaining a good interpretation of the mantle structures can be quite challenging. In order to investigate the resolution on mantle structures, the resistivity structure of the anisotropy resistivity models were modified (Fig. 8.17 and 8.18). For each station, the global data misfit of the perturbed models were compared to the misfit associated with the original anisotropic model. The responses were also compared for some key sites, whose penetration depths are substantially high (Fig. 8.12). For ***test a***, the crustal conductor was extended to the upper mantle to check for the possible extension of the crustal conductive anomaly to the mantle. In ***test b***, the validity of the deep resistor present at the southern end of the profile was checked by replacing the model structure by a more conductive deep mantle. In ***test c***, the resolution of the deep conductive structure in the middle of the profile was evaluated by adding a more resistive mantle. Finally, for ***test d*** a more conductive deep mantle was added in the northern part of the profile to check the resolution on the resistive mantle present in the 600 model. From this study, it can be concluded that most of the mantle features are not artefacts. However, due to the presence of the strong crustal conductor some effects on the responses related to the model perturbations are not particularly significant. However, it is clear that the resolution of the deep (> 120 km) middle part of the profile is not well resolved at all, as the sites global misfits are barely affected.

Due to the resistivity constraints inferred by the new anisotropic model and the results of the study presented above, the upper mantle beneath the northern Tibetan terranes is not as conductive as the crust, which indicates that the upper mantle cannot contain as great a volume of interconnected melt. Furthermore, owing to the presence of the strong crustal conductors the resolution of the middle of the profile is poor for deeper structures but in the north and the south of the profile the resolution is reasonably better. North of the SKF, the upper mantle is far more resistive and must be characterized by colder temperatures and therefore stiffer rheological conditions. In the southern edge of the profile, the deeper part of the mantle (> 100 km depth) is relatively resistive (Fig. 8.17). As the crustal conductor can reduce the resolution of deeper structures, the mantle resistivity imaged by the magnetotelluric model is a minimum bound [*Jones*, 1999] and the true resistivity of this particular feature is likely to be higher. The widespread melt in the northern Tibetan crust, characterized by the conductivity anomaly, is in agreement with the presence of a thin Tibetan lithosphere beneath northern Tibet [*McNamara et al.*, 1997]. The model highlights resistive mantle at a depth of 140 km in the south of the profile, which does not agree with thin Tibetan lithosphere extending farther south of the Bangong-Nujiang suture zone. The resistive feature is too resistive to corroborate the extension of the thin Tibetan plate model [*Zhao et al.*, 2011] further south than the middle of the Qiangtang terrane but is not deep enough to represent the Asian plate model from *Zhao et al.* [2011]. Although, its interpretation remains enigmatic (Fig. 8.12), it could be interpreted as the sub-horizontal underthrusting of Indian lithosphere beneath most of Tibet [*Ni and Barazangi*, 1983; *Zhou and Murphy*, 2005]. In the north of the profile, the mantle high resistivity is in agreement with the model of Asian lithosphere subduction [*Tapponnier et al.*, 2001; *Kind et al.*, 2002; *Zhao et al.*, 2011]. However, it could also be related

to a progressive increase in the depth of the lithosphere-astenosphere boundary (LAB) from a thin Tibetan lithosphere to a thicker Asian lithosphere in the north as seen in the model of [*Jimenez-Munt et al.*, 2008] based on the removal of gravitationally unstable thickened lithosphere in northern Tibet [*England and Houseman*, 1989; *Molnar et al.*, 1993].

8.3.4 *Focussed Anisotropic Crustal Model*

In order to investigate in more details the anisotropic feature observed in the crust beneath the Kunlun fault, only 18 sites from the 600 transect, located around the fault were remodelled for periods lower than 1000 s. The geolectric strike was also reanalysed considering only the selected sites leading to a strike estimate of N75°E, still in agreement with the main geological structures. The decomposed data was then modelled using the same 2D anisotropic algorithm [*Mackie*, 2002]. The data were inverted for TM, TE modes and the vertical magnetic field (Hz) transfer function. Error floors of $8\% - 3\%$ and $10\% - 3\%$ were respectively applied for TM and TE apparent resistivity and phase, as well as 0.1 for the geomagnetic transfer function. The smoothness trade-off τ_s used was 1 and the models closeness τ_c was 0.3. More details on the global data misfit for each 18 stations, detailed misfit of the TE and TM apparent resistivity and phase as well as sensitivity maps can be

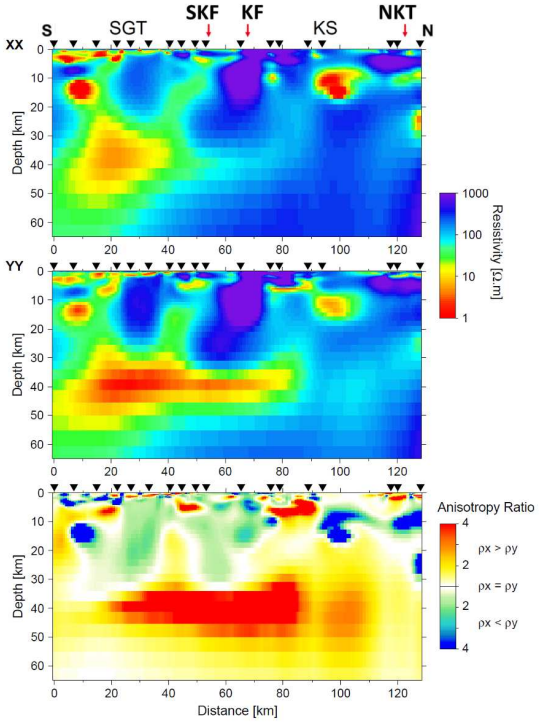

Figure 8.16: Local crustal anisotropic 2D modelling representing only a section of the 600-line focused on the Kunlun Fault area. The resistivity ratio between the xx and yy models are also highlighting the areas of crustal anisotropy: blue areas correspond to structures which are more conductive along-strike whereas the red areas show the anisotropic structures which are more conductive across-strike (profile direction). SGT, Songpan-Ganzi terrane; SKF, South Kunlun Fault; KF, Kunlun Fault; KS, Kunlun Shan; NKT, North Kunlun Thrust; QB, Qaidam Basin.

found in the appendix on INDEPTH III - SUPPLEMENTARY FIGURES in Figures A.8, A.6, A.7and A.9 respectively. The focussed anisotropic modelling highlights a more explicit penetrative extension of the mid-crustal conductive anomaly to the north, crossing the upper-crustal sharp resistivity contrast characterizing the subvertical Kunlun Fault (Fig. 8.16). It can be seen from the sensitivity maps presented in the appendix on INDEPTH III - SUPPLEMENTARY FIGURES, that the conductive structures are well resolved (Fig. A.9). The main resistive feature (> 1000 Ω.m) observed on the models, located just north of the Kunlun fault and extending to a depth of 30 km, likely defines extruded Proterozoic basement and plutonic intrusions characteristic of the Kunlun Shan [*Cowgill et al.*, 2003]. Furthermore, the lateral extent of the mid-crustal conductor north of the Kunlun fault appears to be around 30 km. It is discussed later in the chapter on Synthetic modelling that the apparent extend of the conductive structure observed in the MT models is likely to be underestimated. The resistive structure located just south of the NKT at a depth inferior to 5 km is likely to be part of the Kunlun Batholith, a significant feature of the north Kunlun ranges [*Yin and Harrison*, 2000]. Finally the crustal conductor observed in the upper crust beneath the middle of the Kunlun Shan could either be related to the effects of the conductive Qaidam basin on the TE mode, but might also be associated to the presence of upper crustal fluids involved in the north Kunlun thrust system.

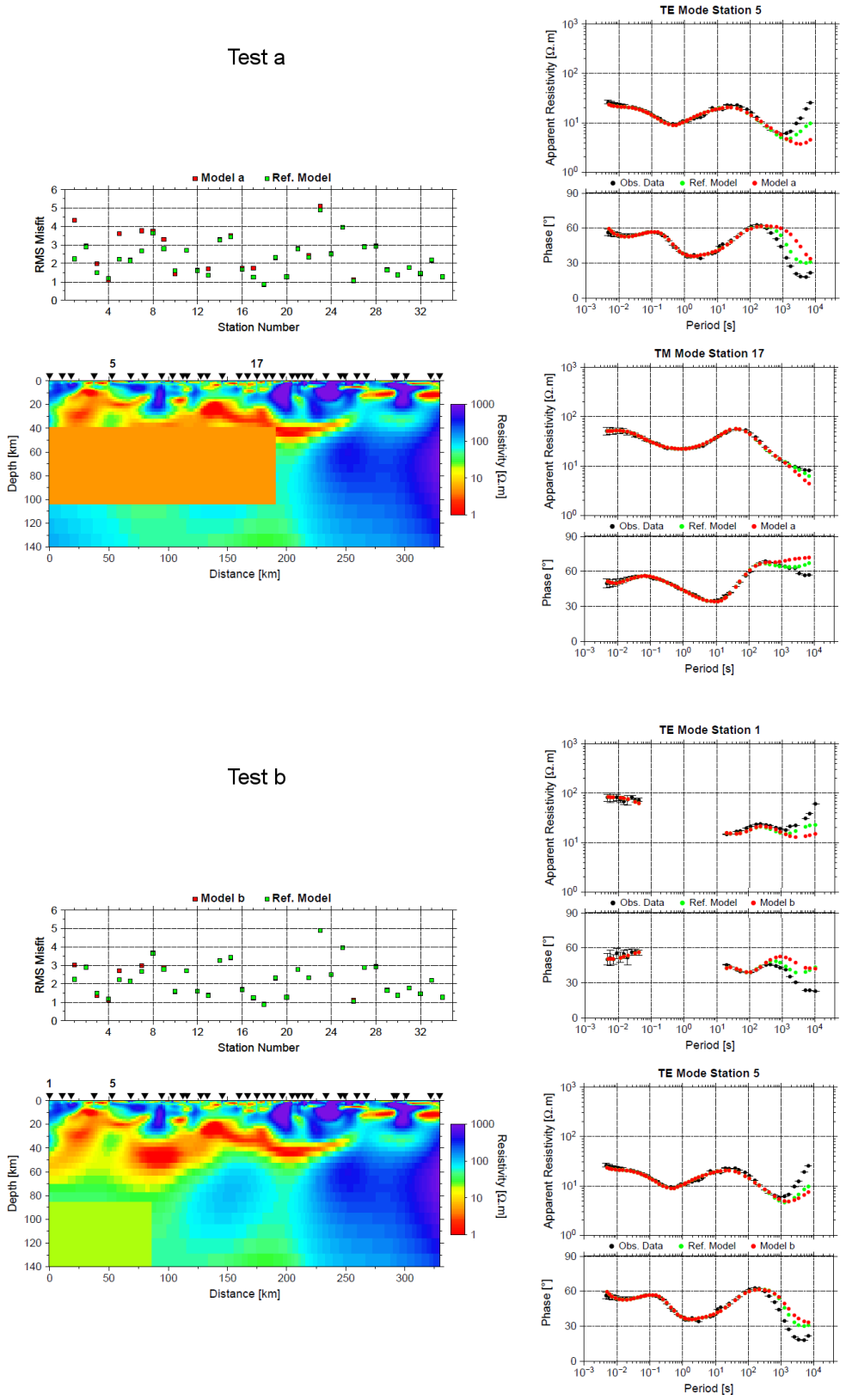

Figure 8.17: **Resolution tests a and b for the INDEPTH III model**: comparison between the responses associated with the final anisotropic model of the 600-line or reference model (green) and the responses generated by forward modelling of perturbed models (red). Although only the perturbation on the yy model is shown here, all models (xx, yy and zz) were modified the same way.

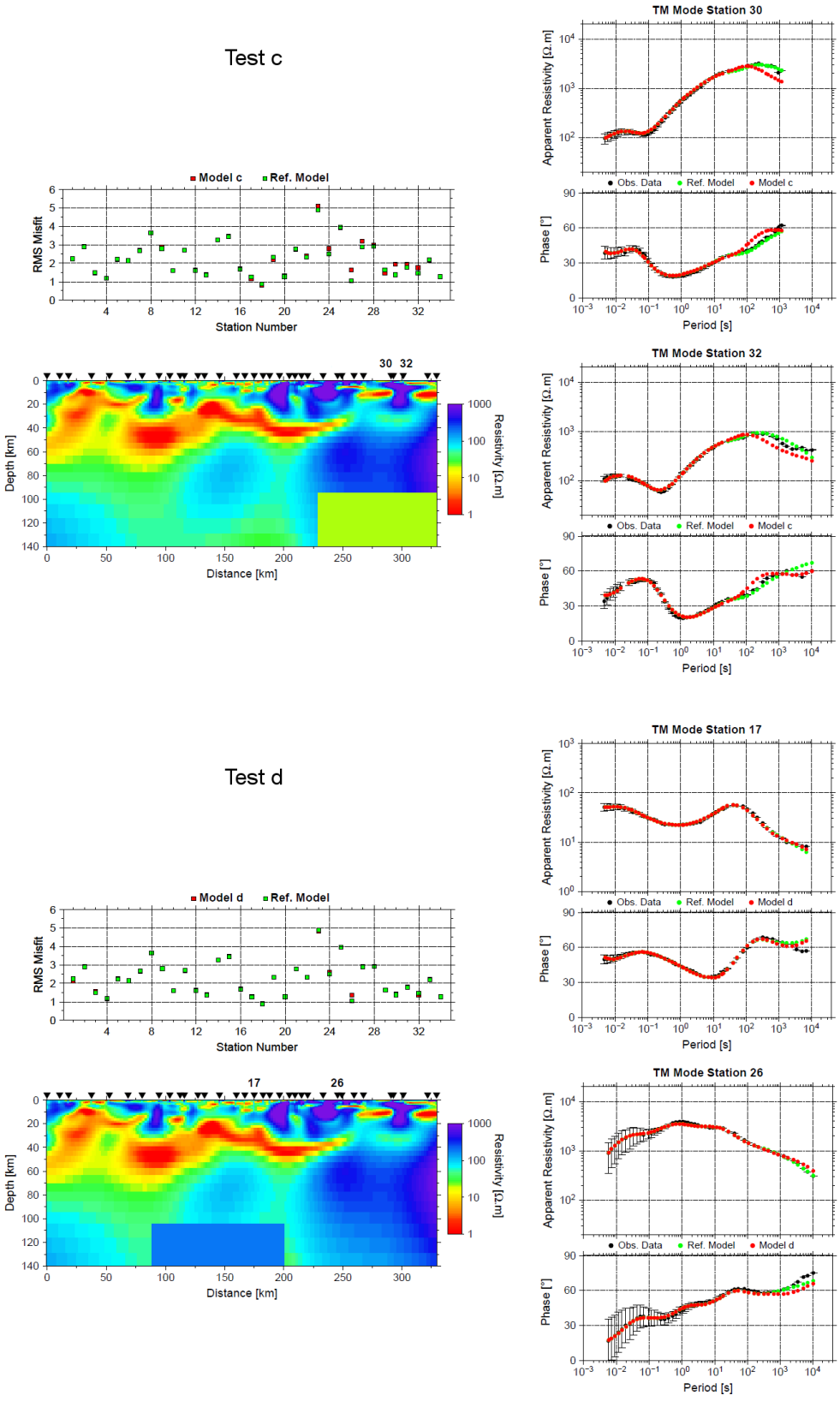

Figure 8.18: **Resolution tests c and d for the INDEPTH III model**: comparison between the responses associated with the final anisotropic model of the 600-line or reference model (green) and the responses generated by forward modelling of perturbed models (red). Although only the perturbation on the yy model is shown here, all models (xx, yy and zz) were modified the same way.

9 INDEPTH IV 2D MODELLING

9.1 PROFILE LOCATION

The INDEPTH IV data were collected between late spring and early summer 2010 and defines the 6000 profile. As seen on Figure 9.1, the new MT profile is located east of the INDEPTH III 600-line presented on the previous chapter and extends from the middle of the Songpan-Ganzi terrane, in the western Bayan Har Shan, to the southern edge of the Qaidam basin. The INDEPTH III and IV profiles become almost aligned in the Qaidam basin as they meet up south of the north Kunlun thrust (NKT). The 6000 MT transect is aligned with the INDEPTH IV seismic profile previously acquired in the area [*Karplus et al.*, 2011]. The 6000 profile considered here consists on 13 long-period magnetotelluric

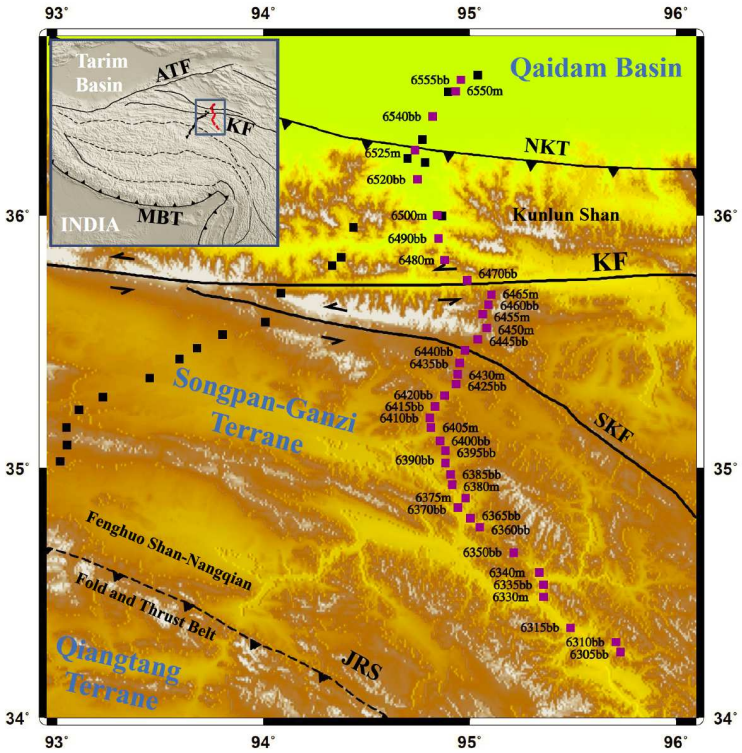

Figure 9.1: Location of the INDEPTH IV 6000-line magnetotelluric stations (purple) associated with the regional tectonic settings. The map shows the locations of the long-period and broadband merged stations (m) as well as broadband-only stations (bb). The black squares represent the neighbour 600-line sites locations. ATF, Altyn Tagh Fault; KF, Kunlun Fault; MBT, Main boundary thrust; NKT, North Kunlun Thrust; SKF, South Kunlun Fault; JRS, Jinsha River Suture.

(LMT) stations and 38 broadband magnetotelluric (BBMT) stations. It is worth noticing, that more sites were available to characterize the profile but were not used due to either

the mismatch of some LMT sites locations with BBMT sites or the high proximity of neighbour sites, in which case only the best of the two was chosen. Furthermore, few more LMT sites were recorded farther north of the profile mapped on Figure 9.1. However, the data was strongly affected by the salt deposits of the Qaidam basin and were discarded from the final set of data considered for analysis and modelling. More details about the INDEPTH IV acquisition survey have also been described in the MT method chapter. All the LMT sites were processed using *Smirnov* [2003]'s processing code. The BBMT data, kindly provided by the China University of Geosciences, Beijing (CUGB) were processed by the CUGB group using the commercial code from Phoenix company based on *Jones and Jödicke* [1984]. Similarly to the 600-line data, the BBMT and LMT data were remerged at common locations, considering the LMT data as the shifting reference for statics control.

9.2 DATA ANALYSIS

The apparent resistivities and phases for each site are plotted for all components XX, XY, YX and YY in the appendix on INDEPTH IV - SUPPLEMENTARY FIGURES (Fig. B.1).

9.2.1 *Phase Tensor and Induction Arrows*

Compared to the INDEPTH III data, the phase tensor results present a better overall consistency between neighbour ellipses (Fig. 9.2). As presented in the appendix on INDEPTH IV - SUPPLEMENTARY FIGURES, the errors on the ellipses parameters are quite significant at high frequencies (Fig. B.2). This is mainly due to the presence of high errors in the phase responses at those frequencies which are highlighted later on Figure 9.8. However, the results for periods higher than 1s can be considered robust enough as the errors on the ellipses become relatively low.

The skew angle β is globally low and roughly comprised between -5° and 5°, but some sites and periods present higher values, particularly for the longest periods (1000 s to 10000 s), which was also observed for the 600-line data. However, as the ellipses principal axes directions still present some consistency over several periods and stations, an approximate 2D configuration may still be valid *Caldwell et al.* [2004].

The results from the last northern six sites located at the northern edge of the profile are once again revealing the presence of the conductive Qaidam basin to the north (Fig. 9.2). First of all, the sites 33, 34 and 35 are likely sensing the basin from periods lower than 0.1 s as the major axes of the ellipses points towards the north direction with almost flat ellipses, reflecting a strong difference between Φ_{min} and Φ_{max}. Furthermore, the sites 36, 37 and 38 are likely located above the strongly conductive salt layer characteristic of the southern edge of the Qaidam basin. For those sites, the Φ_2) estimates are high for most periods (Fig. 9.2. When the ellipses are plotted with depth, the attenuation for those three sites is quite significant since they do not penetrate deeper than 15 km.

One striking similarity with the INDEPTH III data is the high Φ_2 values above 10 s or deeper than 15-20 km, likely characterising the northern Tibet crustal conductor imaged previously by *Unsworth et al.* [2004]. Moreover, compared to the 600-line data, the INDEPTH IV data appear to be less attenuated as more ellipses are reaching depths deeper than 120 km (Fig. 9.3). Finally, beneath 20 km (or periods higher than 5 s) in between sites 10 and 16, the phase tensor ellipses pseudo-sections show significantly flattened ellipses.

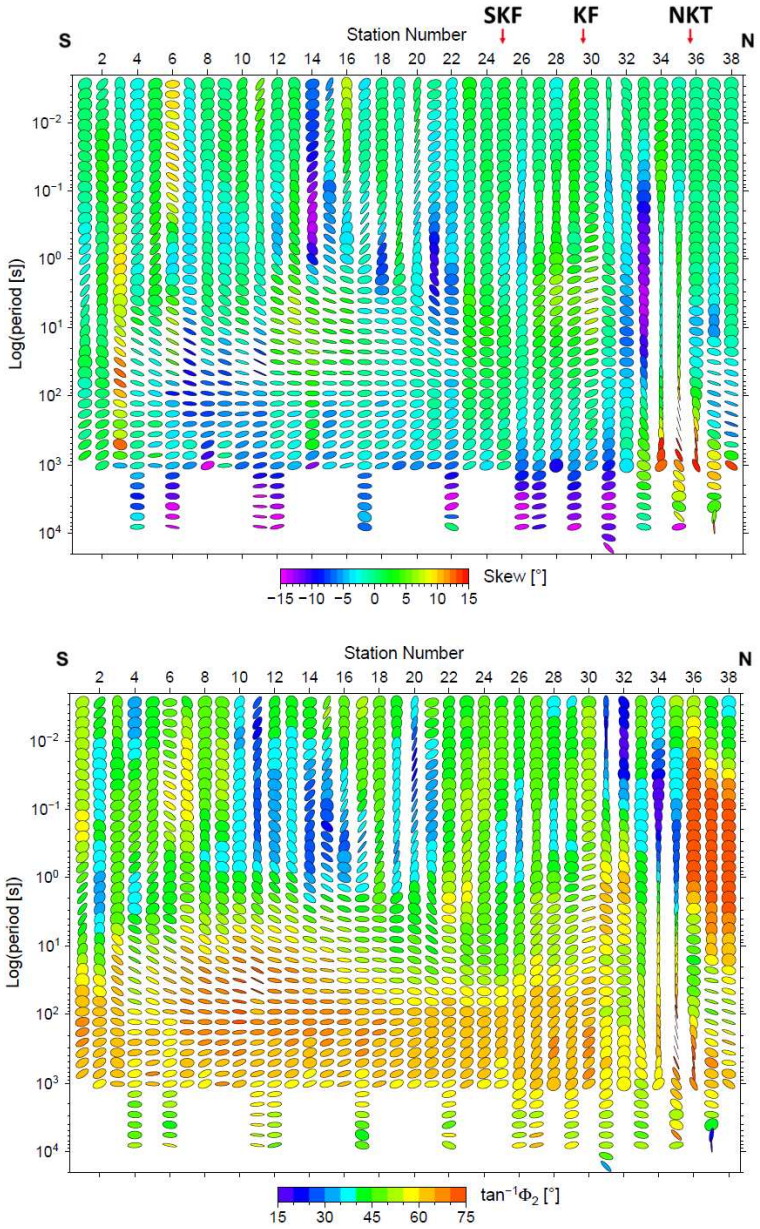

Figure 9.2: Phase tensor ellipses for each periods of each INDEPTH IV sites. The ellipses are normalized by ϕ_{max} and filled with the **skew angle** β and the **geometric mean** Φ_2 ($\sqrt{\phi_{max}\Phi_{min}}$). The ellipses are plotted so that the horizontal axis corresponds to an east-west orientation.

This interesting feature not so clearly seen on the 600-line data characterizes a strong preferred orientation of the inductive currents in the crust, and therefore a preferred orientation of the crustal conductor. It is worth noticing that those ellipses are also defined by a relatively high skew angle ($|\beta| \sim 10°$). Finally, as for the INDEPTH III data, most ellipses main axes show an east-west orientation trend in agreement with the orientation of the main sutures of northern Tibet.

Although, the errors on the length and orientation of the real induction arrows, presented in the appendix on INDEPTH IV - SUPPLEMENTARY FIGURES, are quite high (Fig.

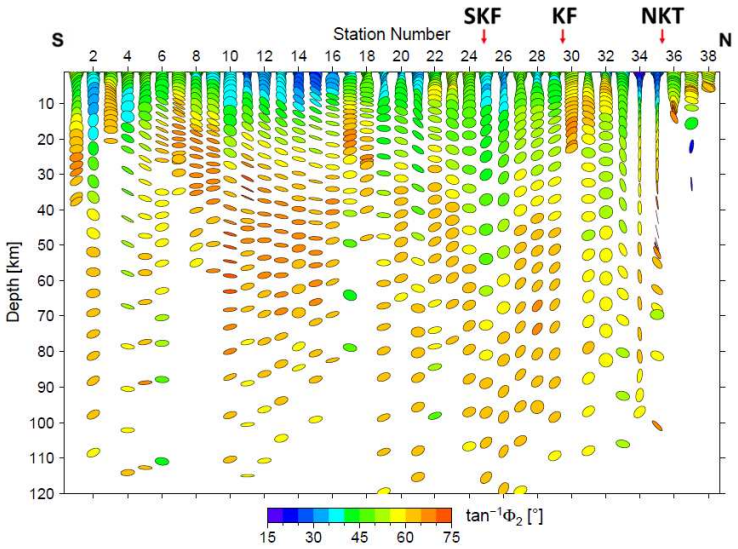

Figure 9.3: Phase tensor ellipses for each INDEPTH IV sites and approximated penetration depths derived for each period from the impedance determinant. The ellipses are normalized by ϕ_{max} and filled with the **geometric mean** Φ_2 ($\sqrt{\phi_{max}\Phi_{min}}$). The ellipses are plotted so that the horizontal axis corresponds to an east-west orientation.

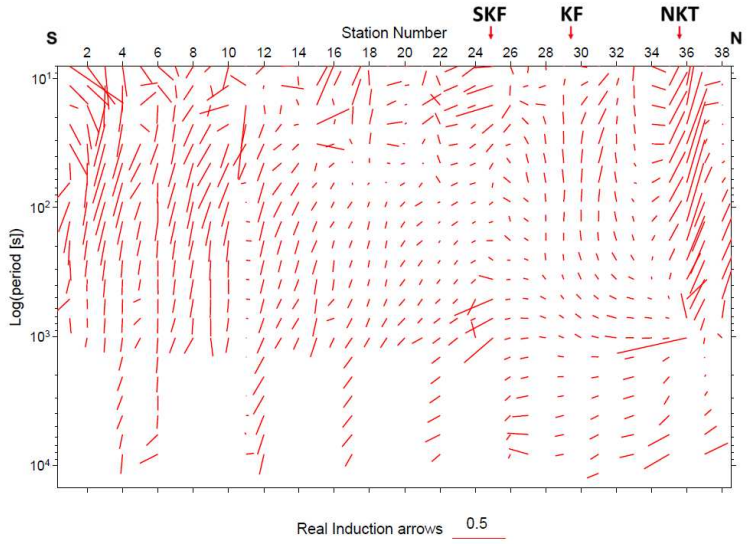

Figure 9.4: Real induction arrows directions for each periods (> 10 s) of each INDEPTH IV sites. The arrows are plotted so that the horizontal axis corresponds to an east-west orientation. Only the direction but not the sense of each vector is plotted here in order to show a clearer trend in the distribution of the vector's direction.

B.3), the strongest real induction vectors are characterized by reasonably low errors for periods higher than 100 s. The main north-south trend of the real induction vectors (Fig. 9.4) present some consistency with the orientation of the main axes of the phase tensor ellipses. The amplitude of the vectors are quite strong in the north (sites 34, 35 and 36) as the arrows are pointing to the conductive layer defined by the Qaidam basin. Similarly, the strong amplitudes characterizing the south and middle of the profile are likely related to the crustal conductor imaged in the Qiangtang and Songpan-Ganzi terranes [*Unsworth*

et al., 2004]. Finally, due to the substantial errors of some of the tipper data, parts of the geomagnetic transfer function data had to be removed for the modelling and the error floor associated with the tipper data was set to a relatively high value of 0.1.

9.2.2 *Strike Analysis and Distortion decomposition*

As seen on Figure 9.5, once again the strike analysis and distortion decomposition is not straightforward and needs to be undertaken with care. It is clear that the strike configuration of the profile is relatively complex and throwing all the strike in the *Strike* code [*McNeice and Jones*, 2001] for a multi-site, multi-frequency analysis in order to obtain a

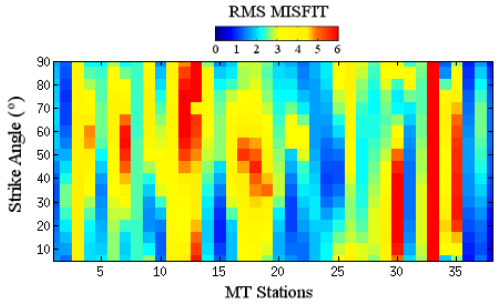

Figure 9.5: Multi-frequency (< 100 Hz), single site Groom-Bailey decomposition misfits associated with different strike angles. Station numbers increase to the north.

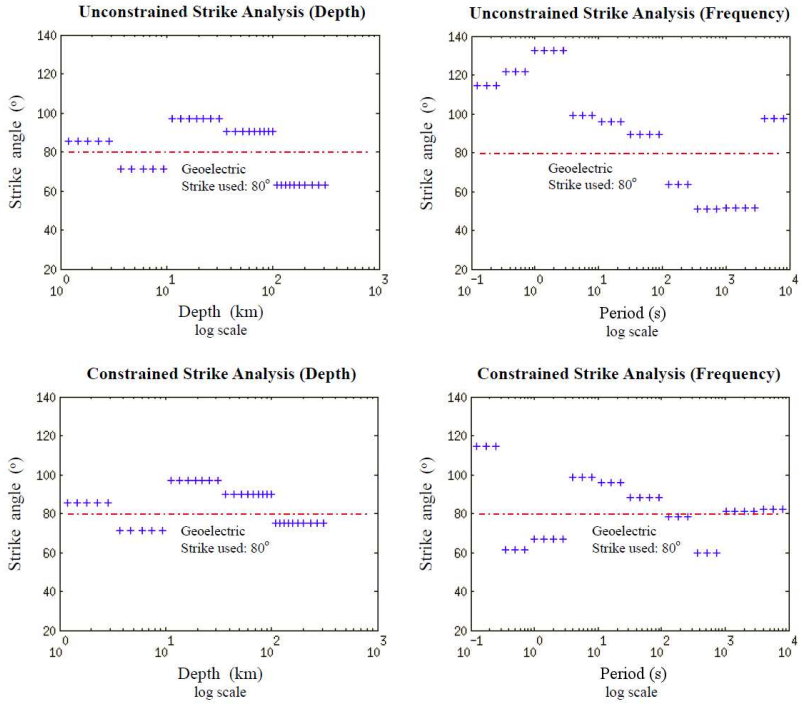

Figure 9.6: Multi-site, multi-period (multi-frequency) and multi-depth unconstrained and constrained strike azimuth estimations for different period and depth bands. For the constrained strike analysis, the strike evaluation was restricted to the interval $[60° - 120°]$.

single strike value makes no sense at all. It is worth noticing some sites are almost 1D as the decompositin model misfit stays low for any strike azimuth.

In order to determine the best strike orientation for the 6000 profile, different approaches were again considered. The data was decomposed for all sites simultaneously but for different periods and depth bands, using *unconstrained* and *constrained* strike analyses (Fig. 9.6). From Figure 9.5, it is clear that most sites do not fit only one preferred strike direction. Therefore, whereas an unconstrained distortion decomposition will solve for the best fitting geoelectric strike, the constrained strike analysis focuses on evaluating the strike direction for a restricted interval only. In this case, an interval of $[60° - 120°]$ was inferred from the surficial geology and complementary information such as the phase tensor and the induction arrows. Furthermore, considering both multi-depth and multi-frequency analysis as well as using different frequency, depth ranges can be really useful to check for consistency in the geoelectric strike evaluation. Figure 9.6 summarises those different approaches applied on the INDEPTH IV 6000-line data. Whereas the unconstrained analysis for different period bands leads to relatively scattered estimations of the strike direction, the constrained analysis relocates the strike estimates around a value of N80°E, particularly at the longest periods. However, when applied on different depth ranges for depths below 1 km, the strike estimates do not vary significantly between the unconstrained and the constrained analysis. In this case, the strike estimates appear less scattered as using depth below 1 km will limit the effects of shallow structures (high frequencies) on the strike azimuths. Overall, choosing a strike of N80°E appears to be a good compromise, knowing from the previous study that the longest periods would have a strong impact on the overall quasi-2D configuration of the area due mainly to the presence of the middle-to-lower crustal conductor.

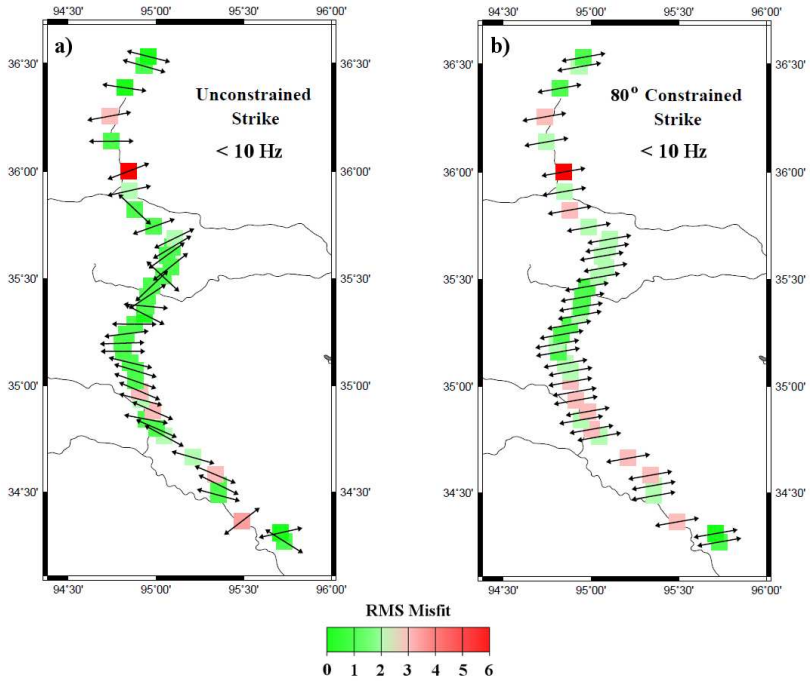

Figure 9.7: Comparison between Groom-Bailey decomposition misfits associated with unconstrained and 80°-constrained multi-frequency (< 10 Hz), single-site strike analyses.

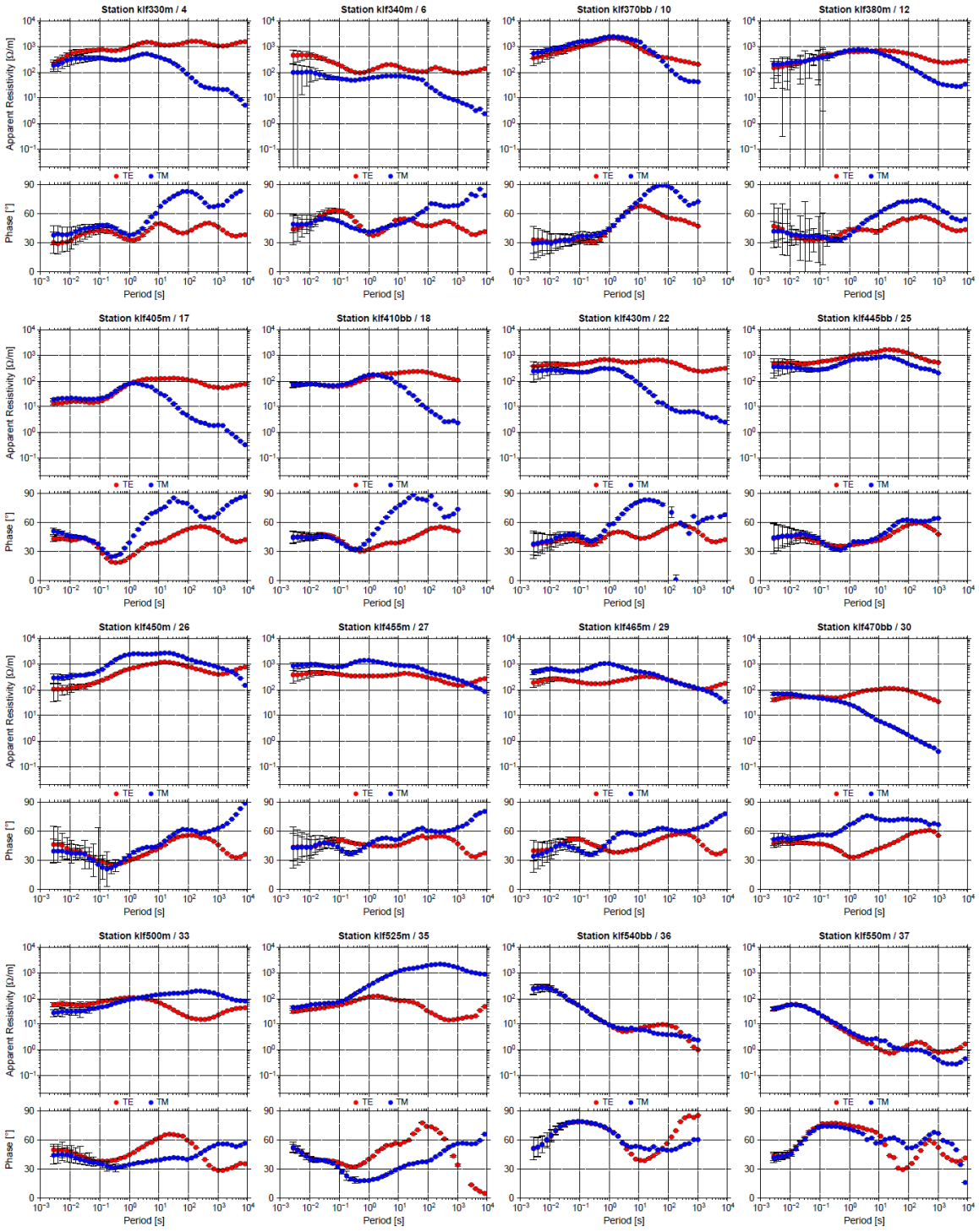

Figure 9.8: Comparison between the TE and TM responses of sites from the 6000 profile which have been decomposed to the N80°E strike direction using the *Strike* program [*McNeice and Jones*, 2001].

Figure 9.7 shows a multi-frequency (< 10 Hz), single-site approach comparing the Groom-Bailey decomposition misfit between decompositions where the geoelectric strike was either unconstrained or constrained to a value of N80°E. The main observation from this study is that the worst fitted sites for the constrained case mostly correspond to sites that were already not properly fitted in the unconstrained situation. Furthermore, in order to reinforce the choice of an azimuth of N80°E but also to check for the sensitivity of the 2D models to the strike direction, the data was inverted for different strike directions varying every 5° from 70° to 110°. The resulting preliminary models did not present major differences. The final 2D modelling of the 6000 data was developed using only data decomposed to the geoelectric strike azimuth of N80°E, a value which also agrees well with the estimates of N85°E for the INDEPTH III 600 profile. Indeed, although both 600 and 6000 MT transects diverge to the south, on the lithospheric scale they remain close enough that the strike estimates should present some consistency.

Figure 9.8 presents the decomposed TE and TM responses of some sites representative of the 6000 profile. Similarly, to the INDEPTH III data the overall data quality is quite good. Except for the northern end of the profile where the MT responses are affected by the presence of the conductive Qaidam basin (sites 6540bb and 6550m), most sites present a similar behaviour as observed on some of the INDEPTH III stations located in the north of the Songpan-Ganzi terrane and the Kunlun mountains. Those responses are defined by relatively high values of apparent resistivity curves, and significant phase splits for periods above 10 s, characterized by substantially high TM phase values. This particular behaviour of the phase is also well highlighted by the flattened shape of the phase tensor ellipses (Fig. 9.2).

It is worth mentioning that the responses from sites 661bb (Fig. 8.9) and 6470bb (Fig. 9.8), located around the Kunlun fault, are very similar. This particular feature is a good support for the 2D assumption in the area as the stations are almost 100 km apart. Furthermore, due to the similarity of the curves, stations 6470 could be located south of the fault and not north of it as seen on the map (Fig. 9.1).

Finally, during the inversion process, some TE mode long period data points of some northern sites were removed as they were obviously affected by the conductive layer of the Qaidam basin and were bringing fake strong upper crustal conductors in the inversion preliminary models.

9.3 2D MODELLING

9.3.1 *Inversion Results*

For the 2D modelling the same process as for the INDEPTH III data was followed consisting on comparing 2D isotropic (Fig. 9.9) and anisotropic (Fig. 9.11) models. Both models were obtained using still the same 2D anisotropic inversion program [*Mackie*, 2002; *Baba et al.*, 2006]. It is worth remembering the 2D anisotropy problem assumes that the anisotropy axes are parallel and perpendicular to the main axis of regional geoelectric strike. This assumption can be considered valid for this region as the main directions of the deformation as well as the orientations of the main sutures and terranes are in agreement with the main strike azimuth. The data were inverted simultaneously for both TE

and TM modes and also the geomagnetic transfer function. For the main isotropic and anisotropic models, the data were inverted for TM, TE modes and the vertical magnetic field (Hz) transfer function, allowing the inversion for static shifts for few selected sites. The error floors of $8\% - 3\%$ and $10\% - 3\%$ were respectively applied for TM and TE apparent resistivity and phase, as well as 0.1 for the geomagnetic transfer function. The smoothness trade-off τ_s used was 7 and the models closeness τ_c was set to 100000 for the isotropic inversion and to 1 for the anisotropic case. More details on the misfit of the TE and TM apparent resistivity and phase can be found for the anisotropic model in the appendix on INDEPTH IV - SUPPLEMENTARY FIGURES in Figures B.4 and B.5. Except for the smoothness τ_c, the exact same inversion parameters were used for both isotropic and anisotropic inversions.

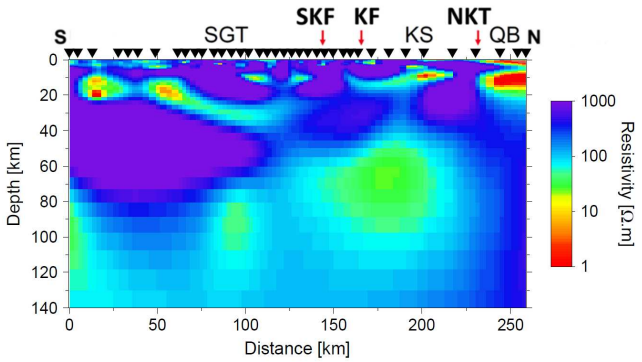

Figure 9.9: Global isotropic 2D resistivity model of the 6000-line.

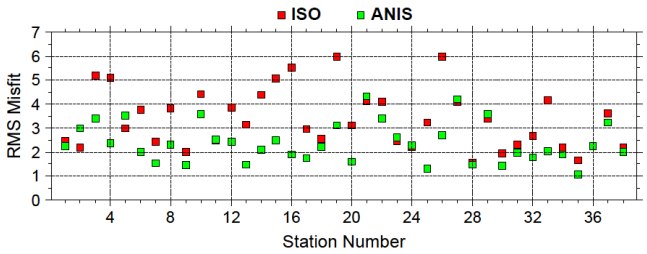

Figure 9.10: Difference between the anisotropic (green) and isotropic (red) RMS misfits. Station numbers increase to the north.

Compared to the INDEPTH III results, the variations between the isotropic (Fig. 9.9) and anisotropic (Fig. 9.11) models is quite significant. Whereas, the main upper crustal structures are similar, considerable changes occur for the middle-to-lower crust and upper mantle features. The huge difference between the models is also highlighted by the RMS misfits (Fig. 9.10) which show an overall change of 1 between the isotropic model and anisotropic model misfits. For a number of sites, the RMS difference between the models is even > 2. Furthermore, the sites locations of the high RMS misfits differences between the isotropic and anisotropic models interestingly correlate pretty well with the locations of the flattened ellipses mentioned above for sites numbers ranging from 10 to 16 below approximate depths of 20 km (Fig. 9.3). Therefore, the specific configuration of the ellipses is likely to describe a particular orientation of 3D structures revealing macroscopic

anisotropy that cannot be fitted by 2D isotropic solutions.

For this particular study, the isotropic 2D model clearly shows the limitations of the isotropic inversion, whereas the 2D anisotropic inversion appears to be the next step in modelling before considering 3D inversions. On this issue, a comparison between 2D anisotropic and 3D modelling is discussed for real and synthetic data in the following chapter. Following the net improvement in the model misfits for the anisotropic results, in further discussions only the anisotropic model of the 6000-line will be considered.

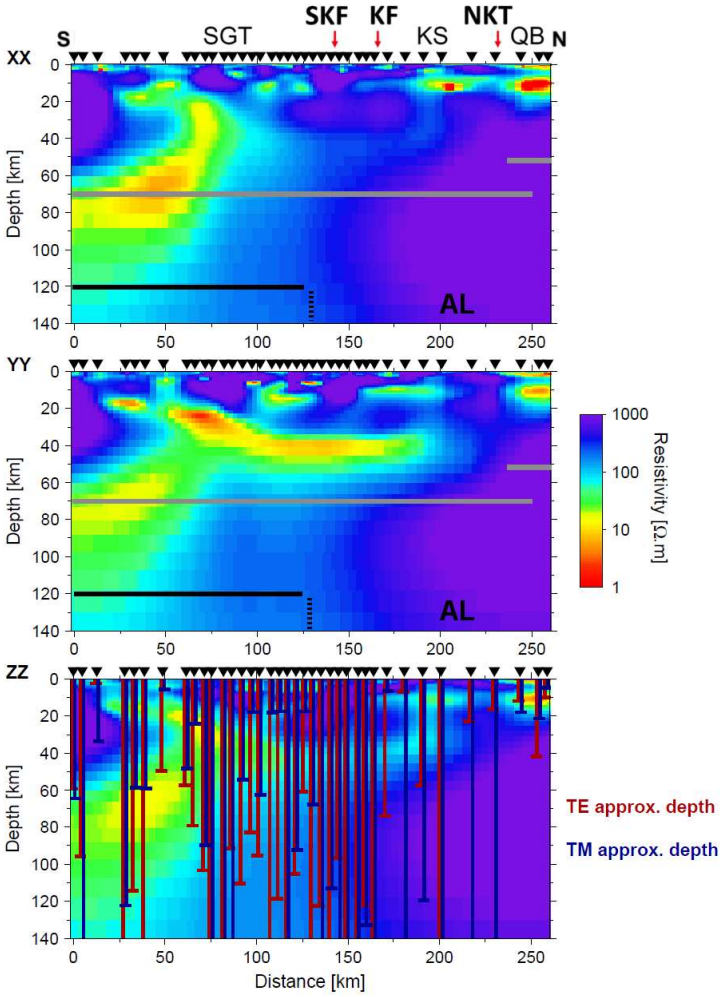

Figure 9.11: Global anisotropic 2D resistivity model of the 6000-line. The approximate Niblett-Bostick penetration depths [*Jones*, 1983b] of TE and TM modes are plotted on top of the zz model. The Moho depth [*Vergne et al.*, 2002; *Karplus et al.*, 2011] is highlighted by the grey lines. The black line shows the lithosphere-asthenosphere boundary location for a thin Tibetan lithosphere in the north part of the plateau imaged by seismic receiver functions [*Zhao et al.*, 2011]. SGT, Songpan-Ganzi terrane; SKF, South Kunlun Fault; KF, Kunlun Fault; KS, Kunlun Shan; NKT, North Kunlun Thrust; QB, Qaidam Basin; AL, Asian lithosphere.

Similarly to the INDEPTH III modelling, correction for static shifts were included in the inversion process. The data was first inverted for the phase only. Observed and cal-

culated responses were then compared between each other but also with the responses of neighbour sites. When significant shifts in the responses between two neighbour sites were observed in both measured and calculated responses, the data was set to be corrected for static shifts in the final inversions. The apparent resistivity curves mainly corrected for static shifts during the inversion appear to be the TE responses of some sites located in the middle of the profile. Except for one or two sites, the TM static coefficients remain relatively unchanged after the inversion (Fig. 9.12).

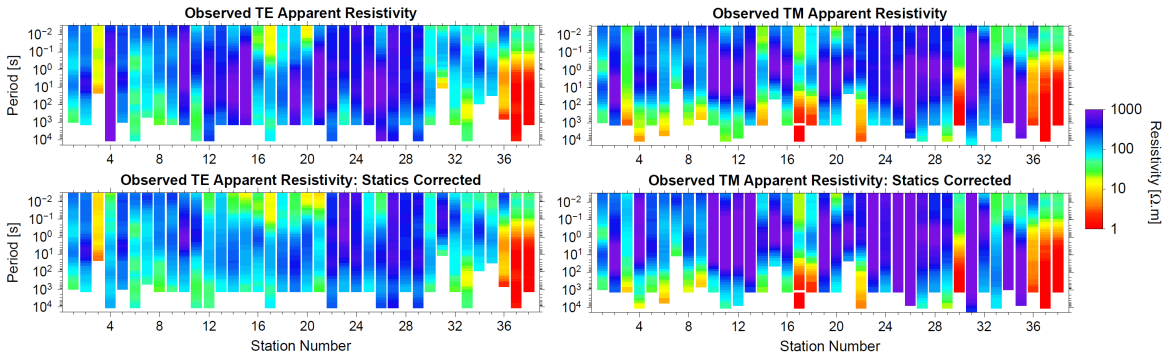

Figure 9.12: Comparison between the TE and TM apparent resistivities before and after static shift correction using the coefficients determined for selected sites during the inversion of the 6000-line data. Station numbers increase to the north.

Furthermore, sensitivity maps were once again generated during the inversion. Both xx and yy sensitivity maps have a good coverage of the models (Fig. 9.13). In the north of the profile, the TM mode, mainly associated to the yy model, compensates for the lack of sensitivity observed for the xx model, mainly associated with the weak penetration of the TE mode (Fig. 9.11). The conductive structures, including the main anisotropic crustal anomaly, appear well resolved as they corroborate with the areas of high sensitivity (Fig. 9.13). As for the INDEPTH III modelling, further investigations on the resolutions of the deeper structures were also carried out. Those are highlighted from the forward modelling resolution tests presented on Figures 9.15 and 9.16, which are discussed in the next section.

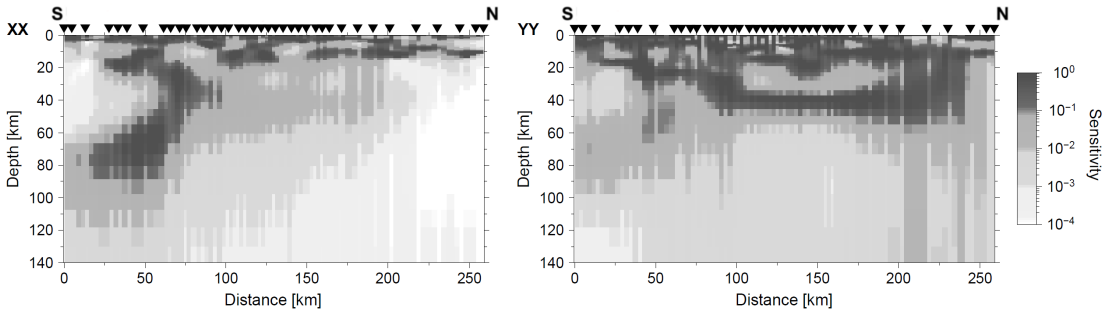

Figure 9.13: Sensitivity maps associated with the 6000-line global anisotropic model. The white areas reflect the lack of sensitivity on the corresponding model structures due to sensitivity values below 10^{-4}.

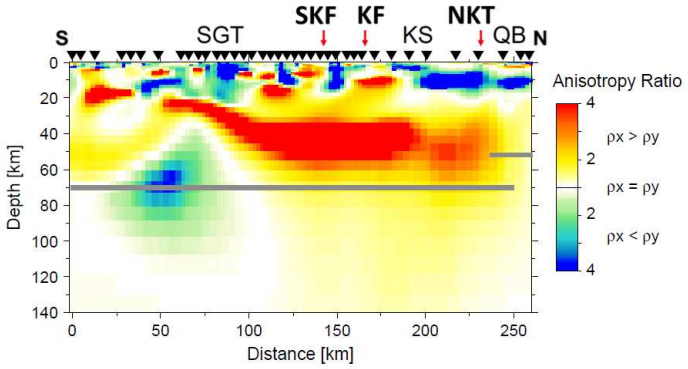

Figure 9.14: Anisotropic differences between the xx and yy models. The resistivity ratio between the xx and yy models are highlighting the areas of crustal anisotropy: blue areas correspond to structures which are more conductive along-strike whereas the red areas show the anisotropic structures which are more conductive across-strike (profile direction). The Moho depth [*Vergne et al.*, 2002; *Karplus et al.*, 2011] is highlighted by the grey lines. SGT, Songpan-Ganzi terrane; SKF, South Kunlun Fault; KF, Kunlun Fault; KS, Kunlun Shan; NKT, North Kunlun Thrust; QB, Qaidam Basin.

Finally, the differences between the xx and yy models were compared by plotting the resistivity ratios between the two models (Fig. 9.14). All the strong anisotropic structures are located in the crust. The main anisotropic structure observed on Figure 9.14 (extended red anomaly) corroborates with the depth and location of the similar anomaly observed on the INDEPTH III models. It is also worth noticing that in this study, the anisotropic structure is more pronounced than in the 600-line results. Although the high anisotropic ratio anomaly stops in the middle of the Kunlun Shan, a slighly lower anisotropic ratio appears to extend as far as the double Moho observed by *Karplus et al.* [2011]. South of the model, a strong "blue" anisotropic anomaly present in the lower crust and not seen on the 600-line results, characterizes an extension of the crustal conductor to a direction perpendicular to the profile (along-strike). Although, this particular feature agrees with the interpretation of the east-west crustal flow in the lower crust of the Songpan-Ganzi terrane [*Klemperer*, 2006], the next chapter discusses the possibilities that it could also be a simple artefact from the inversion.

9.3.2 *Crustal and Mantle Structures*

It is interesting to see that the anisotropic models obtained from the INDEPTH IV data agree quite well with the anisotropic study performed on the INDEPTH III data. Indeed, the 6000 model also presents evidence for anisotropy in the conductivity at the northern edge of the high elevated Tibetan plateau associated with preferred orientation in the extension of a mid-crustal conductor beneath the Kunlun Fault. For the same reasons explained in the INDEPTH III modelling, the main crustal anomaly observed in the lower crust of the Songpan-Ganzi terrane is more than likely related to the presence of partially molten rocks. As in the INDEPTH III model, the crustal highly resistive feature characterizing the crust of the Kunlun Shan and defining the root of the highest mountain peaks of the area is now located south of the Kunlun fault. It is worth noticing that in the 600-line model the resistive anomaly was situated north of the fault. This particular differ-

ence can be seen on the main map (Fig. 9.1) from the position of the highest topography with respect to the location of the fault. This agreement between the map and the models is a reasonable argument in favour of the accuracy in the fault location. To the south, the upper-mid crustal resistor located in the southern part of the model may define the crustal bedrock and plutonic intrusions associated with the Bayan Har mountains. To the north, the high conductivity of the Qaidam basin is also highlighted by the model with the presence of a surficial conductive layer characterizing the salt deposits present in the basin [*Kezao and Bowler*, 1986]. Finally, the Kunlun batholith is characterized by a shallow resistive feature just south of the North Kunlun Thrust in the first 5 km of the crust as also observed on the 600 model.

Similarly to the INDEPTH III models, in order to investigate the resolution on the deep crust and mantle structures, the resistivity structure of the models were modified (Fig. 9.15 and 9.15). For ***test a***, the crustal conductor located in the lower crust at the southern end of the profile was extended to the upper mantle to check for the extension of the lower crustal conductive anomaly. In ***test b***, the resolution of the resistive mantle characterizing the northern part of the profile was tested by adding a more conductive deep mantle. Finally, with ***test c***, the resolution beneath the main middle crust anisotropic anomaly was tested by adding a conductive lower crust and upper mantle. Compared to the resolution of the 600 data, the new 6000 model has a better resolution on the deeper structures. This can also be seen from the penetration depth plots where most sites show a good penetration of the two modes (Fig. 9.11).

As also mentioned for the INDEPTH III model, the upper mantle of the Songpan-Ganzi terrane is not as conductive as the crust and may not contain as great a volume of interconnected melt as its middle and lower crust. Furthermore, beneath the main anisotropic anomaly, the lower crust is likely to be more resistive too as the anisotropic conductor does not show a strong screening effect on the deeper structures. Finally, the results once again confirm the presence of colder temperatures in the north characteristic of the Kunlun-Qaidam block. The presence of a relatively resistive lower crust and upper mantle in the northern part of the Songpan-Ganzi terrane is in favour of a progressive increase in the lithospheric thickness [*Jimenez-Munt et al.*, 2008], starting in the middle of the Songpan-Ganzi terrane around 100 km south of the Kunlun fault. Furthermore, in the southern end of the profile, due to the slightly high resistivity of the upper mantle (compared to the crust) delamination is not likely to occur in northern Tibet but rather convective thinning [*England and Houseman*, 1989] which explains the presence of a thin Tibetan lithosphere [*McNamara et al.*, 1997; *Zhao et al.*, 2011]. As mentioned for the INDEPTH III model, the mantle high resistivity in the north of the Songpan-Ganzi terrane and beneath the Kunlun Mountains is also in agreement with the model of Asian lithosphere subduction [*Zhao et al.*, 2011].

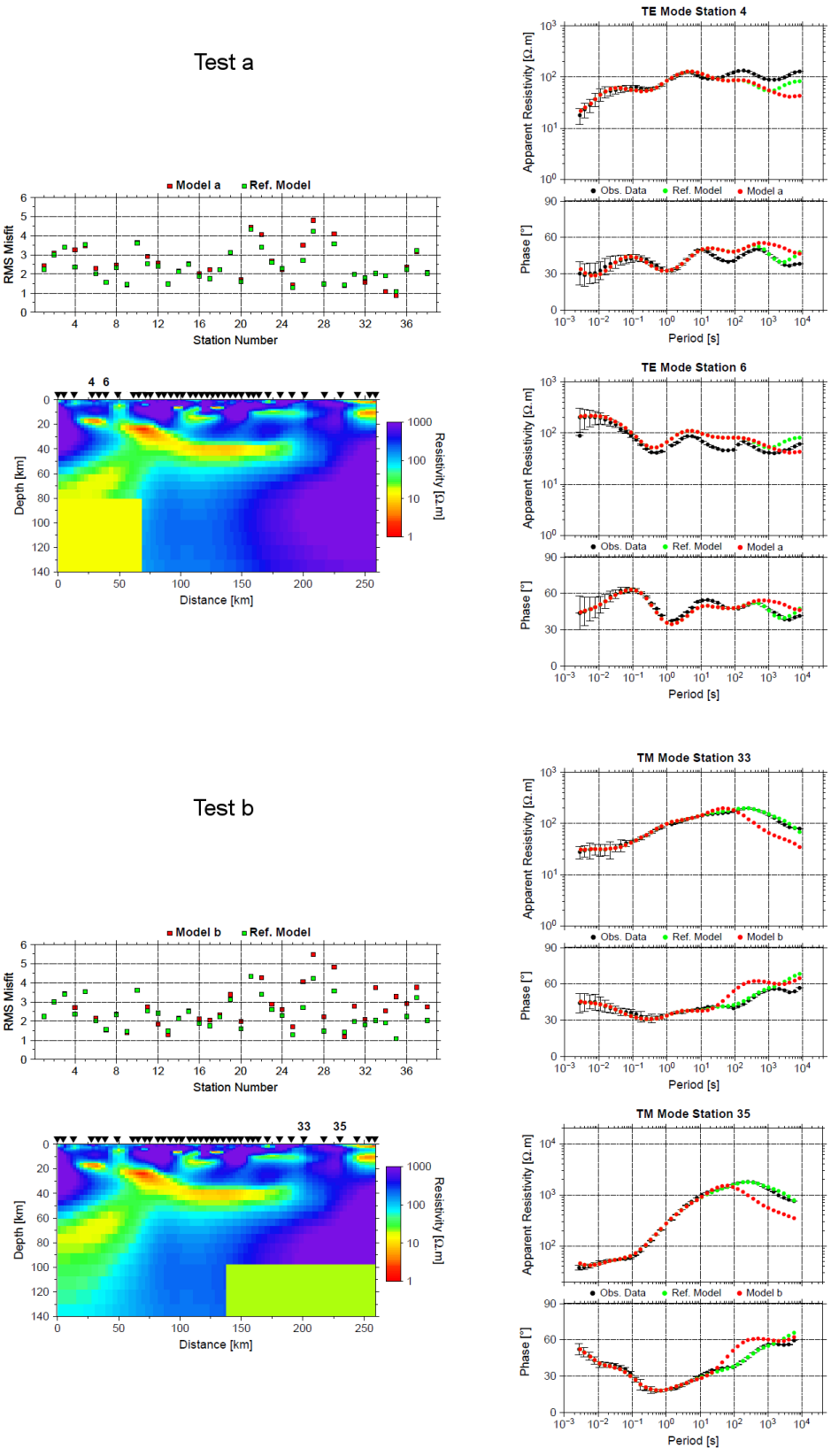

Figure 9.15: **Resolution tests a and b for the INDEPTH IV model**: comparison between the responses associated with the final anisotropic model of the 6000-line or reference model (green) and the responses generated by forward modelling of perturbed models (red). Although only the perturbation on the yy model is shown here, all models (xx, yy and zz) were modified the same way.

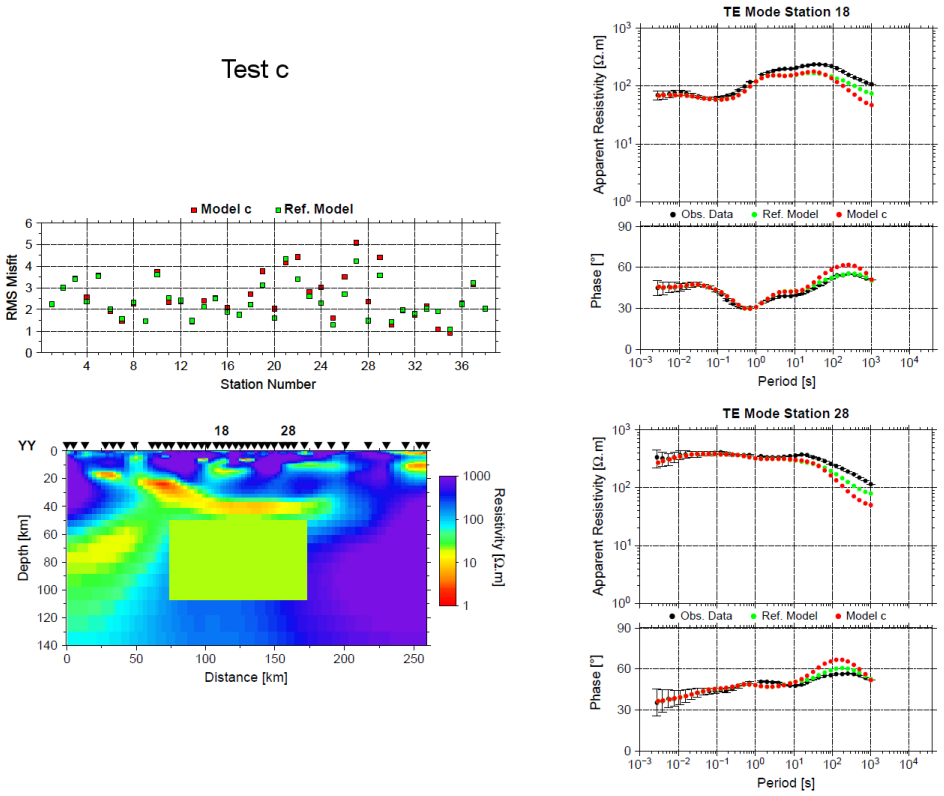

Figure 9.16: **Resolution test c for the INDEPTH IV model**: comparison between the responses associated with the final anisotropic model of the 6000-line or reference model (green) and the responses generated by forward modelling of perturbed models (red). Although only the perturbation on the yy model is shown here, all models (xx, yy and zz) were modified the same way.

10 3D MODELLING

10.1 SYNTHETIC MODELS

10.1.1 *2D Anisotropic Inversion of 3D Synthetic data*

To test the anisotropic feature observed on both INDEPTH III and IV 2D anisotropic inversion model (Fig. 8.12 and 9.11), 3D synthetic modelling (Fig. 10.1) was undertaken to systematically study magnetotelluric sensitivity to the 3D resistivity transition between the Songpan-Ganzi and the more resistive eastern Kunlun-Qaidam block. The presence of melt was modelled by adding a conductive layer in the middle crust. Different types of 3D melt intrusion penetrating into the most resistive block are simulated to account for the anisotropic feature observed in the new INDEPTH MT models.

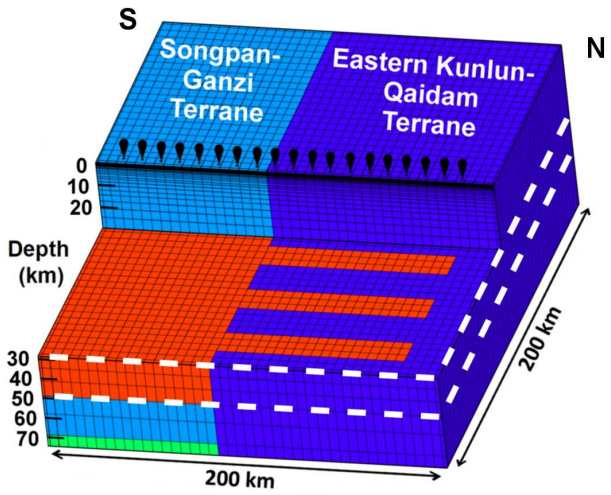

Figure 10.1: 3D synthetic model (5x5 km horizontal gridding). The associated 3D forward synthetic data is characterized by a 19 stations north-south profile whose geoelectric strike azimuth is N90°E.

Six synthetic models were considered in total, each of them being based on the model presented in Figure 10.1, also identified as model A. The only difference between them is the shape of the intrusion characterizing the 30-to-50 km depth conductive layer delimited by white dashed lines on Figure 10.1. Those models associated with different type of channels along a 20 km thick layer are defined as models A, B, C, D, E and F (Fig. 10.2). For each model, the 3D synthetic data were generated using WinGLink [*Mackie et al.*, 1994] for 19 stations and random noise was added to the synthetic apparent resistivity (5%) and phase (1.5°) independently. For all the different plots and modelling considered later on, only the noisy synthetic data were considered. The main strike direction associated with the synthetic profile is east-west (Fig. 10.1 and 10.2), therefore for each model the data

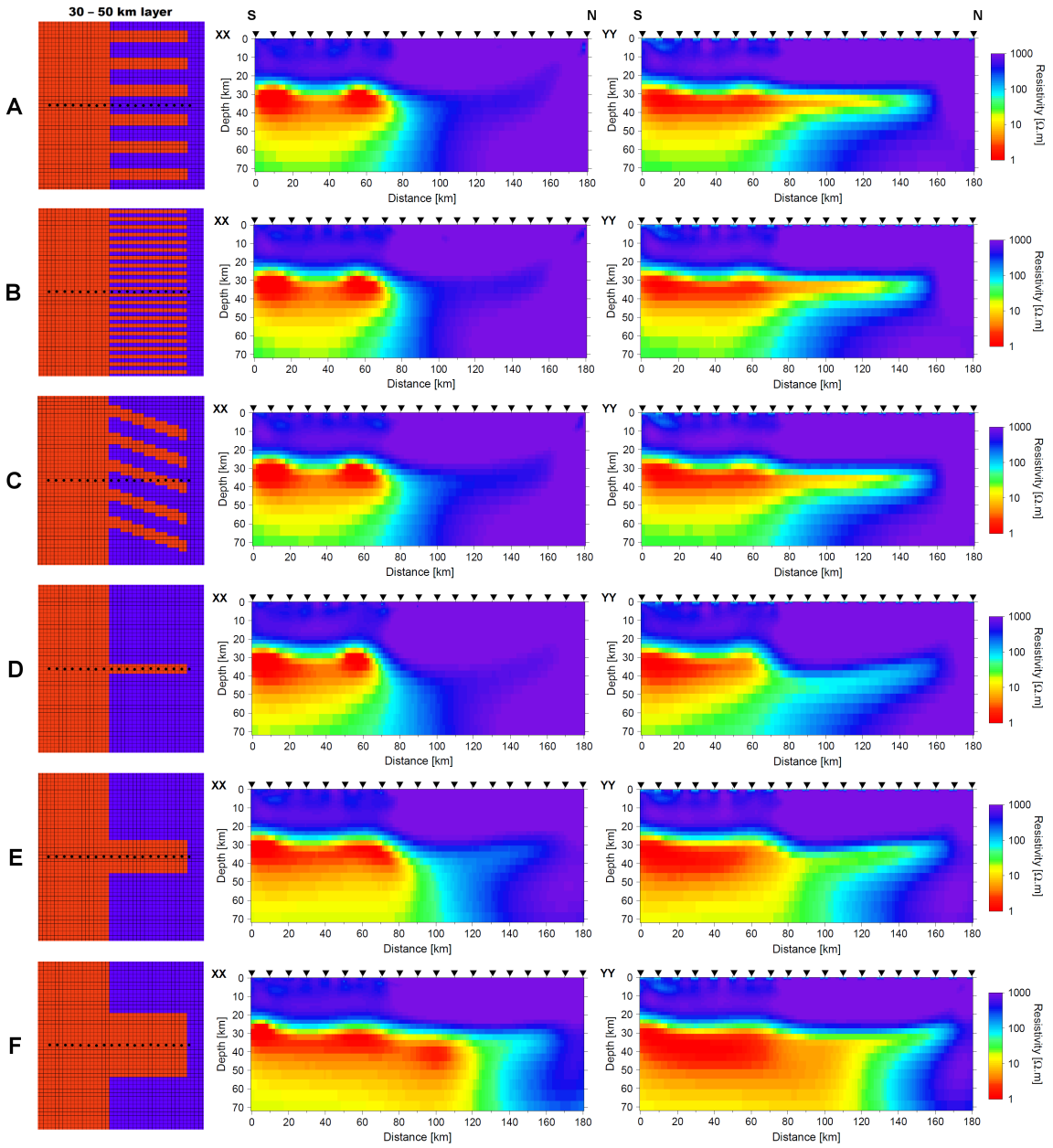

Figure 10.2: 3D synthetic models (plan view of the 30-50 km layer) and associated 2D anisotropic inversion models. Each 3D model characterizes a particular configuration of the 30-50 km layer delimited by the dashed lines in the model presented on Figure 10.1. The synthetic data associated with each 3D model were inverted using the 2D anisotropic inversion.

were decomposed to N90°E using the *Strike* program [*McNeice and Jones*, 2001]. The resulting TE and TM synthetic data responses were inverted with the same 2D anisotropic inversion as the observed data using error floors of 8% – 3% and 10% – 5% for respectively TM and TE apparent resistivity and phase. No tipper data were used in the modelling. The smoothness trade-off τ_s used was 3 and the model closeness τ_c was 1. The resulting 2D anisotropic models are presented on Figure 10.2.

Whereas the model A, B and C describe different anisotropic structures (macroscopic anisotropy), the model D, E and F are characterized only by a single 3D intrusion of different widths. Those models were considered to study the resolution of anisotropy at depths of 30 km (similar to the depths of the observed anisotropic conductive anomalies on INDEPTH models), but also to differentiate single 3D anomalies from anisotropic anomalies. First of all, the 2D anisotropic models generated from model A, B and C are almost identical. Therefore, the shape of the anisotropic structure responsible for the observed anomalies cannot be resolved at those depths. However, the anisotropic signature of the synthetic data is clearly sensed as the difference between the xx and yy model resistivity is quite strong in the northern end of the models. Those results agree quite well with the observed anisotropic models associated with INDEPTH III and IV data. Furthermore, obtaining similar 2D anisotropic models from a single intrusion was not as successful. If the intrusion is too thin (model D), the anomaly in the resulting 2D yy model is not conductive enough. But if the intrusion is too wide, the resulting 2D models are almost isotropic. However, it may be difficult to discard the model E straight away as the resulting model is not too different from the observed anisotropic models in northern Tibet. The results of the 2D anisotropic inversion of synthetic data have shown that the models A, B, C have led to almost identical models. Furthermore, depending on the resistivity contrast between the injected conductor and the surrounding medium, one may think an *intermediate* single intrusion model such a model E could also explain the results from 600 and 6000 line. Therefore, the INDEPTH anisotropic MT 2D models of northern Tibet could be representative of a model of type A (as well as B or C) characterized by several conductive intrusion (anisotropic structure) or a model of type E defining a single conductive intrusion of reasonable width.

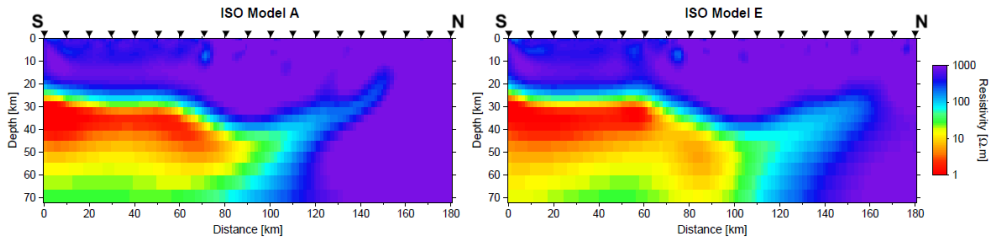

Figure 10.3: Isotropic models obtained from the responses corresponding to models A and E.

It can be noticed as well that the 2D isotropic models for the A and E synthetic data are quite similar (Fig. 10.3). The isotropic models were obtained using the same parameters as for the anisotropic models, except the closeness τ_c was set to 100000. The isotropic modelling of the synthetic data highlights the limitations of the isotropic solution for models where the width of the 3D intrusions are not large enough.

In the next section, responses associated with the model A (anisotropic intrusion) and model E (single intrusion) are investigated for a better understanding of the MT data associated with those two types of models but also to compare them with the INDEPTH III and IV data.

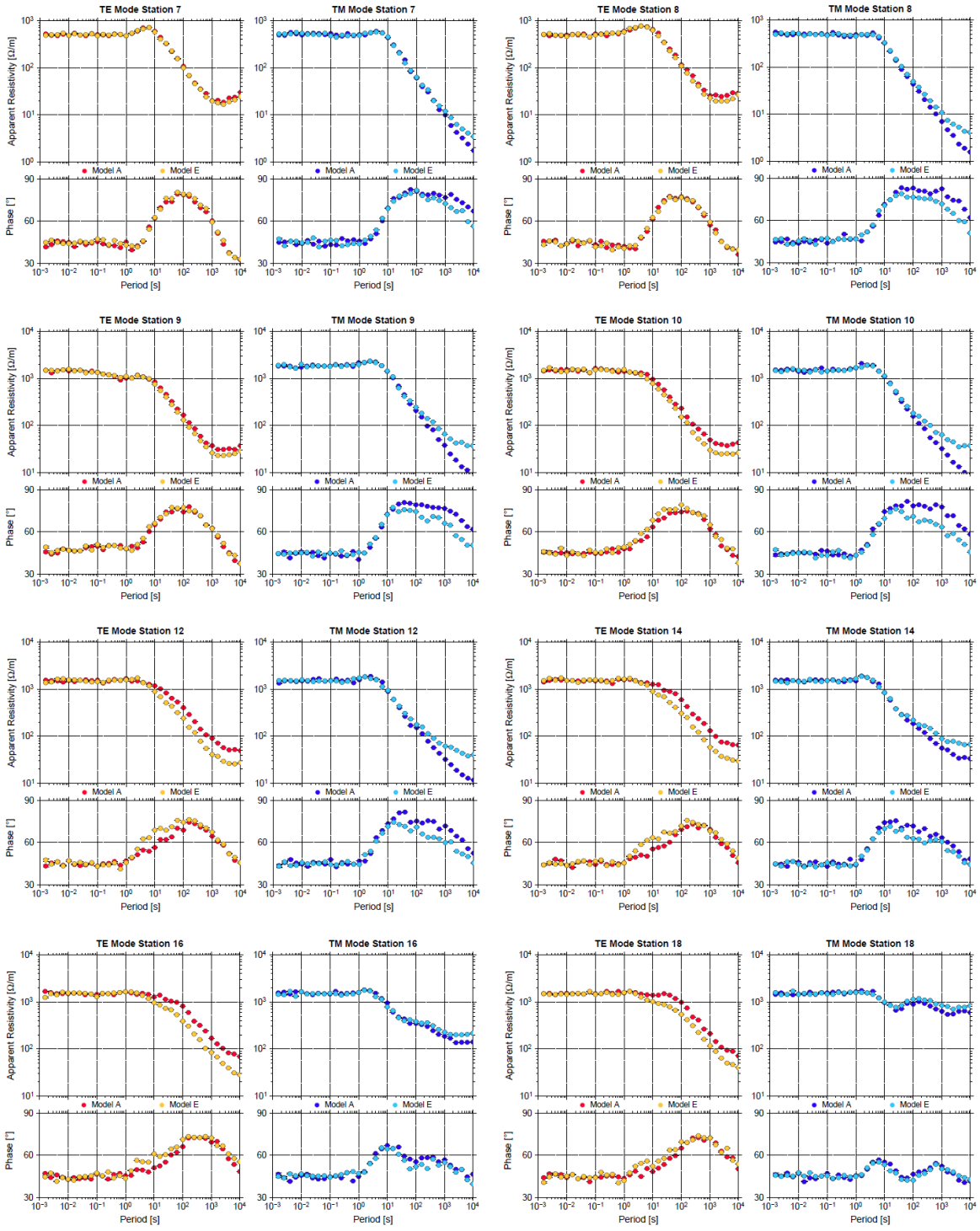

Figure 10.4: Comparison of the TE and TM synthetic responses generated from the 3D synthetic models A and E and decomposed to a strike direction of N90°E using the *Strike* program [*McNeice and Jones*, 2001].

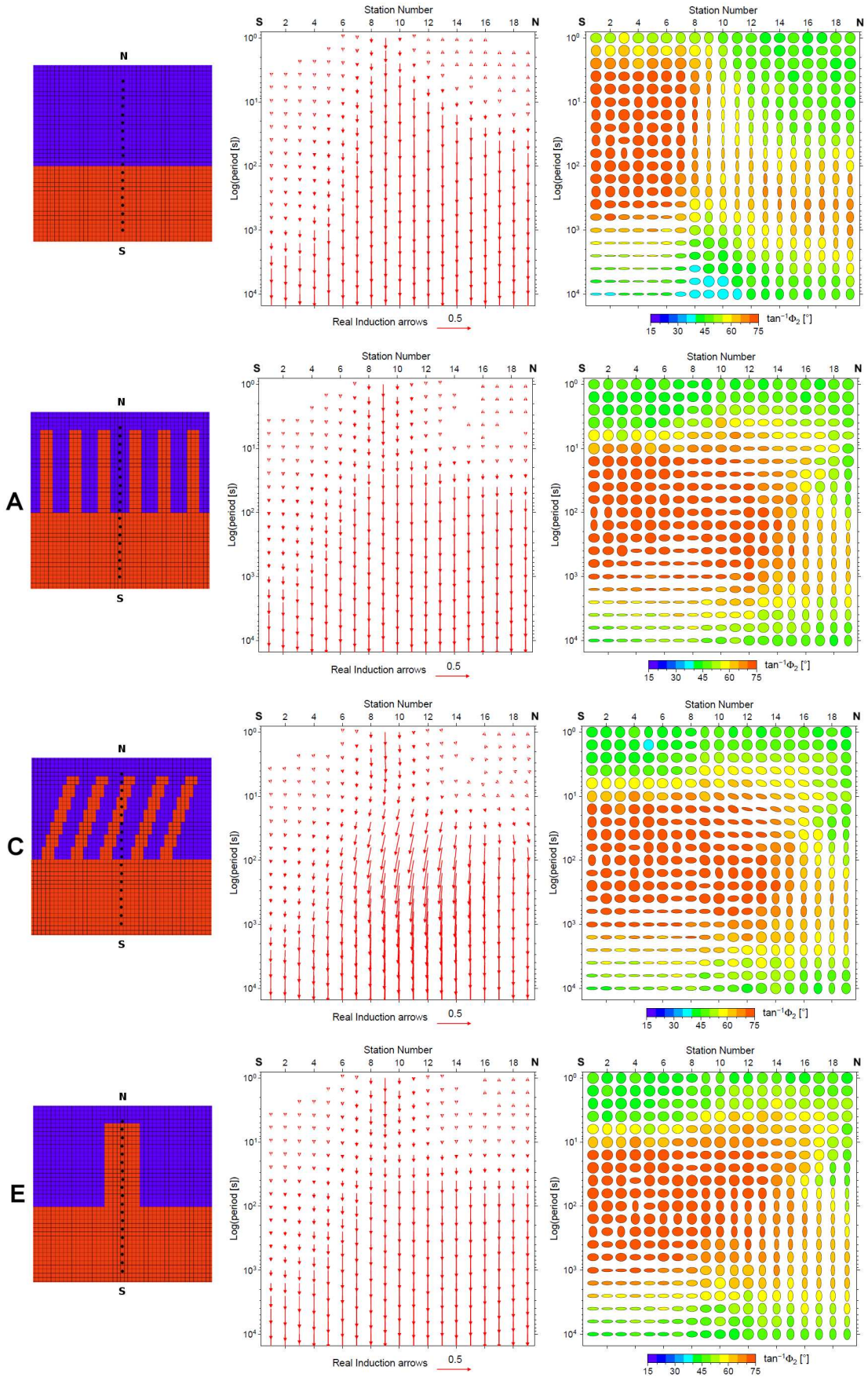

Figure 10.5: Induction arrows (Parkinson's convention) and Phase tensor pseudo-sections associated with the data generated by 3D synthetic models A, C and E, as well as a reference model with no intrusion.

10.1.2 *Anisotropic vs Single Intrusion*

In order to better understand the difference between the model A and E, their responses were compared on Figure 10.4 for sites located in the northern section of the 3D synthetic models above the anisotropic and single intrusions. The major differences between the two models are mainly observed for the TM mode. For the model A, the TM phase are higher and the apparent resistivities lower for periods above 10 s. This behaviour is clearly seen on the responses of sites 8, 9, 10, 12 and 14. For those sites, the TM phase increases for both models but remains high for the model A over almost two period decades whereas the phase responses of the model E decrease more rapidly. Overall sites, the TE modes responses of the two models are relatively similar. It is quite difficult to compare directly the synthetic responses with the observed data, as the later will be affected by different structures. However as the 6000-line models present evidence for strong anisotropy, it was worth comparing its responses with the synthetic data. The main correlation with the anisotropic synthetic responses is defined by the high phases observed for the TM modes at sites 6370bb, 6405m, 6410bb and 6430m for periods above 1 s. 9.8). Furthermore, a strong increase of the TM phases is also seen in the responses of sites 6450m, 6455m and 6465m but in this case for periods above 1000 s.

The correlation between the anisotropic responses of the synthetic and 6000-line models are even more clear when compared with phase tensor ellipses associated with the model A, C and E (Fig. 10.5). For this study, a reference model with no intrusions is used to distinguish the effects related to the 1D conductive layer located in the southern part of the models from the effects associated with the conductive intrusions characterized by the model A, C and E. One of the main differences between the three models occurs in a zone located between sites 8 and 17 for period ranges of around 5 s to 50 s. Compared to the single intrusion defined by the model E, the ellipses are flatter for the anisotropic models A and C in this particular zone. Furthermore, for the model C, the ellipses main axes orientations are also affected by the directions of the conductive intrusions. This particular behaviour can also be seen on the phase tensor ellipses associated with the INDEPTH IV data between sites 4 and 20 for similar period ranges observed for the synthetic data (Fig. 9.2 and 9.3). Finally, it is also interesting to see that the induction arrows are not really affected by the anisotropic structure, except for slight variations observed for the C model data. However such result is probably due to the strong conductance of the homogeneous layer present in the southern section of the models.

The main difference between the model A and E can also be highlighted by conductance plots characteristic of their associated 2D anisotropic models (Fig. 10.6). The conductance of a particular layer is described in Siemens (S) and defines the integration of the conductivity of the layer over its own thickness h. More details on the estimation of the electrical conductance are presented in the next chapter. As seen on Figure 10.6, the split between the conductances of both xx and yy models related to the E synthetic data is less pronounced than for the models associated with the A synthetic data. Furthermore, the later presents conductance differences between its xx and yy models more in agreement with the differences observed for the INDEPTH 2D anisotropic models (Fig. 11.6). Similar observations can also be made for the anisotropic ratio defined from the xx and yy models (Fig. 10.6).

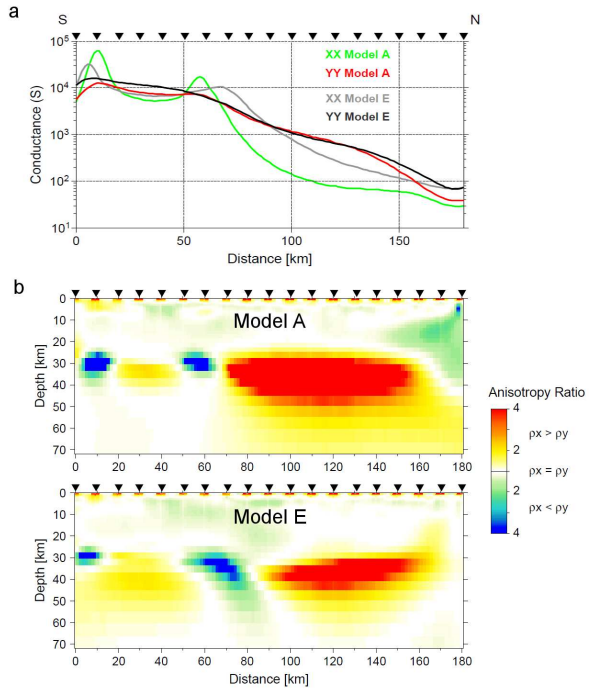

Figure 10.6: a - Conductance characteristic of the xx and yy 2D anisotropic models obtained from the synthetic data generated by models A and E. b- Anisotropic differences between the xx and yy models defining the main 2D anisotropic inversion results associated with models A and E. The resistivity ratio between the xx and yy models are highlighting the areas of crustal anisotropy: blue areas correspond to structures which are more conductive along-strike whereas the red areas show the anisotropic structures which are more conductive across-strike (profile direction).

Finally, it is worth noticing that the strong "blue" anisotropic anomalies observed on Figure 10.6 are artefacts from the inversion as no particular anisotropic structures were introduced in this part of the models. Therefore, although those erroneous anomalies appear to be quite localized, one needs to be careful when interpreting anisotropic structures derived from the 2D anisotropic code by [*Mackie*, 2002].

10.2 3D INVERSION

10.2.1 *Synthetic data*

In order to understand what would be the limits of the 3D inversion code on anisotropic structures, the inversion was first tested on the 3D structures presented in the synthetic modelling section. The 3D inversion code WSINV3DMT [*Siripunvaraporn et al.*, 2005] was used to invert the data sets associated with three of the synthetic 3D models presented previously: A, C, and E . The data was inverted for off-diagonal elements only and full tensor. Only the later is discussed here as it led to a better resolution of the model C which shows orientations of the conductive intrusions different from the 2D strike. The initial model used in the inversions was a simple half-space of 100 Ω.m. The error floors used were 2.5% for all the impedance tensor elements. The results are presented in Figures

10.7 and 10.8. Whereas, the RMS misfits for model A and E are reasonably low with values of respectively 2.43 and 2.86, the model C, more complex, presents an RMS misfit of 3.73. However, it is worth mentioning that knowing the original structures of the model, this study was mainly realized for resolution purposes. Therefore, the presented models were chosen more for their closeness to the original 3D synthetic models than for their final RMS misfit.

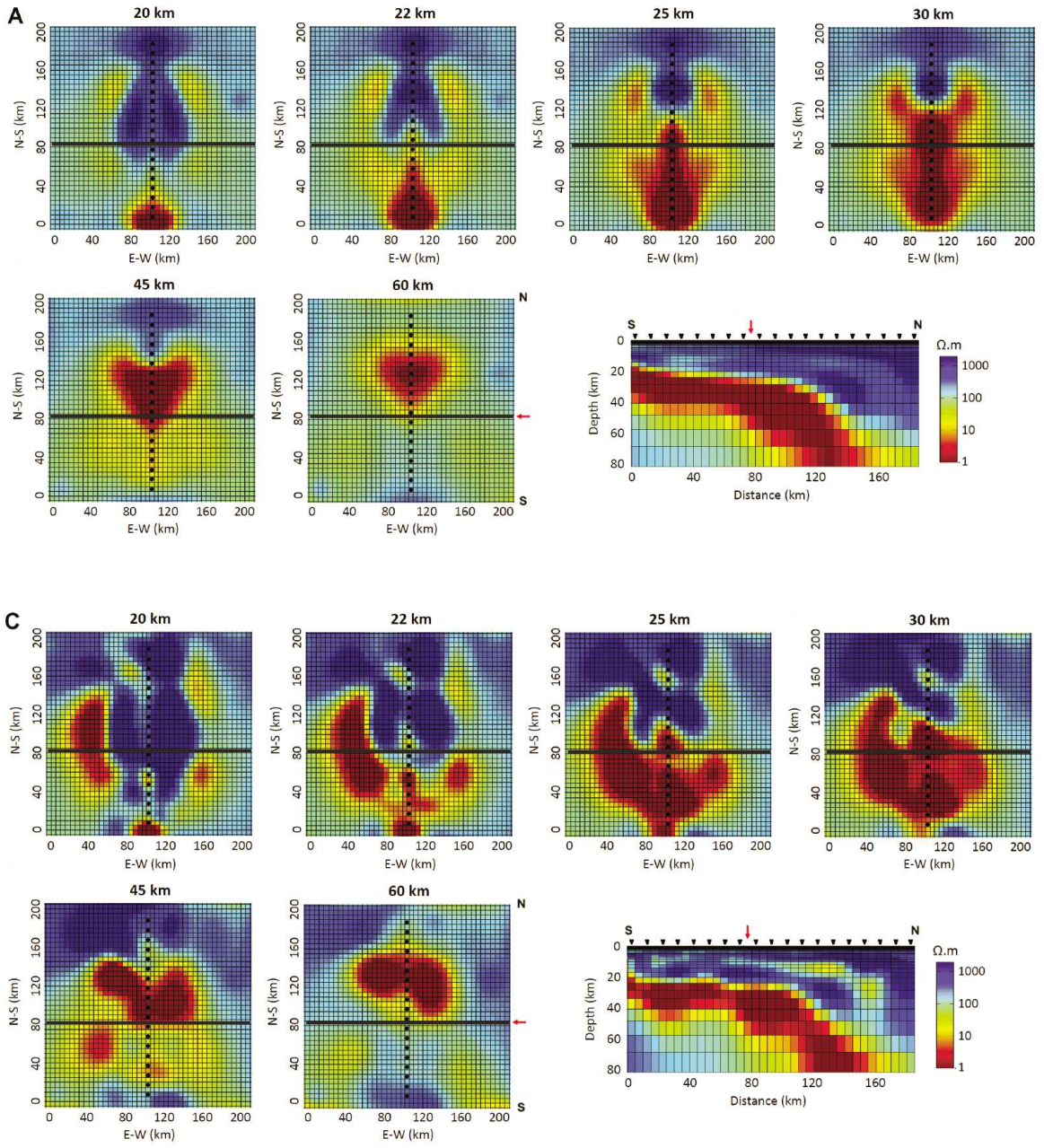

Figure 10.7: 3D models obtained from inverting the data generated by the synthetic models A and C (Fig. 10.2). The 3D models were obtained from the inversion of the full impedance tensor and are presented with horizontal slices for different depths as well as north-south cross-sections right beneath the stations.

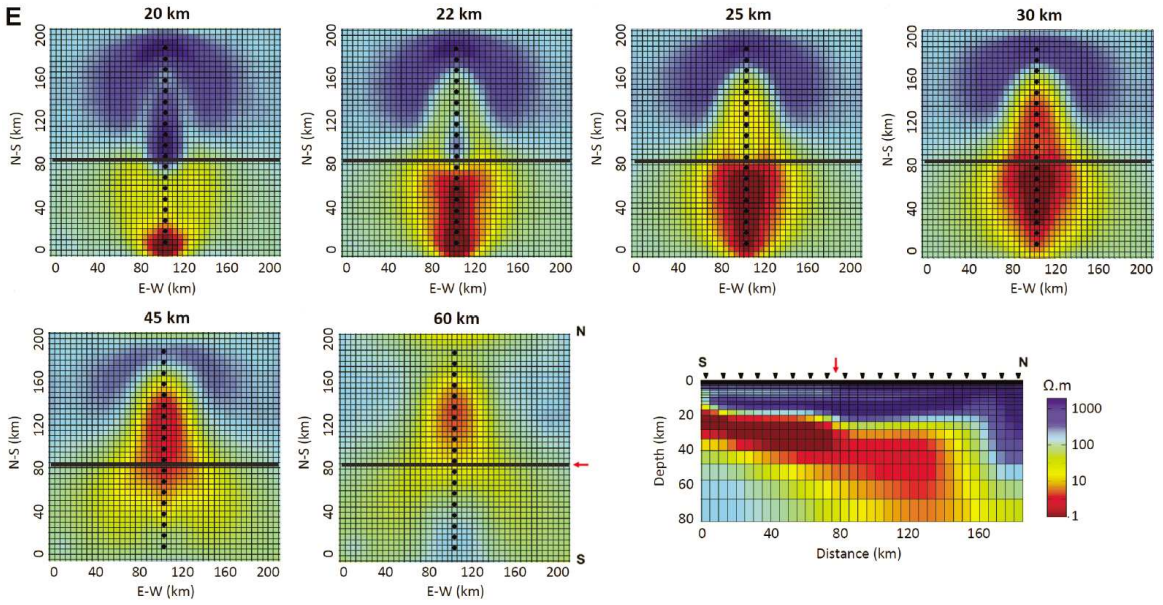

Figure 10.8: 3D model obtained from inverting the data generated by the synthetic model E (Fig. 10.2). The 3D model was obtained from the inversion of the full impedance tensor and is presented with horizontal slices for different depths as well as a north-south cross-section right beneath the stations.

The main conductive structures characteristic of the original synthetic models appear to be best resolved at the top of the conductor. Indeed, for model A and C, the surrounding conductive structures are relatively well resolved as seen on the 20 to 25 km depth horizontal slices (Fig. 10.7). However, the extension of the intrusive conductors for the model C is not as well recovered as for the model A. Deeper in the models, those structures tend to vanish and form only a thick homogeneous conductor whose thickness is not constrained due to the smearing of the anomaly with depth. Furthermore, for all three models, it can be seen on the cross-sections that the south of the profile is really well resolved as the thickness of the conductive layer is recovered. However, to the north, whereas for the model E the extension of the conductor is quasi-horizontal on the cross-section (Fig. 10.8), the models A and C show a dipping of the conductor to the north probably due to the presence of the anisotropic structures.

Due to time constraints, those results are only preliminary. However, they have shown interesting differences between models associated with anisotropic structures or single "intermediate width" intrusion. It is also worth mentioning that without knowing the structure of the 3D synthetic original model, the interpretation of the 3D inversion models would be quite difficult.

10.2.2 *INDEPTH III & IV data*

Selected sites from both INDEPTH III and IV transects (Fig. 10.9), mainly focussed on the northern edge of the Kunlun fault area, were inverted using the 3D code WSINV3DMT by *Siripunvaraporn et al.* [2005]. The error floors used were set to 5% for all the impedance tensor elements. The data were inverted for the off-diagonal elements only (Fig. 10.10) and for

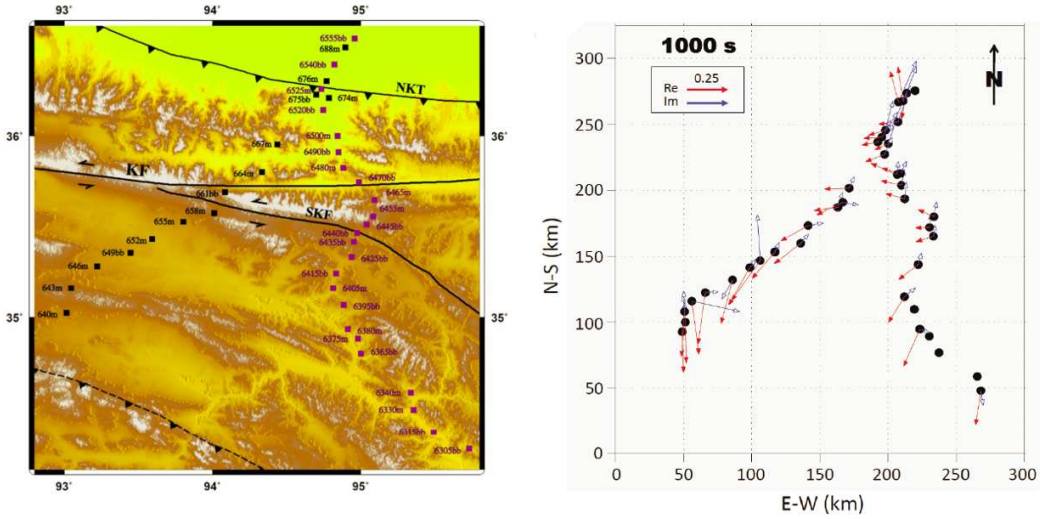

Figure 10.9: **On the left** - Sites location for the MT data used in the 3D inversion. The data used combine selected sites from both INDEPTH III (black) and IV (purple) profiles. **On the right** - *Parkinson* real and imaginary induction arrows at a period of 1000 s. KF, Kunlun Fault; SKF, South Kunlun Fault; NKT, North Kunlun Thrust.

the full impedance tensor (Fig. 10.11). No tipper data were used in the modelling. The final RMS misfit for the inversion with only off-diagonal elements was 1.33. For the inversion using the full impedance tensor, the final RMS was 2.9. The initial model used in the inversion was a simple half-space of 100 Ω.m. However, contrary to the 3D inversions of the synthetic data, the final RMS misfit was improved by running few successive inversions using each resulting model as the *a priori* model in the next inversions. Both types of inversion show globally similar results. The real induction arrows (Fig. 10.9) plotted at 1000 s in the Parkinson's convention [*Parkinson*, 1959] (pointing towards the conductive features) show three main trends that are consistent with the anomalies observed on the models. For the northern sites, the real vectors are pointing towards the conductive Qaidam basin, not seen on the model as too shallow. For the southern sites, they particularly highlight the presence of the widespread crustal conductor present in the middle-to-lower crust of northern Tibet.

In the Kunlun Shan, the real induction vectors are pointing laterally and are likely revealing the presence of the anisotropic conductive anomaly associated with the 2D anisotropic modelling performed in the previous INDEPTH III and IV chapters. The stronger anisotropy observed on the INDEPTH IV 2D models and also highlighted by the particular shape of the phase tensor ellipses (Fig. 9.2) is likely to reflect the alternation between N-S elongated conductive and resistive structures surrounding the 6000 profile up to the south of the NKT. This particular feature can be observed in the 35 km depth horizontal slice of the full tensor model (Fig. 10.11). From the results of the previous section on the 3D modelling of synthetic data, it is likely that this feature is not an artefact. Indeed, it can be seen from the 3D inversion results for model A that the lateral resolution is quite good at mid-crustal depths. Finally, the main resistive features observed on both 3D models corroborate relatively well with the resistive Kunlun Shan crust in the north and the resistive crust of the western Bayan Har mountains at the southern end of the

INDEPTH IV profile.

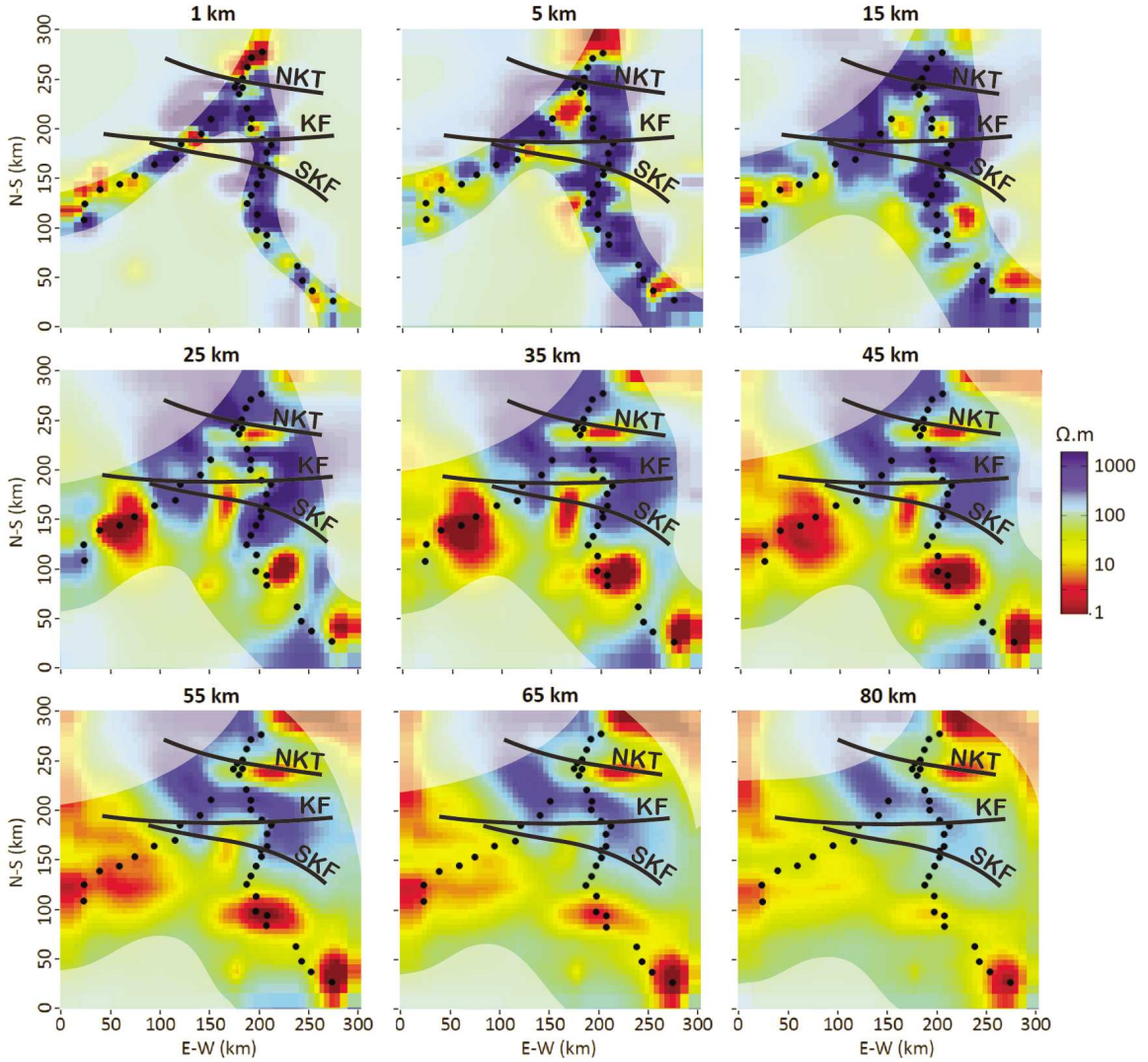

Figure 10.10: 3D model combining both INDEPTH III (black) and IV (purple) profiles (Fig. 10.9) obtained from the **inversion of the off-diagonal elements of the impedance tensor only**. The 3D model is plotted for several horizontal slices at different depths. For each slices, untrusted features are roughly masked in agreement with the depth of interest and the global penetration of the signal under each station. KF, Kunlun Fault; SKF, South Kunlun Fault; NKT, North Kunlun Thrust.

The 3D inversion models of the INDEPTH data, although only constrained by two profiles are really interesting as they show significant correlations with the 2D anisotropic modelling, particularly for the full tensor 3D models. Furthermore, from the observed results it is more than likely that the observed 2D anisotropic anomaly is not due to one single "intermediate width" intrusion. Finally, it is worth mentioning that compared to isotropic 2D models, the 2D anisotropic modelling can have a strong impact in the interpretation of the 3D inversion models too.

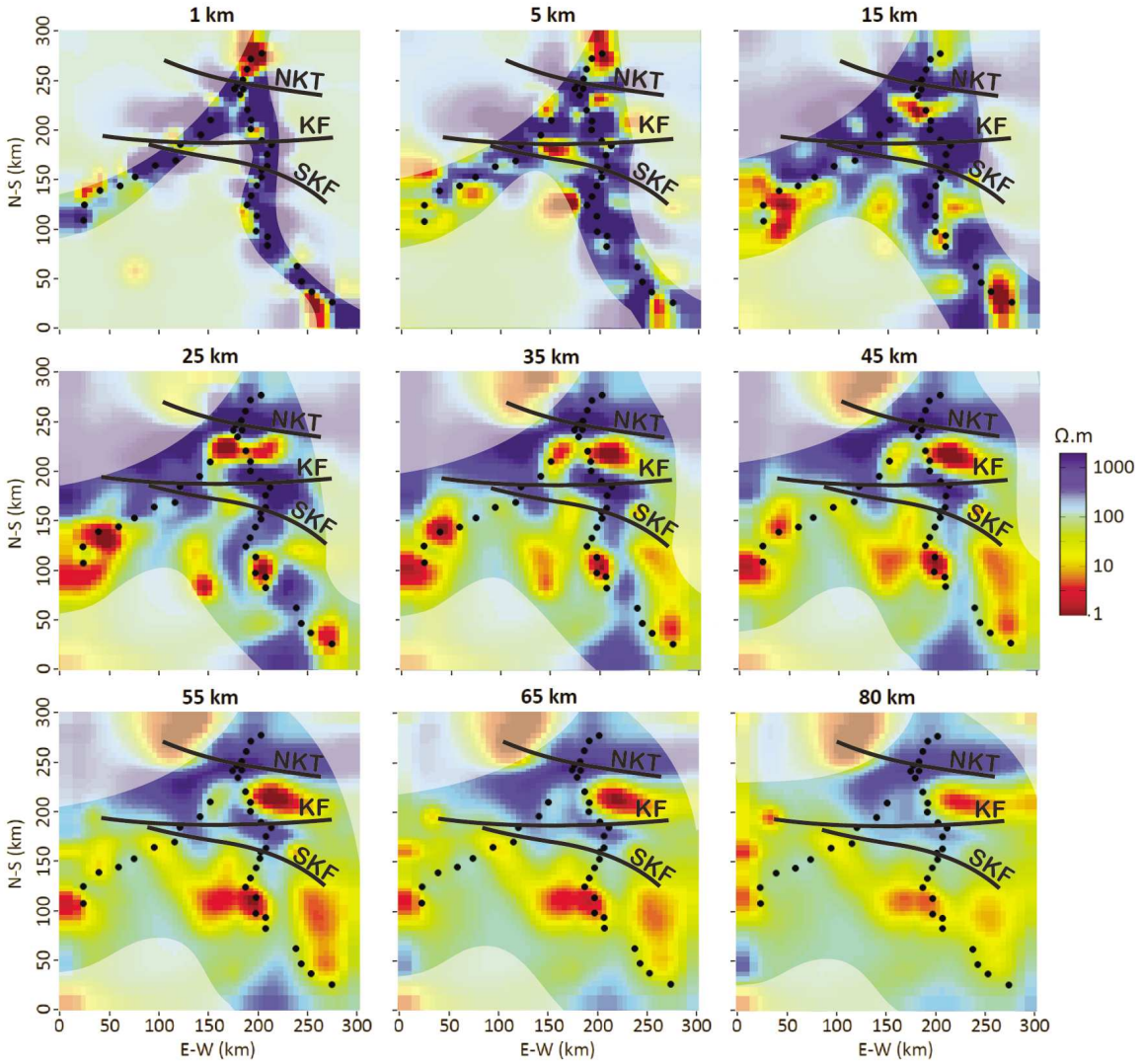

Figure 10.11: 3D model combining both INDEPTH III (black) and IV (purple) profiles (Fig. 10.9) obtained from the **inversion of the full impedance tensor**. The 3D model is plotted for several horizontal slices at different depths. For each slices, untrusted features are roughly masked in agreement with the depth of interest and the global penetration of the signal under each station. KF, Kunlun Fault; SKF, South Kunlun Fault; NKT, North Kunlun Thrust.

10.3 SUMMARY

The 2D anisotropic and 3D inversions of 3D synthetic data as well as 3D inversion of the INDEPTH data confirm that the 2D anisotropic observations from the 600 and 6000 MT profiles are likely corroborating an anisotropic feature characterized by finger-shaped melt intrusions as opposite to a single intrusion. However, the width, thickness and deviations in the orientation of those finger-shaped intrusions cannot be resolved at the observed depths with the data. According to the synthetic study, the 2D anisotropic inversion results present a better estimation of the depth and extension of the anisotropic structures compared to the 3D inversion results. However, for a synthetic strong anomaly which is

at least 80 km long and 20 km thick, in the 2D anisotropic inversion results the anomaly appears only to be 50 to 60 km long and 5 km thick. Therefore, it is possible that the anisotropic anomaly is likely to be thicker or stronger and even extend somewhat further north than in the INDEPTH 2D models, which are regularized to be optimally smooth as they are fitting the data.

11 INTERPRETATION AND DISCUSSION

11.1 COMPARISON WITH RECENT SEISMIC RESULTS

As presented in the first chapter, several seismic surveys have been carried out across the Tibetan plateau and a good number of them agree quite well with the interpretation of partial melting also inferred from MT studies. In this section, the INDEPTH III and IV MT models presented above are mainly compared with recent seismic studies and particularly with the INDEPTH IV seismic profile whose main focus has been to characterize the crustal structure of northern Tibetan.

11.1.1 *P wave velocities and Seismic Reflection*

The main advantage of the new INDEPTH IV 6000 MT profile is its proximity with *Karplus et al.* [2011]'s wide-angle P wave model also collected as part of phase IV of the INDEPTH project (map on Fig. 11.1). Therefore, a direct comparison between the MT 6000 model and the seismic Vp model is possible. Investigations on correlations between MT and seismic data have been considered [*Bedrosian et al.*, 2007], but those may not always be successful since each method have their own limits. Whereas the velocities will be more sensitive to the rock matrix, the electrical resistivity will mainly vary with the interconnection of fluid phases within the rock. Therefore, both seismic velocity and resistivity are usually compared as complementary information for one another, rather than a quantitative comparison. However, due to the similar locations of the seismic and MT INDEPTH IV profiles, a study on the correlation between the velocity and resistivity was worth a try (Fig. 11.1). The Vp model and associated velocity values were graciously provided by Marianne Karplus in order to work on a direct comparison between the two models. The seismic mesh being coarser, the MT mesh and corresponding resistivity values had to be interpolated in agreement with the Vp model. The interpolation was made using the *Nearest-neighbour interpolation* function from the software *Matlab*. Due to smoother variations in the velocity and resistivity values of the middle-to-lower crust, the investigation of the correlation between the two quantities was only focused on the 20 to 70 km depth range (area limited by the red lines on Fig. 11.1). Furthermore, the profile was divided into three different sections (a, b, and c) in order to limit the effect of significant lateral variations during the comparison. Both xx and yy resistivity model have been compared with the P velocity model for each of those sections (Fig. 11.1). The results mainly show an increase of the correlation to the north between both xx and yy resistivity values and the P velocities. Due to the absence of fluid phases, the bulk resistivity of the *section c* is likely to be more characteristic of the rock matrix and therefore shows a better correlation with the seismic velocities. Although the correlation is less obvious to the south, it is worth noticing that resistivity values below 100 Ω.m correspond to seismic velocities < 6.8 km/s. This particular observation could be related to the presence of a different

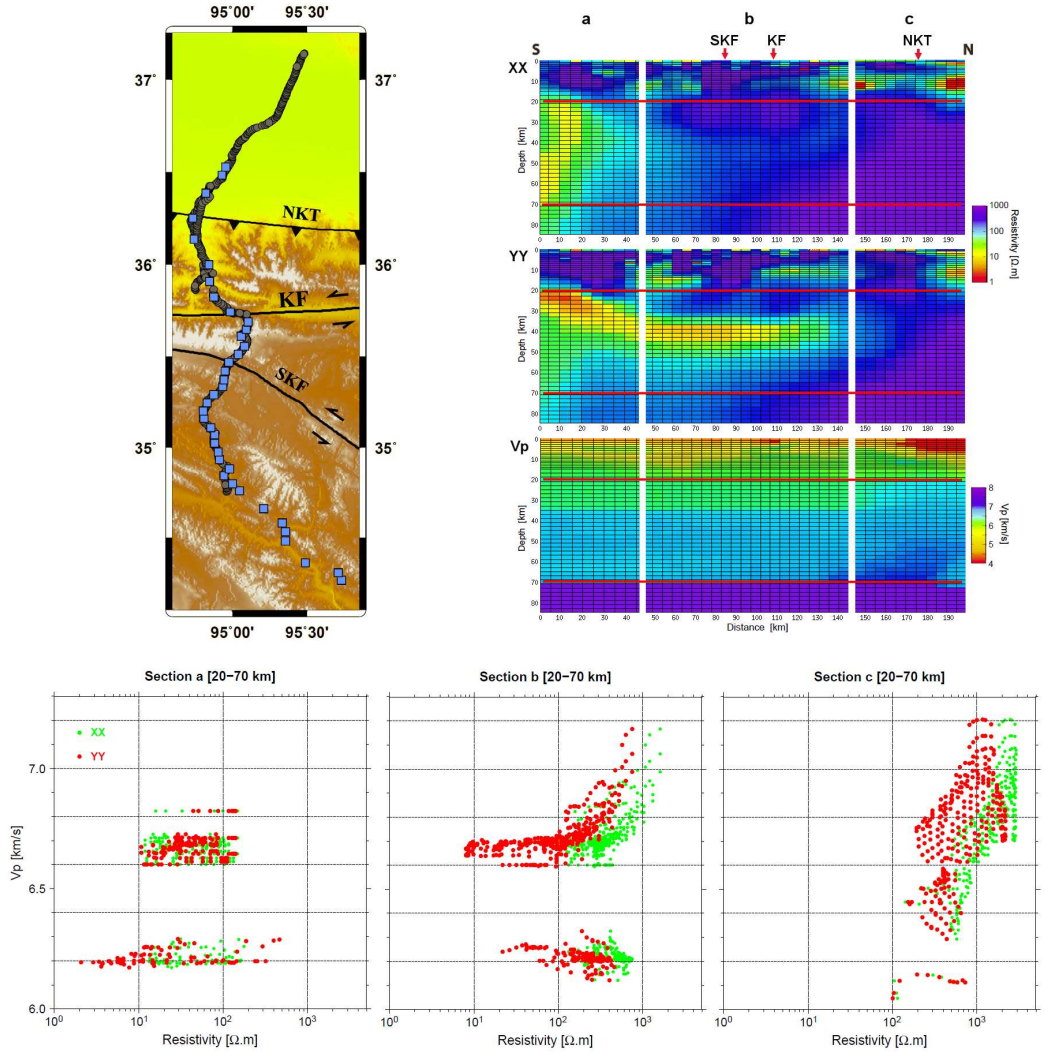

Figure 11.1: Quantitative comparison between seismic P wave velocities and electrical resistivity in northern Tibet along the INDEPTH IV profile. The map represents the locations of both MT (blue) and seismic (grey) stations. Each xx and yy resistivity models have been interpolated with respect to the Vp model from *Karplus et al.* [2011]. The velocity are plotted with the resistivity of each xx and yy model for different sections of the profile.

type of rock likely to be more subject to partial melting. The overall differences in the correlation between the resistivity and the P velocities, although not straightforward, may still highlight the changes in the middle-to-lower crustal rock types beneath the Kunlun mountains. This particularity is also mentioned in the next section when presenting the Poisson's ratio model of the INDEPTH IV profile from *Mechie et al.* [2012]. On this note, it would have also been interesting to do a similar correlation study between the resistivity and the Poisson's ratio (Fig. 11.4).

The resistivity structures inferred from INDEPTH III and IV models can also be compared with the main intra-crustal seismic reflectors highlighted by *Karplus et al.* [2011] along the INDEPTH IV profile. As seen on Figure 11.2, the seismic reflectors agree quite

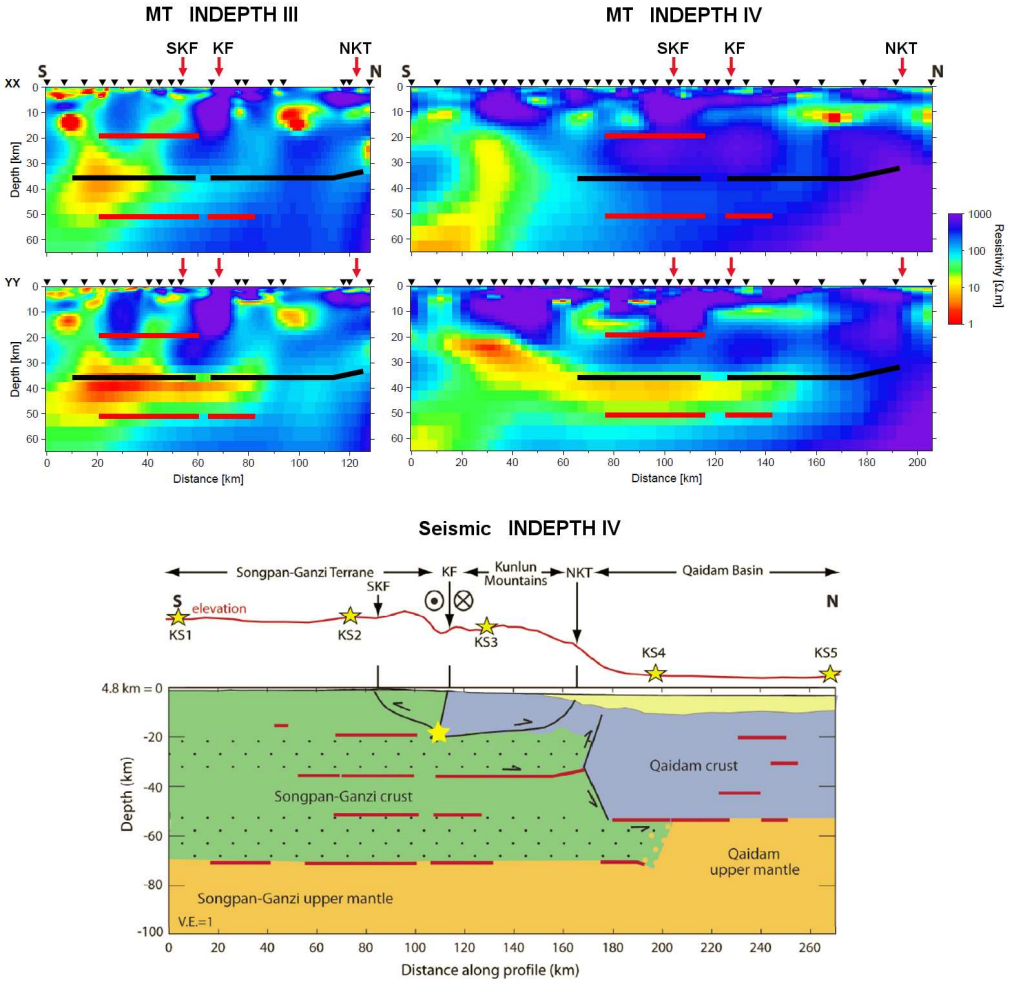

Figure 11.2: Indepth III and Indepth IV crustal models compared with the seismic reflectors and tectonic model taken from *Karplus et al.* [2011]. On the tectonic model, black dots indicate regions of relatively low velocity zones that have been interpreted as ductile flow associated with partial melt. The seismic reflectors highlight either the top (red lines) or the bottom (black lines) of two relatively low seismic velocity layers [*Karplus et al.*, 2011]

well with the locations of the main crustal conductive features. The intra-crustal seismic reflectors highlight the location of two separate crustal zones of relatively low P velocities [*Karplus et al.*, 2011]. Whereas in the southern part of the MT models the conductive features seems to be in agreement with the relatively low velocity zones defined by the Vp seismic data (particularly the case for the INDEPTH IV MT model), the extending crustal conductor observed on both INDEPTH III and IV models appears to be located in between those two zones.

11.1.2 *Shear wave velocities and Poisson's ratio*

As the shear wave velocities Vs would be more sensitive to the presence of melt in the crust, the MT models were compared with a recent 1D profile Vs data of the area kindly provided by Matthew Agius. The Vs profile defines a regional average of the shear velocity,

characteristic of northern Tibet, inferred from joint inversion of Rayleigh and Love wave phase velocities [*Agius and Lebedev*, 2010]. The shear wave velocity profile shows a mid-crustal low-velocity zone (LVZ) in the 20-45 km depth range. As seen on Figure 11.3, the LVZ corroborates well with the mid-crustal high conductivity imaged in the Songpan-Ganzi terrane for both INDEPTH III and IV MT models. Although, the thickness of the conductor is difficult to resolve with the MT method, the top of the conductor, which agrees well with the top of the LVZ, is usually well resolved. Furthermore, *Yang et al.* [2012] also characterized a similar LVZ from Rayleigh waves only. The correlation between the seismic LVZ and the mid-crustal conductor reinforce the interpretation of partial melting in the middle crust of the Songpan-Ganzi terrane.

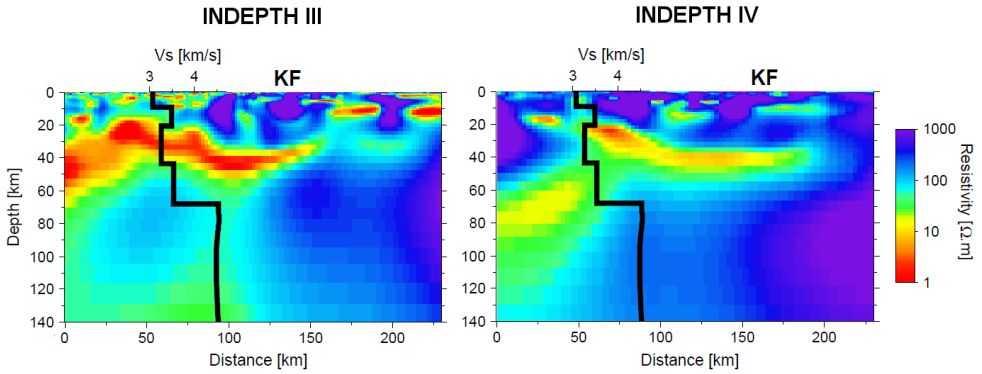

Figure 11.3: Comparison of the Indepth III and IV MT yy models with a shear wave velocity 1D model from *Agius and Lebedev* [2010].

Recently, [*Mechie et al.*, 2012] presented crustal shear velocities and Poisson's ratio models derived from wide-angle seismic data from the same profile as *Karplus et al.* [2011] and therefore along the INDEPTH IV MT profile too. The authors mentioned that the tomographic model for the S velocity structure is limited to the upper 10-15 km of the crust and therefore, the deeper structures are only defined by an average velocity structure derived from S wave Moho reflections (SmS) phase travel times. Despite being a more localized integration of seismic shear wave velocities, the average estimation from [*Mechie et al.*, 2012] based only on Moho reflections phases appears less robust than [*Agius and Lebedev*, 2010]'s shear velocity model for the Songpan-Ganzi crust. However, *Mechie et al.* [2012]

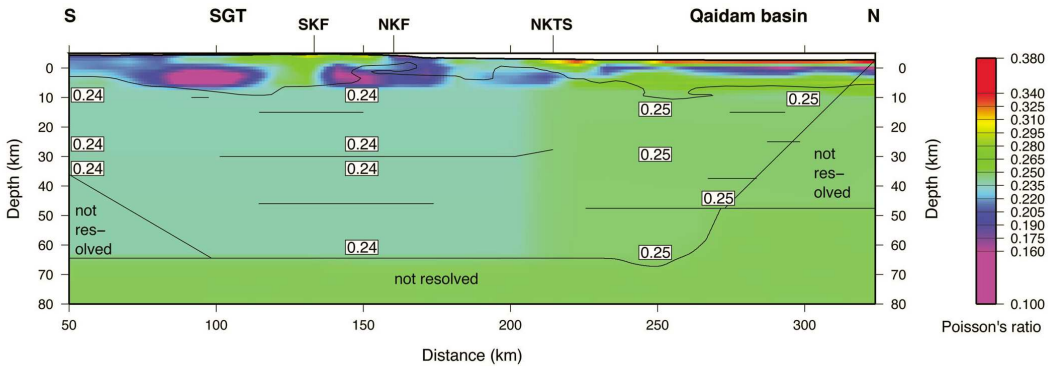

Figure 11.4: Poisson's ratio model for the INDEPTH IV profile from *Mechie et al.* [2012].

determined a Poisson's ratio model for the INDEPTH IV profile by combining their Vs model with *Karplus et al.* [2011]'s crustal P velocity model which has a better resolution at depth due to the presence of intra-crustal reflections of the P waves (Fig. 11.4). Below the upper 10-15 km of the crust, the model exhibits an average Poisson's ratio of 0.25 beneath the Qaidam basin and an average of 0.24 beneath the Songpan-Ganzi terrane and Kunlun mountains (Fig. 11.4) which were interpreted to characterize an easily deformable lower crust including intermediate granulites on top of granulite facies metapelites [*Mechie et al.*, 2012]. Those Poisson's ratio values lie in between previous estimates of the Poisson's ratio for northern Tibet, with crustal ratio average of 0.25 in the northern Qiangtang terrane [*Galvé et al.*, 2006] and 0.22 north of the Jinsha suture [*Jiang et al.*, 2006]. However, it is worth mentioning that *Owens and Zandt* [1997] predicted higher Poisson's ratios of 0.34-0.36 over a 30 km thickness in the middle-to-lower crust of northern Tibet which were interpreted to be related to the presence of partial melt. Furthermore, the crust beneath the Qaidam basin presents a relatively low Poisson's ratio compared to the average ratio of other surrounding stable areas such as the stronger crust present beneath the Tarim basin (average ratio of 0.26) [*Wang et al.*, 2003] and the Sichuan (average ratio of 0.27) [*Wang et al.*, 2010a]. Therefore, *Mechie et al.* [2012] interpreted the Qaidam crust to be more felsic and then more deformable. Although the Poisson's ratios from the INDEPTH IV model (Fig. 11.4) does not particularly highlight the presence of melt, the transition from a values of 0.24 to 0.25 beneath the Kunlun Shan is quite consistent with the end of the extension of the mid-crustal anisotropic conductive zone beneath the Kunlun mountains. This transition could characterize the northern limit of the crustal anatexis inferred from the MT models associated with changes in the mid-crustal lithologies.

11.2 CRUSTAL ANATEXIS IN NORTHERN TIBET

As mentioned by [*Whittington et al.*, 2009], the temperature of the continental crust can be enhanced by the following potential heat sources: *heat flow from the mantle*, *radiogenic heat*, *strain heating in ductile shear zones* and *intrusion of mantle-derived basaltic magma*. Beneath the Qiangtang and Songpan-Ganzi terranes, the crust is supposed to be relatively dry [*Hacker et al.*, 2000; *Rapine et al.*, 2003] compared to southern Tibet [*Li et al.*, 2003; *Unsworth et al.*, 2005]. Therefore, it was assumed that the main crustal isotropic conductive features of INDEPTH III and IV models observed beneath the northern Tibetan terranes are likely to be mainly due to partial melting of the crust under anomalously high temperatures [*Owens and Zandt*, 1997; *Mechie et al.*, 2004], in to the presence of a thin lithosphere [*Zhao et al.*, 2011] which enhances the heat flow in a crust already exceptionally thick enough to produce a high radiogenic heat generation. However, the presence of well resolved relatively thick resistive mantle underneath the observed anisotropic conductive anomaly characterizing the new INDEPTH MT models, excludes the presence of a significant mantle heat flow or an intrusion of mantle-derived basaltic magma beneath the southern Kunlun Shan. Furthermore, [*Wang et al.*, 2012] mentioned the presence of Miocene to Quaternary felsic magmas close to the Kunlun fault area which were interpreted to originate from crustal melts. Those observations confirm that the anisotropic conductive anomaly is likely to characterize partial melt in the crust. Therefore, in this study the presence of melt associated with the anisotropic anomaly extending to the north across the Kunlun fault is interpreted to be associated with the possible northward channel flow of the partially

molten Songpan-Ganzi crust [*Karplus et al.*, 2011; *Beaumont et al.*, 2001] or/and strain heating [*Whittington et al.*, 2009; *Nabelek et al.*, 2010] associated with heat production during ductile deformation in a mid-crustal shear zone located beneath the Kunlun fault.

11.2.1 *Electrical Conductance*

Although, MT models will be usually described by resistivity (conductivity) values, the conductance of a particular layer of the models is usually better constrained by the MT data [*Jones*, 1992] and therefore more representative of the bulk conductivity of a media rather than a single conductivity value taken directly from the models. The conductance of a layer is expressed in Siemens (S) and characterizes the integration of the conductivity of the layer over its own thickness h. Therefore, the conductance is commonly defined by a simple conductivity-thickness product. However, with magnetotellurics it is always difficult to define the extension of a conductor with depth as the method is mainly sensitive to the top of the conductive layer and its conductance rather than its thickness. In consequence, the estimation of the conductance characteristic of a particular conductive anomaly from the MT model is not straightforward.

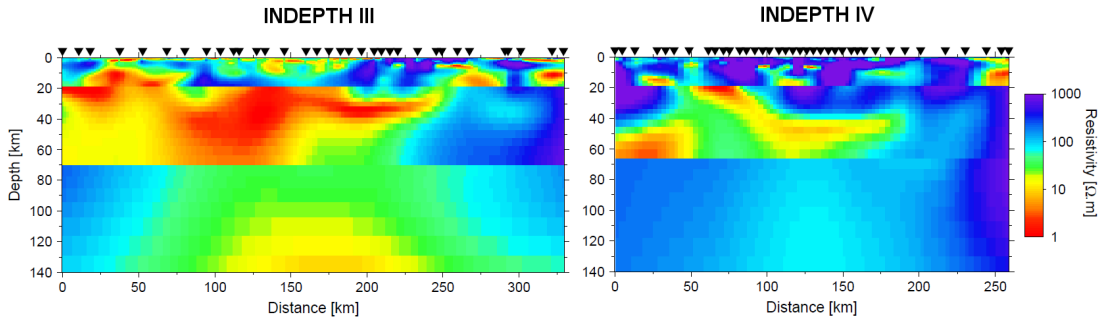

Figure 11.5: Constrained crustal layer for the Indepth III and IV MT yy models. The models were obtained by including a 20-70 km *tear zone* during the inversion process.

In order to constrain the conductance for the conductive anomaly observed for INDEPTH III and IV models, it was assumed that most of the melt responsible for the anomaly is likely to be mainly located in the crust. This assumption is based on the presence of temperature high enough to generate partial melting of the crust [*Owens and Zandt*, 1997; *Mechie et al.*, 2004; *Klemperer*, 2006; *Wang et al.*, 2012] but also on the fact that partial melting is likely to be widespread across the Tibetan crust [*Wei et al.*, 2007; *Fan and Lay*, 2003]. Furthermore, the resolution tests presented previously for each MT models (Fig. 8.17, 8.17 9.15 and 9.16) highlight sensitivity through the crustal conductor, at least from some sites, revealing a slightly more resistive upper mantle. The crustal conductance characteristic of the anomaly was integrated from each models between 20 km depth, as the temperature are probably too low above this depth for crustal melting [*Mechie et al.*, 2004], and 70 km, the average Moho depth in northern Tibet [*Vergne et al.*, 2002; *Karplus et al.*, 2011]. In order to get a better constraint of the conductance between those depths, the 2D anisotropic inversions were rerun for the INDEPTH III and IV MT data including a *tear zone* [*Mackie*, 2002] between 20-70 km. During the inversion, the *tear zone* will allow for sharp resistivity contrasts at its boundaries, avoiding mainly the smearing of the conductive layer to the upper mantle under the assumption that the conductive anomaly is

mainly located in the crust. In the models obtained by including a 20-70 km *tear zone* during the inversion process, the high conductive crustal anomaly is mainly constrained in the area defined by the *tear zone* (Fig. 11.5). The final RMS misfits associated with those alternative MT models are similar to the RMS of the main original models, although slightly lower due to the inhibition of the overall smoothness generated by the presence of the *tear Zone*.

The integrated conductance of the 20-70 km layer were evaluated for several models of different smoothness τ_s values in order to check for the consistency in the conductance estimations (Fig. 11.6). This approach was done for the INDEPTH III and IV data but also for the 2D models obtained when inverting the data generated from the synthetic 3D models A, B and C presented in the previous chapter. The crustal conductances issued from the 600 and 6000 profile present strong similarities with relatively high values > 10000 S in the Qiangtang and Songpan-Ganzi terranes consistent with previous studies by *Rippe and Unsworth* [2010] and [*Bai et al.*, 2010]. It decreases to the north as the split between the xx and yy conductance increases. The yy conductance is characterized by values of $1000 - 2000$ S beneath the Kunlun fault. Those particular trends are also quite well highlighted by the 2D models generated from synthetic data. Furthermore, two relevant observations are worth noticing. First, the consistency between the conductances evaluated from models with different smoothness, reveals the robustness of the main conductive features in the models. Second, when compared with the synthetic 3D models (dashed lines), the corresponding 2D anisotropic inversion models show a strong correlation of the conductance in the southern part of the models where the melt layer is 1D isotropic. Therefore knowing the true thickness of the conductive layer, the conductivity of the 3D synthetic models could be recovered. However, for the northern part of the models, Figure 11.6 highlights that even if the thickness of the intrusive conductive channels is known, the recovered conductivity can only be an underestimation of the true conductivity of the channels. In consequence, it is worth keeping in mind that in such 3D/anisotropic context, the conductance or conductivity values characteristic of those parts of the synthetic models would probably lead to underestimated melt fractions values. This assumption is made from simple synthetic models and the reality is certainly more complex. However, as the melt fractions associated with the INDEPTH models are estimated in the next section, it is worth mentioning that the "anisotropic sections" of the models will likely define lower bounds for the melt fraction estimates.

11.2.2 *Estimation of Melt fractions*

The estimation of the melt fractions associated with the crustal conductive features defining the INDEPTH III and IV models were realized using a similar approach as *Li et al.* [2003], *Rippe and Unsworth* [2010] and *Bai et al.* [2010]. This approach consists on using the conductance of a particular crustal layer instead of considering a single resistivity value directly taken from the model which may not be representative of the melt fraction of a particular area. Therefore, in order to estimate the melt fractions, two representative crustal (20-70 km) conductances where taken from Figure 11.6: a conductance of *15000 S* representative of the northern terranes of the plateau (mainly taken from the 600-line

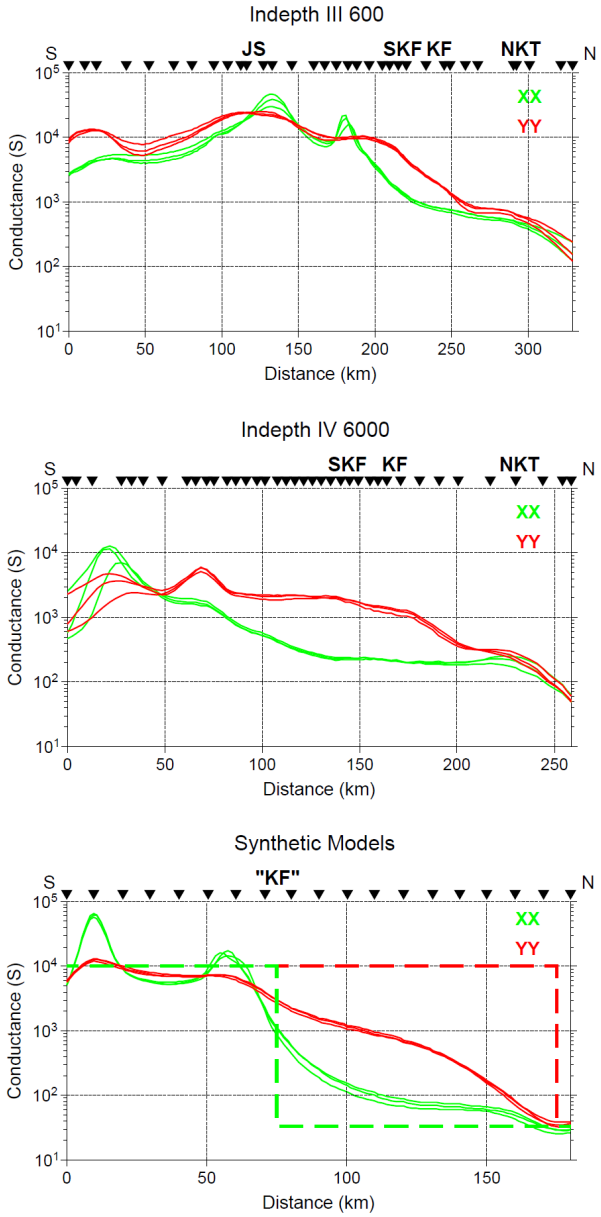

Figure 11.6: Integrated conductance between 20 and 70 km for INDEPTH III and IV models, and 2D anisotropic models obtained from the A, B, C synthetic data (Fig. 10.2). In each case, the conductance was estimated for both xx and yy models. For the 600 and 6000 data, the models were inverted for three different smoothness parameters (τ_s values of 5, 7 and 10). On the synthetic models' plot, the dashed lines represent the max and min bounds of the conductance defined by the original 3D synthetic models A, B, and C.

model at it presents a more global integration of the crust of the terranes) and a value of *1500 S* associated with the crustal conductance beneath the Kunlun fault.

The melt fractions X_m were estimated using the Hashin-Shtrikman upper bound (HS+), the Tube model and the Archie's law presented in the chapter on the Electrical properties of the Earth, assuming a good interconnection of the melt phase. As discussed by *ten Grotenhuis et al.* [2005], the Archie's law appears to get closer to the Tube model for low

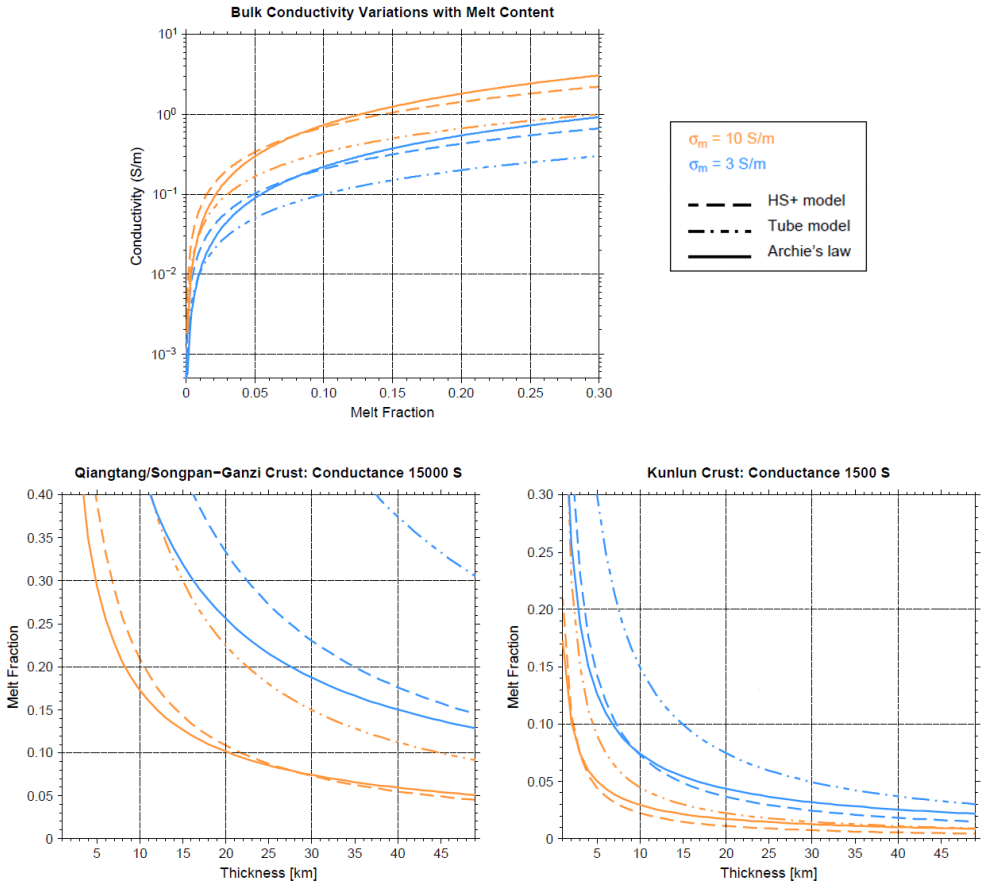

Figure 11.7: **Bulk conductivity** estimated from the Hashin-Shtrikman upper bound (HS+) model, the Tube model and the Archie'law for different melt fractions and using melt conductivities of 3 S/m and 10 S/m. - **Melt fractions** predicted from the thickness of the crustal conductive layer and its associated bulk conductivity derived from the conductances characteristic of the Qiangtang/Songpan-Ganzi terranes (15000 S) and the Kunlun crust (1500 S). The melt fractions are estimated for the HS+ model, the Tube model and the Archie'law for the melt conductivities of 3 S/m and 10 S/m.

melt fractions whereas it gets relatively close to the HS+ model for higher fractions (Fig. 11.7). The bulk conductivity modelled from the Archie's law is independent on the rock matrix (solid phase) conductivity, however for the two other models a matrix conductivity of 0.0005 S/m (2000 Ω.m) was used. The melt conductivities of 3 S/m and 10 S/m, characteristic of mid-to-lower crustal depth, were chosen with respect to similar studies [*Partzsch et al.*, 2000; *Rippe and Unsworth*, 2010; *Bai et al.*, 2010].

In order to quantify X_m, the equations characterizing those three two-phases-mixing models (Tab. 5.1) can be rewritten as:

Hashin-Shtrikman upper bound:

$$X_m = \frac{3\sigma_m(\sigma_s - \sigma_{eff})}{(\sigma_{eff} + 2\sigma_m)(\sigma_s - \sigma_m)} \tag{11.1}$$

Tube model:

$$X_m = \frac{(\sigma_s - \sigma_{eff})}{\sigma_s - \sigma_m/3} \tag{11.2}$$

Archie's law:

$$X_m = \exp[\frac{\ln(\sigma_{eff}/C\sigma_m)}{n}] \tag{11.3}$$

As for *Rippe and Unsworth* [2010]'s study, values of C=1.47 and n=1.3 defined by *ten Grotenhuis et al.* [2005] were used for the melt estimations made from Archie's law.

The bulk conductivity (σ_{eff}) can be derived from the conductance for different layer thicknesses (Conductance = conductivity x thickness). Therefore, considering different thicknesses (1 to 50 km) for the crustal conductor located between 20-70 km will lead to different estimations of the melt fractions (Fig. 11.7). For a layer with a relatively high conductance of 15000 S, the Tube model seems to lead to erroneous estimates as those are quite unrealistic even for a 50 km thick layer. However, the estimates from the HS+ model and Archie's law are relatively close. For the lower conductance of 1500 S, all models predict melt fractions inferior to 0.05 for thicknesses superior to 30 km. Although, the model's estimates seem less scattered than for higher conductance, the Tube model still present some high estimates particularly for a melt conductivity of 3 S/m. The Archie's law, also used by *Rippe and Unsworth* [2010] and *Bai et al.* [2010], appeared to be a good compromise between the HS+ model and the Tube model (Fig. 11.7). Therefore, the Archie's law, which is independent on the solid matrix conductivity, was concluded to be the more appropriate model for the further estimations of the melt fractions associated with meaningful estimates for the thickness of the crustal conductive layer.

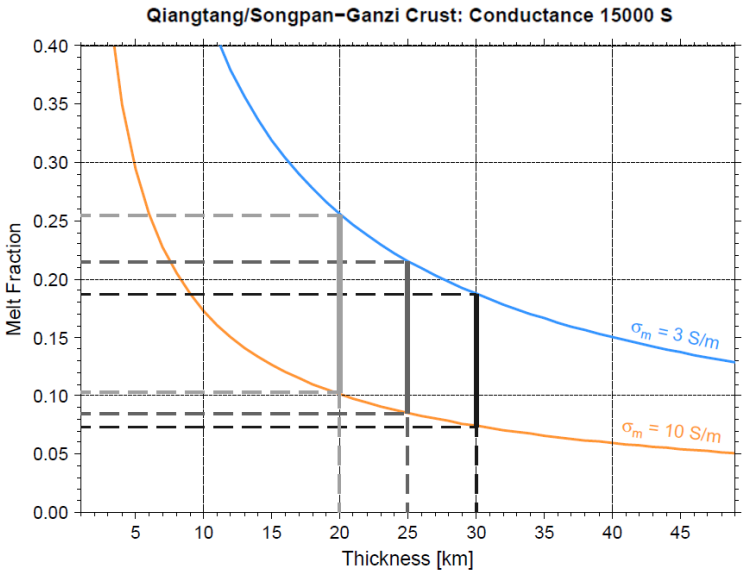

Figure 11.8: Melt fractions for the Qiangtang/Songpan-Ganzi terranes (15000 S) predicted for thicknesses of 20 km, 25 km and 30 km constrained from seismic studies [*Owens and Zandt*, 1997; *Agius and Lebedev*, 2010; *Karplus et al.*, 2011; *Yang et al.*, 2012]. The melt fractions are estimated from the Archie'law for the melt conductivities of 3 S/m and 10 S/m.

According to Figure 11.8, the melt fractions present in the middle-to-lower crust of the north Qiangtang and Songpan-Ganzi terranes are likely to range between 7% to 25%, which agree with the previous studies from *Rippe and Unsworth* [2010] and [*Bai et al.*, 2010]. The layer thickness of the partially molten crust was assumed between 20 and 30 km according to the seismic constraints from [*Owens and Zandt*, 1997], [*Agius and Lebedev*, 2010], [*Karplus et al.*, 2011] and [*Yang et al.*, 2012] presented above.

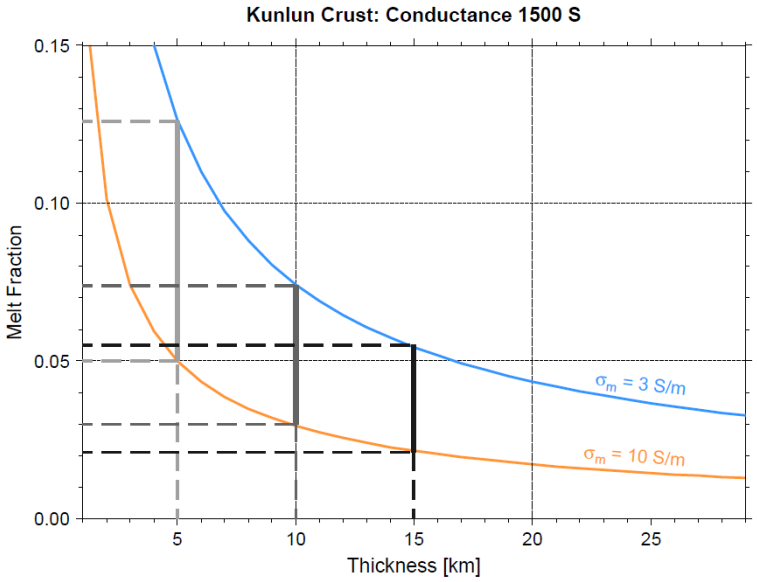

Figure 11.9: Melt fractions for the Kunlun crust (1500 S) predicted for thicknesses of 5 km, 10 km and 15 km constrained by the strain heating [*Nabelek et al.*, 2010] and channel flow [*Beaumont et al.*, 2001] models. The melt fractions are estimated from the Archie'law for the melt conductivities of 3 S/m and 10 S/m.

In this study, the anisotropic conductive anomaly present in the middle crust of the southern Kunlun Shan is interpreted to be characterized by channel flow or/and strain heating models. The thickness for the channel flow model was considered to range between 10-15 km [*Beaumont et al.*, 2001], which is more or less in agreement with the depth separation of the intra-crustal seismic reflectors highlighted by *Karplus et al.* [2011]. Furthermore, the width of the shear zone associated with strain heating in the model from [*Whittington et al.*, 2009; *Nabelek et al.*, 2010] was 3 km. The thickness of the anisotropic conductive anomaly was constrained between 5 and 15 km, leading to melt fractions estimates ranging between 2% to 12% (Fig. 11.9).

11.3 TECTONIC MODEL OF NORTHERN TIBET

11.3.1 *Qiangtang and Songpan-Ganzi terranes*

The partial melt characterized by high conductivity in the Qiangtang and Songpan-Ganzi crust will follow variation in surface magmatism in both space and time [*Chung et al.*, 2005]. Eocene to Oligocene magmatism in the Qiangtang terrane is mainly associated with reactivation of the Mesozoic Bangong and Jinsha sutures, with northward subduction of Lhasa

terrane and southward subduction of Songpan-Ganzi terrane, respectively [*Ding et al.*, 2003]. Middle-Miocene to Quaternary magmatism, although minor, is widely distributed in the Songpan-Ganzi terrane and more locally in the northern Qiangtang terrane [*Ding et al.*, 2003]. The conductivity of a partially molten rock depends on the interconnectivity of melt, as opposed to melt insulated in pockets, and melt interconnectivity exists at low melt fractions [*Partzsch et al.*, 2000]. Large-volume fractions of melt are not required to explain the INDEPTH III and IV MT models, however, the models highlight and reconfirm that melt is widespread in the crust, as previously proposed [*Wei et al.*, 2001]. Furthermore, in partially molten rocks, the strength of the rock is mainly controlled by the degree of interconnection of melt [*Rosenberg and Handy*, 2005]. Although melt fractions of 25% are probably unrealistic, a lower bound of 7% is sufficient (Fig. 11.10) to produce a significant strength reduction in the crust [*Rosenberg and Handy*, 2005], localizing the deformation and allowing for mechanical flow of the crust in the north Qiangtang and Songpan-Ganzi terranes [*Clark and Royden*, 2000; *Klemperer*, 2006; *Bai et al.*, 2010].

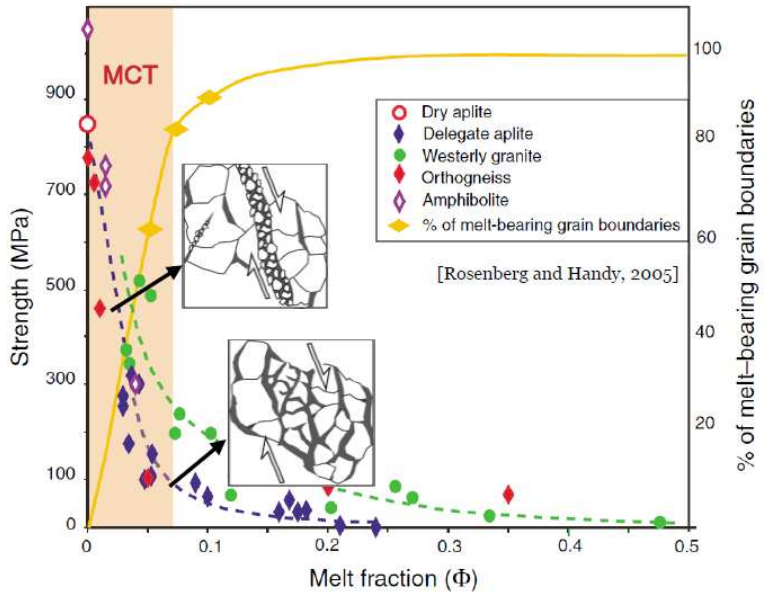

Figure 11.10: Aggregate strength vs melt fraction. Data references can be found in [*Rosenberg and Handy*, 2005]. MCT = Melt Connectivity Transition. *from* [*Rosenberg and Handy*, 2005]

Furthermore, the recent volcanism in northern Tibet, as well as the widespread crustal melting, is likely to be the consequence of the southward subduction of Asian lithospheric mantle beneath the Songpan-Ganzi terrane, imaged by seismic receiver functions [*Zhao et al.*, 2011], associated with convective thinning of the Tibetan mantle lithosphere [*Chung et al.*, 2005; *Zhao et al.*, 2011; *Arnaud et al.*, 1992]. The thinning of the Tibetan lithosphere explains the widespread distribution of potassic volcanism in the Songpan-Ganzi terrane [*Ding et al.*, 2003; *Chung et al.*, 2005]. Finally, during the Eocene, the Tanggula thrust system (TTS) may have played a major role in the uplift of the early Tibetan plateau [*Wang et al.*, 2008], in association with the reactivation of the Jinsha river suture [*Roger et al.*, 2000]. The Tibetan plateau probably grew through major thrust systems such as the TTS [*Wang et al.*, 2008], with the modern equivalent being the North Kunlun Thrust bounding the northern edge of the plateau with a major drop in elevation. The decoupling of the deformation,

generated by the presence of a weak middle-lower crust, associated with the step-by-step thickening of the crust [*Vergne et al.*, 2002], probably contributed to the atypical topography of the plateau.

11.3.2 *Crustal Transition Zone beneath the Kunlun Fault*

The INDEPTH III and IV anisotropic modelling highlights a transgressive, penetrative extension of the Tibetan mid-crustal conductive anomaly to the north, crossing the upper-crustal sharp resistivity contrast characterizing the subvertical Kunlun fault. The new resistivity models show that the anisotropic structure is consistent with wide-angle seismic data [*Karplus et al.*, 2011; *Mechie et al.*, 2012]. Furthermore, the results agree quite well with the model of *Owens and Zandt* [1997] defining a mid-crustal LVZ crossing the Kunlun Fault and represented on Figure 4.16. According to the 3D synthetic modelling, the anisotropic conductive anomaly is likely to be a finger-like intrusion of melt beneath the Kunlun Shan. The melt fractions associated with those intrusions are estimated to range between 2% to 12%. As the greatest strength drop occurs for low-melt fractions (Fig. 11.10) [*Rosenberg and Handy*, 2005], those melt estimates will still have a significant effect on the rheology of the Kunlun crust. The weak middle crust crossing the Kunlun fault may be decoupling locally the upper-crust deformations from the lower crust and mantle. Therefore, the Kunlun fault is not likely to be a lithospheric discontinuity [*Meyer et al.*, 1998] and its extension in depth is rather limited to the upper crust. The weaker Kunlun crust thickens vertically in response to the crustal shortening between India and the more rigid Asian blocks represented here by the Qaidam lithosphere, leading to a Moho offset at the Kunlun-Qaidam border [*Shi et al.*, 2009]. The finger-like penetrative melt extension to the north, weakening the Kunlun crust, stops at this offset at the present time [*Karplus et al.*, 2011]. However, the anisotropy anomaly may not be homogeneous along the whole of the northern Tibetan border and its depth and horizontal extension to the north is likely to vary. Furthermore, under the INDEPTH IV profile, the variation in the mid-crustal lithologies south of the north Kunlun thrust observed from Poisson's ratio [*Mechie et al.*, 2012], might define the northern limit of the partially molten crust observed on the MT models.

The conductive anomaly is likely to characterize a mid-crustal shear zone located beneath the Kunlun fault, decoupling the deformations associated with the southward subduction of Asian lithosphere [*Zhao et al.*, 2011] and the northward motion of the upper crust highlighted by the GPS data [*Gan et al.*, 2007] (Fig. 3.5). The presence of partial melt extending to the north across the Kunlun fault along this mid-crustal shear zone, can be interpreted to define the northward channel flow of the partially molten Songpan-Ganzi crust [*Karplus et al.*, 2011] probably in a similar manner as the "tunnel flow model" presented by *Beaumont et al.* [2001]. The intrusive north-south channel flow could have been facilitated by strain heating [*Whittington et al.*, 2009; *Nabelek et al.*, 2010]. Whereas the channel flow model describes the motion of the partially molten middle crust relative to the lower and upper crust [*Beaumont et al.*, 2001], strain heating will generate melt at a particular location in the ductile shear zone [*Nabelek et al.*, 2010]. The anisotropic signature of the conductive anomaly might characterize different levels of strain along the northern Tibetan border which could explain the presence of separated intrusive channels.

To conclude, the melt intrusions in the Kunlun middle crust may have been triggered by strain heating associated with heat production during ductile deformation in a mid-crustal shear zone located beneath the Kunlun fault in the southern Kunlun ranges. As melt fractions increase to values > 5%-7% (Fig. 11.10), the shear zone may develop into channels where the Songpan-Ganzi partially molten crust flows to the north and mechanically weaken the Kunlun crust. In addition to the eastward crustal flow in eastern Tibet [*Bai et al.*, 2010] characterizing the east-west extension of the plateau, the melt penetration across the Kunlun Fault through intrusive channels is accommodating crustal shortening in northern Tibet. Furthermore, it may also characterize a transition zone [*Medvedev and Beaumont*, 2006] between the weak partially molten crust of the plateau and the more rigid Qaidam lithosphere, associated with the growth of the plateau to the north (Fig. 11.11), with extension of the crustal thickening to the south of the Qaidam Basin [*Karplus et al.*, 2011].

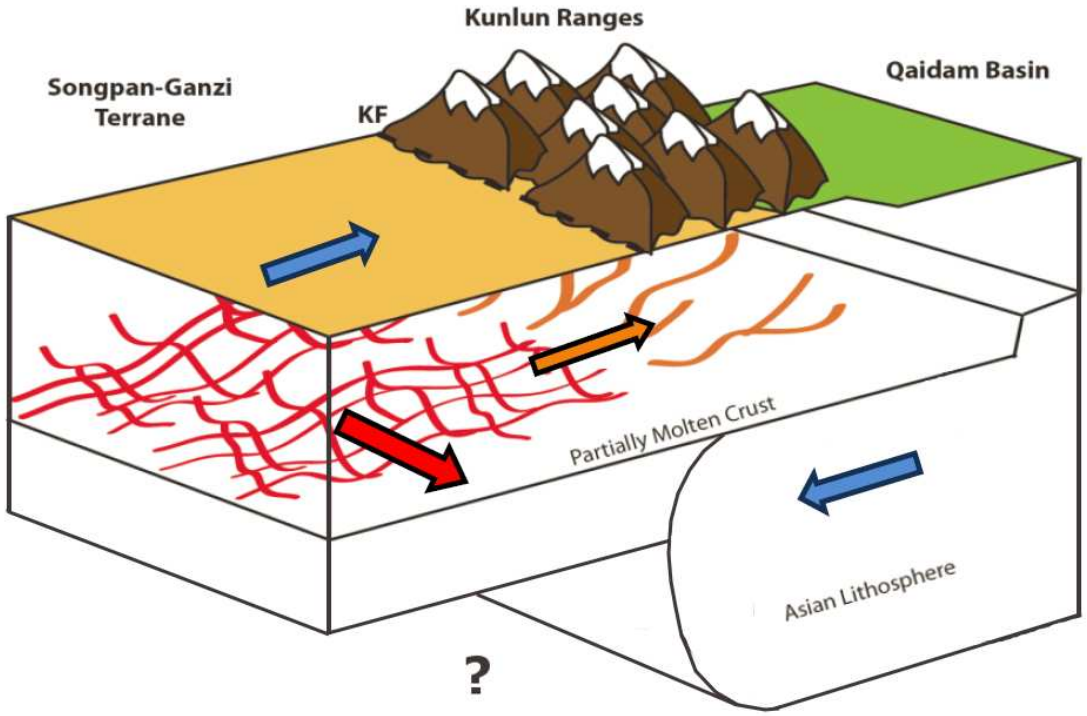

Figure 11.11: Simple tectonic model inferred from the MT modelling of Northern Tibet. The **blue arrows** represent the opposite motion of the Asian lithospheric mantle and the Tibetan upper crust. - The **red arrow** represent the eastward channel flow imaged by [*Bai et al.*, 2010]. - The **orange arrow** characterizes the penetration of partial melt into intrusive crustal channels defining a transition zone beneath the Kunlun ranges. - The **interrogation mark ?** defines a lack of information from the MT models. This zone of the model may be defined by the southward subduction of Asian lithospheric mantle beneath the Songpan-Ganzi terrane associated with the convective thinning of the Tibetan mantle lithosphere.

Part IV

CONCLUSION, APPENDICES AND BIBLIOGRAPHY

12 SUMMARY AND MAIN CONCLUSIONS

In this study, 2D isotropic, 2D anisotropic and 3D isotropic magnetotelluric (MT) modelling has been investigated for two MT profiles characterized by the INDEPTH III 600 and INDEPTH IV 6000 transects crossing the Kunlun fault, one of the major northern tectonic boundaries for the atypical topography of the Tibetan plateau. The apparent surficial deformation associated with the sinistral strike-slip Kunlun fault reflects the absorption of the convergence between India and Asia by accommodating the eastward extrusion of the Tibetan plateau in the south, and the northeastward motion of the northern terranes of the Himalyan-Tibetan orogen in the north. However, the results from the presented MT modelling highlight a more complex deformation process occurring at mid-crustal depths, decoupled from the upper crustal brittle deformation linked to the fault. The main conclusions from the MT results are summarised as follows:

- The revised INDEPTH III and INDEPTH IV MT models show unequivocal evidence for electrical anisotropy observed at the northern edge of the Tibetan plateau, compromising the prior characterization of the Kunlun fault as a significant rheological boundary between weak, warm Tibetan crust and the rigid Eastern Kunlun-Qaidam block. Furthermore, the sinistral deformation associated with the fault is likely to be limited to the upper crust.

- The middle-to-lower crustal conductive structures located in the north Qiangtang and Songpan-Ganzi terranes re-confirm widespread partial melting in northern Tibet, but also exhibit compelling spatial correlations with major regional tectonic features, implying structural control of crustal melt distribution leading to localized decoupling of the deformation in time and space.

- The resistivity constraints on the presence of widespread partial melt in the crust and colder, thicker lithosphere beneath the Kunlun Shan are interpreted to characterize the southward subduction of Asian lithospheric mantle beneath the Songpan-Ganzi terrane, associated with convective thinning in the upper mantle beneath the northern Tibetan terranes.

- For this study, the 2D and 3D modelling reveal the limitations of isotropic solutions. The 2D anisotropic models show a net improvement from 2D isotropic models and also present a better estimation of the depth and extent of the anisotropic conductive anomaly compared to the 3D inversion models.

- Both 3D synthetic modelling and inversions, confirm the interpretation that the observed conductive anisotropic anomaly is likely to characterize a finger-like intrusion of melt defining separated channels beneath the Kunlun Shan. However, their width, thickness and deviations in orientation cannot be resolved at the observed depths.

- The resistivity models were compared with recent seismic wide-angle refraction, reflection and surface waves studies, confirming the presence of melt in northern Tibet. Furthermore, the correlation between the seismic and MT results indicate a variation in the mid-crustal lithologies south of the north Kunlun thrust, which likely defines the northern limit of the anisotropic crustal anatexis inferred from the MT models.
- In the crust of the north Qiangtang and Songpan-Ganzi terranes, the melt fraction estimates reconfirm the presence of localized crustal deformation allowing for mechanical flow of the middle-to-lower crust beneath Tibet.
- In northern Tibet, the partial melt associated with the anisotropic anomaly observed on the new INDEPTH resistivity models is interpreted as the result of strain heating and intrusive channels in a sub-horizontal shear zone located beneath the Kunlun fault and southern Kunlun Shan. This shear zone may be characterized by different levels of strain along the whole of the northern Tibetan border, which develops into north-south intrusive channels as partial melt is generated during strain heating.

The identified crustal melt intrusions across the Kunlun fault inferred from magnetotelluric modelling probably characterizes the growth of the plateau to the north, but also accommodates the north-south crustal shortening in Tibet through decoupling upper crustal from lower crustal and upper mantle deformation. Finally, the intrusive north-south channels likely define a transition zone between the main Tibetan crustal flow model and the more stable Qaidam lithosphere, as the high elevation of the Tibetan plateau is probably extending to the north.

Outlook

Although INDEPTH phase IV is likely to mark the end of the INDEPTH project, geophysical investigation in Tibet has never been so active, in particular the Chinese SINOPROBE project. In the framework of SINOPROBE, magnetotelluric and seismic surveys are conducted in North China and the Tibetan Plateau with reduced station spacing, aiming to obtain a well constrained 3D model of the whole of China in the long-term. The large quantity of MT data associated with SINOPROBE and ongoing improvements in the 3D inversion schemes may hopefully generate strong constraints on the intrusive channels highlighted by this study. Finally, it has been shown the 2D anisotropic modelling can bring strong constraints in the interpretation of the 3D inversion models. Therefore, 3D anisotropic inversion seems to be the next step to get a better resolution of the observed anisotropic structures. Meanwhile, incorporating 2D anisotropic inversion results as a priori information into the 3D inversions may define a first stage for future 3D anisotropic modelling.

INDEPTH III - SUPPLEMENTARY FIGURES

A

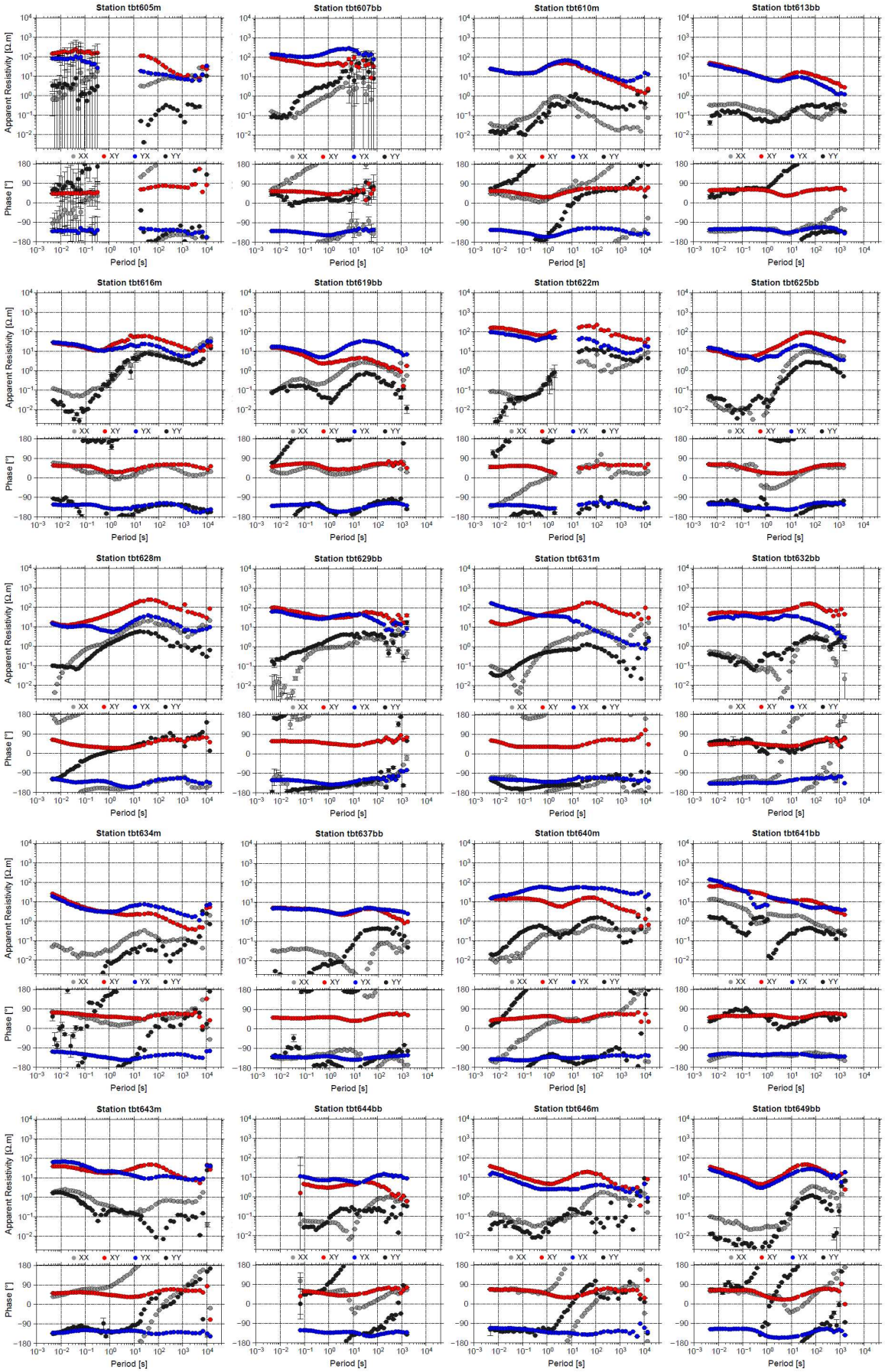
Station tbt605m
Station tbt607bb
Station tbt610m
Station tbt613bb
Station tbt616m
Station tbt619bb
Station tbt622m
Station tbt625bb
Station tbt628m
Station tbt629bb
Station tbt631m
Station tbt632bb
Station tbt634m
Station tbt637bb
Station tbt640m
Station tbt641bb
Station tbt643m
Station tbt644bb
Station tbt646m
Station tbt649bb
Apparent Resistivity [Ω.m]
Phase [°]
Period [s]
XX
XY
YX
YY

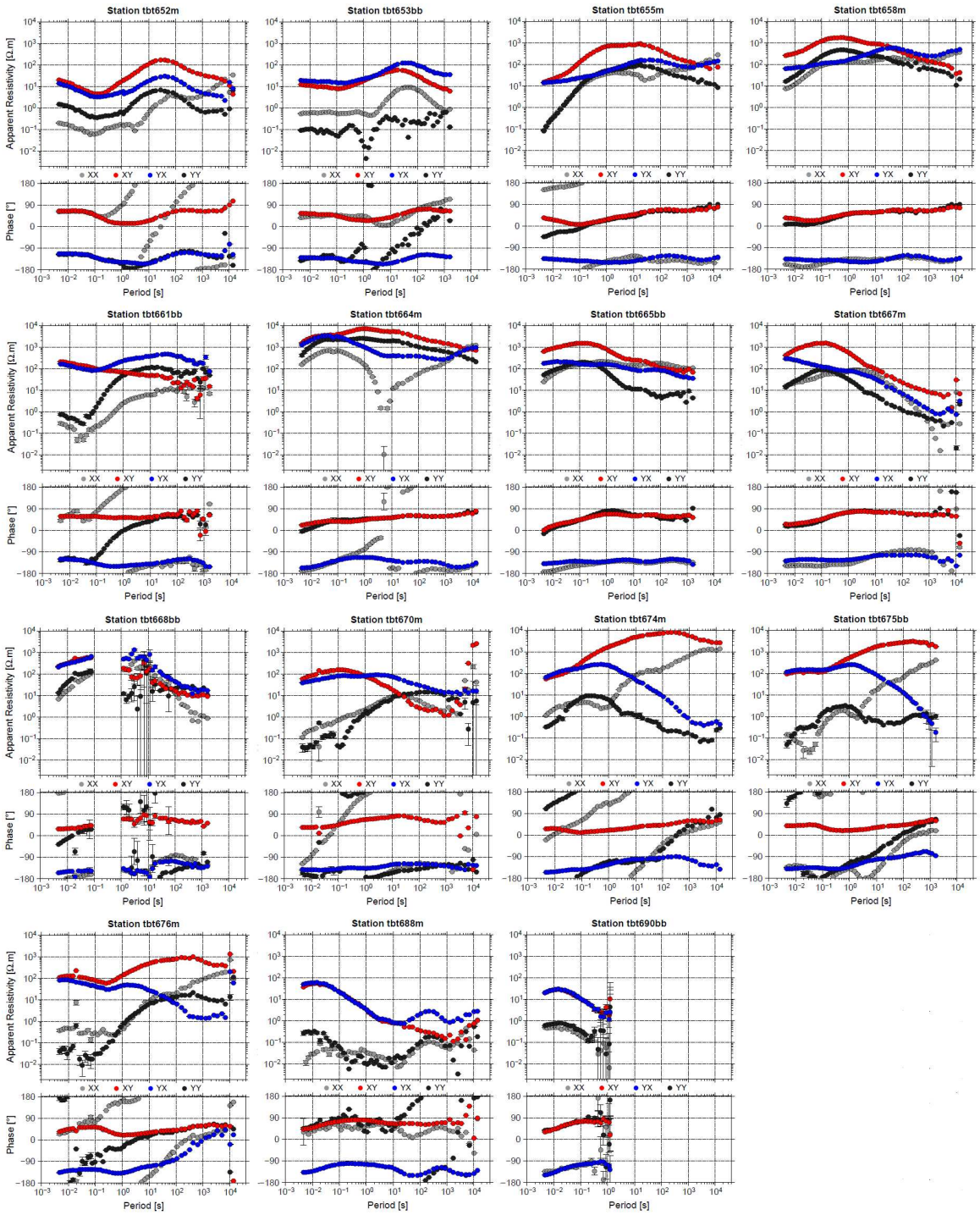

Figure A.1: INDEPTH III 600-line original data plotted for all 4 components XX, XY, YX and YY.

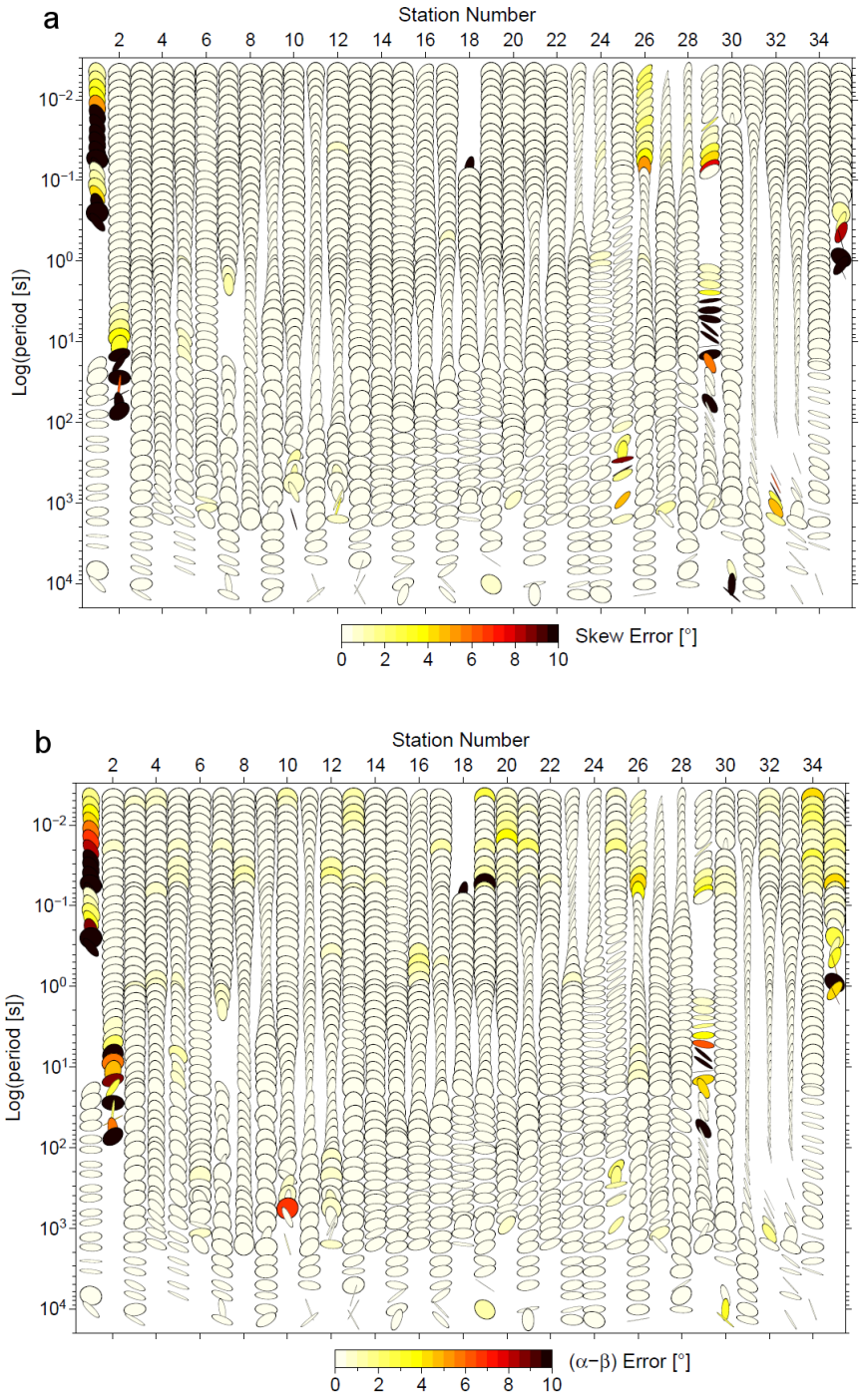

Figure A.2: Errors on the skew angle (a) and orientation of the phases tensor ellipses (b) for the 600-line data. The ellipses are plotted so that the horizontal axis corresponds to an east-west orientation.

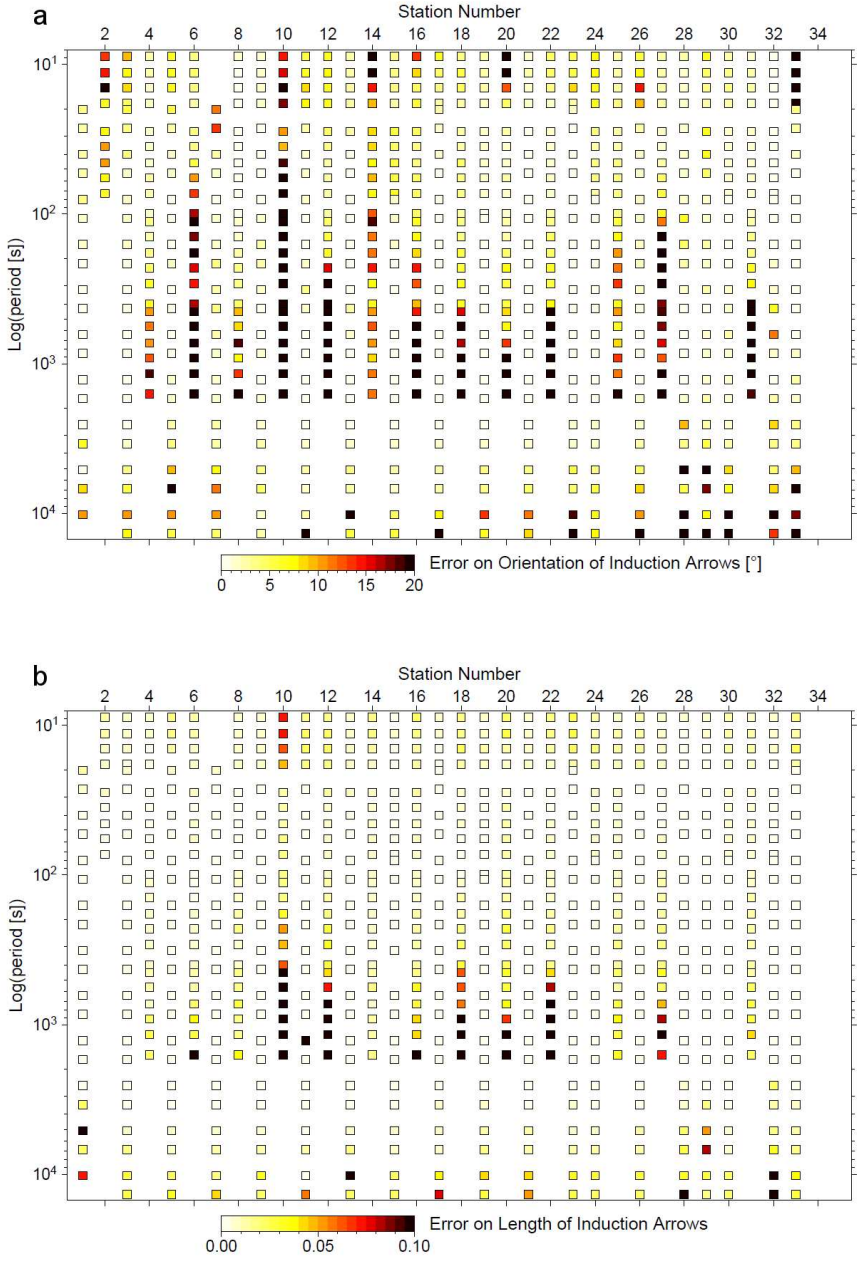

Figure A.3: Errors on the orientation (a) and length (b) of the real induction arrows for the 600-line data. Station numbers increase to the north.

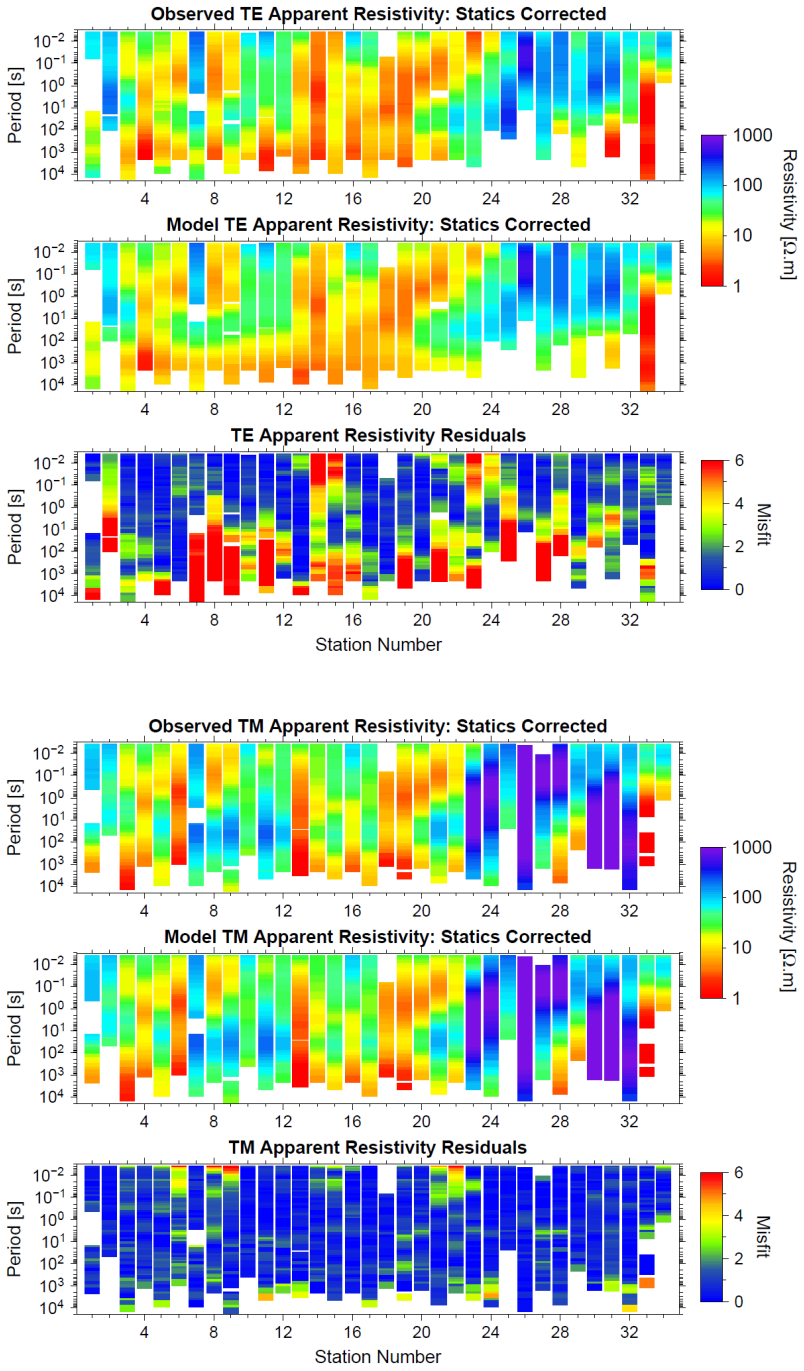

Figure A.4: Residuals for the TE and TM apparent resistivities associated with the **global** anisotropic inversion of the 600-line data. Station numbers increase to the north.

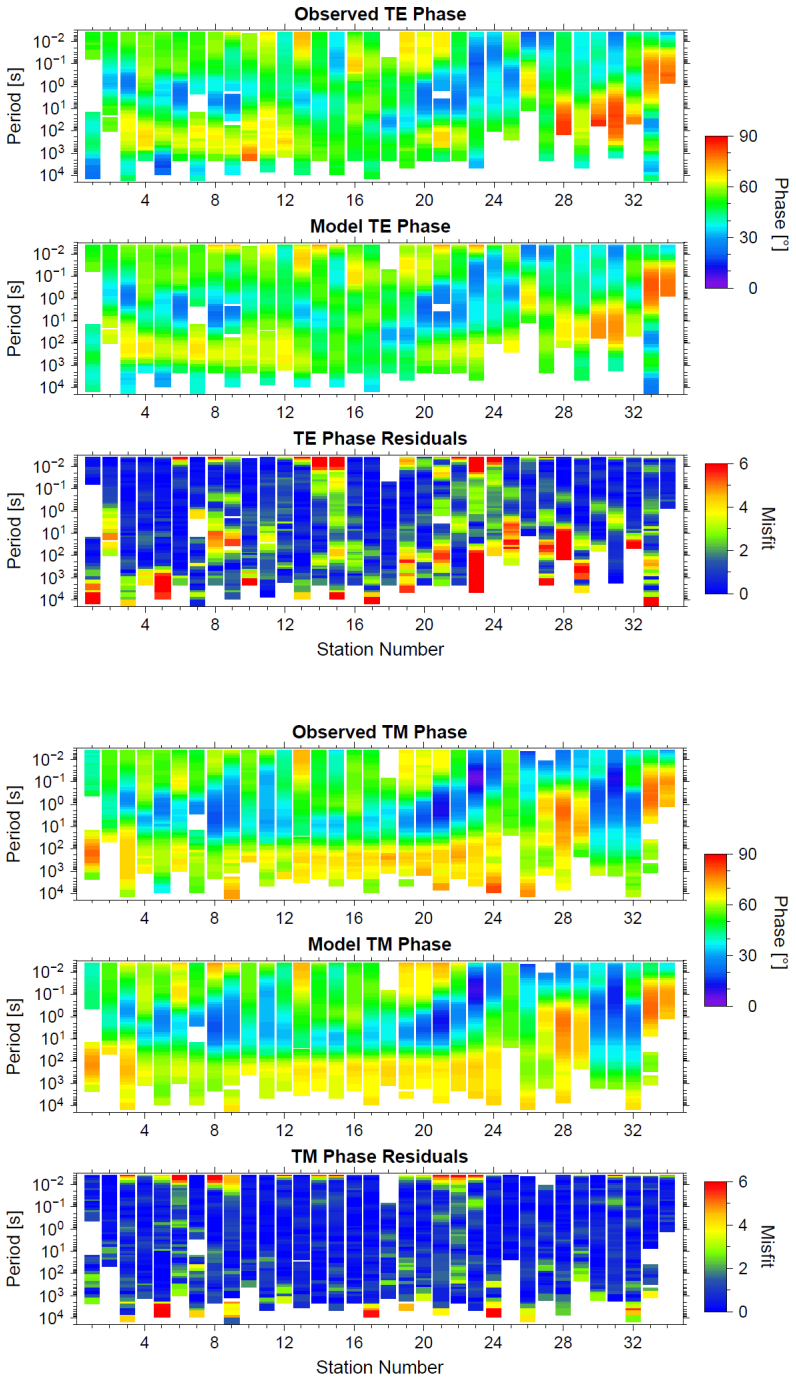

Figure A.5: Residuals for the TE and TM phases associated with the **global** anisotropic inversion of the 600-line data. Station numbers increase to the north.

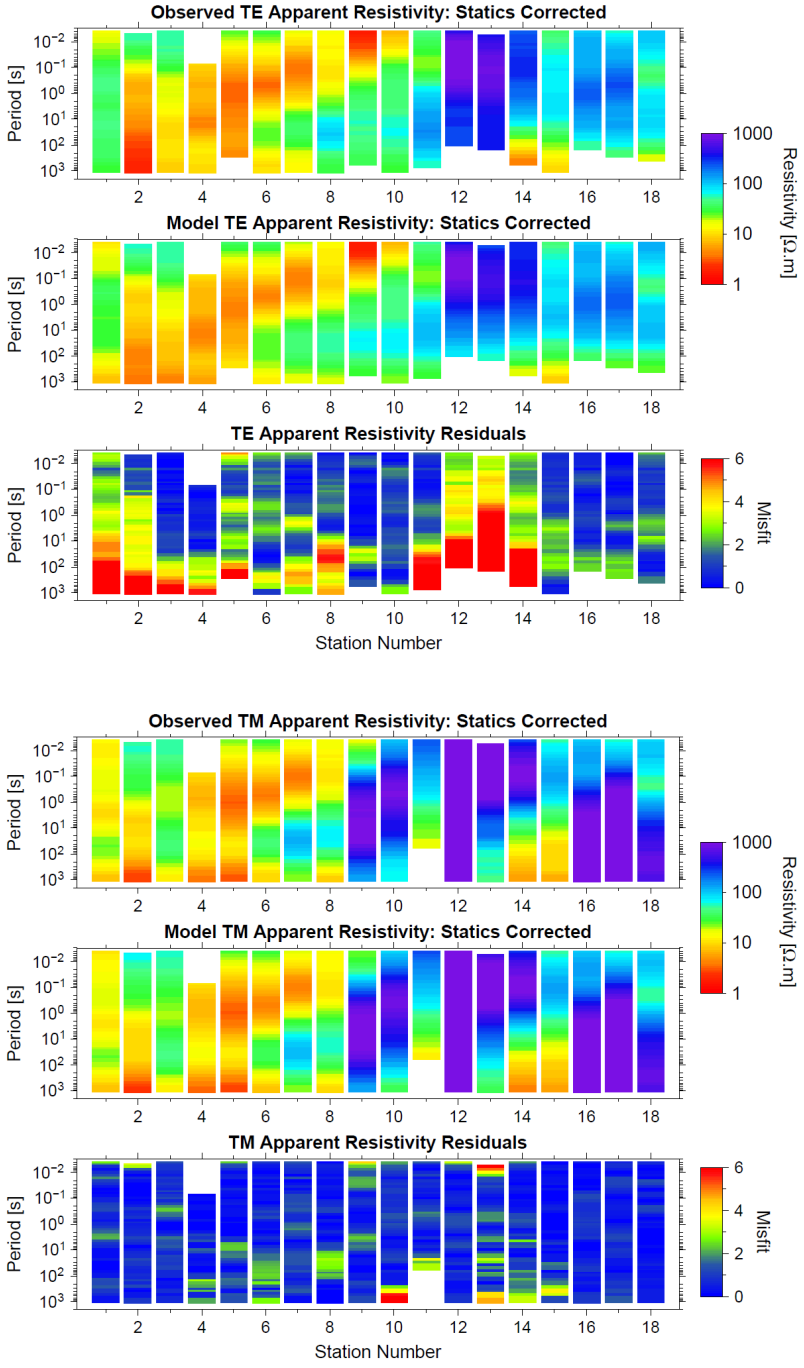

Figure A.6: Residuals for the TE and TM apparent resistivities associated with the **focussed** anisotropic inversion of the 600-line data. Station numbers increase to the north.

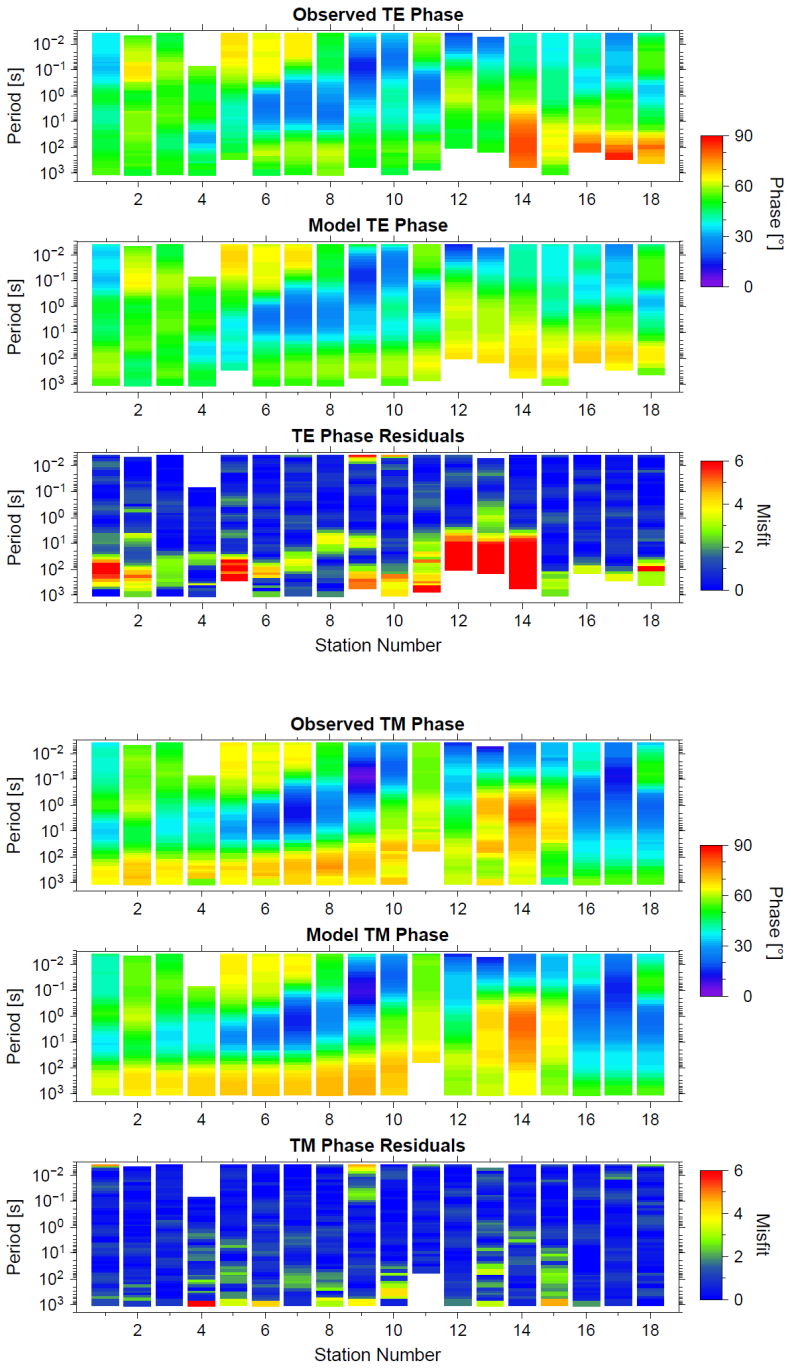

Figure A.7: Residuals for the TE and TM phases associated with the **focussed** anisotropic inversion of the 600-line data. Station numbers increase to the north.

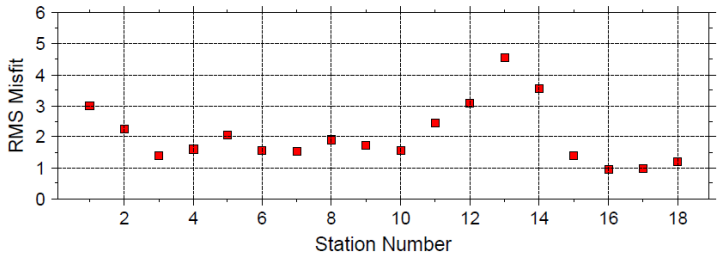

Figure A.8: Global data misfit for each station associated with the **focussed** anisotropic inversion of the 600-line data.

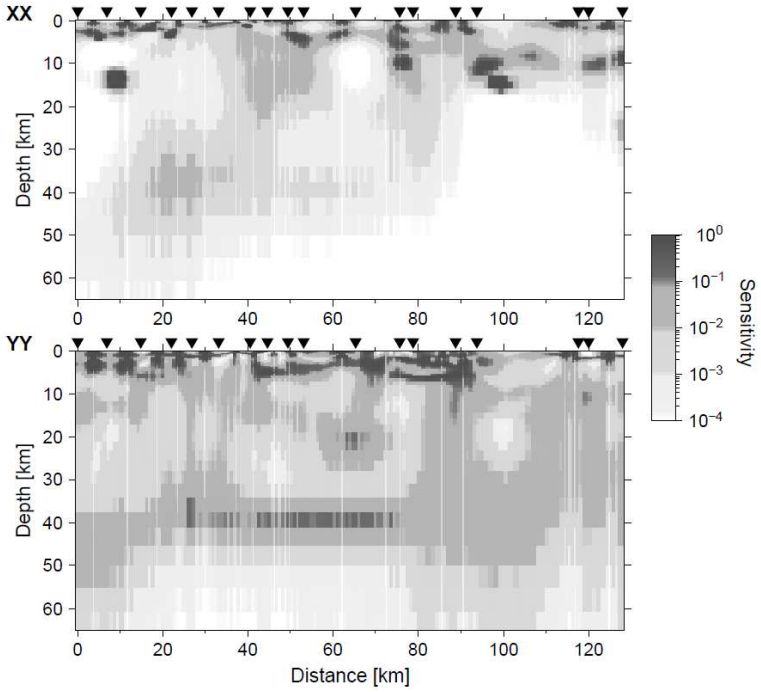

Figure A.9: Sensitivty maps associated with the **focussed** anisotropic inversion of the 600-line data. Station numbers increase to the north.

INDEPTH IV - SUPPLEMENTARY FIGURES

B

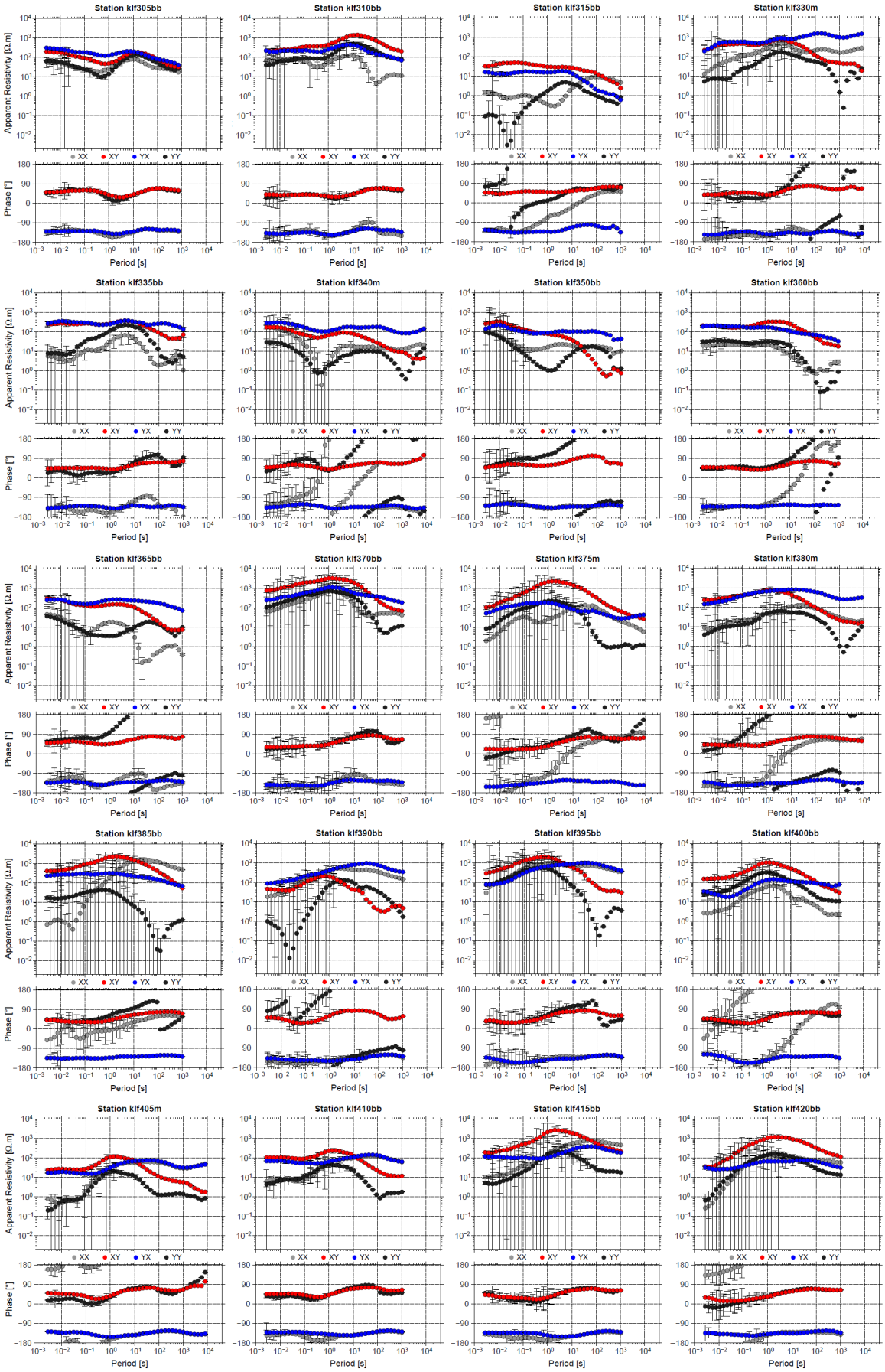
Station klf305bb
Station klf310bb
Station klf315bb
Station klf330m
Station klf335bb
Station klf340m
Station klf350bb
Station klf360bb
Station klf365bb
Station klf370bb
Station klf375m
Station klf380m
Station klf385bb
Station klf390bb
Station klf395bb
Station klf400bb
Station klf405m
Station klf410bb
Station klf415bb
Station klf420bb
Apparent Resistivity [Ω.m]
Phase [°]
Period [s]
XX
XY
YX
YY

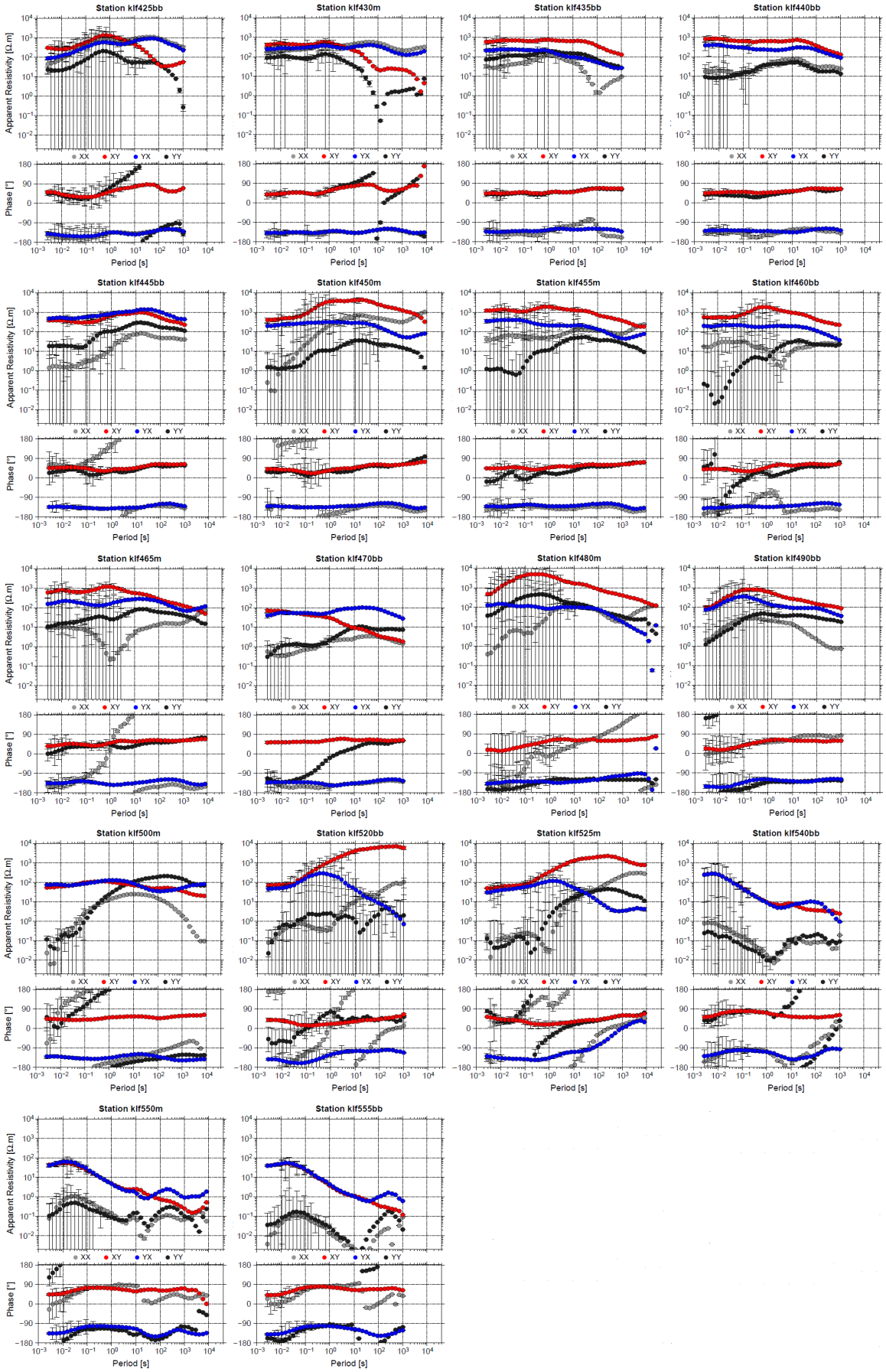

Figure B.1: INDEPTH IV 6000-line original data plotted for all 4 components XX, XY, YX and YY.

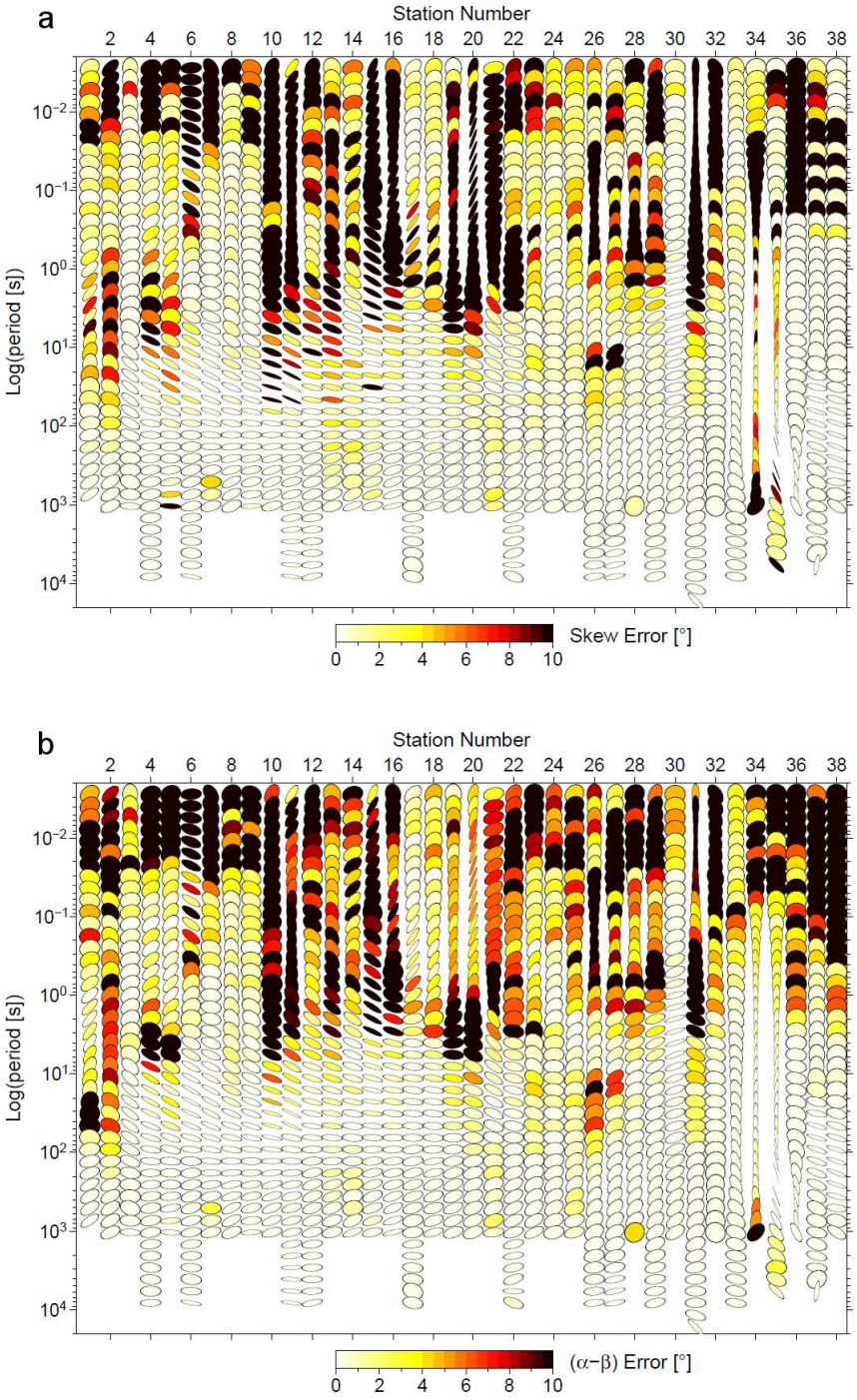

Figure B.2: Errors on the skew angle (a) and orientation of the phases tensor ellipses (b) for the 6000-line data. The ellipses are plotted so that the horizontal axis corresponds to an east-west orientation.

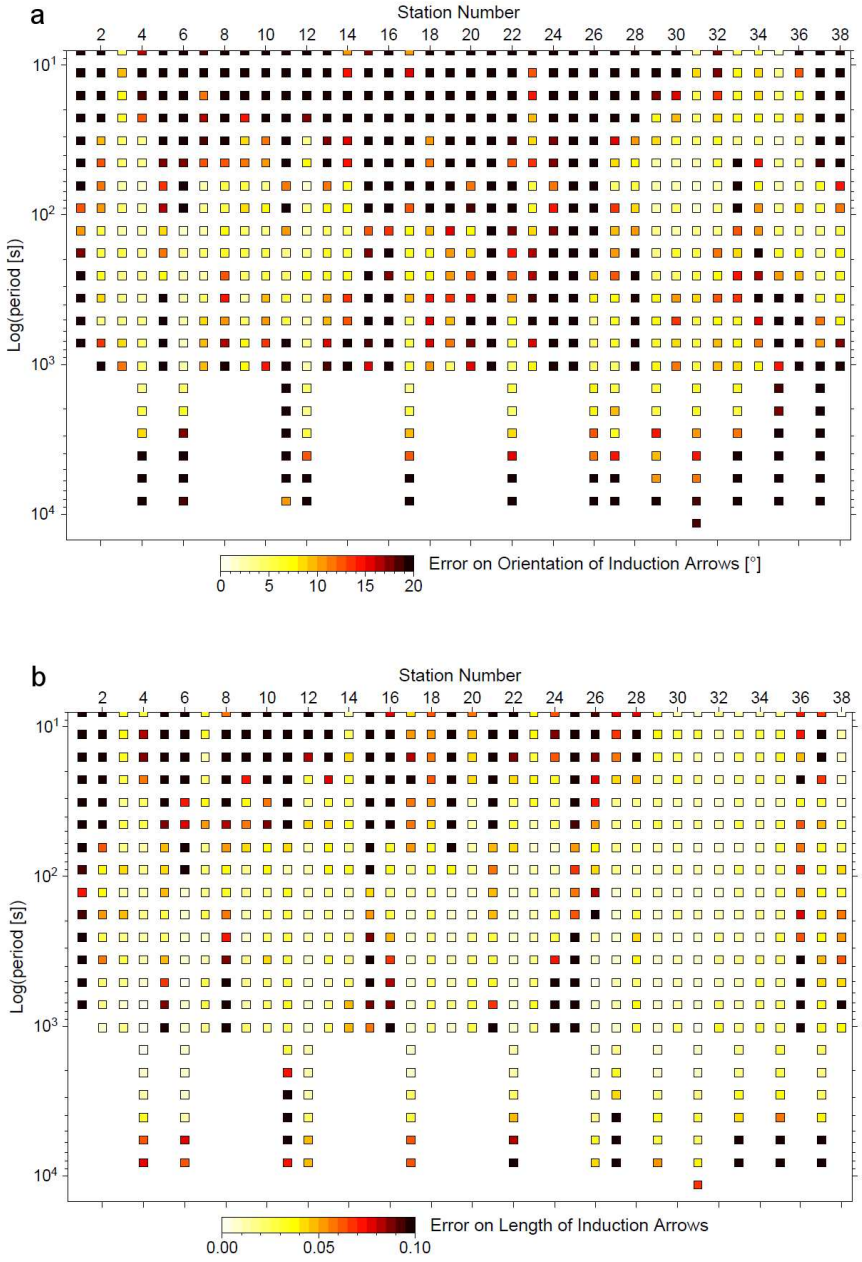

Figure B.3: Errors on the orientation (a) and length (a) of the real induction arrows for the 6000-line data. Station numbers increase to the north.

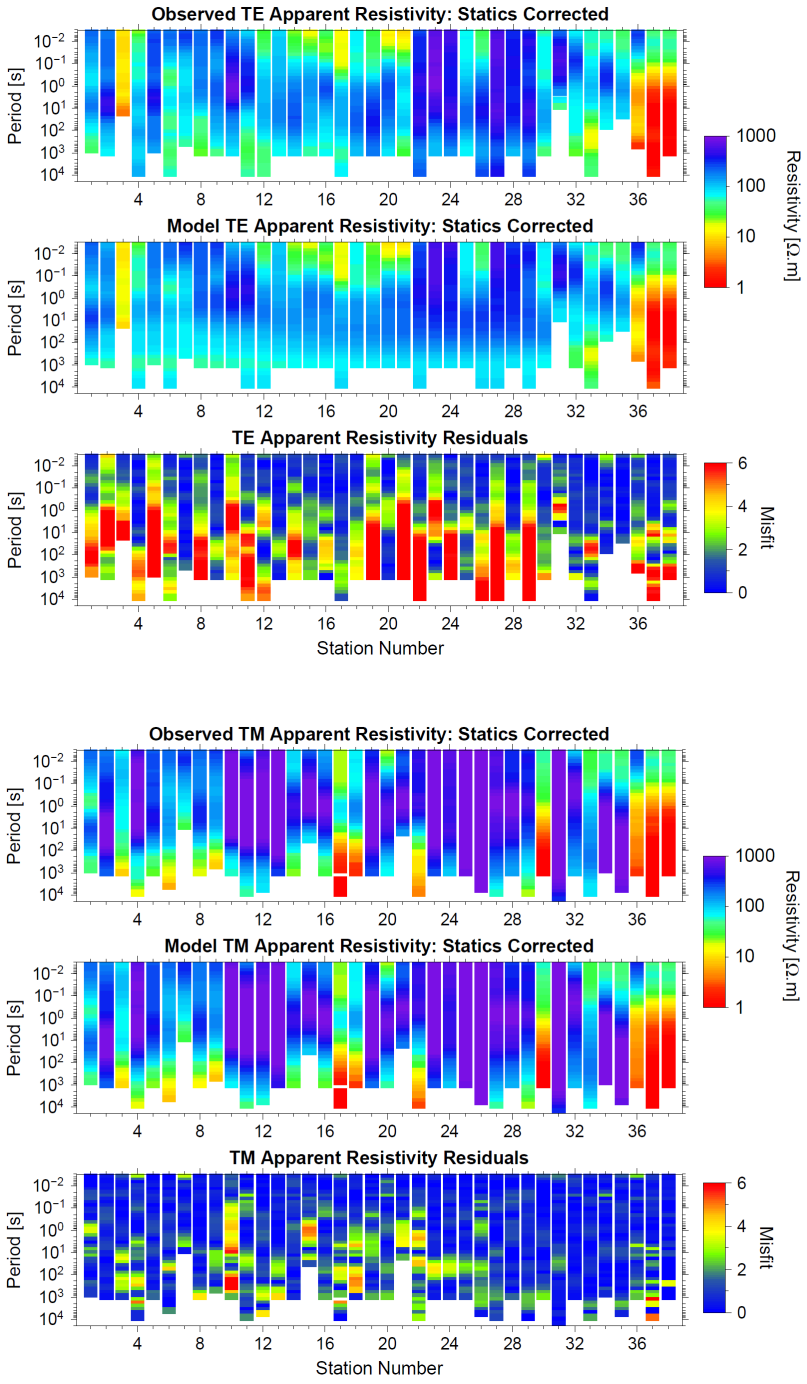

Figure B.4: Residuals for the TE and TM apparent resistivities associated with the **global** anisotropic inversion of the 6000-line data. Station numbers increase to the north.

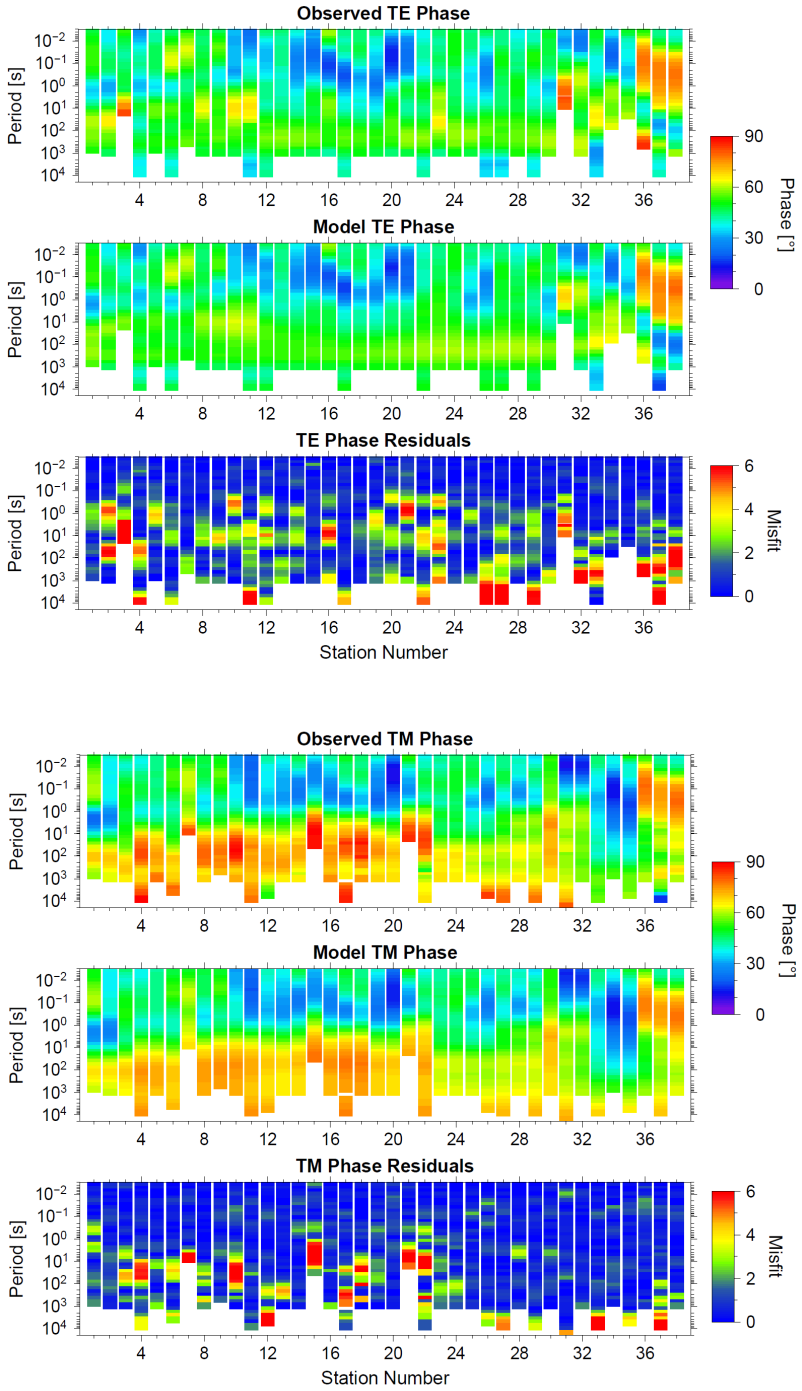

Figure B.5: Residuals for the TE and TM phases associated with the **global** anisotropic inversion of the 6000-line data. Station numbers increase to the north.

BIBLIOGRAPHY

Agius, M. R., and S. Lebedev, Shear velocity profiles in the crust and lithospheric mantle across tibet, *American Geophysical Union, Fall Meeting 2010*, 2010.

Aitchison, J. C., J. R. Ali, and A. M. Davis, When and where did India and Asia collide?, *Journal of Geophysical Research*, *112*, B05,423, 2007.

Alfvén, H., Theory of magnetic storms and of the aurorae, *K. Sven. Vetenskapakad. Handl., Ser. 3*, *18*(3), 1939.

Allègre, C. J., Structure and evolution of the Himalayan-Tibet orogenic belt, *Nature*, *307*, 17–22, 1984.

Andersen, D., and T. Fuller-Rowell, The ionosphere, *in Space Environment Topics, National Oceanic and Atmospheric Administration (NOAA)*, 1999.

Archie, G., The Electrical Resistivity Log as an Aid in Determining Some Reservoir Characteristics, *Trans. Am. Inst. Mineral. Met.*, *146*, 54–62, 1942.

Argand, E., La tectonique de l'asie, *Proceedings of the 13th International Geological Congress*, *7*, 171–372, 1924.

Armijo, R., P. Tapponnier, J. L. Mercier, and H. Tong-Lin, Quaternary extension in southern Tibet: Field observations and tectonic implications, *J. Geophys. Res.*, *91*, 13,803–13,872, 1986.

Armijo, R., P. Tapponnier, and H. Tonglin, Late cenozoic right-lateral strike-slip faulting in southern tibet, *J. Geophys. Res.*, *94*, 2787–2838, 1989.

Arnaud, N. O., P. Vidal, P. Tapponnier, P. Matte, and W. M. Deng, The high K2O volcanism of northwestern Tibet: Geochemistry and tectonic implications, *Earth Planet. Sci. Lett.*, *111*, 351–367, 1992.

Avdeev, D. B., A. V. Kuvshinov, O. V. Pankratov, and G. A. Newman, Three-dimensional induction logging problems, part I-An integral equation solution and model comparisons, *Geophysics*, *67*, 413–426, 2002.

Avouac, J. P., and P. Tapponnier, Kinematic model of active deformation in central Asia, *Geophys. Res. Lett.*, *20*, 895–898, 1993.

Baba, K., A. D. Chave, R. L. Evans, G. Hirth, and R. L. Mackie, Mantle dynamics beneath the East Pacific Rise at 17°s: Insights from the Mantle Electromagnetic and Tomography (MELT) experiment, *J. Geophys. Res.*, *111*, B02,101, 2006.

Bahr, K., Interpretation of the magnetotelluric impedance tensor: regional induction and local telluric distortion, *Journal of Geophysics*, *62*, 119–127, 1988.

Bai, D., et al., Crustal deformation of the eastern Tibetan plateau revealed by magnetotelluric imaging, *Nature Geoscience*, *3*, 2010.

Bailey, R. C., Inversion of the geomagnetic induction problem, *Proceedings of the Royal Society of London*, *315*, 185–194, 1970.

Bally, A. W., I.-M. Chou, R. Clayton, H. P. Eugster, S. Kidwell, L. D. Meckel, R. T. Ryder, A. B. Watts, and A. A. Wilson, Notes on sedimentary basins in China report of the American Sedimentary Basins delegation to the People's Republic of China, *USGS Open File Report 86-327*, *108*, 1986.

Bartels, J., N. H. Heck, and H. F. Johnston, The three-hour range index measuring geomagnetic activity, *Geophys. Res.*, *44*, 411–454, 1939.

Baxter, A. T., J. C. Aitchison, and S. V. Zyabrev, Radiolarian age constraints on Mesotethyan ocean evolution, and their implications for development of the Bangong-Nujiang suture, *J. Geol. Soc.*, *166*, 689–694, 2009.

Beaumont, C., R. A. Jamieson, M. H. Nguyen, and B. Lee, Himalayan tectonics explained by extrusion of a low-viscosity channel coupled to focused surface denudation, *Nature*, *414*, 738–742, 2001.

Beaumont, C., R. A. Jamieson, M. H. Nguyen, and S. Medvedev, Crustal channel flows: 1. Numerical models with applications to the tectonics of the Himalayan-Tibetan orogen, *Journal of Geophysical Research*, *109*(B06406), 2004.

Bedrosian, P. A., M. J. Unsworth, and F. Wang, Structure of the Altyn Tagh Fault and Daxue Shan from magnetotelluric surveys: Implications for faulting associated with the rise of the Tibetan Plateau, *Tectonics*, *20*, 474–486, 2001.

Bedrosian, P. A., N. Maercklin, U. Weckmann, Y. Bartov, T. Ryberg, and O. Ritter, Lithology-derived structure classification from the joint interpretation of magnetotelluric and seismic models, *Geophys. J. Int.*, *170*, 737–748, 2007.

Berdichevsky, M. N., Marginal notes on magnetotellurics, *Surveys in Geophysics*, *20*, 341–375, 1999.

Berdichevsky, M. N., and V. I. Dimitriev, Distortion of magnetic and electric fields by near-surface lateral inhomogeneities, *Acta. Geodaet., Geophys. et Montanist Acad. Sci. Hung.*, *11*, 447–483, 1976a.

Berdichevsky, M. N., and V. I. Dimitriev, *Geoelectric and Geothermal Studies*, chap. Principles of Interpretation of Magnetotelluric Sounding Curves, pp. 165–221, A. Adam ed., KAPG Geophysical Monograph, Akademiai Kiado, 1976b.

Berdichevsky, M. N., and M. S. Zhdanov, Advanced Theory of Deep Geomagnetic Sounding, *Elsevier Sci. Pub., Amsterdam*, p. 408, 1984.

Berdichevsky, M. N., I. A. Bezruk, and O. M. Chinavera, Magnetotelluric sounding with the use of mathematical filters, *Izv. Akad. Nauk. SSSR Fiz. Zeml.*, *3*, 72–92, 1973.

Berdichevsky, M. N., L. L. Vanyan, and V. I. Dmitriev, Methods used in the USSR to reduce near-surface inhomogeneity effects on deep magnetotelluric soundings, *Physics of the Earth and Planetary Interiors*, *53*, 194–206, 1989.

Berryman, J. G., Measures of microstructure to improve estimates and bounds on elastic constants and transport coefficients in heterogeneous media, *Mechanics and materials*, *732*, 732–747, 2006.

Besse, J., and V. Courtillot, Revised and synthetic apparent polar wander paths of the African, Eurasian, North American and Indian Plates, and true polar wander since 200 ma, *J. Geophys. Res.*, *96*, 4029–4050, 1991.

Bird, P., Continental delamination and the Colorado Plateau, *J. Geophys. Res.*, *84*, 7561–7571, 1979.

Bird, P., Lateral extrusion of lower crust from under high topography, in the isostatic limit, *Journal of Geophysical Research*, *96*, 10,275–10,286, 1991.

Bird, P., and J. Baumgardner, Steady propagation of delamination events, *J. Geophys. Res.*, *86*, 4891–4903, 1981.

Bird, P., and K. Piper, Plane-stress finite-element models of tectonic flow in southern California, *Phys. Earth Planet Inter.*, *21*, 158–175, 1980.

Bourjot, L., and B. Romanowicz, Crust and upper mantle tomography in Tibet using surface waves, *Geophys. Res. Lett.*, *19*, 881–884, 1992.

Brasse, H., and D. Eydam, Electrical conductivity beneath the Bolivian Orocline and its relation to subduction processes at the South American continental margin, *J. Geophys. Res.*, *113*(B07109), 2008.

Brasse, H., P. Lezaeta, V. Rath, K. Schwalenberg, W. Soyer, and V. Haak, The bolivian altiplano conductivity anomaly, *J. Geophys. Res.*, *107(B5)*(2096), 2002.

Brookfield, M. E., The Himalayan passive margin from Precambrian to Cretaceous times, *Sediment. Geol.*, *84*, 1–35, 1993.

Brown, L. D., et al., Bright spots, structure, and magmatism in Southern Tibet from INDEPTH seismic reflection profiling, *Science*, *274*, 1688–1691, 1996.

Burchfiel, B. C., Z. Chen, L. H. Royden, Y. Liu, and C. Deng, Extensional development of Gabo Valley, southern Tibet, *Tectonophysics*, *194*, 187–193, 1991.

Burchfiel, B. C., Z. Chen, Y. Liu, and L. H. Royden, Tectonics of the Longmen Shan and adjacent regions, central China, *Int. Geol. Rev.*, *37*, 661–735, 1995.

Burg, J. P., Introduction to Tectonics, *ETH ZÃŒrich and Universität Zürich*, 2011.

Cagniard, L., Basic theory of the magnetotelluric method of geophysical prospecting, *Geophysics*, *18*, 605–645, 1953.

Caldwell, T. G., H. M. Bibby, and C. Brown, The magnetotelluric phase tensor, *Geophys. J. Int.*, *158*, 457–469, 2004.

Carrasquilla, A., and L. Rijo, Analysis of electrojet-distorted magnetotelluric sounding curves, *Journal of Applied Geophysics*, *40*, 187–204, 1998.

Cawood, P. A., M. R. W. Johnson, and A. A. Nemchin, Early Paleozoic orogenesis along the indian margin of Gondwana: Tectonic response to Gondwana assembly, *Earth Planet. Sci. Lett.*, *255*, 70–84, 2007.

Célérier, J., T. M. Harrison, O. Beyssac, F. Herman, W. J. Dunlap, and A. A. G. Webb, The Kumaun and Garwhal Lesser Himalaya, India: Part 2. Thermal and deformation histories, *GSA Bulletin*, *121*, 1281–1297, 2009.

Cemic, L., G. Will, and E. Hinze, Electrical conductivity measurements on olivines Mg2SiO4-Fe2SiO4 under defined thermodynamic conditions, *Phys. Chem. Min.*, *6*, 95–107, 1980.

Chan, G. H. N., D. J. Waters, M. P. Searle, J. C. Aitchison, M. S. A. Horstwood, Q. Crowley, C. H. Lo, and J. S. L. Chan, Probing the basement of southern Tibet: evidence from crustal xenoliths entrained in a Miocene ultrapotassic dyke, *Journal of the Geological Society*, *166*, 45–52, 2009.

Chave, A. D., *The Magnetotelluric Method: Theory and Practice*, chap. Estimation of the magnetotelluric response function, pp. 165–218, A. D. Chave and A. G. Jones ed., Cambridge University Press, 2012.

Chave, A. D., and A. G. Jones, Electric and magnetic field distortion decomposition of BC87 data, *Journal of Geomagnetism and Geoeletricity*, *49*, 767–789, 1997.

Chave, A. D., and J. T. Smith, On electric and magnetic galvanic distortion tensor decompositions, *Journal of Geophysical research*, *99*, 4669–4682, 1994.

Chave, A. D., and D. J. Thomson, Bounded influence magnetotelluric response function estimation, *Geophysical Journal International*, *157*, 988–1006, 2004.

Chave, A. D., D. J. Thomson, and M. E. Ander, On the robust estimation of power spectra, coherencies, and transfer functions, *J. Geophys. Res.*, *92*, 633–648, 1987.

Cheadle, M. J., M. T. Elliott, and D. McKenzie, Percolation threshold and permeability of crystallizing igneous rocks: The importance of textural equilibrium, *Geology*, *32*(9), 757–760, 2004.

Chen, L., J. R. Booker, A. G. Jones, N. Wu, M. J. Unsworth, W. Wenbo, and H. Tan, Electrically conductive crust in southern Tibet from INDEPTH magnetotelluric surveying, *Science*, *274*, 1694–1696, 1996.

Cheng, Y. Q., Outline of Chinese Regional Geology, *Beijing: Geologic Publishing House (in Chinese)*, p. 517, 1994.

Chung, S. L., et al., Tibetan tectonic evolution inferred from spatial and temporal variations in post-collisional magmatism, *Earth-Science Rev.*, *68*, 173–196, 2005.

Clark, M. K., and L. H. Royden, Topographic ooze: Building the eastern margin of Tibet by lower crustal flow, *Geology*, *28*, 703–706, 2000.

Clark, M. K., J. W. M. Bush, and L. H. Royden, Dynamic topography produced by lower crustal flow against rheological strength heterogeneities bordering the Tibetan Plateau, *Geophysical Journal International*, *162*, 575–590, 2005.

Cole, K. S., and R. H. Cole, Alternating current characteristics, *J. Chem. Phys.*, *9*, 341–351, 1941.

Coleman, M., and K. V. Hodges, Evidence for Tibetan Plateau uplift before 14 myr ago from a new minimum age for east-west extension, *Nature*, *374*, 49–52, 1995.

Constable, S., SEO3: A new model of olivine electrical conductivity, *Geophys. J. Int.*, *166(1)*, 435–437, 1992.

Constable, S., T. J. Shankland, and A. Duba, The electrical conductivity of an isotropic olivine mantle, *J. Geophys. Res.*, *97(B3)*, 3397–3404, 1992.

Constable, S. C., R. L. Parker, and C. G. Constable, Occam's inversion to generate smooth two-dimensional models from magnetotelluric data, *Geophysics*, *52(03)*, 289–300, 1987.

Coulon, C., H. Maluski, C. Bollinger, and S. Wang, Mesozoic and cenozoic volcanic rocks from central and southern tibet: 39Ar/40Ar dating, petrological characteristics and geodynamical significance, *Earth Planet. Sci. Lett.*, *79*, 281–302, 1986.

Coward, M. P., and R. W. H. Butler, Thrust tectonics and the deep structure of the Pakistan Himalaya, *Geology*, *13*, 417–420, 1985.

Coward, M. P., W. S. F. Kidd, Y. Pan, R. M. Shackleton, and H. Zhang, The structure of the 1985 Tibet Geotraverse, Lhasa to Golmud, *Royal Society of London Philosophical Transactions*, *327*, 307–336, 1988a.

Coward, M. P., et al., Folding and imbrication of the Indian crust during Himalayan collision, *Phil. Trans. R. Soc. Lond.*, *326*, 89–116, 1988b.

Cowgill, E., A. Yin, T. M. Harrison, and W. Xiao-Feng, Reconstruction of the Altyn Tagh fault based on U-Pb geochronology: Role of back thrusts, mantle sutures, and heterogeneous crustal strength in forming the Tibetan Plateau, *J. Geophys. Res.*, *108(B7)*, 2346, 2003.

CSBS, (chinese state bureau of seismology). the altyn tagh active fault system, *Beijing: Seismology Publishing House*, p. 319, 1992.

Dachnov, W., Geofiziceskie metody opredelenija kollektorskich svoistv is neftegasonasyscenija gornich porod, *Izdat. Nedra, Moscow*, 1975.

Darby, B. J., and G. E. Gehrels, Detrital zircon reference for the North China block, *J. Asian Earth Sci.*, *26*, 637–648, 2006.

Davy, P., and P. Cobbold, Indentation tectonics in nature and experiment, 1. experiments scaled for gravity, *Bull. Geol. Inst., Univ. Uppsala*, *14*, 129–141, 1988.

Debye, P., Polare molekeln, *Verlag S. Hirzel, Leipzig*, 1927.

DeCelles, P. G., D. M. Robinson, J. Quade, T. P. Ojha, C. N. Garzione, P. Copeland, and B. N. Upreti, Stratigraphy, structure, and tectonic evolution of the Himalayan fold - thrust belt in western Nepal, *Tectonics*, *20*, 487–509, 2001.

DeCelles, P. G., D. M. Robinson, and G. Zandt, Implications of shortening in the Himalayan fold-thrust belt for uplift of the Tibetan plateau, *Tectonics*, *21*(6), 1062, 2002.

DeCelles, P. G., P. Kapp, L. Ding, and G. E. Gehrels, Late cretaceous to middle tertiary basin evolution in the central tibetan plateau: Changing environments in response to tectonic partitioning, aridification, and regional elevation gain, *Geol. Soc. Am. Bull.*, *119*, 654–680, 2007.

deGroot-Hedlin, C., Short note: Removal of static shift in two dimensions by regularized inversion, *Geophysics*, *56(12)*, 2102–2106, 1991.

deGroot-Hedlin, C., and S. Constable, Occam's inversion to generate smooth two-dimensional models from magnetotelluric data, *Geophysics*, *55(12)*, 1613–1624, 1990.

Deng, W., Cenozoic volcanism and intraplate subduction at the northern margin of the Tibetan Plateau, *Chinese Journal of Geochemistry*, *10*, 140–152, 1991.

Dewey, J. F., Extensional collapse of orogens, *Tectonics*, *7*, 1123–1140, 1988.

Dewey, J. F., R. M. Shackelton, C. Chengfa, and S. Yiyin, The tectonic evolution of the Tibetan Plateau, *Philos. Trans. R. Soc. London, Ser. A*, *327*, 379–413, 1988.

Dewey, J. F., S. Cande, and W. C. Pitman, Tectonic evolution of the India-Eurasia collision zone, *Ecol. Geol. Helv.*, *82*, 717–734, 1989.

Dezes, P., Tectonic and metamorphic Evolution of the Central Himalayan Domain in Southeast Zanskar (Kashmir, India), *Memoires de Geologie. Doctoral thesis (Universite de Lausanne)*, *32*, 149, 1999.

Ding, L., P. Kapp, D. Zhong, and W. Deng, Cenozoic Volcanism in Tibet: Evidence for a Transition from Oceanic to Continental Subduction, *Journal of Petrology*, *44*(10), 1833–1865, 2003.

Ding, L., P. Kapp, Y. Yue, and Q. Lai, Postcollisional calc-alkaline lavas and xenoliths from the southern Qiangtang terrane, central Tibet, *Earth and Planetary Science Letters*, *254*, 28–38, 2007.

Dmitriev, V. I., and M. N. Berdichevsky, The fundamental model of magnetotelluric sounding, *Proc. IEEE*, *67*, 1034–1044, 1979.

Du Frane, W. L., J. J. Roberts, D. A. Toffelmier, and J. A. Tyburczy, Anisotropy of electrical conductivity in dry olivine, *Geophys. Res. Lett.*, *32*(L24315), 2005.

Ducea, M. N., and S. K. Park, Enhanced mantle conductivity from sulfide minerals, southern sierra nevada, california, *Geophys. Res. Lett.*, *27*, 2405–2408, 2000.

Dürr, S. B., Provenance of Xigaze forearc basin clastic rocks (Cretaceous, south Tibet), *Geol. Soc. Am. Bull.*, *108*(6), 669–684, 1996.

Duvall, A. R., and M. K. Clark, Dissipation of fast strike-slip faulting within and beyond northeastern Tibet, *Geology*, *38*, 223–226, 2010.

Eddy, J. A., The maunder minimum, *Science*, *192*(4245), 1189–1202, 1976.

Egbert, G. D., Robust multiple-station magnetotelluric data processing, *Geophys. J. Int.*, *130*, 475–496, 1997.

Egbert, G. D., and J. R. Booker, Robust estimation of geomagnetic transfer functions, *Geophys. J. R. Astro. Soc.*, *87*, 173–194, 1986.

Ellis, S., C. Beaumont, R. A. Jamieson, and G. Quinlan, Continental collision including a weak zone: The vise model and its application to the Newfoundland Appalachians, *Canadian Journal of Earth Sciences*, *5*, 1323–1346, 1998.

England, P., and D. P. McKenzie, A thin viscous sheet model for continental deformation, *Geophys. J. R. Astron. Soc.*, *70*, 295–321, 1982.

England, P., and P. Molnar, Active deformation of asia: From kinematics to dynamics, *Science*, *278*, 647–650, 1997.

England, P., and P. Molnar, Late Quaternary to decadal velocity fields in Asia, *J. Geophys. Res.*, *110*(B12401), 2005.

England, P. C., and G. A. Houseman, The mechanics of the Tibetan plateau, *Phil. Trans. Roy. Soc. Lond.*, *326*, 301–319, 1988.

England, P. C., and G. A. Houseman, Extension during continental convergence, with application to the Tibetan Plateau, *J. Geophys. Res.*, *94*, 17,561–17,579, 1989.

Evans, R., *The Magnetotelluric Method: Theory and Practice*, chap. Earth's electromagnetic environment: 3A. Conductivity of Earth materials, pp. 50–95, A. D. Chave and A. G. Jones ed., Cambridge University Press, 2012.

Evans, R. L., G. Hirth, K. Baba, D. Forsyth, A. Chave, and R. Mackie, Geophysical evidence from the melt area for compositional controls on oceanic plates, *Nature*, *437*, 249–252, 2005.

Fan, G.-W., and T. Lay, Strong Lg wave attenuation in the Northern and Eastern Tibetan Plateau measured by a two-station/two-event stacking method, *Geophys. Res. Lett.*, *30(10)*, 1530, 2003.

Ferguson, I. J., *The Magnetotelluric Method: Theory and Practice*, chap. Instrumenttation and field procedures, pp. 412–479, A. D. Chave and A. G. Jones ed., Cambridge University Press, 2012.

Flesch, L. M., A. J. Haines, and W. E. Holt, Dynamics of the india-Eurasia collision zone, *J. Geophys. Res.*, *106*, 16,435–16,460, 2001.

Frost, B. R., W. S. Fyfe, K. Tazaki, and T. Chan, Grain-boundary graphite in rocks and implications for high electrical conductivity in the lower crust, *Nature*, *340*, 134–136, 1989.

Fu, B., and Y. Awata, Displacement and timing of left-lateral faulting in the Kunlun Fault Zone, northern Tibet, inferred from geologic and geomorphic features, *J. Asian Earth Sci.*, *29*, 253–265, 2007.

Fullea, J., M. R. Muller, and A. G. Jones, Electrical conductivity of continental lithospheric mantle from integrated geophysical and petrological modeling: Application to the Kaapvaal Craton and Rehoboth Terrane, southern Africa, *J. Geophys. Res.*, *116*(B10202), 2011.

Fuller, B. D., and S. H. Ward, Linear System Description of Electrical Parameters of Rocks, *IEEE Trans. GE-8*, *1*, 7–13, 1970.

Fyhn, M. B. W., L. O. Boldreel, and L. H. Nielsen, Geological development of the Central and South Vietnamese margin: Implications for the establishment of the South China Sea, Indochinese escape tectonics and Cenozoic volcanism, *Tectonophysics*, *478*, 184–214, 2009.

Gaetani, M., and E. Garzanti, Multicyclic history of the northern India continental margin (northwestern Himalaya), *Am. Assoc. Pet. Geol. Bull.*, *75*, 1427–1446, 1991.

Gaillard, F., Laboratory measurements of electrical conductivity of hydrous and dry silicic melts under pressure, *Earth Planet. Sci. Lett.*, *218(1-2)*, 215–228, 2004.

Gaillard, F., B. Scaillet, and M. Pichavant, Evidence of present-day leucogranite pluton growth in Tibet, *Geology*, *32*, 801–804, 2004.

Gaillard, F., M. Marki, G. Iacono-Marziano, M. Pichavant, and B. Scaillet, Carbonatite melts and electrical conductivity in the asthenosphere, *Science*, *32*, 1363–1365, 2008.

Galvé, A., M. Jiang, A. Hirn, M. Sapin, M. Laigle, B. de Voogd, J. Gallart, and H. Qian, Explosion seismic p and s velocity and attenuation constraints on the lower crust of the North-Central Tibetan Plateau, and comparison with the Tethyan Himalayas: implications on composition, mineralogy, temperature, and tectonic evolution, *Tectonophysics*, *412*, 141–157, 2006.

Galy, V., O. Beyssac, C. France-Lanord, and T. Eglinton, Recycling of Graphite During Himalayan Erosion: A Geological Stabilization of Carbon in the Crust, *Science*, *322*, 943, 2008.

Gamble, T. D., W. M. Goubau, and J. Clarke, Magnetotellurics with a remote magnetic reference, *Geophyiscs*, *44(1)*, 53–68, 1979.

Gan, W., P. Zhang, Z. K. Shen, Z. Niu, M. Wang, Y. Wan, D. Zhou, and J. Cheng, Present-day crustal motion within the Tibetan Plateau inferred from GPS measurements, *Journal of Geophysical Research*, *112*(B08416), 2007.

Garcia, X., and A. G. Jones, *Three-Dimensional Electromagnetics. Methods in Geochemistry and Geophysics*, vol. 35, chap. Decomposition of three-dimensional magnetotelluric data, pp. 235–250, M. S. Zhdanov and P. E. Wannamaker ed., Elsevier, 2001.

Garcia, X., and A. G. Jones, Atmospheric sources for audio-magnetotelluric (amt) sounding, *Geophysics*, *67*(2), 448–458, 2002.

Gehrels, G. E., and A. Yin, Magmatic history of the northeastern Tibetan Plateau, *J. Geophys. Res.*, *108(B9)*, 2423, 2003.

Gehrels, G. E., et al., Detrital zircon geochronology of pre-Tertiary strata in the Tibetan-Himalayan orogen, *Tectonics*, *30*, TC5016, 2011.

Girardeau, J., J. Marcous, C. J. Allegre, J. P. Bassoullet, and Y. Tang, Tectonic environment and geodynamic significance of the Neo-Cimmerian Donqiao ophiolite, Bangong-Nujiang suture zone, Tibet, *Nature*, *307*, 27–31, 1984.

Glover, P. W. J., Graphite and Electrical Conductivity in the Lower Continental Crust: A Review, *Phys. Chem. Earth.*, *21*(4), 279–287, 1996.

Glover, P. W. J., A generalized Archie's law for n phases, *Geophysics*, *75*, E247–E265, 2010.

Glover, P. W. J., and F. J. Vine, Electrical conductivity of carbon-bearing granulite at raised temperatures and pressures, *Nature*, *360*, 24–31, 1992.

Godin, D., D. Grujic, R. D. Law, and M. P. Searle, *Channel Flow, Ductile Extrusion and Exhumation in Continental Collision Zones*, vol. 268, chap. Channel flow, ductile extrusion and exhumation in continental collision zones: an introduction, pp. 1–23, R. D. Law, M. P. Searle and L. Godin ed., Geological Society, London, Special Publications, 2006.

Gold, T., Motions in the Magnetosphere of the Earth, *J. Geophys. Res.*, *64*, 1219–1224, 1959.

Goodwin, A. M., Principles of Precambrian Geology, *Academic, San Diego, Calif.*, p. 327, 1996.

Goubau, W. M., T. D. Gamble, and J. Clarke, Magnetotelluric data analysis: removal of bias, *Geophysics*, *43*, 1157–1169, 1978.

Groom, R. W., and K. Bahr, Corrections for near surface effects: Decomposition of the magnetotelluric impedance tensor and scaling corrections for regional resistivities: A tutorial., *Surveys in Geophysics*, *13*, 341–379, 1992.

Groom, R. W., and R. C. Bailey, Decomposition of magnetotelluric impedance tensors in the presence of local three-dimensional galvanic distortion, *J. Geophys. Res.*, *94*, 1913–1925, 1989.

Groom, R. W., R. D. Kurtz, A. G. Jones, and D. E. Boerner, A quantitative methodology to extract regional magnetotelluric impedances and determine the dimension of the conductivity structure, *Geophysical Journal International*, *115*, 1095–1118, 1993.

Guo, Z., M. Wilson, and J. Liu, Post-collisional adakites in south Tibet: Products of partial melting of subduction-modified lower crust, *Lithos*, *96*, 205–224, 2007.

Guynn, J., P. Kapp, A. Pullen, M. Heizler, G. Gehrels, and L. Ding, Tibetan basement rocks near amdo reveal "missing" Mesozoic tectonism along the Bangong suture, central Tibet, *Geology*, *34*, 505–508, 2006.

Hacker, B., et al., Near-ultrahigh pressure processing of continental crust: Miocene crustal xenoliths from the Pamir, *Journal of Petrology*, *46*, 1661–1687, 2005.

Hacker, B. R., E. Gnos, L. Ratschbacher, M. Grove, M. McWilliams, S. V. Sobolev, J. Wan, and W. Zhenhan, Hot and dry deep crustal xenoliths from Tibet, *Science*, *287*, 2463–2466, 2000.

Haines, S. S., S. L. Klemperer, L. Brown, G. Jingru, J. Mechie, R. Meissner, A. Ross, and Z. Wenjin, INDEPTH III seismic data: From surface observations to deep crustal processes in Tibet, *Tectonics*, *22*(1001), 2003.

Hale, G. E., On the probable existence of a magnetic field in sunspots, *The Astrophysical Journal*, *28*(315), 1908.

Hall, R., M. W. A. van Hattum, and W. Spakman, Impact of India - Asia collision on SE Asia: The record in Borneo, *Tectonophysics*, *451*(366-389), 2008.

Hampel, R. F., M. E. Ronchetti, P. J. Rousseeuw, and W. A. Stahel, Robust Statistics. The Approach Based on Influence Functions, *Wiley, New York*, 1986.

Harris, N., Channel flow and the Himalayan-Tibetan orogen: a critical review, *Journal of the Geological Society*, *164(3)*, 511–523, 2007.

Harris, N. B. W., X. Ronghua, C. L. Lewis, C. J. Haweksworth, and Z. Yuquan, Isotope geochemistry of the 1985 Tibet Geotraverse, Lhasa to Golmud, *Royal Society of London Philosophical Transactions*, *327*, 263–285, 1988.

Harrison, T. M., P. H. Leloup, F. J. Ryerson, P. Tapponnier, R[]Lacassin, and W. Chen, *The Tectonic Evolution of Asia*, chap. Diachronousinitiation of transtension along the Ailao Shan-Red River shear zone, Yunnan and Vietnam, pp. 208–226, A. Yin and T. M. Harrison ed., New York: Cambridge University Pres, 1996.

Hashin, Z., and A. Shtrikman, A Variational Approach to the Theory of Effective Magnetic Permeability of Multiphase Materials, *J. Appl. Phys.*, *33*, 3125–3131, 1962.

Hauck, M. L., K. D. Nelson, L. D. Brown, W. Zhao, and A. R. Ross, Crustal structure of the Himalayan orogen at $\sim 90^{o}$ east longitude from Project INDEPTH deep reflection profiles, *Tectonics*, *17*, 481–500, 1998.

He, J., and J. Chery, Slip rates of the altyn tagh, kunlun and karakorum faults (tibet) from 3d mechanical modeling, *Earth and Planetary Science Letters*, *274*, 50–58, 2008.

He, S., P. Kapp, P. G. DeCelles, G. E. Gehrels, and M. T. Heizler, Cretaceous-Tertiary geology of the Gangdese Arc in the Linzhou area, southern Tibet, *Tectonophysics*, *433*, 15–37, 2007.

Heise, W., and J. Pous, Anomalous phases exceeding 90^{o} in magnetotellurics: anisotropic model studies and a field example, *Geophys. J. Int.*, *155*, 308–318, 2003.

Heise, W., T. G. Caldwell, H. M. Bibby, and C. Brownb, Anisotropy and phase splits in magnetotellurics, *Physics of the Earth and Planetary Interiors*, *158*, 107–121, 2006.

Hermance, J. F., Electromagnetic induction in the earth by a moving ionospheric current system, *Geophys. J. R. astr. Soc.*, *55*, 557–576, 1978.

Hermance, J. F., The electrical conductivity of materials containing partial melt: a simple model of Archie's law, *Geophys. Res. Lett.*, *6*, 613–616, 1979.

Hermance, J. F., and W. R. Peltier, Magnetotelluric fields of a line current, *J. Geophys. Res.*, *75*, 3351–3356, 1970.

Herquell, G., G. Wittlinger, and J. Guilbert, Anisotropy and crustal thickness of Northern-Tibet. New constraints for tectonic modeling, *Geophys. Res. Lett.*, *22*, 1925–1928, 1995.

Hetényi, G., R. Cattin, F. Brunet, L. Bollinger, J. Vergne, J. L. Nabelek, and M. Diament, Density distribution of the India plate beneath the Tibetan Plateau: Geophysical and petrological constraints on the kinetics of lower crustal eclogitization, *Earth and Planetary Science Letters*, *264*, 226–244, 2007.

Hibbs, R. D., and F. W. Jones, The calculation of the electromagnetic fields of a sheet current with arbitrary intensity distribution over a layered half space-I: The general method and results, *Geophys. J. R. astr. Soc.*, *46*, 433–452, 1976a.

Hibbs, R. D., and F. W. Jones, The calculation of the electromagnetic fields of a sheet current with arbitrary intensity distribution over a layered half space-II: The computer program and its application, *Geophys. J. R. astr. Soc.*, *46*, 453–465, 1976b.

Hill, G. J., T. G. Caldwell, W. Heise, D. G. Chertkoff, H. M. Bibby, M. K. Burgess, J. P. Cull, and R. A. F. Cas, Distribution of melt beneath Mount St Helens and Mount Adams inferred from magnetotelluric data, *Nature Geosci.*, *2*, 785–789, 2009.

Hirn, A., et al., Seismic anisotropy as an indicator of mantle flow beneath the himalayas and tibet, *Nature*, *375*, 571–574, 1995.

Hirsch, L. M., T. J. Shankland, and A. G. Duba, Electrical conduction and polaron mobility in fe-bearing olivine, *Geophys. J. Int.*, *114(1)*, 36–44, 1993.

Hodges, K. V., Tectonics of the Himalaya and southern Tibet from two perspectives, *Geol. Soc. Am. Bull.*, *112*, 324–350, 2000.

Hopkins, M., T. M. Harrison, and C. E. Manning, Low heat flow inferred from >4 Gyr zircons suggests Hadean plate boundary interactions, *Nature*, *456*, 493–496, 2008.

Houseman, G., and P. England, *The Tectonic Evolution of Asia*, chap. A lithospheric thickening model for the Indo-Asian collision, pp. 3–17, A. Yin and T. M. Harrison ed., New York: Cambridge University Pres, 1996.

Hoyt, D. V., and K. H. Schatten, Group sunspot numbers: A new solar activity reconstruction. part 1., *Solar Physics*, *179*, 189–219, 1998a.

Hoyt, D. V., and K. H. Schatten, Group sunspot numbers: A new solar activity reconstruction. part 2., *Solar Physics*, *181*, 491–512, 1998b.

Hsu, K. J., P. Guitang, and A. M. C. Sengor, Tectonic evolution of the Tibetan Plateau: a working hypothesis based on the archipelago model of orogenesis, *Int. Geol. Rev.*, *37*, 473–508, 1995.

Huang, C. K., et al., Geological Map of the People's Republic of China, *SinoMaps Press, Xian.*, 2004.

Huang, H., Q. Huang, and Y. Ma, Geology of Qaidam Basin and its Petroleum Prediction, *Beijing: Geological Publishing House*, p. 257, 1996.

Huang, W. C., et al., Seismic polarization anisotropy beneath the central Tibetan Plateau, *J. Geophys. Res.*, *105*, 27,979–27,989, 2000.

Huber, P. J., Robust statistics, *Wiley, New York*, 1981.

Huebner, J. S., and R. G. Dillenburg, Impedance spectra of hot, dry silicate minerals and rock: Qualitative interpretation of spectra, *Am. Mineral.*, *80(1-2)*, 46–64, 1995.

Hughes, N. C., and P. A. Jell, *In Himalaya and Tibet: Mountain Roots to Mountain Tops*, vol. 328, chap. Biostratigraphy and biogeography of Himalayan Cambrian trilobite, pp. 109–116, A. Macfarlane and R.B. Sorkhabi ed., Geol. Soc. Am. Spec. Pap., 1999.

Hyndman, R. D., L. L. Vanyan, G. Marquis, and L. K. Lawa, The origin of electrically conductive lower continental crust: saline water or graphite?, *Physics of the Earth and Planetary Interiors*, *81(1-4)*, 325–345, 1993.

Jiang, C., J. Yang, B. Feng, Z. Zhu, and M. Zhao, Opening-closing tectonics of kunlun mountains, *Beijing: Geologic Publishing House (in Chinese with English abstract)*, p. 224, 1992.

Jiang, M., A. Galvé, A. Hirn, B. de Voogd, M. Laigle, H. P. Su, J. Diaz, J. C. Lépine, and Y. X. Wang, Crustal thickening and variations in architecture from the Qaidam basin to the Qang Tang (North - Central Tibetan Plateau) from wide-angle reflection seismology, *Tectonophysics*, *412*, 121–140, 2006.

Jimenez-Munt, I., M. Fernandez, J. Verges, and J. P. Platt, Lithosphere structure underneath the Tibetan Plateau inferred from elevation, gravity and geoid anomalies, *Earth and Planetary Science Letters*, *267*, 276–289, 2008.

Jiracek, G. R., Near-surface and topographic distortions in electromagnetic induction, *Surveys in Geophysics*, *11*, 163–203, 1990.

Johnson, D. L., and P. N. Sen, Dependence of the Conductivity of a Porous Medium on Electrolyte Conductivitys, *Phys. Rev. B*, *33*, 3502–3510, 1988.

Johnson, M. R. W., Shortening budgets and the role of continental subduction during the India-Asia collision, *Earth-Science Reviews*, *59*, 101–123, 2002.

Johnson, M. R. W., G. J. H. Oliver, R. R. Parrish, and S. P. Johnson, Synthrusting metamorphism, cooling, and erosion of the Himalayan Kathmandu complex, Nepal, *Tectonics*, *20*, 394–415, 2001.

Johnson, P. R., and B. Woldehaimanot, *Proterozoic East Gondwana: Supercontinent Assembly and Breakup*, vol. 206, chap. Development of the Arabian-Nubian Shield: Perspectives on accretion and deformation in the northern East African Orogen and the assembly of Gondwana, pp. 289–325, Geol. Soc. Spec. Publ., 2003.

Jolivet, M., et al., Neogene extension and volcanism in the Kunlun Fault zone, northern Tibet: New constraints on the age of the Kunlun Fault, *Tectonics*, *22*, TC1052, 2003.

Jones, A. G., The problem of current channelling: a critical review, *Geophysical Surveys*, *6*, 79–122, 1983a.

Jones, A. G., On the Equivalence of the "Niblett" and "Bostick" Transformations in the Magnetotelluric Method, Journal of Geophysics, *Journal of Geophysics*, *53*, 72–73, 1983b.

Jones, A. G., Parkinson's pointers' potential perfidy!, *Geophysical Journal of the Royal Astronomical Society*, *87*, 1215–1224, 1986.

Jones, A. G., Static shift of magnetotelluric data and its removal in a sedimentary basin enviroment, *Geophysics*, *53(7)*, 967–978, 1988.

Jones, A. G., *The Continental Lower Crust*, chap. Electrical conductivity of the continental lower crust, pp. 81–143, D. M. Fountain, R. J. Arculus and R. W. Kay ed., Elsevier, New York, 1992.

Jones, A. G., Imaging the continental upper mantle using electromagnetic methods, *Lithos*, *48*, 57–80, 1999.

Jones, A. G., Electromagnetic interrogation of the anisotropic Earth: Looking into the Earth with polarized spectacles, *Physics of the Earth and Planetary Interiors*, *158*, 281–291, 2006.

Jones, A. G., *The Magnetotelluric Method: Theory and Practice*, chap. Distortion of magnetotelluric data: its identification and removal, pp. 219–302, A. D. Chave and A. G. Jones ed., Cambridge University Press, 2012.

Jones, A. G., and H. Jödicke, Magnetotelluric transfer function estimation improvement by a coherence-based rejection technique, *54th Ann. Mtg. Soc. of Expl. Geophys., Atlanta, Georgia*, 1984.

Jones, A. G., and J. E. Spratt, A simple method for deriving the uniform field mt responses in auroral zones, *Earth and Planetary Science Letters*, *54*, 443–450, 2001.

Jones, A. G., A. D. Chave, G. D. Egbert, D. Auld, and K. Bahr, A comparison of techniques for magnetotelluric response function estimates, *J. Geophys. Res.*, *94*, 14,201–14,213, 1989.

Jones, A. G., T. J. Katsube, and P. Schwann, The longest conductivity anomaly in the world explained: Sulphides in fold hinges causing very high electrical anisotropy, *J. Geomagn. Geoelectr.*, *49*, 1619–1629, 1997.

Jones, A. G., I. J. Ferguson, A. D. Chave, R. L. Evans, and G. W. McNeice, Electric lithosphere of the Slave craton, *Geology*, *29*(5), 423–426, 2001.

Jones, A. G., J. Fullea, R. L. Evans, and M. R. Muller, Water in cratonic lithosphere: Calibrating laboratory determined models of electrical conductivity of mantle minerals using geophysical and petrological observations, *Geochemistry, Geophysics, Geosystems*, *13*(Q06010), 2012.

Jones, F. W., and A. T. Price, The perturbations of alternating geomagnetic fields by conductivity anomalies, *Geophys. J. R. astr. Soc.*, *20*, 317–334, 1970.

Jordan, T. A., and A. B. Watts, Gravity anomalies, flexure and the elastic thickness structure of the India Eurasia collisional system, *Earth Planet. Sci. Lett.*, *236*, 732–750, 2005.

Kapp, P., Blueschist-bearing metamorphic core complexes in the Qiangtang block reveal deep crustal structure of northern Tibet: Reply, *Geology*, *29*, 664, 2001.

Kapp, P., A. Yin, C. E. Manning, M. Murphy, T. M. Harrison, M. Spurlin, L. Ding, X.-G. Deng, and C.-M. Wu, Blueschist-bearing metamorphic core complexes in the qiangtang block reveal deep crustal structure of northern tibet, *Geology*, *28(1)*, 19–22, 2000.

Kapp, P., A. Yin, C. E. Manning, T. M. Harrison, M. H. Taylor, and D. Lin, Tectonic evolution of the early mesozoic blueschist-bearing qiangtang metamorphic belt, central tibet, *Tectonics*, *22*(4), 1043, 2003.

Kapp, P., A. Yin, T. M. Harrison, and L. Ding, Cretaceous-tertiary shortening, basin development, and volcanism in central tibet, *Geological Society of America Bulletin*, *117*, 865–878, 2005.

Kapp, P., P. G. DeCelles, A. L. Leier, J. M. Fabijanic, S. He, A. Pullen, G. E. Gehrels, and L. Ding, The Gangdese retroarc thrust belt revealed, *GSA Today*, *17*, 4–9, 2007.

Karato, S., The role of hydrogen in the electrical conductivity of the upper mantle, *Nature*, *347*, 272–273, 1990.

Karplus, M. S., W. Zhao, S. L. Klemperer, Z. Wu, J. Mechie, D. Shi, L. D. Brown, and C. Chen, Injection of Tibetan crust beneath the south Qaidam Basin: Evidence from INDEPTH IV wide-angle seismic data, *J. Geophys. Res.*, *116*(B07301), 2011.

Kay, R. W., and S. M. Kay, Andean adakites: three ways to make them, *Acta Pet. Sin.*, *18*, 303–311, 2002.

Kearey, P., K. A. Klepeis, and F. J. Vine, *Global Tectonics, 3rd Edition*, Wiley-Blackwell, 2009.

Keller, G. V., Electrical properties, *Practical Handbook of Physical Properties of Rocks and Minerals, R. S. Carmichael, ed.: Boca Raton, FL, CRC Press*, pp. 359–428, 1989.

Keller, G. V., and F. C. Frischknecht, *International Series of Monographs in Electromagnetic Waves*, vol. 10, chap. Electrical methods in geophysical prospecting, A.L. Cullen, V.A. fock and J.R. Wait ed., Pergammon Press, Oxford, 1966.

Kezao, C., and J. M. Bowler, Late pleistocene evolution of salt lakes in the Qaidam basin, Qinghai province, China, *Palaeogeography, Palaeoclimatology, Palaeoecology*, *54*, 1986.

Kidd, W. S. F., and P. Molnar, Quaternary and active faulting observed on the 1985 Academia Sinica-Royal Society Geotraverse of Tibet, *Phil. Trans. R. Soc. Lond. A*, *327*, 337–363, 1988.

Kind, R., et al., Evidence from earthquake data for a partially molten crustal layer in southern Tibet, *Nature*, *274*, 1692–1694, 1996.

Kind, R., et al., Seismic images of crust and upper mantle beneath Tibet: evidence for Eurasian plate subduction, *Science*, *298*, 1219–1221, 2002.

Kirby, E., P. W. Reiners, M. A. Krol, K. X. Whipple, K. V. Hodges, K. A. Farley, W. Tang, and Z. Chen, Late Cenozoic evolution of the eastern margin of the Tibetan Plateau:Inferences from 40Ar/39Ar and (U-Th)/He thermochronology, *Tectonics*, *21*(1001), 2002.

Kirby, E., N. Harkins, E. Wang, X. Shi, C. Fan, and D. Burbank, Slip rate gradients along the eastern kunlun fault, *Tectonics*, *26*(TC2010), 2007.

Klemperer, S., *Channel Flow, Ductile Extrusion and Exhumation in Continental Collision Zones*, vol. 268, chap. Crustal flow in Tibet: geophysical evidence for the physical state of Tibetan lithosphere, and inferred patterns of active flow, pp. 39–70, R. D. Law, M. P. Searle and L. Godin ed., Geological Society, London, Special Publications, 2006.

Klootwijk, C. T., J. S. Gee, J. W. Peirce, G. M. Smith, and P. L. McFadden, An early India-Asia contact: Paleomagnetic constraints from Ninetyeast Ridge, ODP Leg 121, *Geology*, *20*, 395–398, 1992.

Kohn, M. J., S. K. Pau, and S. L. Corrie, The lower Lesser Himalayan sequence: A Paleoproterozoic arc on the northern margin of the Indian plate, *Geol. Soc. Am. Bull.*, pp. 323–335, 2010.

Kosarev, G., G. R. Kind, S. V. Sobolev, X. Yuan, W. Hanka, and S. Oreshin, Seismic evidence for a detached Indian lithospheric mantle beneath Tibet, *Science*, *283*, 1306–1309, 1999.

Koskinen, H. E. J., R. E. Lopez, R. J. Pellinen, T. I. Pulkkinen, D. N. Baker, and T. Bösinger, Pseudobreakups and substorm growth phase in the ionosphere and magnetosphere, *J. Geophys. Res.*, *98*, 5801–5813, 1993.

Kunetz, G., Processing and interpretation of magnetotelluric soundings, *Geophysics*, *37*, 1005–1021, 1972.

Lacassin, R., et al., Large-scale geometry, offset and kinematic evolution of the karakorum fault, tibet, *Earth Planet. Sci. Lett.*, *219*, 255–269, 2004.

Lapenta, G., Lecture notes on space weather, *Centrum voor Plasma Astrofysica, Katholieke Universiteit Leuven*, 2011.

Laporte, D., and A. Provost, Equilibrium geometry of a fluid phase in a polycrystalline aggregate with anisotropic surface energies: Dry grain boundaries, *J. Geophys. Res.*, *105(B11)*, 25,937–25,953, 2000.

Lasserre, C., G. Peltzer, F. Crampe, Y. Klinger, J. V. der Woerd, and P. Tapponnier, Coseismic deformation of the 2001 mw 7.8 kokoxili earthquake in tibet, measured by synthetic aperture radar interferometry, *J. Geophys. Res.*, *110*(B12408), 2005.

Lavé, J., J. P. Avouac, R. Laccassin, P. Tapponnier, and J. P. Montagner, Seismic anisotropy beneath Tibet: evidence for eastward extrusion of the Tibetan lithosphere?, *Earth Planet. Sci. Lett.*, *140*, 83–96, 1996.

Le, G., J. A. Slavin, and R. J. Strangeway, Space technology 5 observations of the imbalance of regions 1 and 2 field-aligned currents and its implication to the cross-polar cap pedersen currents, *J. Geophys. Res.*, *115*(A07202), 2010.

Ledo, J., 2D versus 3D magnetotelluric data interpretation, *Surveys in Geophysics*, *26*, 511–543, 2006.

Ledo, J., A. G. Jones, I. J. Ferguson, and L. Wolynec, Lithospheric structure of the Yukon, northern Canadian Cordillera, obtained from magnetotelluric data, *Journal of Geophysical Research*, *109*(B04410), 2004.

Lee, T. Y., and L. A. Lawver, Cenozoic plate reconstruction of Southeast Asia, *Tectonophysics*, *251*, 85–138, 1995.

Leeder, M. R., A. B. Smith, and J. Yin, Sedimentology, palaeoecology and palaeoenvironmental evolution of the 1985 Lhasa to Golmud Geotraverse, *Phil. Trans. R. Soc. Lond.*, *A327*, 107–143, 1988.

Leloup, P. H., T. M. Harrison, F. J. Ryerson, W. Chen, Q. Li, P. Tapponnier, and R. Lacassin, Structural, petrological and thermal evolution of a Tertiary ductile strike-slip shear zone, Diancang Shan (Yunnan, PRC), *J. Geophys. Res.*, *98*, 6715–6743, 1993.

Leloup, P. H., R. Lacassin, P. Tapponnier, D. Zhong, X. Lui, L. Zhang, and S. Ji, Kinematics of Tertiary left-lateral shearing at the lithospheric scale in the Ailao Shan-Red River shear zone (Yunnan, China), *Tectonophysics*, *251*, 3–84, 1995.

LEMI-417M, Long-period magnetotelluric instrument LEMI-417M: User Manual, Lviv centre of institute for space research, *Lviv Centre of Institute for Space Research, 5-A Naukova St., Lviv, 79000, Ukraine*, *296*(5575), 2015–2017, 2009.

León Soto, G., E. Sandvol, J. F. Ni, L. Flesch, T. M. Hearn, F. Tilmann, J. Chen, and L. D. Brown, Significant and vertically coherent seismic anisotropy beneath eastern Tibet, *J. Geophys. Res.*, *117*(B05308), 2012.

Lezaeta, P., A. Chave, A. G. Jones, and R. Evans, Source field effects in the auroral zone: Evidence from the slave craton (nw canada), *Physics of the earth and planetary interiors*, *164*, 21–35, 2007.

Li, S., M. J. Unsworth, J. R. Booker, W. Wei, H. Tan, and A. G. Jones, Partial melt or aqueous fluids in the Tibetan crust: Constraints from INDEPTH magnetotelluric data, *Geophys. J. Int.*, *153*, 289–304, 2003.

Li, Y., C. Wang, G. Xu, X. Zhao, and C. Ma, Crustal Shortening in the Tanggula-Tuotuohe Area, Northern Tibet, *25th Himalaya-Karakoram-Tibet Workshop San Francisco - June 2010*, 2010.

Li, Y., C. Wang, X. Zhao, and A. Y. amd C[] Ma, Cenozoic thrust system, basin evolution, and uplift of the Tanggula Range in the Tuotuohe region, central Tibet, *Gondwana Research, in Press*, 2012.

Lin, A., B. Fu, J. Guo, Q. Zeng, G. Dang, W. He, and Y. Zhao, Co-Seismic Strike-Slip and Rupture Length Produced by the 2001 ms 8.1 Central Kunlun Earthquake, *Science*, *296*(5575), 2015–2017, 2002.

Liu, Z. Q., Geologic Map of the Qinghai-Xizang Plateau and its Neighboring Regions (scale at 1:1,500,000), *Chengdu Institute of Geology and Mineral Resources. Beijing: Geologic Publishing House*, 1988.

Lyon-Caen, H., Comparison of the Upper Mantle Shear Wave Velocity Structure of the Indian Shield and the Tibetan Plateau and Tectonic Implications, *Geophysical Journal of the Royal Astronomical Society*, *86*, 727–749, 1986.

Mackie, R. L., User manual and software documentation for two-dimensional inversion of magnetotelluric data. Anisotropy Version 6.7, *GSY-USA Inc. San Francisco, CA, USA*, 2002.

Mackie, R. L., J. T. Smith, and T. R. Madden, Three-dimensional electromagnetic modeling using finite difference equations: the magnetotelluric example, *Radio Sci.*, *29*, 923–935, 1994.

Makovsky, Y., and S. L. Klemperer, Measuring the seismic properties of Tibetan bright spots. Evidence for free aqueous fluids in the Tibetan middle crust, *J. Geophys. Res.*, *104*, 10,795–10,825, 1999.

Mareschal, M., Source effects and the interpretation of geomagnetic sounding data at sub-auroral latitudes, *Geophys. J. R. astr. Soc.*, *67*, 125–136, 1981.

Mareschal, M., Modelling of natural source of magnetospheric origin in the interpretation of regional induction studies: a review, *Surv. Geophys.*, *8*, 261–300, 1986.

Martí, M., The role of electrical anisotropy in magnetotelluric responses: From modelling and dimensionality analysis to inversion and interpretation, *21st EM Induction Workshop, Darwin, Australia*, 2012.

Martí, M., P. Queralt, J. Ledo, and C. Farquharsonb, Dimensionality imprint of electrical anisotropy in magnetotelluric responses, *Physics of the Earth and Planetary Interiors*, *182*, 139–151, 2010.

Matte, P., P. Tapponnier, N. Arnaud, L. Bourjot, J. P. Avouac, P. Vidal, Q. Liu, Y. Pan, and Y. Wang, Tectonics of Western Tibet, between the Tarim and the Indus, *Earth Planet. Sci. Lett.*, *142*, 311–330, 1996a.

Matte, P., P. Tapponnier, N. Arnaud, L. Bourjot, and J. P. A. et al., Tectonics of western tibet, between the tarim and the indus, *Earth Planet. Sci. Lett.*, *142*, 311–330, 1996b.

Maunder, E. W., Note on the distribution of sun-spots in heliographic latitude, 1874-1902, *Monthly Notices of the Royal Astronomical Society*, *64*, 747–761, 1904.

Maus, S., Conductivity of the ionosphere, *CIRES, University of Colorado*, 2006.

McCaffrey, R., and J. Nabelek, Role of oblique convergence in the active deformation of the Himalayas and southern Tibet plateau, *Geology*, *26*, 691–694, 1998.

McKenna, L. W., and J. D. Walker, Geochemistry of crustally derived leucocratic igneous rocks from the Ulugh Muztagh area, Northern Tibet and their implications for the formation of the Tibetan Plateau., *Journal of Geophysical Research*, *95*, 21,483–21,502, 1990.

McKenzie, D., and K. Priestley, The influence of lithospheric thickness variations on continental evolution, *Lithos*, *102*, 1–11, 2008.

McNamara, D. E., T. J. Owens, P. G. Silver, and F. T. Wu, Shear wave anisotropy beneath the Tibetan Plateau, *J. Geophys. Res.*, *99*, 13,655–13,665, 1994.

McNamara, D. E., W. R. Walter, T. J. Owens, and C. J. Ammon, Upper mantle velocity structure beneath the Tibetan Plateau from pn travel time tomography, *J. Geophys. Res.*, *102(B1)*, 493–505, 1997.

McNamara, L. F., and C. S. Wright, Disappearing solar filaments and geomagnetic activity, *Nature*, *299*, 537–538, 1982.

McNeice, G. W., and A. G. Jones, Multi-site, Multi-frequency tensor decomposition of magnetotelluric data, *Geophysics*, *66*, 158–173, 2001.

McPherron, R. L., Magnetic pulsations: their sources and relation to solar wind and geomagnetic activity, *Surveys in Geophysics*, *26*, 545–592, 2005.

Meade, B. J., Present-day kinematics at the India-Asia collision zone, *Geology*, *35*, 81–84, 2007.

Mechie, J., et al., Precise temperature estimation in the tibetan crust from seismic detection of the α-β quartz transition, *Geology*, *32*, 601–604, 2004.

Mechie, J., et al., Crustal shear (s) velocity and poisson's ratio structure along the INDEPTH IV profile in northeast tibet as derived from wide-angle seismic data, *Geophys. J. Int.*, *191*, 369–384, 2012.

Medvedev, S., and C. Beaumont, *Channel Flow, Ductile Extrusion and Exhumation in Continental Collision Zones*, vol. 268, chap. Growth of continental plateaus by channel injection: models designed to address constraints and thermomechanical consistency, pp. 147–164, R. D. Law, M. P. Searle and L. Godin ed., Geological Society, London, Special Publications, 2006.

Metcalfe, I., Gondwanaland dispersion, Asian accretion, and evolution of eastern Tethys, *Aust. J. Earth Sci.*, *43*, 605–623, 1996.

Meyer, B., P. Tapponnier, L. Bourjot, F. Metivier, Y. Gaudemer, G. Peltzer, G. Shunmin, and C. Zhitai, Crustal thickening in Gansu Qinghai, lithospheric mantle subduction, and oblique, strike slip controlled growth of the Tibet plateau, *Geophysical Journal International*, *135(1)*, 1–47, 1998.

Miller, C., M. Tiioni, W. Frank, B. Grasemann, U. Klotzli, P. Guntli, and E. Draganits, The early Palaeozoic magmatic event in the Northwest Himalaya, India: Source, tectonic setting and age of emplacement, *Geol. Mag.*, *138*, 237–251, 2001.

Mitra, S., K. Priestley, A. K. Bhattacharyya, and V. K. Gaur, Crustal structure and earthquake focal depths beneath northeastern India and southern Tibet, *Geophys. J. Int.*, *160*, 227–248, 2005.

Molnar, P., S-wave residuals from earthquakes in the Tibetan region and lateral variations in the upper mantle, *Earth Planet. Sci. Lett.*, *101*, 68–77, 1990.

Molnar, P., and W. P. Chen, S-p travel time residuals and lateral inhomogeneity in the mantle beneath Tibet and the Himalaya, *J. Geophys. Res.*, *89(B8)*, 6911–6917, 1984.

Molnar, P., and P. Tapponnier, Cenozoic tectonics of Asia: effects of a continental collision, *Science*, *189*, 419–426, 1975.

Molnar, P., and P. Tapponnier, Active tectonics of Tibet, *J. Geophys. Res.*, *85*, 5361–5375, 1978.

Molnar, P., B. C. Burchfiel, Z. Ziyun, L. Kuangyi, W. Shuji, and H. Minmin, Geologic evolution of northern tibet: results from an expedition to Ulugh Muztagh, *Science*, *235*, 299–305, 1987.

Molnar, P., P. C. England, and J. Martinod, Mantle dynamics, uplift of the Tibetan Plateau, and the Indian monsoon, *Rev. Geophys.*, *31*, 357–396, 1993.

Monteiro Santos, F. A., A. Mateus, E. P. Almeida, J. Pous, and L. A. Mendes-Victor, Are some of the deep crustal conductive features found in SW Iberia caused by graphite?, *Earth and Planetary Science Letters*, *201*, 2002.

Moombarriga Geoscience, Magnetotelluric methods, www.moombarriga.com.au.

Moores, E. M., and R. W. Fairbridge, *Encyclopedia of European and Asian Regional Geology*, 825 pp., Encyclopedia of Earth Sciences Series, London, 1998.

Morency, C., and M. P. Doin, Numerical simulations of the mantle lithosphere delamination, *J. Geophys. Res.*, *109*(B03410), 2004.

Murphy, J. B., and R. B. Nance, Supercontinent model for the contrasting character of Late Proterozoic orogenic belts, *Geology*, *19*, 469–472, 1991.

Murphy, M. A., A. Yin, T. M. Harrison, S. B. Durr, Z. Chen, F. J. Ryerson, W. S. F. Kidd, X. Wang, and X. Zhou, Did the Indo-Asian collision alone create the Tibetan plateau?, *Geology*, *25*, 719–722, 1997.

Murphy, M. A., A. Yin, P. Kapp, T. M. Harrison, C. E. Manning, F. J. Ryerson, L. Ding, and J. Guo, Structural evolution of the Gurla Mandhata detachment system, southwest Tibet: Implications for the eastward extent of the karakoram fault system, *Geol. Soc. Am. Bull.*, *114*, 428–447, 2002.

Myrow, P. M., N. C. Hughes, J. W. Goodge, C. M. Fanning, I. S. Williams, S. Peng, O. N. Bhargava, S. K. Parcha, and K. R. Pogue, Extraordinary transport and mixing of sediment across Himalayan central Gondwana during the Cambrian - Ordovician, *Geol. Soc. Am. Bull.*, *122*, 1660–1670, 2010.

Nábelek, J., et al., Underplating in the Himalaya-Tibet Collision zone revealed by the Hi-CLIMB Experiment, *Science*, *325*(5946), 1371–1374, 2009.

Nabelek, P. I., A. G. Whittington, and A. M. Hofmeister, Strain heating as a mechanism for partial melting and ultrahigh temperature metamorphism in convergent orogens: Implications of temperature!dependent thermal diffusivity and rheology, *J. Geophys. Res.*, *115*(B12417), 2010.

NASA, National aeronautics and space administration, http://www.nasa.gov.

Nelson, K. D., et al., Partially molten middle crust beneath southern Tibet: Synthesis of Project INDEPTH results, *Science*, *274*, 1684–1686, 1996.

Nesbitt, B. E., Electrical resistivities of crustal fluids, *J. Geophys. Res.*, *98*, 4301–4310, 1993.

Ni, J., and M. Barazangi, Hig-frequency seismic wave propagatio beneath the Indian Shield, Himilayan Arc, Tibetan Plateau and surrounding regions, high uppermost mantle velocities and different propagation beneath Tibet, *Geophys. J. R. astr. Soc.*, *72*, 665–689, 1983.

Nie, S., A. Yin, D. Rowley, and Y. Jin, Exhumation of the dabie shan ultra-high pressure rocks and accumulation of the songpan-ganzi flysch sequence, central china, *Geology*, *22*, 999–1002, 1994.

NOAA, National oceanic and atmospheric administration, http://www.noaa.gov.

Northrup, C. J., L. H. Royden, and B. C. Burchfiel, Motion of the pacific plate relative to eurasia and its potential relation to cenozoic extension along the eastern margin of eurasia, *Geology*, *23*, 719–722, 1995.

Nover, G., Electrical properties of crustal and mantle rocks: a review of laboratory measurements and their explanation, *Surveys in Geophysics*, *26*, 593–651, 2005.

Olhoeft, G. R., Electrical properties of rocks, *in Physical Properties of Rocks and Minerals, eds Touloukian, Y. S., Judd, W. R. and Roy, R. F., McGraw-Hill, New York*, 1980.

Olhoeft, G. R., Low Frequency Electrical Properties, *Geophysics*, *50*, 2492–2503, 1985.

Osipova, I. L., S. C. O. Hjelt, and L. L. Vanyan, Source field problems in northern parts of the baltic shield, *Phys. Earth Planet. Inter.*, *53*, 337–342, 1989.

Owens, T. J., and G. Zandt, Implications of crustal property variations for models of Tibetan plateau evolution, *Nature*, *387*, 37–43, 1997.

Padilha, A. L., Behaviour of magnetotelluric source dields within the equatorial zone, *Earth Planets Space*, *51*, 1119–1125, 1999.

Padilha, A. L., I. Vitorello, and L. Rijo, Effects of the equatorial electrojet on magnetotelluric surveys: Field results from northwest brazil, *Geophys. Res. Lett.*, *24*, 89–92, 1997.

Pan, G., L. Ding, D. Yao, and L. Wang, Geologic map of Chinghai-Xizang (Tibet) Plateau and adjacent areas, scale 1:1,500,000, *Chengdu Inst. of Geol. and Miner. Res., Geol. Publ., Beijing*, 2004.

Pan, Y., *Geologic Evolution of the Karakorum and Kunlun Mountains*, chap. Regional geologic evolution and conclusion, pp. 263–288, P. Yunsheng ed., Seismological Press, Beijing, 1996.

Park, S. K., Distortion of Magnetotelluric Sounding curves by Three-Dimensional Structures, *Geophysics*, *50*, 785–797, 1985.

Parker, R. L., Geophysical inverse theory, *Princeton Univ. Press.*, 1994.

Parker, R. L., and J. R. Booker, The inverse problem of electromagnetic induction: existence and construction of solutions based upon incomplete data, *J. Geophys. Res.*, *85*, 4421–4428, 1980.

Parker, R. L., and J. R. Booker, Optimal one-dimensional inversion and bounding of magnetotelluric apparent resistivity and phase measurements, *Physics of the Earth and Planetary Interiors*, *98*, 269–282, 1996.

Parker, R. L., and K. A. Whaler, Numerical methods for establishing solutions to the inverse problem of electromagnetic induction, *J. Geophys. Res.*, *86*, 9574–9584, 1981.

Parkinson, W. D., Directions of rapid geomagnetic fluctuations, *Geophysical Journal of the Royal Astronomical Society*, *2(1)*, 1–14, 1959.

Parkinson, W. D., and F. W. Jones, The geomagnetic coast effect, *Rev. Geophys. Space Phys.*, *17*, 1999–2015, 1979.

Parrish, R. R., and K. V. Hodges, Isotopic constraints on the age and provenance of the Lesser and Greater Himalayan sequences, Nepalese Himalaya, *Geol. Soc. Am. Bull.*, *108*, 904–911, 1996.

Partzsch, G. M., F. R. Schilling, and J. Arndt, The influence of partial melting on the electrical behavior of crustal rocks: laboratory examinations, model calculations and geological interpretations, *Tectonophysics*, *317*, 189–203, 2000.

Patriat, P., and J. Achache, Indian-Asia collision chronology has implications for crustal shortening and driving mechanisms of plates, *Nature*, *311*, 615–621, 1984.

Pearce, J. A., and H. Mei, Volcanic rocks of the 1985 Tibet Geotraverse Lhasa to Golmud, *Phil. Trans. R. Soc. Lond. A*, *327*, 203–213, 1988.

Pedersen, L. B., and M. Engels, Routine 2D inversion of magnetotelluric data using the determinant of the impedance tensor, *Geophysics*, *70*(2), G33–G41, 2005.

Pek, J., and F. A. M. Santos, Magnetotelluric impedances and parametric sensitivities for 1D anisotropic layered media, *Computers and Geosciences*, *28*, 939–950, 2002.

Pek, J., and T. Verner, Finite-difference modelling of magnetotelluric fields in two-dimensional anisotropic media, *Geophys. J. Int.*, *128*, 505–521, 1997.

Pellerin, L., and G. W. Hohman, Transient electromagnetic inversion: A remedy for magnetotelluric static shift, *Geophysics*, *55(9)*, 1242–1250, 1990.

Peltier, W. R., and J. F. Hermance, Magnetotelluric fields of a gaussian electrojet, *Can. J. Earth Sci.*, *8*, 338–346, 1971.

Peltzer, G., and F. Saucier, Present-day kinematics of Asia derived from geologic fault rates, *J. Geophys. Res.*, *101*, 27,943–27,956, 1996.

Peltzer, G., and P. Tapponnier, Formation and evolution of strike-slip faults, rifts, and basins during the India-Asia collision: an experimental approach, *J. Geophys. Res.*, *93*, 15,085–15,117, 1988.

Phillips, R. J., R. R. Parrish, and M. P. Searle, Age constraints on ductile deformation and long-term slip rates along the Karakoram fault zone, Ladakh, *Earth Planet. Sci. Lett.*, *226*, 305–319, 2004.

Phillips, T., "solar cycle 24 begins", *NASA*, 2008.

Phoenix MTU, V5 system 2000 mtu/mtu-a user guide, *Phoenix Geophysics Limited, 3781 Victoria Park Avenue, Unit 3, Toronto, ON Canada M1W 3K5*, 2010.

Pichon, X. L., M. Fournier, and L. Jolivet, Kinematics, topography, shortening, and extrusion in the India-Eurasia collision, *Tectonics*, *11*, 1085–1098, 1992.

Pirjola, R., Modelling the electric and magnetic fields at the earth's surface due to an auroral electrojet, *Journal of Atmospheric and Solar-Terrestrial Physics*, *60*, 1139–1148, 1998.

Platt, J. P., and P. England, Convective removal of lithosphere beneath mountain belts: thermal and mechanical consequences, *Am. J. Sci.*, *294*, 307–336, 1994.

Poe, B. T., C. Romanero, and J. Tyburzcy, Effect of Dissolved Water on the Electrical Conductivity of Wadsleyite, *Annual Report, Bayrisches Geoinstitut*, 2001.

Poe, B. T., C. Romano, F. Nestola, and J. R. Smyth, Electrical conductivity anisotropy of dry and hydrous olivine at 8 GPa, *Phys. Earth Planet. Inter.*, *181(3-4)*(103-111), 2010.

Pommier, A., and E. L. Trong, SIGMELTS: A web portal for electrical conductivity calculations in geosciences, *Computers and Geosciences*, *37*, 1450–1459, 2011.

Pommier, A., P. Tarits, S. Hautot, M. Pichavant, B. Scaillet, and F. Gaillard, A new petrological and geophysical investigation of the present-day plumbing system of Mount Vesuvius, *Geochem. Geophys. Geosyst.*, *11*(Q07013), 2010.

Pommier, A. F., M. Gaillard, and M. P. B. Scaillet, Laboratory measurements of electrical conductivities of hydrous and dry Mount Vesuvius melts under pressure, *J. Geophys. Res.*, *113*(B05205), 2008.

Potemra, T., Magnetospheric substorms, *Washington, D.C.: Am. Geophysical Union*, p. 488, 1991.

Price, A. T., The theory of magnetotelluric fields when the source field is considered, *J. Geophys. Res.*, *67*, 1907–1918, 1962.

Priestley, K., E. Debayle, D. McKenzie, and S. Pilidou, Upper mantle structure of eastern Asia from multi-mode surface waveformtomography, *J. geophys. Res.*, *111*(B10304), 2006.

Priestley, K., J. Jackson, and D. McKenzie, Lithospheric structure and deep earthquakes beneath India, the Himalaya and southern Tibet, *Geophysical Journal International*, *172*, 345–362, 2008.

Pullen, A., P. K. G. E. Gehrels, J. D. Vervoort, and L. Ding, Triassic continental subduction in central Tibet and Mediterranean-style closure of the paleo-Tethys ocean, *Geology*, *36*, 351–354, 2008.

Pullen, A., P. Kapp, G. E. Gehrels, L. Ding, and Q. Zhang, Metamorphic rocks in central Tibet: Lateral variations and implications for crustal structure, *GSA Bulletin*, *123*(3-4), 585–600, 2011.

Qin, J., J. Din, D. Zhang, B. Rusk, C. Liu, and Q. Zhang, Tectonic settings of porphyry Cu-Mo-Au deposits in the Himalayan-Tibetan orogen, East Tethys, *International Geology Review*, *54*(3), 302–312, 2012.

Rapine, R., F. Tilmann, M. West, J. Ni, and A. Rodgers, Crustal structure of northern and southern Tibet from surface wave dispersion analysis, *J. Geophys. Res.*, *108*(B2), 2120, 2003.

Reid, A., C. J. L. Wilson, L. Shun, N. Pearson, and E. Belousova, Mesozoic plutons of the Yidun arc, SW China: U/Pb geochronology and Hf isotopic signature, *Ore Geol. Rev.*, *34*, 88–106, 2007.

Replumaz, A., and P. Tapponnier, Reconstruction of the deformed collision zone between India and Asia by backward motion of lithospheric blocks, *J. Geophys. Res.*, *108(B6)*(2285), 2003.

Revil, A., M. Darot, and P. A. Pezard, From Surface Electrical Properties to Spontaneous Potentials in Porous Media, *Surv. Geophys.*, *17*, 331–346, 1996.

Righter, K., Metal-Silicate Partitioning of Siderophile Elements and Core Formation in the Early Earth, *Annu. Rev. Earth Planet. Sci.*, *31*, 135–174, 2003.

Rippe, D., and M. Unsworth, Quantifying crustal flow in Tibet with magnetotelluric data, *Physics of the Earth and Planetary Interiors*, *179*, 107–121, 2010.

Ritts, B. D., and U. Biffi, Magnitude of post-Middle Jurassic (Bajocian) displacement on the central Altyn Tagh fault system, northwest China, *Geological Society of America Bulletin*, *112*, 61–74, 2000.

Roberts, J. J., and J. A. Tyburczy, Frequency dependent electrical properties of polycrystalline olivine compacts, *J. Geophys. Res.*, *96*, 16,205–16,222, 1991.

Roberts, J. J., and J. A. Tyburczy, Partial Melt Electrical Conductivity: influence of Melt Composition, *J. Geophys. Res.*, *104*, 7055–7065, 1999.

Robinson, A. C., Geologic offsets across the northern Karakorum fault: Implications for its role and terrane correlations in the western Himalayan-Tibetan orogen, *Earth Planet. Sci. Lett.*, *279*, 123–130, 2009.

Rodi, W., and R. L. Mackie, Nonlinear conjugate gradients algorithm for 2D magnetotelluric inversion, *Geophysics*, *66*, 174–187, 2001.

Roger, F., P. Tapponnier, N. Arnaud, U. Scharer, M. Brunel, Z. Xu, and J. Yang, An Eocene magmatic belt across central Tibet: mantle subduction triggered by the Indian collision?, *Terra Nova*, *12*, 102–108, 2000.

Roger, F., N. Arnaud, S. Gilder, P. Tapponnier, M. Jolivet, M. Brunel, J. Malavieille, Z. Xu, and J. Yang, Geochronological and geochemical constraints on Mesozoic suturing in east central Tibet, *Tectonics*, *22*(4), 1037, 2003.

Roger, F., M. Jolivet, and J. Malavieille, Tectonic evolution of the Triassic fold belts of Tibet, *Comptes Rendus. Geosciences*, *340*(2-3), 180–189, 2008.

Rosenberg, C. L., and M. R. Handy, Experimental deformation of partially melted granite revisited: implications for the continental crust, *J. Metamorphic Geol.*, *23*, 19–28, 2005.

Rowley, D. B., Minimum age of initiation of collision between India and Asia north of Everest based on the subsidence history of the Zhepure mountain section, *J. Geol.*, *106*, 229–235, 1998.

Royden, L. H., Coupling and decoupling of crust and mantle in convergent orogens: Implications for strain partitioning in the crust, *Journal of Geophysical Research*, *101*, 17,679–17,705, 1996.

Royden, L. H., B. C. Burchfiel, R. W. King, E. Wang, Z. Chen, F. Shen, and Y. Liu, Surface deformation and lower crustal flow in eastern Tibet, *Science*, *276*, 788–790, 1997.

Royden, L. H., B. C. Burchfiel, and R. D. van der Hilst, The Geological Evolution of the Tibetan Plateau, *Science*, *321*, 1054, 2008.

Rudnick, R. L., Making continental crust, *Nature*, *378*, 571–578, 1995.

Rudnick, R. L., W. F. McDonough, and B. W. Chappell, Carbonatite metasomatism in the northern Tanzanian mantle: petrographic and geochemical characteristics, *Earth and Planetary Science Letters*, *114*, 463–475, 1993.

Ruffet, C., M. Darot, and Y. Gueguen, Surface Conductivity in Rocks: A Review, *Surv. Geophys.*, *16*, 83–105, 1995.

Rui, G., C. Xiangzhou, and W. Gongjian, Lithospheric structure and geodynamic model of the Golmud-Ejn transect in northern Tibet, *Geol. Soc. Am.*, *328*, 9–17, 1999.

Ryerson, F. J., P. Tapponnier, R. C. Finkel, A. S. Meriaux, J. V. der Woerd, C. Lassiere, M. L. Chevalier, X. Xiwei, and L. Harbing, Applications of morphochronology to the active tectonics of Tibet, *Spec. Pap. Geol. Soc.*, *415*, 2006.

Sandvol, E., J. Ni, R. Kind, and W. Zhao, Seismic anistropy beneath the southern himalayas-tibet collision zone, *J. Geophys. Res.*, *102*, 1997.

Savage, M. K., Seismic anisotropy and mantle deformation: What have we learned from Shear Wave Splitting?, *Rev. Geophys. 37*, *37*, 1999.

Schelling, D., The tectonostratigraphy and structure of the eastern Nepal Himalaya, *Tectonics*, *11*, 925–943, 1992.

Schilling, F. R., et al., *The Andes - Active Subduction Orogeny*, chap. Partial Melting in the Central Andean Crust: a Review of Geophysical, Petrophysical, and Petrologic Evidence, pp. 459–474, O. Oncken and G. Chong and G. Franz and P. Giese and H. J. Götze and V. A. Ramos and M. R. Strecker and P. Wigger ed., Springer, 2006.

Schmeling, H., Numerical models on the influence of partial melt on elastic, anelastic and electrical properties of rocks. Part II: electrical conductivity, *Physics of the Earth and Planetary Interiors*, *43*, 123–136, 1986.

Schmucker, U., Regional induction studies: a review of methods and results, *Phys. Earth. Plant. Inter.*, *7*, 365–378, 1973.

Schmucker, U., *Numerical Data and Functional Relationships in Science and Technology*, vol. 2, chap. Geophysics of the solid Earth, the Moon and the Planets, pp. 31–73, K. uchs and H. Soffel ed., Springer-Verlag, Berlin-Heidelberg, 1985.

Schock, R. N., A. G. Duba, and T. J. Shankland, Electrical conduction in olivine, *J. Geophys. Res.*, *94(B5)*, 5829–5839, 1989.

Schulte-Pelkum, V., G. Monsalve, A. Sheehan, M. R. Pandey, S. Sapkota, R. Bilham, and F. Wu, Imaging the indian subcontinent beneath the Himalaya, *Nature*, *435*, 1222–1225, 2005.

Schwab, M., et al., Assembly of the Pamirs: age and origin of magmatic belts from the southern Tien Shan to the southern Pamirs and their relation to Tibet, *Tectonics*, *23*(TC4002), 2004.

Schwalenberg, K., V. Rath, and V. Haak, Sensitivity studies applied to a two-dimensional resistivity model from the central andes, *Geophys. J. Int.*, *150*, 673–686, 2002.

Searle, M. P., *Geology and Tectonics of the Karakoram Mountains*, Wiley, New York, 1991.

Searle, M. P., *The Tectonic Evolution of Asia*, chap. Cooling history, erosion, exhumation, and kinematics of the Himalaya-Karakoram-Tibet orogenic belt, pp. 110–137, A. Yin and T. M. Harrison ed., Cambridge Univ. Press, New York, 1996a.

Searle, M. P., Geological evidence against large-scale pre-Holocene offsets along the Karakoram Fault: Implications for the limited extrusion of the Tibetan Plateau, *Tectonics*, *15*, 171–186, 1996b.

Searle, M. P., J. R. Elliott, R. J. Phillips, and S. L. Chung, Crustal-lithospheric structure and continental extrusion of Tibet, *Journal of the Geological Society, London*, *168*, 633–672, 2011.

Searle, R. L. C. B. S., M. P., and J. McCarron, Structure of the north indian continental margin in the Ladakh-Zanskar Himalayas: Implications for the timing of obduction of the Spontang ophiolite, India-Asia collision and deformational events in the Himalaya, *Geol. Mag.*, *134*, 297–316, 1997.

Sengör, A. M. C., Plate tectonics and orogenic research after 25 years: a Tethyan perspective, *Earth Sci. Rev.*, *27*, 1–201, 1990.

Sengör, A. M. C., D. Altiner, A. Cin, T. Ustaomer, and K. J. Hsü, Origin and assembly of the Tethyside orogenic collage at the expense of Gondwana land, *in Gondwana and Tethys, Geol. Soc. Spec. Publ.*, *37*, 119–181, 1988.

Shapiro, N. M., M. H. Ritzwoller, P. Molnar, and V. Levin, Thinning and flow of Tibetan crust constrained by seismic anisotropy, *Science*, *305*, 233–236, 2004.

Shen, F., L. H. Royden, and B. C. Burchfiel, Large-scale crustal deformation of the Tibetan Plateau, *Journal of Geophysical Research*, *106*(6793-6816), 2001.

Shen, Z. K., J. Lü, M. Wang, and R. Bürgmann, Contemporary crustal deformation around the southeast borderland of the Tibetan Plateau, *J. Geophys. Res.*, *110*(B11409), 2005.

Shi, D., Y. Shen, W. Zhao, and A. Li, Seismic evidence for a Moho offset and south-directed thrust at the easternmost Qaidam-Kunlun boundary in the Northeast Tibetan plateau, *Earth and Planetary Science Letters*, *288(1-2)*, 329–334, 2009.

Shin, Y. H., H. Xu, C. Braitenberg, J. Fang, and Y. Wang, Moho undulations beneath Tibet from GRACE-integrated gravity data, *Geophys. J. Int.*, *170*, 971–985, 2007.

SIDC, Solar influences data analysis center, http://sidc.oma.be/.

Siegel, A. F., Robust regression using repeated medians, *Biometrika*, *69*, 242–244, 1982.

Simons, F., and R. D. van der Hilst, Seismic and mechanical anisotropy and the past and present deformation of the Australian lithosphere, *Earth Planet Sci. Lett.*, *211*, 271–286, 2003.

Simpson, F., and K. Bahr, *The Tectonic Evolution of Asia*, Cambrigde University Press, 2005.

Siripunvaraporn, W., Three-Dimensional Magnetotelluric Inversion: An Introductory Guide for Developers and Users, *Surv. Geophys.*, *33*, 5–27, 2012.

Siripunvaraporn, W., and G. Egbert, An efficient data-subspace inversion method for 2D magnetotelluric data, *Geophysics*, *65(3)*, 791–803, 2000.

Siripunvaraporn, W., G. Egbert, Y. Lenbury, and M. Uyeshima, Three-dimensional magnetotelluric inversion: data-space method, *Physics of the Earth and Planetary Interiors*, *150*, 3–14, 2005.

Smirnov, M. Y., Magnetotelluric data processing with a robust statistical procedure having a high breakdown poin, *Geophysical Journal International*, *152*, 1–7, 2003.

Smith, C. S., Grain phases and interfaces: An interpretation of microstructure, *American Institute of Mechanical Engineers Transactions*, *75*, 15–51, 1948.

Snodgrass, H. B., and R. K. Ulrich, Rotation of doppler features in the solar photosphere, *Astrophysical Journal*, *351*, 309–316, 1990.

Sobel, E. R., and N. Arnaud, A possible middle Paleozoic suture in the Altun Shan, NW China, *Tectonics*, *18*, 64–74, 1999.

Sol, S., et al., Geodynamics of the southeastern Tibetan Plateau from seismic anisotropy and geodesy, *Geology*, *35*, 563–566, 2007.

Solon, K. D., et al., Structure of the crust in the vicinity of the Banggong-Nujiang suture in central Tibet from INDEPTH magnetotelluric data, *J. Geophys. Res.*, *110*(B10102), 2005.

Song, T., and X. Wang, Structural styles and stratigraphic patterns of syndepositional faults in a contractional setting: Examples from Qaidam basin, northwestern China, *American Association of Petroleum Geologists Bulletin*, *77*, 102–117, 1993.

spacetoday.org, "the sun: Did you say the sun has spots?". space today online, http://www.spacetoday.org/solsys/sun/sunspots.html.

Spratt, J. E., A. G. Jones, K. D. Nelson, and M. J. Unsworth, Crustal structure of the India-Asia collision zone, southern Tibet, from INDEPTH MT investigations, *Physics of the Earth and Planetary Interiors*, *150*, 227–237, 2005.

Srivastava, S. P., Methods of interpretation of magnetotelluric data when the source field in considered, *J. Geophys. Res.*, *70*, 945–954, 1965.

Stampfli, G. M., and G. D. Borel, A plate tectonic model for the paleozoic and mesozoic constrained by dynamic plate boundaries and restored synthetic oceanic isochrons, *Earth and Planetary Science Letters*, *196*, 17–33, 2002.

Stott, P. A., G. S. Jones, and J. F. B. Mitchell, Do models underestimate the solar contribution to recent climate change, *Journal of Climate*, *16*, 4079–4093, 2003.

Swift, C. M., A magnetotelluric investigation of an electrical conductivity anomaly in the southwestern united states, *Geology and Geophysics. Ph.D. thesis, Massachusetts Institute of Technology, Cambridge, MA.*, 1967.

Tapponnier, P., and P. J. Molnar, Active faulting and tectonics of China, *J. Geophys. Res.*, *82*, 2905–2930, 1977.

Tapponnier, P., G. Peltzer, A. Y. Ledain, R. Armijo, and P. R. Cobbold, Propagating extrusion tectonics in Asia: New insights from simple experiments with plasticine, *Geology*, *10*, 611–616, 1982.

Tapponnier, P., Z. Q. Xu, F. Roger, B. Meyer, N. Arnaud, G. Wittlinger, and J. S. Yang, Oblique stepwise rise and growth of the Tibet plateau, *Science*, *294*, 1671–1677, 2001.

Taylor, M., A. Yin, F. J. Ryerson, P. Kapp, and L. Ding, Conjugate strike-slip faulting along the Bangong-Nujiang suture zone accommodates coeval east-west extension and north-south shortening in the interior of the Tibetan Plateau, *Tectonics*, *22*(1044), 2003.

ten Grotenhuis, S. M., M. R. Drury, C. J. Spiers, and C. J. Peach, Melt distribution in olivine rocks based on electrical conductivity measurements, *Journal of Geophysical Research*, *110*(B12201), 2005.

Thatcher, W., Microplate model for the present-day deformation of Tibet, *Journal of Geophysical Research*, *112*(B01401), 2007.

Tikhonov, A. N., On determining electric characteristics of the deep layers of the earth's crust, *Dolk. Acad. Nauk. SSSR*, *73*, 295–297, 1950.

Tikhonov, A. N., Mathematical basis of the theory of electromagnetic soundings, *USSR Comp. Math. Phys.*, *5*, 201–211, 1965.

Tikhonov, A. N., and V. Y. Arsenin, Solutions of ill-posed problems, *V. H. Winston and Sons.*, 1977.

Tilmann, F., J. Ni, and I. I. S. Team, Seismic imaging of the downwelling Indian lithosphere beneath central Tibet, *Science*, *300*, 1424–1427, 2003.

Tousey, R., *The Solar Corona, in Space Research XIII*, M. J. Rycroft and S. K. Runcorn ed., 713 pp., Akademie-Verlag, Berlin, 1973.

Turner, S., C. J. Hawkesworth, J. Liu, N. Rogers, S. Kelley, and P. van Calsteren, Timing of Tibetan uplift constrained by analysis of volcanic rocks, *Nature*, *364*, 50–53, 1993.

Turner, S., N. Arnaud, J. Liu, N. Rogers, C. Hawkesworth, N. Harris, S. Kelley, P. van Calsteren, and W. Deng, Postcollision, shoshonitic volcanism on the Tibetan plateau: Implications for convective thinning of the lithosphere and the source of ocean island basalts, *Journal of Petrology*, *37*, 45–71, 1996.

Tyburczy, J. A., and H. S. Waff, Electrical conductivity of molten basalt and andersite to 25 kilobars pressure: geophysical significance and implications for charge transport and melt structure, *J. Geophys. Res.*, *88*, 2413–2430, 1983.

Unsworth, M., W. Wei, A. G. Jones, S. Li, P. Bedrosian, J. Booker, S. Jin, M. Deng, and H. Tan, Crustal and upper mantle structure of northern Tibet imaged with magnetotelluric data, *J. Geophys. Res.*, *109*, B02,403, 2004.

Unsworth, M., A. G. Jones, W. Wei, G. Marquis, S. G. Gokarn, J. E. Spratt, and I.-M. Team, Crustal rheology of the Himalaya and southern Tibet inferred from magnetotelluric data, *Nature*, *438*, 2005.

Vacher, P., and O. Verhoeven, Modelling the electrical conductivity of iron-rich minerals for planetary applications, *Planet. Space Sci.*, *55(4)*, 455–466, 2005.

Valli, F., et al., Twenty million years of continuous deformation along the karakorum fault, western tibet: A thermochronological analysis, *Tectonics*, *26*(TC4004), 2007.

van der Woerd, J., F. J. Ryerson, P. Tapponnier, Y. Gaudemer, R. Finkel, A. S. Meriaux, M. Caffee, G. Zhao, and Q. He, Holocene left-slip rate determined by cosmogenic surface dating on the Xidatan segment of the Kunlun fault (Qinghai, China), *Geology*, *26*, 695–698, 1998.

van der Woerd, J., et al., Uniform slip-rate along the Kunlun fault: Implication for seismic behaviour and large-scale tectonics, *Geophys. Res. Lett.*, *27*, 2353–2356, 2000.

van Hinsbergen, D. J. J., P. Kapp, G. Dupont-Nivet, P. C. Lippert, P. G. DeCelles, and T. H. Torsvik, Restoration of cenozoic deformation in asia and the size of greater india, *Tectonics*, *30*, TC5003, 2011.

Vanyan, L. L., A. P. Shilovsky, B. A. Okulessky, V. Y. Semenov, and T. A. Sidelnikova, Electrical conductivty of the crust of the siberian platform, *Physics of the Earth and Planetary Interiors*, *54*, 163–168, 1989.

Vergne, J., G. Wittlinger, V. Farra, and H. Su, Evidence for upper crustal anisotropy in the Songpan Ganze (northeastern Tibet) terrane, *Earth Planet. Sci.*, *203*, 25–33, 2002.

Viljanen, A., R. Pirjola, and L. Häkkinen, An attempt to reduce induction source effects at high latitudes, *J. Geomag. Geoelectr.*, *45*, 817–831, 1993.

Viljanen, A., R. Pirjola, and O. Amm, Magnetotelluric source effect due to 3d ionospheric current systems using the complex image method for 1d conductivity structures, *Earth Planets Space*, *51*, 933–945, 1999.

Vilotte, J. P., R. Madariaga, M. Daigniéres, and O. Zienkiewicz, Numerical study of continental collision: Influence of buoyancy forces and initial stiff inclusion, *Geophys. J. R. Astron. Soc.*, *84*, 279–310, 1986.

Vozoff, K., The magnetotelluric method, *Electromagnetic methods in applied geophysics - Applications, Chapter 8*, 1991.

Waff, H. S., Theoretical considerations of electrical conductivity in a partially molten mantle and implications for geothermometry, *J. Geophys. Res.*, *79*(26), 4003–4010, 1974.

Walker, J. D., and J. W. Geissman, compilers, Geologic Time Scale, *Geological Society of America*, 2009.

Wan, X., L. Wang, C. Wang, and J. Luba, Discovery and significance of Cretaceous fossils from the Xigaze Forearc Basin, Tibet, *Journal of Asian Earth Sciences*, *16*, 217–233, 1998.

Wang, C., Z. Liu, H. Yi, X. Zhao, and S. Liu, Tertiary crustal shortening and peneplanation in the Hoh Xil region: implications for the tectonic history of the northern Tibetan Plateau, *J. Asian Earth Sci.*, *20*, 211–223, 2002.

Wang, C., et al., Constraints on the early uplift history of the Tibetan Plateau, *PNAS*, *105(13)*, 4987–4992, 2008.

Wang, C. Y., L. Zhu, H. Lou, B. S. Huang, Z. Yao, and X. Lou, Crustal thicknesses and poisson's ratios in the eastern Tibetan plateau and their tectonic implications, *J. Geophys. Res.*, *115*(B11301), 2010a.

Wang, D. J., M. Mookherjee, Y. S. Xu, and S. Karato, The effect of water on the electrical conductivity of olivine, *Nature*, *443(7114)*, 977–980, 2006.

Wang, E., and B. C. Burchfiel, Interpretation of Cenozoic tectonics in the right-lateral accommodation zone between the Ailao Shan shear zone and the eastern Himalayan syntaxis, *Int. Geol. Rev.*, *39*, 191–219, 1997.

Wang, E., B. C. Burchfiel, L. H. Royden, Z. Chen, J. Chen, W. Li, and Z. Chen, Late Cenozoic Xiangshuihe-Xiaojiang, Red River, and Dali fault systems of southwestern Sichuan and central Yunnan, China, *China. Geol. Soc. Am. Spec.*, *327*, 1–108, 1998.

Wang, Q., and M. P. Coward, The Qaidam basin (nw china): formation and hydrocarbon potential, *J. Pet. Geol.*, *13*, 93–112, 1990.

Wang, Q., S. L. Chung, X. H. Li, D. Wyman, Z. X. Li, W. D. Sun, H. N. Qiu, Y. S. Liu, and Y. T. Zhu, Crustal Melting and Flow beneath Northern Tibet: Evidence from Mid-Miocene to Quaternary Strongly Peraluminous Rhyolites in the Southern Kunlun Range, *Journal of Petrology, pusblished online on October 4*, 2012.

Wang, Q., et al., Eocene north-south trending dikes in central Tibet: New constraints on the timing of east-west extension with implication for early plateau uplift, *Earth and Planetary Science Letters*, *298*, 205–216, 2010b.

Wang, Y., W. D. Mooney, X. Yuan, and R. G. Coleman, The crustal structure from the Altai Mountains to the Altyn Tagh fault, *J. Geophys. Res.*, *108*(2322), 2003.

Wannamaker, P. E., Comment on "the petrologic case for a dry lower crust" by Bruce W. D. Yardley and John W. Valley, *Journal of Geophysical Research*, *105*(B3), 6057–6064, 2000.

Wannamaker, P. E., Anisotropy Versus Heterogeneity in Continental Solid Earth Electromagnetic Studies: Fundamental Response Characteristics and Implications for Physicochemical State, *Surveys in Geophysics*, *265*(6), 733–765, 2005.

Wannamaker, P. E., J. A. Stodt, and L. Rijo, A stable finite element solution for twodimensional magnetotelluric modelling, *Geophysical Journal of the Royal Astronomical Society*, *88*, 277–296, 1987.

Wannamaker, P. E., et al., Lithospheric dismemberment and magmatic processes of the Great Basin-Colorado Plateau transition, Utah, implied from magnetotellurics, *Geochem. Geophys. Geosyst.*, *9*(Q05019), 2008.

Washburn, Z., J. R. Arrowsmith, G. Dupont-Nivet, W. X. Feng, Z. Y. Qiao, and C. Zhengle, Paleoseismology of the Xorxol Segment of the Central Altyn Tagh Fault, Xinjiang, China, *Annali di Geofisica*, *46*, 1015–1034, 2003.

Watanabe, T., and K. Kurita, The relationship between electrical conductivity and melt fraction in a partially molten system: Archie's law behaviour, *Phys. Earth Planet. Inter.*, *78*, 9–17, 1993.

Waxman, M. H., and L. J. Smits, Electrical Conduction in Oil Bearing Sands, *Soc. Petr. Eng. J.*, *8*, 107–122, 1968.

Weaver, J. T., A. K. Agarwal, and F. E. M. Lilley, Characterization of the magnetotelluric tensor in terms of its invariants, *Geophysical Journal International*, *141*, 321–336, 2000.

Wei, W., S. Jin, G. Ye, M. Deng, H. Tan, M. Unsworth, J. Booker, A. G. Jones, and S. Li, Features of faults in the central and northern Tibetan plateau based on results of INDEPTH (III)-MT, *Front. Earth Sci. China*, *1(1)*, 121–128, 2007.

Wei, W., et al., Detection of widespread fluids in the Tibetan crust by magnetotelluric studies, *Science*, *292*, 716–718, 2001.

Weidelt, P., The inverse problem of geomagnetic induction, *Z. Geophys.*, *38*, 257–289, 1972.

Weidelt, P., 3D Conductivity Models: Implications of Electrical Anisotropy, *Geophys. Dev. Series, Soc. Explor. Geophys., Tulsa*, *7*, 119–137, 1999.

Weinberg, R. F., G. Mark, and H. Reichardt, Magma ponding in the Karakoram shear zone, Ladakh, NW India, *Geological Society of America Bulletin*, *121*, 278–285, 2009.

Weislogel, A. L., Tectonostratigraphic and geochronologic constraints on evolution of the northeast Paleotethys from the Songpan-Ganzi complex, central China, *Tectonophysics*, *451*, 331–345, 2008.

Wen, D. J., S. L. Chung, D. Y. Liu, J. Q. Ji, M. F. Chu, B. Song, C. H. Lo, and T. Y. Lee, New SHRIMP U-Pb zircon ages from the Gangdese batholith and implications for the trans-Himalayan magmatic evolution, *Abst. EGS-AGU-EUG Joint Meeting*, p. 494, 2003.

Whipple, K. X., The influence of climate on the tectonic evolution of mountain belts, *Nature Geoscience*, *2*, 97–104, 2009.

Whittington, A. G., A. M. Hofmeister, and P. I. Nabelek, Temperature-dependent thermal diffusivity of the earth's crust and implications for magmatism, *Nature*, *458*, 319–321, 2009.

Wiese, H., Geomagnetische tiefentellurik. ii. die streichrichtung der untergrundstrukturen des elektrischen widerstandes, erschlossen aus geomagnetischen variationen, *Geofis. Pura Appl.*, *52*, 83–103, 1962.

Wittlinger, G., F. Masson, G. Poupinet, P. Tapponnier, G. Hequel, J. Guilbert, U. Achauer, X. Guanqi, and S. Danian, Seismic tomography of northern Tibet and Kunlun: Evidence for crustal blocks and mantle velocity contrasts, *Earth Planet. Sci. Lett.*, *139*, 263–279, 1996.

Wittlinger, G., P. Tapponnier, G. Poupinet, J. Mei, D. Shi, G. Herquel, and F. Masson, Tomographic evidence for localized lithospheric shear along the Altyn Tagh fault, *Science*, *282*, 74–76, 1998.

Wittlinger, G., J. Vergne, P. Tapponnier, V. Farra, G. Poupinet, M. Jiang, H. Sud, G. Herquel, and A. Paul, Teleseismic imaging of subducting lithosphere and Moho offsets beneath western Tibet, *Earth and Planetary Science Letters*, *221*, 117–130, 2004.

Worzewski, T., M. Jegen, H. Kopp, H. Brasse, and W. T. Castillo, Magnetotelluric image of the fluid cycle in the Costa Rican subduction zone, *Nature Geoscience*, *4*, 108–111, 2011.

Xia, L., Z. Xia, and X. Xu, Origin of the oceanic island arc system in the northern qilian shan, *Beijing: Geological Publishing House*, p. 153, 1996.

Xie, J., R. Gok, J. Ni, and Y. Aoki, Lateral variations of crustal seismic attenuation along the INDEPTH profiles in Tibet from Lg Q inversion, *J. Geophys. Res.*, *109*(B10308), 2004.

Xu, R., Y. Zhang, Y. Xie, ph[] Vidal, and N. Arnaud, *Geological Evolution of the Karakorum and Kunlun Mountains*, chap. Isotopic geochemistry of plutonic rocks, pp. 137–186, P. Yusheng ed., Beijing: Seismological Press, 1996.

Xu, Y., T. J. Shankland, and B. T. Poe, Laboratory-based electrical conductivity in the Earth's mantle, *J. Geophys. Res.*, *105(B12)*, 27,865–27,875, 2000.

Yang, J. S., P. T. Robinson, C. F. Jiang, and Z. Q. Xu, Ophiolites of the Kunlun Mountains, china and their tectonic implications, *Tectonophysics*, *258*, 215–231, 1996.

Yang, Y., M. H. Ritzwoller, Y. Zheng, W. Shen, A. L. Levshin, and Z. Xie, A synoptic view of the distribution and connectivity of the mid-crustal low velocity zone beneath Tibet, *J. Geophys. Res.*, *117*(B04303), 2012.

Yao, H. J., C. Beghein, and R. D. Van Der Hilst, Surface wave array tomography in SE Tibet from ambient seismic noise and two-station analysis-II. Crustal and upper-mantle structure, *Geophysical Journal International*, *173*, 205–219, 2008.

Yardley, W. D., and W. Walley, The petrologic case for a dry lower crust, *J. Geophys. Res.*, *102*, 12,173–12,185, 1997.

Yardley, W. D., and W. Walley, Comment on "the petrologic case for a dry lower crust" by Bruce W. D. Yardley and John W. Valley - reply, *J. Geophys. Res.*, *105*(B3), 6065–6068, 2000.

Yin, A., Mode of Cenozoic east-west extension in Tibet suggestinga common origin of rifts in asia during the Indo-Asian collision, *J. Geophys. Res.*, *105*(B9), 21,745–21,759, 2000.

Yin, A., and T. M. Harrison, Geologic Evolution of the Himalayan-Tibetan Orogen, *Annual Review of Earth and Planetary Sciences*, *28(1)*, 211–280, 2000.

Yin, A., and S. Nie, An indentation model for North and South China collision and the development of the Tanlu and Honam fault systems, eastern Asia, *Tectonics*, *12*, 801–813, 1993.

Yin, A., and S. Nie, A phanerozoic palinspastic reconstruction of China and its neighboring regions, *In The Tectonics of Asia, ed. A. Yin, T.M. Harrison, New York: Cambridge Univ. Press*, pp. 442–485, 1996.

Yin, A., P. Kapp, C. E. Manning, T. M. Harrison, L. Din, and X. Deng, Extensive exposure of Mesozoic melange in Qiangtang and its role in the Cenozoic development of the Tibetan plateau, *Eos*, *79*, 816, 1998.

Yin, A., T. M. Harrison, M. A. Murphy, M. Grove, S. Nie, F. J. Ryerson, W. X. Feng, and C. Z. Le, Tertiary deformation history of southeastern and southwestern tibet during the indo-asian collision, *Geol. Soc. Am. Bull.*, *111*, 1644–1664, 1999a.

Yin, A., P. A. Kapp, M. A. Murphy, C. E. Manning, M. Harrison, M. Grove, L. Ding, X. G. Deng, and C. M. Wu, Significant late Neogene east-west extension in northern Tibet, *Geology*, *27*, 787–790, 1999b.

Yin, A., X. Chen, M. W. McRivette, L. Wang, and W. Jiang, Cenozoic tectonic evolution of qaidam basin and its surrounding regions (part 1): The north qaidam thrust system, *Geological Society of America Bulletin*, *120*, 813–846, 2008.

Yin, J., J. Xu, C. Liu, and H. Li, The Tibetan plateau: regional stratigraphic context and previous work, *Phil. Trans. R. Soc. Lond.*, *A327*, 5–52, 1988.

Yoshino, T., Laboratory Electrical Conductivity Measurement of Mantle minerals, *Surveys in Geophysics*, *31*(2), 163–206, 2010.

Yoshino, T., T. Matsuzaki, S. Yamashita, and T. Katsura, Hydrous olivine unable to account for conductivity anomaly at the top of the asthenosphere, *Nature*, *437*, 249–252, 2006.

Yoshino, T., G. Manthilake, T. Matsuzaki, and T. Katsura, The effect of water on the electrical conductivity of olivine aggregates and its implications for the electrical structure of the upper mantle, *Earth Planet. Sci. Lett.*, *288(1-2)*, 291–300, 2009.

Yu, L., R. L. Evans, and R. N. Edwards, Transient electromagnetic responses in seafloor with triaxial anisotropy, *Geophys. J. Int.*, *129*, 292–304, 1997.

Zhang, J., Z. Xu, H. Xu, and H. L. H., Framework of north qilian caledonian subduction-accretionary wedge and its deformation dynamics, *Sci. Geol. Sin.*, *33*, 290–299, 1998.

Zhang, K. J., Qiangtang block reveal deep crustal structure of northern Tibet: Comment, *Geology*, *29*, 90, 2001.

Zhang, P. Z., Z. Shen, M. Wang, W. J. Gan, R. Burgman, and P. Molnar, Continuous deformation of the Tibetan Plateau from global positioning system data, *Geology*, *32*, 809–812, 2004.

Zhao, J., et al., The boundary between the Indian and Asian tectonic plates below Tibet, *Proceedings of the National Academy of Sciences*, doi:10.1073/pnas.1001921107, 2010.

Zhao, W., K. D. Nelson, and Project INDEPTH, Deep seismic reflection evidence for continental underthrusting beneath southern Tibet, *Nature*, *366*, 557–559, 1993.

Zhao, W., et al., Crustal structure of central Tibet as derived from project INDEPTH wide-angle seismic data, *Geophys. J. Int.*, *145*, 486–498, 2001.

Zhao, W., et al., Tibetan plate overriding the Asian plate in central and northern Tibet, *Nature Geosci.*, *4*, 870–873, 2011.

Zhou, D., and S. A. Graham, Songpan-Ganzi Triassic flysch complex as a remnant ocean basin along diachronous collision orogen, central China, *Geol. Soc. Am. Abstr. with Programs*, *25*, A118, 1993.

Zhou, D., and S. A. Graham, *The Tectonic Evolution of Asia*, chap. The Songpan-Ganzi complex of the western Qinling Shan as a Triassic remnant ocean basin, pp. 486–640, A. Yin and T. M. Harrison ed., Cambridge Univ. Press, New York, 1996.

Zhou, H., and M. Murphy, Tomographic evidence for wholesale underthrusting of India beneath the entire Tibetan plateau, *J. Aeronaut. Sci.*, *25*, 445–457, 2005.

Zhu, D. C., X. X. Mo, Y. Niu, Z. D. Zhao, L. Q. Wang, G. T. Pan, and F. Y. Wu, Zircon U-Pb dating and in-situ Hf isotopic analysis of Permian peraluminous granite in the Lhasa terrane, southern Tibet: Implications for Permian collisional orogeny and paleogeography, *Tectonophysics*, *469*, 48–60, 2009.

Zhu, D. C., X. X. Mo, Z. D. Zhao, Y. Niu, L. Q. Wang, Q. H. Chuand, G. T. Pan, J. F. Xu, and C. Y. Zhou, Presence of Permian extension and arc type magmatism in southern Tibet: Paleogeographic implications, *Geol. Soc. Am. Bull.*, *122*, 979–993, 2010.